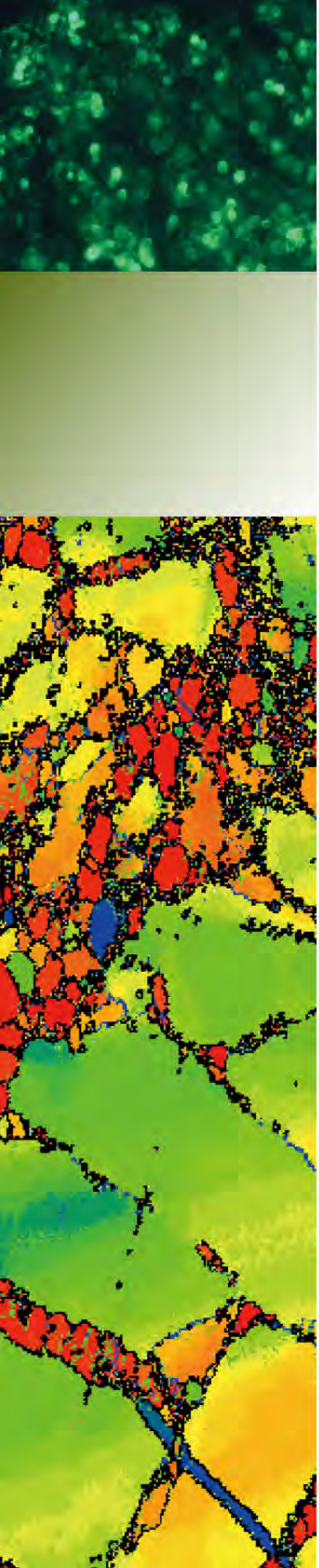

Vol.1 ,No.1, July 2012

Transactions on GIGAKU

Nagaoka University of Technology

2012 Editorial Board

Aim

What is GIGAKU? GIGAKU is a term composed of two Japanese word-roots; GI and GAKU. The word GI〔技〕literally stands for all kinds of arts and technology, and GAKU〔学〕stands for scientific disciplines in general when used as a suffix. The term was originally coined to describe the fundamental philosophy of education and research of Nagaoka University of Technology (NUT) when it was established in 1976. Through this term the founders of NUT intended to express their recognition that all technical challenges in the real world require a scientific approach. And NUT has a relentlessly pursued GIGAKU since then.

Thirty-five years have passed and all surrounding conditions have changed dramatically during those years. We are witnessing rapidly globalizing economics and huge scale changes in demographic, industrial and employment structures. All those changes seem to necessitate the further evolution of GIGAKU. In response to this, NUT recently announced its new “Growth Plan” and a renewed definition of the term is given;

> *GIGAKU is a science of technologies, which gives us an angle to analyze and reinterpret diverse technical processes and objects and thus helps us to advance technologies forward. By employing a broad range of knowledge about science and engineering, management, safety, information technology and life sciences, GIGAKU provides us with workable solution and induces future innovations.*

Nagaoka University of Technology has decided to launch “Transactions on GIGAKU”, which is an online journal (free access) focused on the science and technology related to GIGAKU. The mission of this journal is to spread out the concept of GIGAKU and the fruits of GIGAKU to the global world and to be a strong network for innovations in science and technology and for development of next generations of high-level human resources. This journal, therefore, covers education and research activities related to GIGAKU in broad areas.

Submission and Publishing

"Transactions on GIGAKU" publishes feature issues focusing on education, science, and technology related to GIGAKU. Special issues aligned with conferences are strongly concerned, and guest editors are welcomed. Papers submitted are peer-reviewed before publication.

Publication charge is free for all submitted papers.

Copyright

Transactions on GIGAKU

Volume 1, No. 1, July 2012

The 1st International GIGAKU Conference in Nagaoka (IGCN)
(February 3-5, 2012, Nagaoka University of Technology, Nagaoka, Japan)

The IGCN is designed and organized to provide a cross-border, cross-sector, cross-disciplinary forum for those researchers, educators, and industrial leaders who are creating and practicing GIGAKU in various technology domains in various countries. Some papers presented in the IGCN are published in this first volume of Transactions on GIGAKU.

Table of contents

Transactions on GIGAKU ***1****(2012)01001/1-6*

Engineering Terminology Dictionary: Lessons Learnt from Meiji Japan and NUT-KOSEN's Initiative

Yoshiki Mikami*, Naoko Lee Iizuka*, Kenjiro Nagano*, Katsuko T. Nakahira*
Yoshinori Naruse, Chikatoshi Yamada***, Yoshiko Kawamura******
*Nagaoka University of Technology, **Toyama National College of Technology,*
****Okinawa National College of Technology, ****Tokyo International University*
**1603-1 Kamitomioka-cho, Nagaoka 940-2188, Japan*
**E-mail: mikami@kjs.nagaokaut.ac.jp*

The first part of this paper reviews historical lessons learnt from the experience of Meiji Japan regarding the teaching medium of engineering education. The importance of mother language use in engineering education and of terminology development is illustrated based on findings from investigations on historical documents. The second part of this paper introduces the response of Nagaoka University of Technology and National College of Technology (KOSEN) to those lessons. The language coverage and vocabularies of the Multilingual Engineering Terminology Dictionary developed by the Engineering Dictionary Committee of the university are presented.

1. Introduction

In the first International GIGAKU Conference in Nagaoka (IGCN 2012), Kozo Ishizaki, the former Vice President of Nagaoka University of Technology (NUT) and the chairman of NUT's Engineering Dictionary Committee, stated that "(an) important aspect (of industrial development) is language used in development. Japanese tried to translate every European concept into Japanese for general Japanese people to be blessed by the modern scientific development. It is important not to divide a society into English speaking and non-English speaking classes."

Although engineering subjects were taught in English at the first engineering college of Japan—the Imperial College of Engineering (Kōbu Dai-gakkō)—from the early Meiji period, serious and continuous efforts have been made by pioneering teachers in engineering to translate basic engineering terminologies into Japanese language; gradually, teaching materials had been developed based on these achievements. These sets of teaching materials were the basis of concerted efforts in engineering education and human development in Japan. Without such efforts, the quick adoption of imported technologies, and therefore the rapid industrialization of Meiji-era Japan, might not have been possible.

Similarly, international students currently studying at NUT should be encouraged to propagate their knowledge to people in their native countries using mother language terminology. This recognition and reasoning has formed the basis of the development of a series of trilingual engineering terminology dictionaries by NUT during the last five years.

2. Language used in Engineering Education in Meiji Japan

The first engineering education program was formulated by the initiative of the Meiji government in the 1870s, only a few years after the Meiji Restoration. The Imperial College of Engineering, the cradle of engineering education of modern Japan, was established in Tokyo in 1873 [1]. All teaching staff members were invited from Europe, with the majority of the staff hailing from Scotland, where professional engineering education had been implemented since the early nineteenth century and was considered to be the most advanced engineering education center in the world. The first president of the college, Henry Dyer, came from Glasgow v the nomination by Sir William Thomson.

In this newly-created college, all subjects were taught in English. Applicants to the college had to pass through an entrance examination which included among its subjects English language ability. The weekly calendar of the college shows that students studied English language for two hours every day from Mondays to Fridays during their first two years in the college [2]. At the end of six years of education, students had to submit theses also written in the English language.

The college was later merged with the Imperial University (renamed again to the Imperial University of Tokyo later), when the latter was formulated as a central institute for higher education of Meiji Japan. A lecture notebook and examination paper on "Hydraulics and Hydraulic Machinery" written by Professors Bunji Mano and Ariya Inokuchi of the Department of Mechanical Engineering of the Imperial University of Tokyo has been preserved, and it reveals that lectures and examinations were conducted in English even 40 years after the beginning of engineering education in Japan (**Figure 1**). Professor Mano was the first president of the Japanese Society of Mechanical Engineers (JSME), and the notebook and examination paper were designated as Mechanical Engineering Heritage Documents by the JSME in 2007.

Fig. 1 Lecture Notebook and Examination Paper on "Hydraulics and Hydraulic Machinery" by Professors Bunji Mano and Ariya Inokuchi at the Imperial University of Tokyo, circa 1906.

Takahashi et al [3] conducted an investigation of an archived collection of 2,913 theses submitted by students from both the Imperial College of Engineering (1879-1885) and the Imperial University of Tokyo (1885-1934), and categorized the theses in mechanical, electrical engineering and architecture by languages used. The number of theses according to language is shown in **Figure 2** This result provides succinct evidence of the situation described above.

In the field of mechanical engineering, all theses were written in English until as late as the mid-1910s. In electrical engineering, the vast majority of theses were written in English until as late as the 1920s. In architecture, however, there appeared several differences with the fields of engineering: the researchers found several theses written in Japanese early in the Meiji era, but it was found that these papers were exceptions, and were regarding traditional Japanese temple architecture.

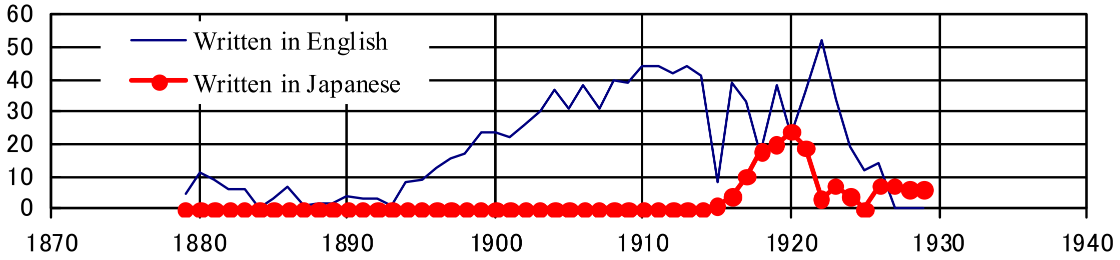

Fig. 2a Number of theses in selected engineering field by language (mechanical engineering)

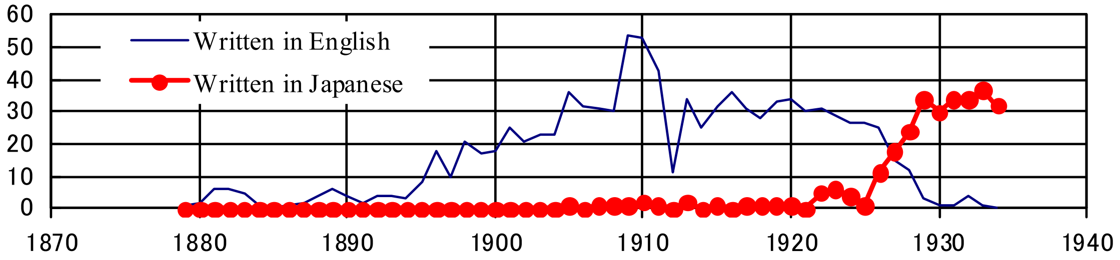

Fig. 2b Number of theses in selected engineering field by language (electrical engineering)

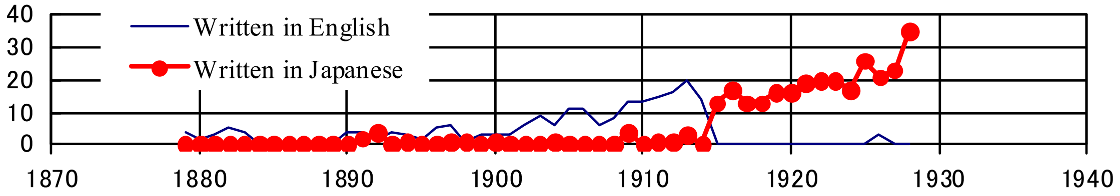

Fig. 2c Number of theses in selected engineering field by language (architecture)

3. The First English-Japanese Engineering Terminology Dictionary

An early Meiji-era philosopher/politician Tatsui Baba (1850-1888, **Figure 3**) expressed his objection to the opinion of the then-education minister Arinori Mori, who advocated adopting English as the official language of newly-born Japan. Baba wrote about the importance of the mother language in preface of his book “Elementary Grammar of the Japanese Language” published in 1873 in London.

> We must try to educate the whole mass of the people and unite them into one, in order to promote the common happiness of the community…. Mr. W.D. Whitney, in his letter to Mr. Mori, says, “Even with a fully developed system of national instruction, it would take a very long time to teach a strange language to so large a part of the population as to raise the letter, in general, to a perceptibly higher level. If the masses to be reached, it must be mainly through their native speech.” We think, also, that it is more desirable to try to enrich and complete that which we have already.[4]

Baba’s concern was exactly the same as that of Professor Ishizaki as mentioned above. Furthermore, in order to enrich and enable a national language to be used for professional education in various subjects, the most urgent and important challenge is to create a sufficient set of vocabulary and terminology in various professional domain areas, such as medicine, engineering, and jurisdiction.

In the field of engineering, efforts had been made to enrich Japanese technical terminology by many voluntary contributors since the Meiji period. The first major step in the development of engineering terminology development was the publication of an English-Japanese Engineering Terminology Dictionary “KOGAKU JII” (**Figure 4**). This dictionary was compiled by a railway engineer named Ryutaro Nomura (1859-1943). He studied at the Imperial University and the dictionary was published by the Engineering Society of Japan in August 1886. Over 6000 engineering terms were covered by this single volume. It is interesting to observe that in this publication, Japanese characters are printed in the traditional vertical orientation, while English terms are in the horizontal orientation (**Figure 4,** right side). This dictionary was followed by continuous expansion and improvements of terminology development and publication of dictionaries. This resulted in increased access to new knowledge in engineering not only for scholars in universities, but also to members of the general public with insufficient fluency in English, especially technicians at workshops, as well as teachers and students at trade schools.

Fig. 3 Photo of Tatsui Baba, date un known

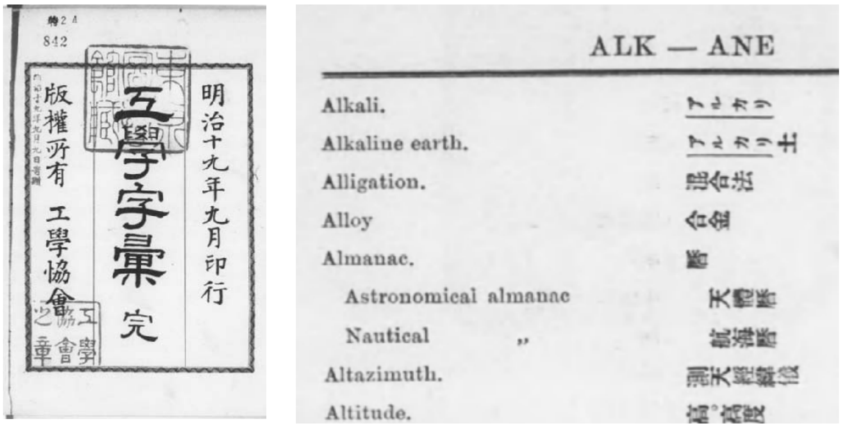

明治十九年九月印行
工學字彙 完
版權所有 工學協會

ALK — ANE

Alkali.	アルカリ
Alkaline earth.	アルカリ土
Alligation.	[illegible]
Alloy	合金
Almanac.	[illegible]
Astronomical almanac	[illegible]
Nautical ,,	[illegible]
Altazimuth.	[illegible]
Altitude.	[illegible]

Fig. 4 The First English-Japanese Engineering Dictionary published in 1886 – Front cover (left) and the first page starting from "Alkali" (right)

Based on achievements in language enrichment and empowerment, the number of books on engineering subjects gradually increased. As shown in **Figure 5**, although there have been books published in Japanese in the fields of mathematics (sūgaku) and physics (butsurigaku) since 1870, books in mechanical engineering (kikai kōgaku) written in Japanese had been published at significant volume only after the turn of the century. Before the publication of the first engineering dictionary in 1886, only four books in Japanese had been published for mechanical engineering. While other factors may have accounted for the observed differences among the different fields—such as the number of potential readers and the nature of the subject matter (basic versus applied) —it is logical that without appropriate terminologies in a mother language, it becomes impossible to publish in-depth technical books in any specialist field in that language.

The lessons learned from this historical experience of Meiji Japan may also apply to present-day countries that are undergoing industrial development. In order to create a broad basis of human resources for industrial development, engineering education should be conducted in each country's mother language. It therefore requires a sufficient set of terminologies translated into mother language. The recognition of the necessity of terminology development led to the decision by NUT to develop a series of engineering terminology dictionary into various languages in order to support the education of engineer students from other countries.

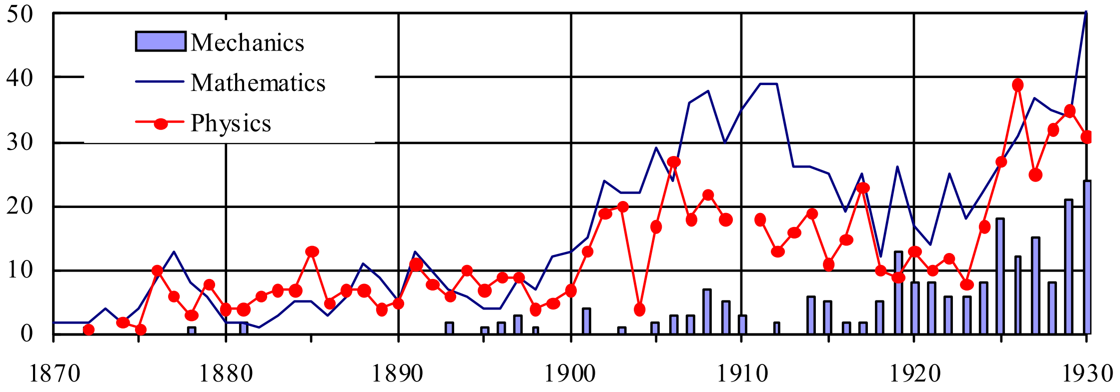

Fig. 5 Number of books in mechanics, mathematics and physics written in Japanese language and published in Japan during 1870-1930. Source: Takahashi et al.[3]

4. Language-based Composition of International Students at NUT

The question that presented itself was for which language should such a dictionary be developed? To address this question, NUT's Engineering Dictionary Committee has set the following selection criteria: (1) the population of international students by country currently enrolled in NUT ; (2) the usage level of their mother language in engineering education in the students' home countries. The first criterion means that the larger the population of speakers of a particular language at NUT campus, the higher the priority given to that language. The second criterion means that if a mother language is not used extensively at home in engineering education, a lower priority is given to that language. This second criterion was added because many countries in Asia actually use English for higher education, including education in engineering. These countries include India, the Philippines, Sri Lanka, and Myanmar.

In terms of the number of speakers for each language, we designated ten languages as the major foreign languages spoken at the NUT campus (**Table 1**). Among these, Myanmar and Sinhalese were dropped due to the second selection criterion, i.e., in Myanmar and Sri Lanka, higher education is given in English. Although Korean and Mongolian have relatively few speakers in NUT at the time of this survey, the Committee decided to add these two languages; the former was added because of its potential importance and geographical proximity to Japan, and the latter was added because of its large presence at Kosen (the National College of Technology).

Table 1 Top ten languages spoken at NUT campus

Language	Number of students		Countries and regions
	As of May 2011	Past maximum	
Vietnamese	80	80	Vietnam
Chinese	54	54	China, Taiwan
Malay	45	76	Malaysia, Brunei, Singapore, etc.
Thai	30	39	Thailand
Spanish	29	41	Mexico, Venezuela, etc.
Myanmar	10	14	Myanmar
Indonesian	7	21	Indonesia
Sinhalese	4	5	Sri Lanka
Mongolian	3	6	Mongolia, China
Korean	2	7	Korea

5. Outline of NUT Multilingual Engineering Terminology Dictionary

After employing the selection criteria, eight languages were chosen for the publication of a multilingual engineering terminology dictionary. The languages were Vietnamese, Chinese, Malay, Thai, Spanish, Indonesian, Korean and Mongolian. Each version of the dictionary contains trilingual entries, i.e., the target language, Japanese and English (**Figure 6**). Users can search for terms using Romanized Japanese spelling arranged in alphabetical order. The Vietnamese version of this dictionary was published in 2008 by a commercial publisher both in Japan and Vietnam [5] [6], and other language versions were printed as private publications of NUT.

The web version also contains terminologies in Lao, Myanmar, and Sinhalese (**Figure7**). This web version is accessible at http://gii2.nagaokaut.ac.jp/mtd/ [7].

Fig. 6 Dictionary page layout displaying engineering terms in Japanese, English, and the target language; in this case, Vietnamese.

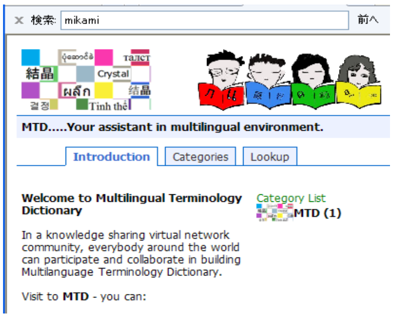

検索: mikami

MTD.....Your assistant in multilingual environment.

Welcome to Multilingual Terminology Dictionary

In a knowledge sharing virtual network community, everybody around the world can participate and collaborate in building Multilanguage Terminology Dictionary.

Visit to **MTD** - you can:

Fig. 7a Web version (top page)

hydrogen bond

Japanese	: 水素結合
Thai	: แขนไฮโดรเจน
Chinese	: 氢键
Korean	: 수소 결합
Malay	: ikatan hidrogen
Vietnamese	: Liên kết hydro
Lao	: · · · · · · · · · ·
Mongolian	: зангуун цаг
Indonesian	: ikatan hidrogen
Sinhala	: · · · · · · · · · ·
Spanish	: enlace de hidrógeno
Myanmar	: ဟိုက်ဒရိုဂျင်စည်း
Romanization	: suiso ketsugou

Fig. 7b Web version (Multilingual page)

The vocabulary set available in the current dictionary is composed of basic terms from major engineering and science subjects taught at NUT campus, namely Civil Engineering, Mechanical Engineering, Architecture, Chemical Engineering, Communication Engineering, Computer Science, Control Engineering, Electric and Electronics, Navigation, Mathematics and Physics. The number of technical terms categorized by subject field is shown in **Table 2**.

Table 2 Number of terms by field

Field of engineering	Number of terms	Field of engineering	Number of terms
Civil Engineering	1,263	Control Engineering	1,545
Mechanical Engineering	1,186	Electric and Electronics	1,200
Architecture	1,798	Navigation	1,403
Chemical Engineering	958	Mathematics	1,284
Communication Engineering	1,410	Physics	945
Computer Science	1,538	Total	14,530

Note: Total number contains duplications in some terms

6. Conclusion

NUT will continue its efforts to enrich the contents of the dictionaries and improve access to these resources by means of online access, as well as the development and commercial publication of pocket dictionaries. Developing an online dictionary of engineering terminology is also critical for international students at KOSEN, because these students are required to self-learn basic specialized subjects at their own pace to catch up with classes. Therefore, there is an urgent need to develop and provide effective self-studying materials for e-learning, supported by the use of an online dictionary of engineering terminology. This type of self-studying environment would enable international students to expand their technical terms and understanding of engineering, and reduce the language barriers between lecturer and student. International students would be better equipped to learn from classes conducted in Japanese, and be at less of a disadvantage when compared to their Japanese peers. This in turn would facilitate a more effective education system, and thereby producing better-educated and competent engineers. The authors encourage feedback and suggestions from readers and users of the dictionary in order to ensure that these resources are consistently improved.

Acknowledgments

This work was supported by a Grant-in-Aid for Scientific Research from the Ministry of Education, Culture, Sports, Science and Technology (MEXT), Japan.

References

[1] Anonymous, An Engineering College in Japan, Nature, April 3, 1873, p. 430 and C.W.C., Engineering Education in Japan, Nature, May 17, 1877, pp. 44–45.

[2] Imperial College of Engineering Tokei, Calendar, Session 1876-77, 1976, p.23.

[3] T. Takahashi, M. Matsuda, S. Kamimura, and Y. Mikami, Language of thesis in early days of engineering education in Japan, The 4th Int'l Symposium on Technological Innovation in Japan, National Museum of Science, Tokyo, Dec. 10, 2008.

[4] T. Baba, An Elementary Grammar of the Japanese Language with Easy Progressive Exercises, London, Trubner and Co., 1873, pp. x-xi

[5] Japanese–Vietnamese (English) Technological Term Dictionary (Nichi-Etsu Kōgaku Yōgo Jiten), Shumpūsha Publishing, 2008.

[6] Từ điển thuật ngữ khoa học Nhật Việt, 2008. Publication in Vietnam is arranged by Oriental Language and Culture Department, Foreign Languages College, Hanoi National University.

[7] O. Htun, Y, Mikami et al. Int. Conf. Computer Applications (ICCA2009), Yangon, February 26–27, 2009.

(Received: 23 May, 2012, Accepted: 12 June, 2012)

Transaction on GIGAKU **1** *(2012) 01002/1-5*

Interdisciplinary Education through Double Degree Programs between Universidad de Guanajuato and Nagaoka University of Technology

Takaomi Kobayashi[1], Sergio Arias-Negrete[2] and Satoshi Sugita[3],

[1] *Department of Materials Science and Technology, Nagaoka University of Technology*
1603-1 Kamitomioka, Nagaoka, Niigata 940-2188, Japan
[2]*Universidad de Guanajuato, Dirección de Cooperación Académica, Lascuráin de Retana No. 5; CP 36000, Guanajuato, Gto., México, sergio@ugto.mx; 2Universidad de Guanajuato, 3 Departamento de Química, División de Ciencias Naturales y Exactas, Col. Noria Alta, CP 36050, Guanajuato, Gto., México;*
**E-mail: takaomi@nagaokaut.ac.jp*

Interdisciplinary education system through Double Degree Program (DDP) between Universidad de Guanajuato and Nagaoka University of Technology has been established as a new educational scheme on 2011. The present paper describes subjects on the master DDP for the innovative education system in order to enhance globalization of students and faculty staffs in both universities. The methodology and the goal of the program are introduced.
.

1. Introduction

Interdisciplinary education is nowadays very important to prepare future researchers in different areas to solve problems, innovate and promote development by using diverse approaches and perspectives. The objectives of the partnership are to be a common capacity and to enhance each other program by cooperating different areas. Thus, to reach this goal, students require training using different methodologies, in order to achieve profound knowledge.

At present, international academic collaboration fosters joint research programs, and it requires student mobility among partners from Higher Education Institutions (HEI). A more complex academic collaboration is currently utilized by HEI. By offering Double Degree Program (DDP), which is a student's working for two different university degrees in parallel, either at the same institution or at different institutions, it has been advantage that both of the participating institutions reduce the amount of time required to be spent at each. Usually, the HEI is from different countries and the language of teaching is different. Therefore, there are some benefits for students pursuing a university academic degree, such as development of intercultural skills, proficiency in the foreign language of the host institution; and importantly, acquiring an international perspective of research and collaboration. Additional benefits are attained by the partner HEI, such as an increase of visibility and prestige, and achievement of a significant impetus in research graduate programs.

2. Higher Education Institutions in UG

The academic tradition and history of Universidad de Guanajuato (UG) date back to the eighteenth century, colonial era of the maximum blossoming of the Villa de Guanajuato afterwards a city since 1741 and its booming mines. The UG boasts an academic staff recognized for its high quality. This staff carries out essential work in the areas of instruction, research, and extension. Because of its quality teachers and the unceasing efforts of its academic bodies, the UG carries out more scientific research than any other institution of higher education in the state; its academic units, institutes, and research centers develop projects with regional applications in benefit of all the citizens of Guanajuato. The public institution in UG offering high school and university education, leader in the context of the Mexican educational system contains in these levels, and exemplary because its quality, coverage, equality and pertinence has been carried our with following academic structure by four campuses, Guanajuato, Celaya-Salvatierra, Irapuato-Salamanca, and León.

It has been noted that DDP offered by HEI from different continents is becoming a common practice as a part of their internationalization process. The UG is a comprehensive institution with a strong determination to instill an international dimension into its academic activities. This Desired

Scenario is indicated in its Development Plan for the 2010-2020 terms. UG is offering some DDP at undergraduate and graduate level, and new DDP for graduate studies are envisaged. The HEIs form Japan and UG have a long and strong academic relationship based on mutual trust and friendship.

Fig.1 Pictures of UG in Guanajuato campus (left) and research view in the chemistry laboratory at Noria Alta for the master DDP student of NUT (right).

3. Japan–Mexico–USA Consortium for Engineering Education

In 2003, Nagaoka University of Technology (NUT) and the UG signed a Letter of Intent for collaboration. The Japan–Mexico–USA Consortium for Engineering Education was created to foster academic collaboration and foundation of DDP, with the participation of NUT, The University of Texas at El Paso (UTEP), The Autonomous University of Ciudad Juarez, (UACJ), Universidad Michoacana de San Nicolás de Hidalgo (UM) and UG. Based upon strategies and concepts aimed at universities' internationalization through the Academic International Collaboration/Cooperative Support Interdisciplinary Program from 2009-2010, NUT was organized and developed engineering education programs accelerating internationalization under the sponsorship by the Ministry of Education, Culture, Sports, Science and Technology (MEXT). This interdisciplinary program developed interactive educational collaboration, such as a credit transfer system and double-degree programs with their foreign partners.

Based upon comprehensive and systematic education programs, it promoted cultivation approaches to leading edge engineering at each university. Through such an interdisciplinary program, we, the five universities of the consortium, could promote international contributions. Cooperation was made as the best use of regional characteristics on enable engineers and researchers to obtain training that included practical skills through close mutual academic exchange programs at the universities. In this consortium, five universities promoted a new mode of international collaboration and contribution for the development of leading engineers with practical and creative abilities. To undertake education of engineers and researchers with practical ability through an international collaboration system, NUT led the international collaboration system with mutual academic and educational cooperation under an interactively developed network (Fig. 2) for the purpose of following; 1) Implement interdisciplinary engineering education among consortium universities through the Master's Double Degree Program, especially streamlining collaboration through overseas internships and training engineers at enterprises in the areas of Mexico and the United States of America to achieve practical reeducation during graduate school,
2) Support for enhancement of international competition in accordance with the contribution toward human resources in overseas enterprises, especially in Japanese enterprises, and 3) Accelerate interdisciplinary education and research globalization through practical cooperation and development of joint international industry–academic research.

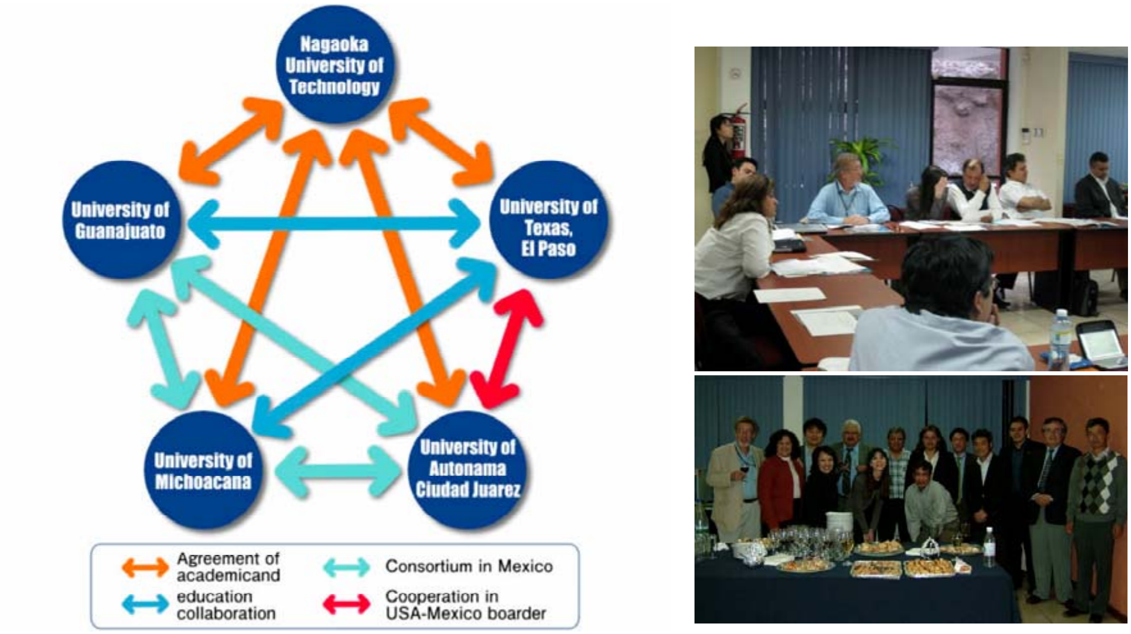

Fig. 2 Interactively developed network scheme in Japan–Mexico–USA Consortium for Engineering Education (right) and Guanajuato reunion in the consortium meeting on 2009 January 14th (left)

4. DDP program between NUT and UG

Implement was that interdisciplinary engineering education among consortium universities was through the Master's DDP, especially in streamlining collaboration through overseas internships and training Mexican students in engineer skill and practical knowledge. Among the consortium, the DDP in master course between NUT and UG was interdisciplinary challenge, which started on successfully to exchange their student candidates on August 2011. In addition with credit transfer system, the comprehensive and systematic education program also could promote cultivation approaches to leading edge engineering at each university. Especially, streamlining collaboration through overseas internships and enhancing exchange students between consortium members were achieved through the construction process.

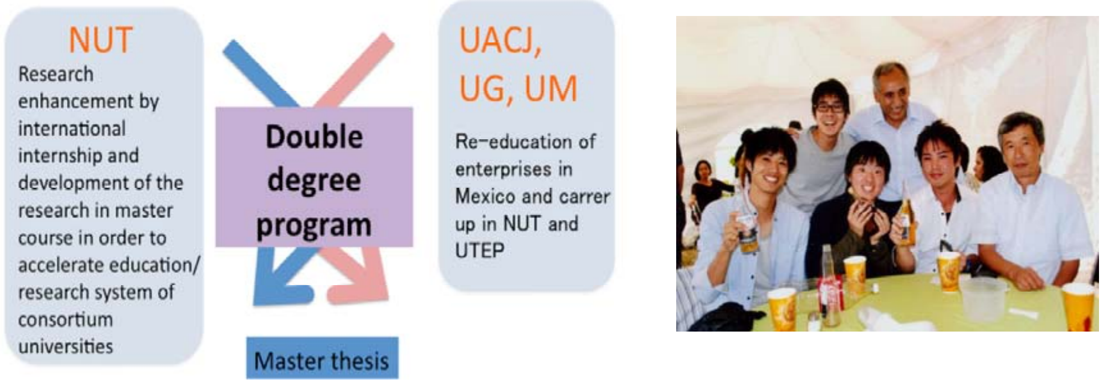

Fig. 3 Relationship scheme between NUT and consortium universities through DDP program in master program (right) and picture of exchange students with cooperation professors of the department of Chemistry in Noria Alta, Guanajuato (left)

At present, NUT and UG can offer a Master DDP, where NUT confers the Master in Engineering Degree and UG confers the Master in Science Degree. Both NUT and UG have agreed to establish a new DDP in their master courses. As presented in Fig. 4, the DDP is an academic program that can enable the students enroll in the graduate program at their Home University to transfer to the program at the Host University in order to obtain master degrees from both universities upon completion of their courses. Each graduate program has specific research projects, but the common link is the Chemical Sciences. In order to be eligible for the DDP program, the student candidates must pass the DDP screening examination held by the respective Host University and they have studied chemistry at the master’s level. As seen in achievement scheme of DDP between NUT and UG, the DDP has implemented according in the bilateral DDP between both universities. The period of stay at the Host University is for a period of one year or more, but not to exceed two years. Therefore, the students of UG can be enrolled in August each year for study lasting two and a half years to obtain a master's degree at both universities. On the other hand, the students of NUT can begin their studies in April of each year for a two-year study period. It is important to construct education systems of DDP in both universities. So, educational and research plans firstly are required for each DDP student, who is decided upon by prior consultation of the academic advisor (thesis supervisor) at the Home University and the Host University. Their plans are necessally for requiring the approval of the authorized committees at both universities and the academic advisor at the Host University ratifies the approval of such committee under its regulation. The academic advisor at the Host University can mainly supervise the DDP students with the assistance of the academic advisor at the Home University.

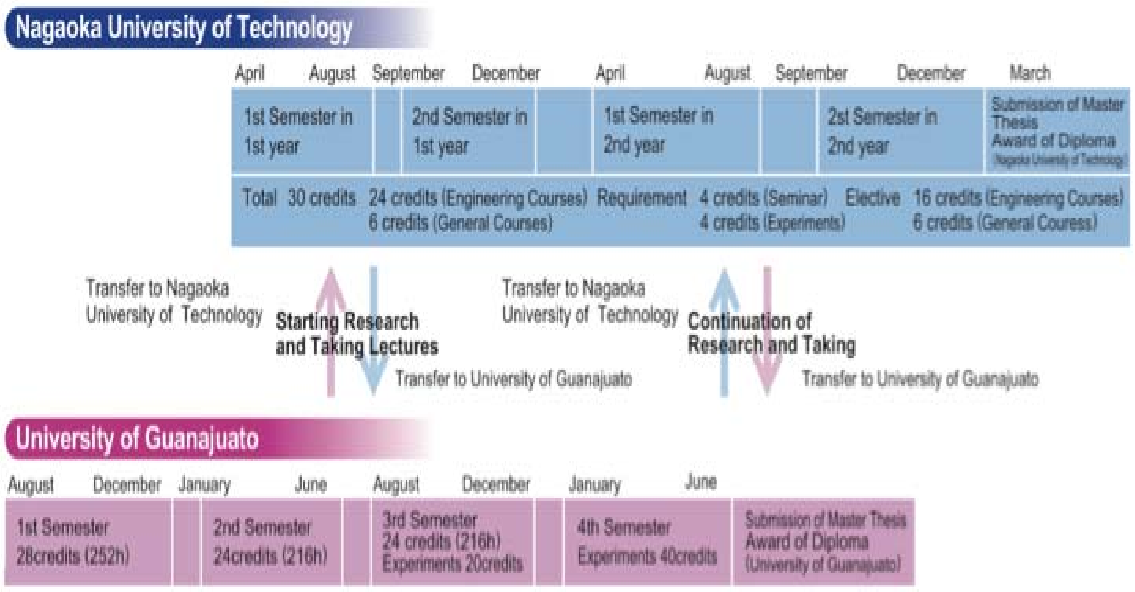

Fig. 4 Scheme of the master DDP between UG and NUT including student transfer from the host university to the guest one.

Moreover, doctoral in chemistry at UG is accredited by Consejo Nacional de Ciencia y Tecnología (CONACYT), whereas doctoral studies at NUT offer a multidisciplinary approach. Therefore, both NUT and UG have agreed to establish a new DDP in their doctoral courses. Faculty of both universities is working coordinately to design the operating rules of the Doctoral DDP from 2011, based on know-how to the interdisciplinary education system of the master program. Under the enhanced collaboration of NUT and UG, an international reference of partnership enables to educate leaders to successfully perform the global program in the doctoral courses.

5. Goals and Spillover Effects

Interdisciplinary education and research through a DDP by operation of the distinctive consortium has following effect on development of our interactive educational collaboration and construction of both credit transfer systems. This is because that international consortium network can enhance education and research through close cooperation. Also, establishment of a re-education system has been taken place for practicing professionals in Mexico. This can accelerate interdisciplinary education and research globalization through practical cooperation and development of joint international industry-academic research. Among them, training engineers at enterprises seems to be very important in the areas of Mexico through cooperative education process in UG and can achieve practical re-education during graduate school through research. Especially through the human-resource training program to re-educate engineers of Japanese industries, students can receive lectures in engineering education and experience in Japanese style production for one year at the NUT. Thereafter, they can receive training and do research work at a Mexican home university to study there on site for one year, participating in their master's degree collaborative study program. This also can support enhancement of international competition in accordance with the contribution toward human resources in overseas enterprises, especially in Japanese enterprises. So the achievement of these goals will contribute to both the development and acceleration of internationalization in graduate education. It will be sure in the near future that the program indirectly may support over 400 Japanese companies that are currently operating businesses in Mexico by providing them with training for engineers and the opportunities for basic research work to maintain and improve their position among others in North America areas.

6. Conclusion

In conclusion, the master DDP between UG and NUT developed jointly by the two universities is discussed in this paper. Actually, the DDP has started from 2011 April on NUT and one student studies (Fig. 1 left) in UG till 2012 June according to the scheme of Fig. 4. These developments can bring effective changes in a culture of academic and professional collaboration, harnessing the strengths of both organizations. These institutions are therefore working in a complementary way to meet mutual and national interests and then to prepare the next Doctoral DDP. It is expected that greater and deeper collaboration between both universities is still processing particularly in areas of master and doctor education and their researches on the basis of enhanced globalization. Thus, this collaboration may also serve as a model for the future beneficial relationships between both countries.

Acknowledgement

This is supported by developed engineering education programs accelerating internationalization under the sponsorship by MEXT.

(Received: 18 May, 2012, Accepted: 17 June, 2012)

Transactions on GIGAKU **1**(2012)01003/1-9

Advanced Program for Strategic Engineering Promotion with Technical College Collaboration : Its Concept and Initial Stage

Kazuo Nakamura[1,*], Makoto Yamazaki[2], Yoshifumi Jodai[3], Yoshihiko Shimizu[4],
Makoto Nanko[1], Yasushi Fukuzawa[1], Masatoshi Takeda[1], Takashi Yamaguchi[1]
1)Nagaoka University of Technology,1603-1 Kamitomioka-cho, Nagaoka 940-2188, Japan
2)Nagaoka National College of Technology,888 Nishikatakai, Nagaoka 940-8532, Japan
3)Kagawa National College of Technology,355 Chokushi-cho, Takamatsu 761-8058, Japan
4) Toyama National College of Technology, Ebie Neriya, Imizu, Toyama 933-0293, Japan
**E-mail: nakamura@kjs.nagaokaut.ac.jp*

Considering the essential change of global industry and economy in the coming era, a project "*Advanced Program for Strategic Engineer Promotion with Technical College Collaboration* (ADV-program) " has been established as a new educational scheme in collaboration of Nagaoka University of Technology (NUT) and technical colleges (KOSENs) for Monodukuri (Craftsmanship) in the coming society. This paper introduces the conceptual framework and the subjects on the initial stage of ADV-program. The proposed program focuses on enhancing the fundamental abilities on "*Specialties on multiple fields*", "*Strategic technology management*" and "*Global leadership.*" On the initial stage at KOSEN, the students of ADV-program gain insights into global trends and consider what is important for elemental technology and training. Furthermore, the course forms the basis for developing promising personnel who will be of benefit to both Japan and the wider world through understanding of technological-systems and creation of strategies in society.

1. Introduction

In the coming era the growth of BRICs power [1,2] with American, European and Japanese one is going to lead the global economic and social conditions. Under the situations industrial activities of Korea and China are rapidly expanding in the worldwide market with specific strategic technology developments [3,4]. And the common human problems on global environment, energy / resource conservation and coping with huge natural / artificial hazard require intellectual resolution by advanced technology. Under such conditions the technology strategy of Japan for "*Monodukuri* (Craftsmanship)" is also required to be changed not only for high-level quality, function and reliability but also for "*generation of unique creative technology*", "*flexible correspondence to variety of needs*" and "*global collaboration and/or rational competition with justice*."

Nagaoka University of Technology (NUT) was established thirty five years ago to aim at providing educational programs for promoting practical and creative leading engineers accepting graduate students from technical colleges (KOSENs). Then the role of NUT is recognized as a supplier of excellent engineers with practical technology in Japan industries. Considering the essential change of global industry and economy in the coming era, however, the scheme of education program in collaboration of NUT and KOSENs should be introduced in new orientation under the common recognition of the above mentioned requirements for Monodukuri in the coming society. Ministry of Education, Culture, Sports, Science and Technology in Japan has supported this orientation of NUT and KOSENs, and the project "*Advanced Program for Strategic Engineer Promotion with Technical College Collaboration* (*ADV -program*) " has been established in 2010.

In this paper the conceptual framework and the initial stage of *ADV-program* are introduced. Its principal objective designates promotion of "*strategic engineer*" coping with the above mentioned requirements for Mono-Dukuri. More specifically the proposed program focuses on enhancing the fundamental abilities on "*Specialties on multiple fields*", "*Strategic technology management*" and "*Global leadership*" as shown in Fig. 1, and prepares several courses on specific subjects enhancing the abilities by collaboration of NUT and KOSENs through the 4th and 5th grades at a KOSEN to graduation from master course at NUT.

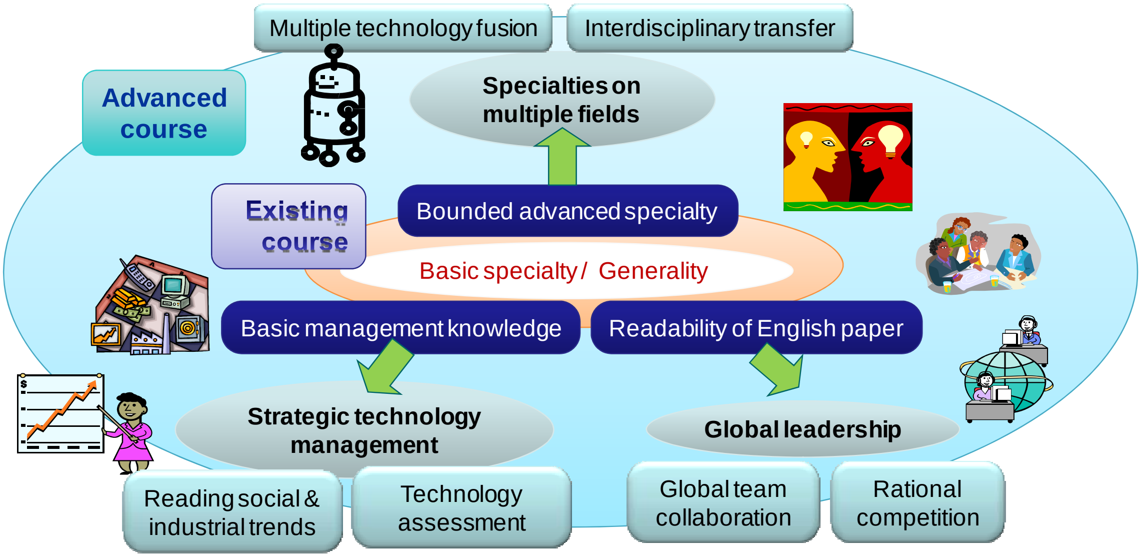

Fig. 1 Conceptual image of the fundamental abilities to be enhanced in *ADV-program*.

On the initial stage the collaborating organization for ADV-program consists of NUT and specific six KOSENs of various types which are managed by Institute of National Colleges of Technology as shown in Fig.2.

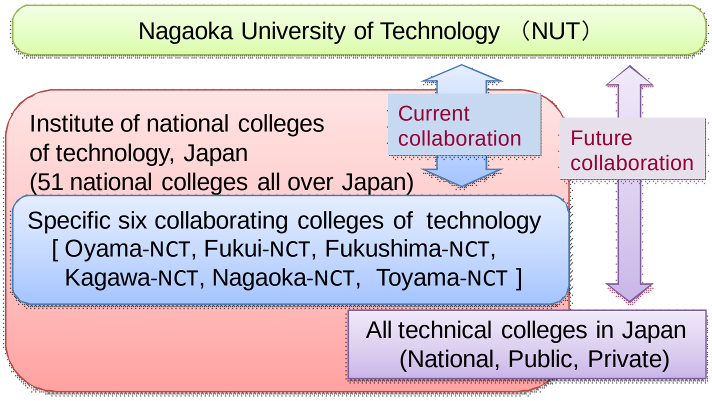

Fig.2 Collaborating organization for ADV-program

In 2011, the second year of the program, 58 students in 4th and 5th grades joined the ADV-program from the six model KOSENs in all over Japan. They participated in "*Introduction to Engineering Frontier*", "*English Oral Presentation*" and "*Mathematics Supporting Technology*" in *Collaborating courses - Part I*, and "*Intensive Seminar/Laboratory Exercise*", "*Advanced Technology Lecture/Practices*" and "*International Conference Exercise*" in *Preceding courses*. The detail on the initial stage of the proposed program and further discussions will be described in the subsequent sections.

2. Collaborating Courses at Technical Colleges

2.1 Introduction to Engineering Frontier

This sub-section shows a newly introduced subject, "*Introduction to Engineering Frontier*", at Kagawa National College of Technology (Kagawa-NCT) [5]. The subject is intended for higher grade students at the college and is offered in cooperation with some private enterprises as well as Nagaoka University of Technology (NUT). The educational objectives of the subject are (1) to understand advanced technology in related to engineering frontier, (2) to grasp social situation in diversification and (3) to find out global human resources required in the technical innovation, corresponding to the three major talents explained in Section 1. In addition, these objectives are also consistent with the educational objectives of Kagawa-NCT as shown in Table 1.

Table 1 Objectives of ADV-program and Kagawa-NCT

Fundamental abilities for strategic engineer (*Key words in Japanese*)	Specialties on multiple fields (*Fukugan-teki*)	Strategic technology management (*Senryaku-teki*)	Global leadership (*Kokusai-teki*)
Educational objectives of "Introduction to Engineering Frontier"	To understand advanced technology in related to engineering frontier	To grasp social situation in diversification	To find out global human resources required in the technical innovation
Educational objectives of Kagawa-NCT	Creative designing on complex problems	Technological knowledge in an ever changing world	Communication skills for international career paths

Table 2 shows a simplified program of the subject with affiliation of each speaker. As shown in the table, a few topics of the closely related field are presented every day so that students of different departments at the two campuses can easily get to the main points. At each class, the students were required to submit a report. Figure 3 shows a group photograph in the "*Introduction to Engineering Frontier*" class. Twelve students including auditor took the course.

Table 2 Program of "*Introduction to Engineering Frontier*"

Day	Class 1	Class 2	Class 3
1	○Multi-functional reservoir	☆Global human resources	□Water environment
2	○Mechanics and processing	□Mechanics and manufacturing	☆Ion exchange
3	○Cloud computing	□Web based information processing	☆Software development for iPhone
4	○Communication engineering (including practice)		
5	○Semiconductor device (including experiment)		

Presented by: ○; Kagawa-NCT, □; NUT, ☆; Company / Institute

Fig. 3 The group engaged in "*Introduction to Engineering Frontier*" at Kagawa-NCT

2.2 English Oral Presentation Seminar

New subject“*English Oral Presentation Seminar*”has started at Toyama-NCT since April in 2011. The Working Group of 11 professors at Toyama-NCT designed this as a subject of *Collaborating courses - Part I* in ADV-program. The aim of this subject at Toyama-NCT is to stimulate students' motivation to become professional engineers or business persons with skills to manipulate English. Toward this goal, this subject provides students with basic knowledge of English writing and with opportunities to make speeches and discussions in English. This is one of the elective subjects in the first semester at Toyama-NCT. This is placed as a 90-minute regular class on Thursday on school time table. This is a two-credit class in 15 weeks. The target students are the fourth and the fifth graders. Toyama-NCT has two campuses. So these two campuses are connected for this subject by using a video conference system. More than 50 students were interested in this seminar and 18 students were allowed to take this seminar in the first year.

This subject is consisted of three stages. The first stage is “Logical Thinking” stage conducted by associate professor at NUT, Dr. Makoto Nanko. It takes students three weeks to acquire how to write their ideas and opinions with flow charts in this stage in Japanese. This basic skill worked successfully at the following stages in this seminar. The second stage is “150-word Paragraph Writing” organized by an instructor at Japan Society for Technical Communication (JSTC), Ms. Yukiko Nakayama. This stage takes seven weeks. Each lecture is focused on “Technical Writing” in English. There are three points as follows. Firstly, students realize what technical writing is like. Secondly, students choose one topic from the following topics; “Hybrid car,” ”Cellular phone,” and ”Nuclear power.” Topics are basic technologies related to students' majors. Finally, students complete their own writing. The teaching methods such as “Peer-Learning”, “Peer-Review” are mainly adapted at this stage. Automatism is required to become better English writers. The third stage is “English Oral Presentation and Discussion” instructed by all professors at Toyama-NCT with the help of an instructor at JSTC, Mr. Koki Tokuda. Students' presentations and discussions are conducted in English. Students are supposed to be positive at this final stage. Professors at Toyama-NCT facilitate students' English discussion. Students experience pseudo International Society at this stage.

Through this seminar, several surveys were conducted to evaluate students' awareness toward their skills. Here are 25 questions of a survey;

1) problem-finding skill, 2) skill to map out, 3) understanding and deepening knowledge,
4) self-learning skill, 5) skill to collect information, 6) skill to arrange information,
7) skill of information analysis, 8) expressiveness with text, 9) expressiveness without text,
10) skill to create simple explanations, 11) presentation skill, 12) questioning mind,
13) communication skill, 14) skill of self-assessment, 15) skill of assessment to others,
16) skill of self-modification, 17) skill of follow-up, 18) skill of action,
19) collaborative learning skill, 20) problem-solving skill, 21) knowledge construction skill,
22) creative mind, 23) fulfillment, 24) accomplishment, 25) research mind.

In Fig. 4 the sequential blue sticks show students' profiles before this seminar starts, and these data says students cannot be confident in the skill to give a presentation. This might be one of the

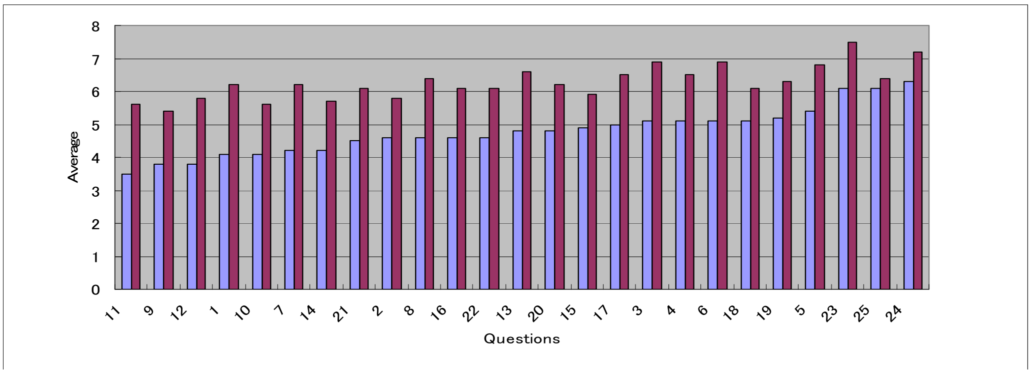

Fig. 4 Students' profile (Surveys BEFORE[:blue] and AFTER[:red] this seminar

reasons they took this seminar. On the other hand, their research mind and their sense of achievement and satisfaction are quite high. That suggests that most of participants in this seminar might get high marks at school. The sequential red sticks in Fig. 4 present students' awareness toward their skills after the seminar. The comparison between blue sticks and red ones proves that the students' awareness toward ALL skills is enhanced from April, "BEFORE students learn" to August, "AFTER students learned" in four month.

Figure 5 reveals how much students' awareness toward all 25 skills are enhanced. This data indicates enhancement of two things through this seminar; knowledge and skills. Firstly, students feel that they were able to comprehend and utilize information correctly and the understanding of their knowledge was deepened. Secondly, students realize that they were able to express their opinions correctly in English writing and at oral presentation and in discussion.

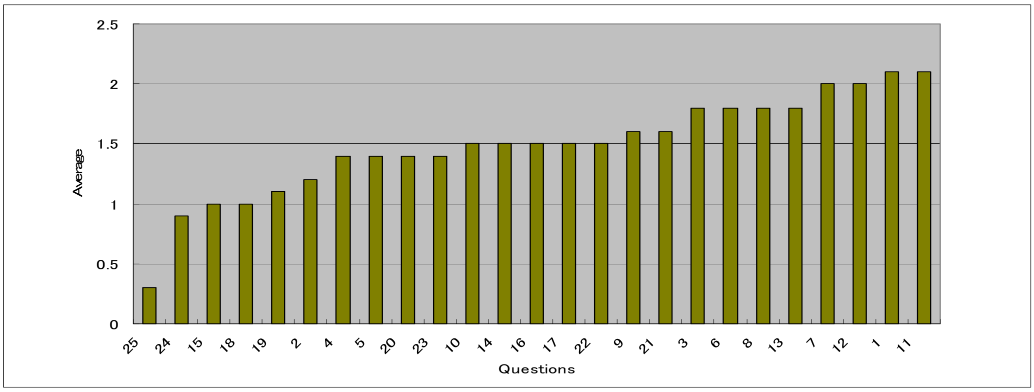

Fig. 5 Enhancement of Students' Awareness toward skills

From these two figures above, it concludes that the teaching methods and syllabus in this seminar worked well and stimulated students' intellectual curiosities deeply and inspired a feeling of achievement. These data also convince us that the collaboration of Toyama-NCT and NUT extremely empower both institutions to foster highly-motivated students. Figure 6 shows some scenes of students' practices on the three stages.

(a) Stage1 (Logical Thinking) (b) Stage2(Technical Writing) (c) Sage3(presentation)

Fig. 6 Scenes of practices on the three stages in "*English oral presentation seminar*"

2.3 Overseas Dispatch Training and the Advanced Program

Nagaoka National College of Technology (Nagaoka-NCT) has been accepting international students since 1985, and has graduated 100 international students. Up to the present, we have had international students from Malaysia, Mongolia, Vietnam, Indonesia, Bangladesh, Gabon, China, etc. At Nagaoka-NCT, we foster well-rounded students through technical school education incorporating activities with the purpose of creating international, cross-cultural understanding. Among the activities promoting international exchange, we have been engaged in overseas dispatch training since 2005. This activity aims to make the most effective use of many international students learning at Nagaoka, and we dispatch Japanese students to their country so as to deepen mutual understanding of various cultures and promote international exchange among students.

Also, one part of the overseas training is designated as "*Overseas Training Workshop*" where groups of Japanese and local students carry out observations at Japanese companies and collaborative programming practice using microcomputers and LEGO MINDSTORMS®. We consider that it is also important to allow students to experience other cultures at the beginning of their engineering education. So far students have been trained on collaborative projects together with local students from China, Malaysia, and Vietnam on collaborative projects (Fig.7) and observed Japanese companies (Fig.8). In addition, in order to support the cooperation of international exchange activities, we established "*Global Lab*" in 2008. The Global Lab activities are devised to encourage exchange between international and Japanese students. In addition, a seminar, "*International Affairs and Communications*" is now being offered to promote cultural understanding. Two projects, the practice of "*Student Support Programs for New Social Needs*" and "*Student Development through Regional Cooperation and Exchange with Higher Education Institutions in Asia*" have also been implemented at Nagaoka-NCT.

Because the only initiatives of one KOSEN have limitations, the "ADV-program," promoted through cooperation with NUT and KOSENs, has been started as an educational program that includes content that we understand to be major themes within engineer training. Three perspectives—"*Specialties on multiple fields*", "*Strategic technology management"* and "*Global leadership*"—are all important in the education of engineers at KOSENs. In accordance with the aims of the *Cooperating Courses – Part I* at KOSENs, the courses, "*Introduction to Engineering Frontier*", "*English Oral Presentation*" and "*Mathematics Supporting Technology*" have been proposed, and some of these courses are beginning to be offered at Nagaoka-NCT. Based on experiences in these courses and on international exchange at KOSEN, students are considered to be able to continue to educate themselves through ADV-program.

Fig. 7 Creative work, "*Monodukuri*" abroad at Vietnam National University

Fig. 8 Factory visit of the Japanese company in Vietnam

3. Preceding Courses at Nagaoka University of Technology

3.1 Intensive Seminar and Laboratory Exercise

New subjects "*Intensive Seminar/Laboratory Exercise*" provided in the preceding courses of ADV-Program started for giving KOSEN students the opportunity to experience laboratory activities for 1 week. The aim of those subjects is to let them know a fun to study with laboratory colleagues and then to enhance their motivation to be creative engineers. Intensive seminar and laboratory exercise are held simultaneously as a subject-unit and include experimental activities, lectures and oral presentation. Figure 9 shows a picture on the scene of the research activity on development of new materials. In the subject-unit, almost students of KOSENs have first experience to give an oral

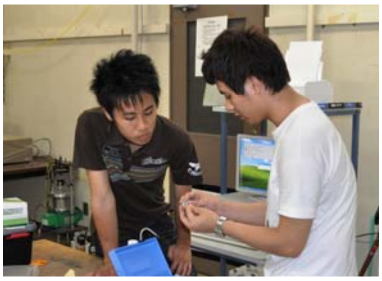

Fig.9 A scene of research activity on development of new materials

Fig.10 A scene of oral presentation in intensive laboratory exercise

presentation based on their research activity. They can obtain not only new knowledge and experimental skills in a particular engineering subject, but also fundamental skill for oral presentation. Figure 10 shows a picture on oral presentation given by a KOSEN student.

In summer of 2011, 51 KOSEN students joined to Intensive Seminar/Laboratory Exercise held in NUT from July 25 to September 16. Figure 11 shows questionnaire results from KOSEN students on the research activity in Intensive Seminar/Laboratory Exercise. The questionnaire results indicate that almost KOSEN students were satisfied with the research activity in this program. To have communication with our students in the master and doctoral programs was also useful for keeping their motivation.

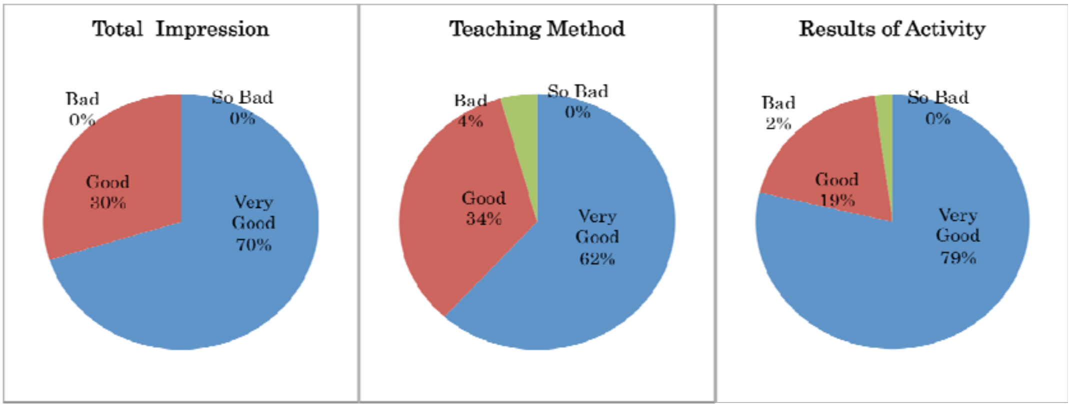

Fig.11 Questionnaire results from KOSEN students on the research activity in Intensive Seminar/Laboratory Exercise

However the schedule for this program was not enough to prepare the system for accepting KOSEN students in our university. Establishment of the entry system for KOSEN students to this program is the most important issue to be solved up to the next academic period.

Finally excellent research results have been obtained in the research activity in "Intensive Seminar/Laboratory Exercise" and presented in some academic conferences [6,7]. These results are given by serious efforts and of a great deal of talent of KOSEN students.

3.2 Advanced Technology Lecture and Practices

The subject "*Advanced Technology Lecture and Practices*" provided in the preceding courses in ADV-program. To progress the multifaceted thinking with flexible idea and the competence for the development of strategic advanced technology, the program students could be entry this course for 1 week. The aim of this subject is to learn the environment surrounding of engineers on the advanced technological field, and the fundamental knowledge about the role of creative engineer in the global world. Landmark of this lecture and practices is to progress the presentation ability for the present subject on the industry and community without regard for their special field. As shown in Table 3, Advanced Technology Lecture was carried out by two instructors in the morning term. One was applied on the special lecturer of Nagaoka University on the theme and background of that day. The other was carried out by the special engineer or CEO (Chief executive officer). After lunch time, students transferred from University to the business facility and the advanced technology practice was carried out. They made the study tour and discussion of the special technology outside of their research field. After returned to the hotel, they wrote the report of the lectures and study tour till next morning. On the last day of this program, the oral presentation was held on each field by several groups. The field and the group member for the presentation were given in the evening of Thursday. The selected filed was outside of their own region and the different college students were jointed.

The oral presentations were criticized by various reviewers, who were professor of NUT and the lectures of the visited companies. This year, the following fields were experienced.

1) Energy ·Security ·Engineering ethics.
2) Enviroment·Civil Engineer·Tranportration
3) Biotechnology·Medical service·Provisions.
4) Management ·Information· Distribution.

In this program, 19 KOSEN students joined. According to comments for this program, most KOSEN students were satisfied with the aim and the activities of the program.

Table 3 Schedule of Advanced Technology Lecture and Practice

	Moring 1	Moring 2	Lunch time	Study tour
Monday	Opening ceremony and lecture(NUT)	Lecture (business facility)	Lunch and transfer (within 1 hour, By bus)	Business facility or Industrial plant Field (1),*1
Tuesday	Lecture(NUT)*2	ditto	ditto	Field (2) , ditto
Wednesday	ditto	ditto	ditto	Field (3), ditto
Thursday	ditto	ditto	ditto	Field (4), ditto
Friday	Preparation of oral presentation	Preparation of oral presentation	Lunch time	Oral presentation *3
Subject	Advanced technology lecture	Advanced technology lecture		Advanced technology practice

*1: Make the reports for lecture and tour, every night from Monday to Thursday.

*2: Turn in report every morning from Tuesday to Friday.

*3: The presentation field number and the group member were announced by the program bureau.

3.3 International Conference Exercise

There is no doubt that English is an important communication tool for engineers. KOSEN students (4th and 5th graders) have been studied English for 6 or 7 years, and most of them have already learned basic English. Learning presentation skill will improve their communication skills in English as well. In this program, they are provided a subject "*International conference exercise*" as an English practice for presentation at conference.

The goal of this subject is to give a short presentation in English on the student's own research. This English course is composed of the following steps to achieve the goal.

1) Writing an abstract in Japanese
2) Writing the "Title" in English
3) Writing the "Objective" in English
4) Writing the "Method" in English
5) Writing the "Result & Discussion" in English
6) Writing the "Conclusion" in English
7) Preparation of 4-sheet presentation file
8) Preparation of notes for presentation in English

The abstract contains "Title", "Objective", "Method", "Result & Discussion", and "Conclusion". The four sheets contain "Objective", "Method", "Result & Discussion", and "Conclusion", respectively.

The course is carried out basically through e-mail and/or Web site, because it is difficult for the KOSEN students to come to NUT every week. In the step 1), the students are requested to write an abstract in Japanese prior to writing it in English. Contents of the abstract and its logical structure is important not only for the students but also for teaching staffs of NUT in order to understand each research work. This is the reason why we request the students to write the abstract in Japanese. NUT staffs make corrections on the submitted Japanese abstract, and give suggestions.

In the steps 2) - 8), the students write each topic in accordance with reference materials sent from NUT staff. The submitted English document for the each step is checked and corrected by NUT staffs with the aid of foreign students of NUT as teaching assistant.

Seven KOSEN students took this English course in 2011. They gave a short presentation (Fig.12) using the 4-sheet presentation file and notes prepared in the steps 7) and 8). After giving a presentation, the student answered questions from NUT staffs and other KOSEN students.

Fig.12 A scene of an oral presentation excise in English

We believe that this English course is a good opportunity for the KOSEN students to practice presentation in English and effective to enhance their communication skills. For further improvement of this course, literature searching should be introduced. This is because enhancement of their vocabulary, particularly technical terms, and pick up useful expressions are necessary for better scientific writing and presentation.

4. Prospective Fruits

This ADV-program is a wide-reaching collaborative education between technical colleges (KOSEN) and Nagaoka University of Technology (NUT), including 4th grade KOSEN students to NUT master's degree students, with the aim at promoting very excellent personnel out over the world.

There are the three pillars of ADV-program consisting "*Specialty on multiple fields*", "*Strategic technology management*" and "*Global leadership*". Three subjects "*Mathematics to Support Technology*", "*Introduction to Engineering Frontier*", and "*English Oral Presentation Seminar*" comprising *Collaborating Courses - Part I* corresponding to the three pillars were provided through discussion between teaching staff from the six model KOSENs, the director of the College of Technology and teaching staff from NUT. And three subjects "*Intensive Seminar/Laboratory Exercise*", "*Advanced Technology Lecture/Practices*" and "*International Conference Exercise*" are simultaneously introduced in *Preceding courses* as a part of NUT program. Collaborating Courses - Part I and preceding courses take introductory roles for ADV-program. At the initial stage, Stage-1, at KOSEN, the students of ADV-program gain insights into global trends and consider what is important for elemental technology and training. Furthermore, the course forms the basis for developing promising personnel who will be of benefit to both Japan and the wider world through understanding of technological-systems and creation of strategies in society.

At Stage-2 in 3rd and 4th grades in NUT, ADV-program carry out "*Second laboratories*" that provide actions on vice-specialty demanded today. With stage-3 in NUT master course, the students of this program will return to the laboratories of a KOSEN as an intern and carries out teaching. The whole ADV-program brings up a global leader being aware of local industry and globalization. This ADV-program is introduced as a model educational program with specified six KOSENs now, but they planned to be expanded as the program for all KOSENs in the future.

Acknowledgments

The authors should express their gratitude to teaching-staffs from companies, KOSEN and NUT for the cooperation. They will be extremely grateful for the paper readers' positive advice and opinions regarding excellent personnel promotion on this ADV-program.

References

[1] D.Wilson and R.Purushothaman, Global Economics, Paper No: 99, Goldman Sachs Global Research Website, https://www.gs.com (2003).

[2] D.Wilson, C.Burgi, and S.Carlson, BRICs Monthly, Issue No:11/06, Goldman Sachs Global Economics, Commodities and Strategy Research, https://360.gs.com (2011).

[3] H.J.Moon (Translated by I. Yoshiwara), Working like Samsung (in Japanese), THENAN Publishing Co. (2010).

[4] T.Ando, M.Kawashima and K.Kan, Technology development and technology transfer in China (in Japanese), Minerva Publishing Co. (2005).

[5] Y. Jodai, Bulletin of Kagawa National College of Technology (in Japanese), **2** (2011) 22.

[6] D.Maruoka, T.Itaya, T.Misaki and M.Nanko, Abstracts on H23 Joint Meeting of the Hokuriku-Shinetsu Branch of JIM and ISIJ, (2011) 120.

[7] D.Maruoka, T.Itaya, T.Misaki and M.Nanko, Abstracts on the Spring Meeting of JIM, (2012) 121.

(Received: 17 May, 2012, Accepted: 15 June, 2012)

Transactions on GIGAKU **1***(2012)01004/1-4*

Engineering Education Programs for International Students toward the integration of Japanese language education and technical education

Seiji KAMIMURA[1,*], Yoshiki MIKAMI[2], Naoko LEE IIZUKA[3], Yoshiro ITO[1]
[1)] *Department of Mechanical Engineering, Nagaoka University of Technology,*
[2)] *Department of System Safety, Nagaoka University of Technology,*
[3)] *Department of General Education, Nagaoka University of Technology,*
1603-1 Kamitomioka-cho, Nagaoka 940-2188, Japan
**E-mail: kami@nagaokaut.ac.jp*

Nagaoka University of Technology (NUT) currently conducts Twinning Programs (TPs) with six universities from three countries. . In their native countries, students take classes in both their specialized fields and Japanese language. However, students are initially taught in their mother tongues for technical classes, and therefore only exposed to technical courses taught in Japanese upon arrival in Japan. Here, we introduce refinements that we have implemented to improve the transition process. The 2 main aspects of these implementations are: (1) Improving the teaching ability of technical education teachers; and (2) Development of teaching materials to improve the integration between Japanese language education and technical education.

Technical lecturers from Japan are periodically sent to partner universities to conduct intensive technical courses in Japanese. As part of Faculty Development, a comprehensive lecturer training package was developed, comprising of pre-training of the lecturer, the actual intensive courses, and a follow-up evaluation stage.

Time constraints for Japanese language classes make it difficult for students to obtain sufficient language ability for further education in Japan. To improve the integration between Japanese language education and technical education, we have developed curricula and teaching materials to improve students' Japanese language ability in their specialized engineering fields. We are currently developing 2 such teaching materials: a textbook to introduce mechanical engineering topics in Japanese and a workbook to support the abovementioned intensive technical courses. These materials, developed through collaborations between Japanese language teachers and technical education academic staff, should improve the quality of the TPs.

1. Introduction

A Twinning Program (TP) is a voluntary partnership program conducted between two universities in different countries. In these programs, participating students spend the first half of their education in one institution and complete their studies in the partner institution. Partner institutions agree in advance to a detailed curricula, and students benefit from the experience of studying overseas with reduced costs. Furthermore, these programs can serve as the starting point for further collaborations between the partner institutions, facilitating research opportunities and the exchange of internships.

In 2003, the Nagaoka University of Technology (NUT) initiated an inaugural TP with Hanoi University of Science and Technology (HUST), the largest technical university in Vietnam. This was the first TP established by a Japanese national university, as well as the first to be formally recognized by the Vietnamese government.

In this TP, students majoring in Mechanical Engineering spend the first two and a half years at HUST, where they are educated in engineering fundamentals as well as Japanese language. At the end of this period, candidate students undergo an examination of both their engineering knowledge and Japanese language capabilities. Students who successfully pass this selection stage enter NUT as third year undergraduates, attending the same classes as Japanese students. The pioneer batch of HUST students graduated from NUT in 2007, and NUT is currently hosting the 9th batch of HUST students.

In the subsequent years, our university has initiated and is currently administrating TPs with six universities from three different countries, covering a range of courses. These universities include HUST, Da Nang University and Ho Chi Minh City University in Vietnam; Universidad Autonoma de Nuevo Leon and Monterrey Institute of Technology and Higher Education in Mexico in Mexico; and Zhengzhou University in China. The details of these TPs are presented in Table 1.

Table 1 Current status of Twinning Programs conducted by NUT

Country	University	Course	Inaugural year
Vietnam	Hanoi University of Science and Technology	(M)	2003
	Da Nang University	(Cv)	2006
	Ho Chi Minh City University	(E)	2006
Mexico	Universidad Autonoma de Nuevo Leon	(Cv)	2008
	Universidad de Monterrey	(M)	2007
China	Zhengzhou University	(Cm)	2007

Legend: (M): Mechanical Engineering Course, (Cv): Civil Engineering Course, (E) electronic Engineering Course, (Cm) Chemical Engineering Course

2. Challenges in Twinning Programs

Mastery of the Japanese language is an essential skill for TP participant students, as lectures in NUT are conducted entirely in Japanese. Furthermore, Japanese language is necessary for daily-life and communicating with fellow students and lecturers. Therefore, ensuring that the students possess adequate Japanese language ability prior to arriving in Japan is essential to the success of these programs.

Figure 1 shows the initial components of Japanese language education within the TPs. Students spend the first two and a half years in their native countries, during which they undergo Japanese language classes. Additionally, NUT periodically sends technical education teachers to conduct intensive technical courses in Japanese, in order to prepare students for the latter half of their education in Japan. During this latter stage, students have access to dictionaries of technical terms in Japanese and their native languages.

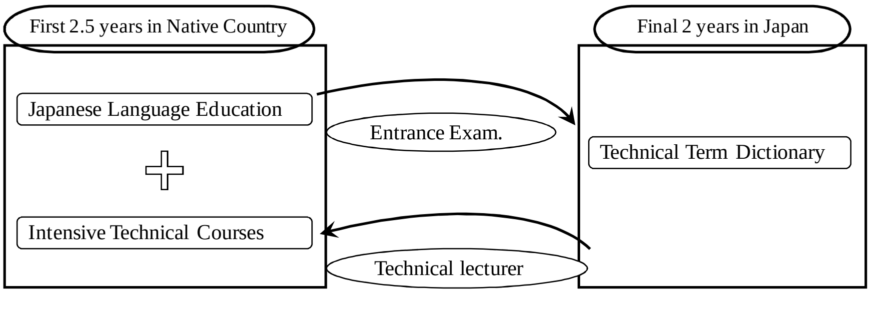

Fig. 1 Course design of the initial Japanese language education components in TPs.

However, the intensive technical courses are infrequent. As such, the students essentially conduct their technical training in their mother-tongue, and are only exposed to academic classes conducted entirely in Japanese upon their arrival in Japan. This sudden and intense exposure to technical classes in Japanese is non-conducive to a successful TP, as the students require lengthy periods of time to adjust.

Furthermore, as students must undergo technical education in addition to Japanese language lessons in their native countries, it is not feasible to significantly increase their language lesson workload. While the maximum number of Japanese language lesson hours available to the students in our TPs is 900 hours, the reality is that it is difficult for students to receive more than 700 lesson hours.

The Japanese language education aspect of the TPs requires improvement in order to better prepare the participant students for their academic life in Japan. However, these improvements need to be conducted within the boundaries of the limitations as outlined above. Our solution was to maximize the available framework by breaking away from the standardized general Japanese language classes, and replacing it with an Integrated Technical Japanese Language Education Program, in which Japanese language education is combined with technical education.

3. Towards A Solution

Current and impending refinements to the TP course design include the following:

Final year Japanese students from NUT are sent on internships to the partner universities for five-month intervals, where they teach fundamental technical terminology in Japanese to candidate TP students using a Basic Scientific Workbook. These TP students are thus exposed to technical terminologies that they would not ordinarily learn in a basic Japanese language class.

Next, Japanese technical education lecturers undergo a comprehensive training package prior to conducting the intensive courses in the partner universities, comprising of pre-training of the lecturer, the actual intensive courses, and a follow-up evaluation stage. Details of the pre-training of technical education lecturers from NUT prior to intensive technical courses are shown in Table 2.

Table 2 Pre-training for lecturers

Date of Pre-training	No. of Participants	Twinning Program	Subject
2008.11.5	2	Hanoi, Vietnam	Manufacturing
			Material Science
2009.1.30	1	Mexico	Thermodynamics
			Hydraulics
2009.3.13	2	Danang, Vietnam	Engineering Disasters
			Hydraulic Engineering
2009.8.6	2	Ho Chi Minh City, Vietnam	Basic Electromagnetics
			Basic Quantum Mechanics
2009.11.5	1	Hanoi, Vietnam	Basic Materials*
2010.1.28	2	Ho Chi Minh City, Vietnam	Electric materials (dielectrics)
			Electric circuit
2010.3.1	2	Danang, Vietnam	General Civil Engineering
2010.5.31	1	Zhengzhou, China	Organic Chemistry
2010.7.28	1	Mexico	Civil Engineering
2010.8.3	2	Ho Chi Minh City, Vietnam	Electronic Engineering

*Conducted for Visiting Professor from Gunma University

The aforementioned training package has the added advantage of providing Faculty Development (FD) opportunities for technical education lecturers in NUT. These lecturers, who have limited experience in teaching foreign students, are trained by Japanese language lecturers, technical lecturers who have experience in conducting intensive courses, as well as current foreign students enrolled in NUT. The pre-training consists of a 20 minute mock lecture, followed by advice and exchanges of opinions. FD can be obtained as these lecturers are trained to appropriately teach foreign students, as well as improving their general teaching abilities. The self-reflection and external advice provided in the follow-up evaluation stage may help to further improve the teaching ability of the lecturers. In addition to ensuring better intensive technical courses in the partner universities, these improvements would be advantageous when these lecturers teach foreign students in Japan.

Refinements are also being conducted with the development of two technical Japanese language textbooks. After obtaining a basic level of Japanese language ability, TP participant students would continue their education in their native countries using "Intermediate Japanese Language through Mechanical Engineering", a textbook that we are currently developing wherein students are exposed to technical Japanese vocabulary and grammar structures. After students arrive in Japan, they would have access to a "Plain Japanese-based Technical Book", in which the technical topics covered in their studies are presented in an easy-to-read format. Furthermore, the collaborative development of the Japanese textbooks involves frequent interactions and communication between technical education staff and Japanese language lecturers, thereby providing FD opportunities for all involved parties. These refinements are summarized below in the Figure 2.

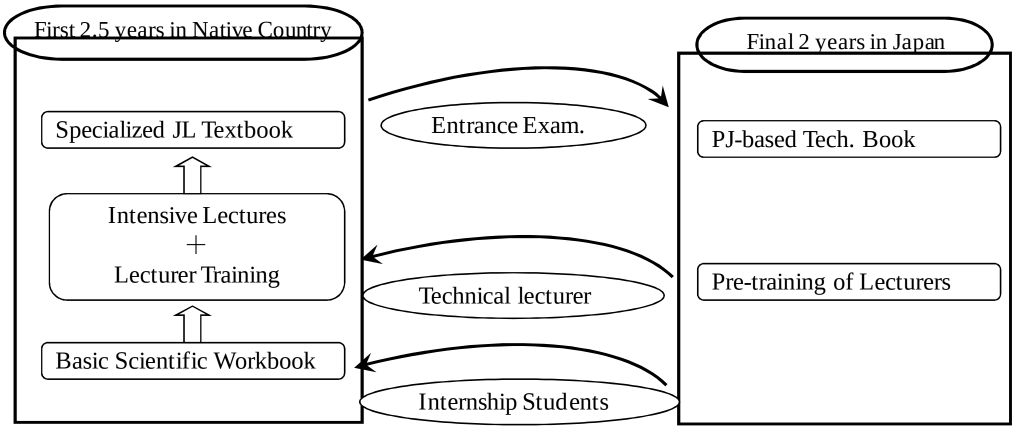

Fig. 2 Course design of the refined Japanese language education components in TPs.

4. Conclusion

While there are limits on the Japanese language lesson hours available to TP participant students, the importance of mastering Japanese language emphasizes the need for refinements and improvements to the program. In response to this need, we have implemented training of technical lecturers to effectively conduct short intensive courses in the partner universities. Furthermore, we have integrated general Japanese language education with technical scientific education, and are developing technical Japanese language textbooks to support this integration.

Acknowledgments

This research was supported by the Program for Promoting High-Quality University Education from the Ministry of Education, Culture, Sports, Science and Technology of Japan (MEXT).

(Received: 18 May, 2012, Accepted: 12 June, 2012)

Transactions on GIGAKU **1** *(2012)01005/1-7*

Nanoscale Deconfinement: Isolation of Nanovolume Leads to Change

Roman Nowak[1,3,*], Dariusz Chrobak[1,3], William W. Gerberich[2] and Koichi Niihara[3]
[1)] *Nordic Hysitron Laboratory, Department of Materials Science & Engineering, School of Chemical Technology, Aalto University, Espoo, FI-02015, Finland*
[2)]*Department of Chemical Engineering & Materials Science, University of Minnesota, Minneapolis, MN 55455, USA*
[3)]*Extreme Energy-Density Research Institute, Nagaoka University of Technology, Nagaoka, Niigata, 940-2188 Japan*
**Email: roman.nowak@alto.fi*

Rapid expansion of nanotechnology is accompanied by growing interest in developing nanoparticles exhibiting mechanical behavior tailored to optimize their production routes and to satisfy the demands of their intended use as electronic materials. Given the evidence of the dramatic impact of crystal imperfections on the functional properties of Si nanovolumes and their biocompatibility, understanding the evolution of lattice defects in Si nanoparticles is essential. Here we present atomistic calculations and supporting experimental results revealing an unknown dislocation-driven mechanism in Si nanoparticles. The initial dislocation activity is reversible, in contrast to the accepted definition of plastic deformation regarded as "permanent". Molecular Dynamics simulations match the experimental data exhibiting striking contrast to deformation of bulk Si surfaces. The observed behavior is examined in the framework of the dilemma concerning dislocation, or phase-transformation origin of the incipient plasticity in nanoscaled semiconductors and ceramics. Our findings reinforce previous studies proposing that the onset of plasticity in nanoscale volumes is driven by the crystallography and geometry of the nanoscale deconfinement.

1. Introduction

Silicon, one of the most extensively studied advanced technology materials exhibits a complex pattern of plastic deformation combining amorphization, phase transformations, and dislocations [1-4]. Recent nanoscale compression and nanoindentation observations [3] demonstrated that deformation of Silicon nanovolumes is markedly different from behavior of the bulk material. The enhanced hardness of Si nanospheres is consistent with the known phenomenon of yield stress increase due to the decreasing dimensions of deformed volumes [5,6]. However, the reversible plasticity exhibited by the compressed Si nanoparticles cannot be justified in the framework of the theories pertinent to the bulk Si surfaces. A model of dislocation-driven onset of plasticity accounting for the unusual behavior of Si nanoparticles has already been proposed [5,6]. Following this idea, we clarify the origin of reversible incipient plasticity in nanosized Si particles by providing the detailed atomistic account of the underlying previously unverified mechanisms.

2. Experiment

In order to model processes initiated in stressed Si nanospheres we performed Molecular Dynamics (MD) simulations designed to match experimental conditions of previously reported nanocompression tests [5,6] and experiments carried out in the present study. MD interactions between Silicon atoms were modeled using the Stillinger-Weber (S-W) potential [7] accurately reflecting elastic behavior and generation of lattice defects in Silicon [8]. Simulations were performed for Si spheres radii R_1=5.16 nm (30691 atoms) and R_2=3.81 nm (10041 atoms) compressed between two rigid parallel plates (Fig. 1a). Loading was conducted via 0.25 Å symmetrical displacement (δ) increments applied to both plates (Fig. 1a). The atomic structure of the deformed nanospheres was relaxed during 20000 time steps (2 fs) for each displacement increment occurring at a temperature of zero K. Deformation history of the Si nanospheres was captured in load-strain (P- ε) curves and contact pressure-strain (p_c- ε) relationships (parameter definition given in Fig. 1) derived from MD-simulations. Our examination was concluded with visualization of the atomistic structural changes during MD deformation of silicon deconfined to nanoscale volumes.

The hypersonic plasma particle deposition (HPPD) technique [9] used for synthesis of Si nanoparticles utilizes an argon-hydrogen plasma into which a vapor-phase silicon tetrachloride is injected. Particles achieve hypersonic velocities upon expanding to low pressure through a converging diverging nozzle and the resulting particle beam is deposited on a sapphire chip substrate.

A PicoIndenter (PI-95, Hysitron Inc.) was used for compressing the evaluated nanospheres with radii ranging from 33 to 169 nm. The employment of a relatively rigid substrate and the diamond flat-punch diamond indenter allowed us to follow the conditions of our computer experiments.

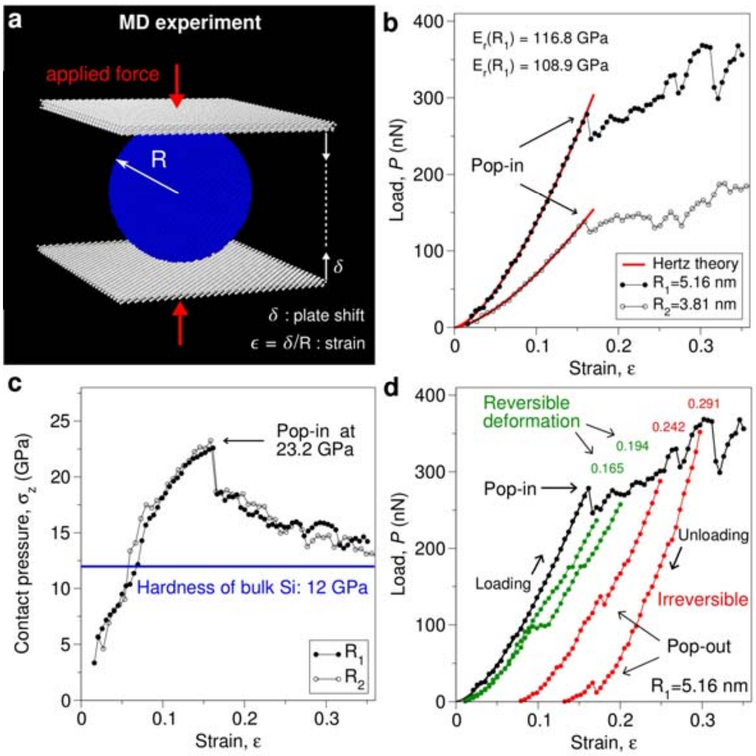

Fig. 1 MD simulated compression of silicon nanoparticles (a) quantified in terms of load–strain relationship (P-ε) obtained for the nanoparticles of two different radii, R_1 = 5.16 nm and R_2 = 3.81 nm (b)(c)(d). Elastic deformation follows Hertzian theory (red curves), providing an estimate of reduced Young's modulus (b). After the pop-in multiple singularities in the P - ε curve reflect plastic deformation. The relationship of contact pressure, $p_c = P/A$, (A actual contact area) versus strain $\varepsilon = \delta / R$ demonstrates that the hardness of the nanoparticles (~23 GPa) is nearly two times higher than hardness of bulk silicon (~12 GPa), Unloading paths [(d) - red and green lines] calculated for the larger Si nanosphere prove the complete particle shape recovery after unloading. Despite the prominent pop-in the initial plasticity in the investigated Si nanoparticles is reversible. Straining to higher levels $\varepsilon \geq 0.242$ red curves) produces permanent deformation.

3. Results and Discussion

Perfectly elastic behavior of Si nanoparticles during initial stages of deformation (Fig. 1b) conforms to classic continuum mechanics expressed by the 13 decades old Hertzian equation [10]. In agreement with the results of MD simulations by Valentini, Gerberich and Dumitrica [11], our MD calculated elastic moduli for the nanoparticles (E_{R1}=116.8 GPa and E_{R2}=108.9 GPa) were lower than the ~160 GPa measured for the bulk Si [5]. The reduction of Young's modulus with decreasing particle size is attributed to the high surface-to-volume ratio of nanospheres [11] consistent with the recent results by Mo *et al.* [12]. Our MD simulations registered pressure reaching 23 GPa (Fig. 1c) matching the experimentally observed elevated yield-point stress of the Si nanopartices [5,6]. This value is almost two times higher than the hardness of the bulk Si [5], while nearly identical to the magnitude of peak stress reached at the point of elastic-plastic transition in previous simulations [11]. The analysis of load-strain response and the magnitude of stress at the onset of plasticity demonstrates consistency between the experimental [5,6] and MD-modeled elastic deformation prompting the conclusion that elastic behavior in Si nanoparticles is accurately reflected by both Tersoff [11] and S-W potentials. However, beyond the elastic limit (Fig. 1), the two potentials predict markedly different behavior. MD results obtained with the Tersoff potential indicated that contact pressure remained constant after reaching its peak value [11]. Such behavior was attributed to the stress-induced transformation to a β-tin phase, considerably harder than the original diamond structure of Silicon. Consistent with the contact pressure stabilization, the load-displacement response calculated with the Tersoff potential maintained its smoothness through the pressure-induced transition [11].

Our simulations with the S-W potential contrast the results based on the Tersoff potential [11], and reveal that the maximum contact pressure is followed by a sudden, dramatic decay of the load (Fig. 1b) leading to a continuous drop in contact pressure (Fig. 1c). The apparent decrease of the contact pressure under the maintained constant rate of displacement increase (Fig. 1c) is tantamount to the ‘pop-in’ observed during nanoindentation experiments [13-17]. Pop-in, alternatively referred to as ‘the yield point’, marks the onset of plasticity in defect-free crystals. For load controlled experiments, pop-in appears as rapid displacement increase whereas its incidence under displacement control is evident as a load drop [18].

Consistent with the previous experiments [5,6], contact pressure continues to gradually decrease after the pop-in approaching hardness of bulk Si at 12 GPa. Remarkably, despite a distinguishable pop-in event, deformation of Si nanoparticles is reversible (yields no residual deformation) for strains up to the threshold $0.194 < \varepsilon_c < 0.242$ (Fig. 1d). Only after exceeding this threshold, the nanospheres begin to exhibit conventional plastic behavior involving permanent deformation with limited elastic recovery (Fig. 1d). In excellent agreement with our atomistic simulations (Fig. 1d), the previous experiments [5,6] showed the reversible plastic deformation in the Si nanoparticles after the pop-in.

Clarification of the pop-in mechanism in nanoscale Si volumes needs to be viewed in retrospect with previous research. For nearly a decade, nucleation of the first dislocations was thought to be the only possible mechanism giving rise to the pop-ins observed during contact loading of defect-free crystals [13,14,19]. Chrobak, Nordlund and Nowak [16] were the first to demonstrate by atomistic modeling that pop-ins in GaAs are borne by phase transformation. Recent nanoscale electrical resistance evaluation [17] proved the validity of the earlier simulations [16] and removed the certainty of attributing the pop-in to dislocation nucleation. These newly emerged experimental findings clarified by Nowak *et al.* [17] using *ab initio* calculations raised a possibility that the pop-in phenomenon observed during compression of the Si nanoparticles might also be caused by phase transformations. This would be consistent with the previously well documented mechanisms of the contact-induced plasticity in bulk Si invoking a combination of amorphization and a series of phase transformations [1,2].

Curiously, discernable singularities are noticeable in the unloading segments of the MD simulated P - ε relationships (Fig. 1d). The appearance of these singularities is reminiscent of ‘pop-outs’ observed during indentation into bulk Si and determined to be a signature of transformation from β-tin phase formed during loading to Si-III and Si-XII phases [1,2] during unloading. Pop-outs occur as a discontinuous displacement decrease during load controlled experiments and as a discontinuous load increase during displacement controlled experiments. In contrast to the results of our MD-simulated response of Si nanospheres (Fig. 1), the loading response of bulk Si surfaces is generally smooth [1,2] (Fig. 2a). Therefore, the peculiar combination of pop-in (PI) and pop-out (PO) phenomena during the loading-unloading cycle (Fig. 1d) which we choose to name PI-PO effect, is unique to the nanoscale deconfinement as opposed to nanodeformation of bulk volumes (Fig. 2a).

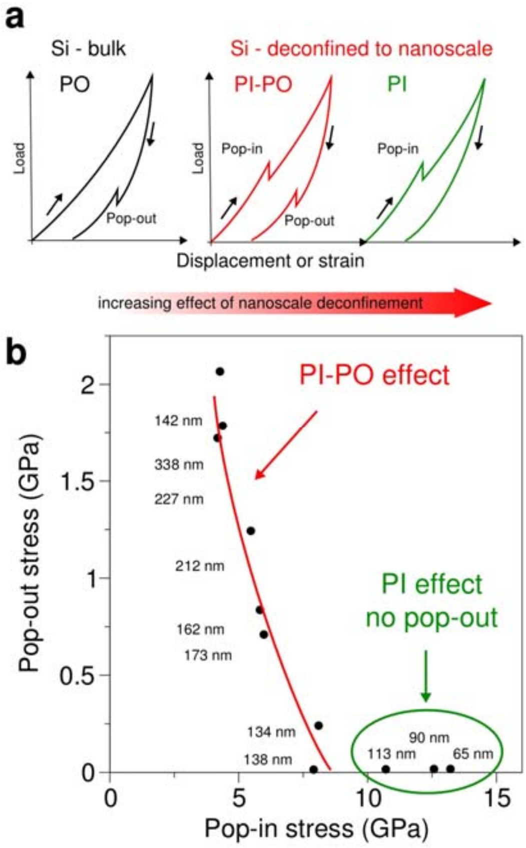

Fig. 2 Mechanical response of Silicon in bulk and deconfined state shown schematically (a) and observed from nanocompression test results (b). A combination of pop-in (PI) during loading (L) and pop-out (PO) during unloading (U) is denoted as PI-PO effect. The sequence PO→PI-PO→PI agrees with the findings by Ge *et al*. for 2D nanodeconfined silicon [3] (a), and is confirmed by our results of nanocompression tests on Si nanospheres for radii from 33 to 169 nm. The PI only (green) response occurs consistently for all nanoparticle sizes while the combination of PI-PO (red) is only present for nanoparticles larger than a threshold size of 65 nm. This output agrees with the results of our computer experiment shown in Figure 1d and suggests that the onset of plastic deformation in “large” (R > 65 nm) and “small” (R < 65 nm) Si nanospheres involves essentially different mechanisms. We propose that PI only events in smaller particles and PI-PO events in larger particles reflect two types of dislocation involvement while the PO events are indicative of the phase transformation.

In order to verify the results of our MD calculations predicting the PI-PO effect, we performed nanocompression experiments utilizing the PicoIndenter system. Experimental P - ε curves obtained for Si nanospheres reveal two distinct kinds of mechanical response, namely the PI behavior during loading and the ‘PI-PO effect’ (Fig. 2a) during loading and unloading. The PO effect typical for bulk Si [1,2] disappears and PI becomes more and more pronounced with the increasing degree of nanoscale 3D deconfinement (Fig. 2a). The experimental relationship between PO stress and PI stress (Fig. 2b) indicates the PI-PO effect systematically occurring for Si nanoparticles of radii larger than the threshold value of 65 nm. This threshold value marks a transition from PI-PO effect to PI only response.

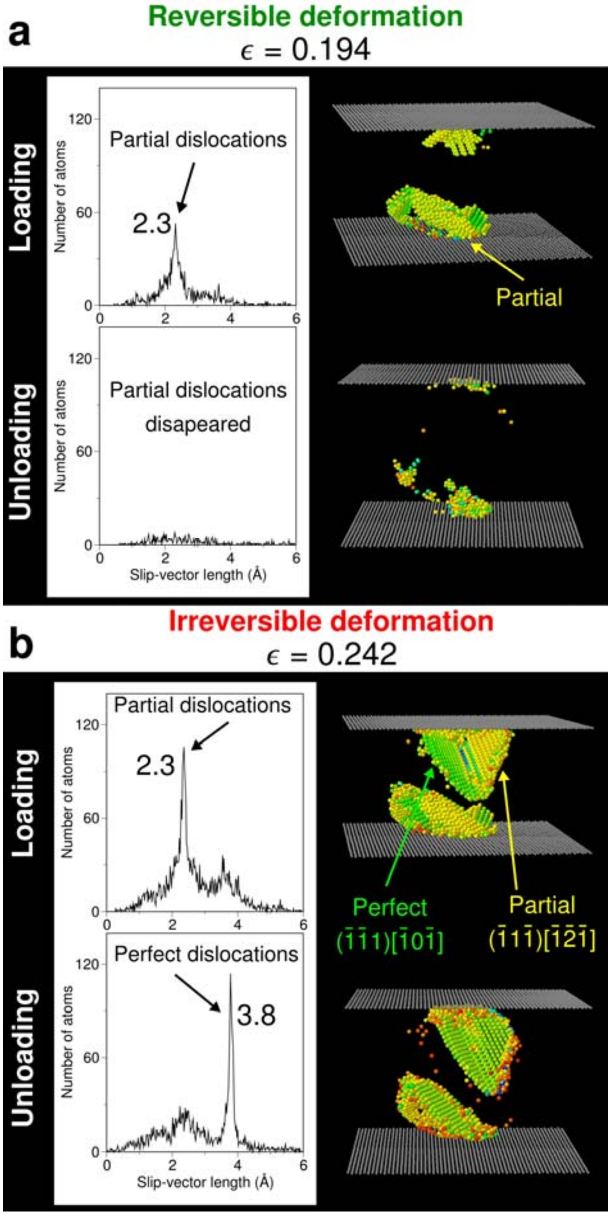

Fig. 3 Dislocations activity analyzed in terms of the slip-vector (SV) distribution and the evolution of the stressed atomistic structure in a case of reversible (a) and irreversible (b) deformation. SV single peak at 2.3 Å indicates plastic deformation accommodated exclusively via formation of a stacking fault bounded by partial dislocations $|\vec{b}|$ = 1/6|[$\bar{1}\,\bar{2}\,\bar{1}$]| = 2.228 Å (atoms marked in yellow), and after unloading the structure perfectly recovers to the undistorted defect-free configuration (a). Inception of the permanent plastic deformation upon attaining higher strain of ε = 0.242 resulted in the appearance of a new SV peak at $|\vec{b}|$ = 1/2|[$\bar{1}\,0\,\bar{1}$]| = 3.84 Å (atoms denoted in green). Unloading from strain ε = 0.242 invokes transition from partial to perfect dislocations as proved by the visualization of the strained Si nanosphere structure.

A previous study evaluating size effects in Si nanowedges under 2D deconfinement [3] concluded that pop-ins and pop-outs are generated during loading-unloading cycles when wedge size is under 1.6 microns, while pop-in without pop-out occurs in the submicron range. TEM observations linked the pop-outs to plasticity accommodated by a combination of phase transformation and dislocations and attributed pop-ins to dislocation activity exclusively [3]. The results of our atomistic modeling (Fig. 1) and nanocompression experiments (Fig. 2) shine new light on the previously reported effects of 2D deconfinement [3]. Our findings inspire the idea that nanoscale 3D deconfinement causes a transition from phase transformation-dominated to dislocation-driven incipient plasticity. Indeed, deformation in nanospheres of radii exceeding 65 nm is adequately described by the approach proposed by Valentini *et al.* [11], while our atomistic modeling predicts that dislocation-driven plasticity is appropriate for particles of diameters smaller than this threshold value.

The picture of nanoscale plastic deformation in Si under nanoscale 3D deconfinement was completed by explicit identification of the lattice defects with slip vector (SV) method [20]. SV analysis enabled us to detect two kinds of dislocations on the $\{111\}$ planes, namely partial and perfect dislocations with respective Burgers vector lengths of 1/6|[$\bar{1}\bar{2}\bar{1}$]| = 2.228 Å and 1/2|[$\bar{1}0\bar{1}$]| = 3.84 Å. These systems were previously observed during nanoindentation loading of Silicon crystals [3]. At strains $\varepsilon < 0.242$ plasticity is accommodated entirely via formation of stacking faults bound by partial dislocations as apparent from the SV peak at 2.3 Å obtained at strain $\varepsilon = 0.194$ (Fig. 3a). Complete disappearance of this peak after unloading confirms again reversible plastic deformation. All partial dislocations introduced during loading vanish (Fig. 3a).

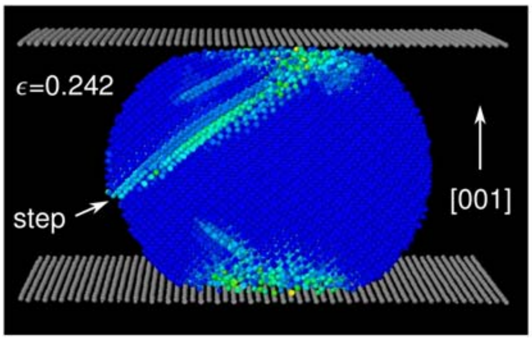

Fig. 4 MD simulated cross-sectional view of the highly strained Si nanosphere Atom colors correspond to calculated SV values. The blue part of the nanoparticle is associated with homogeneous deformation (zero slip vector value), while green bands mark inhomogeneous strain distribution produced by dislocations. Anchoring at the surface facilitates evolution of partial dislocations into perfect dislocations. Irreversible deformation is produced by formation of a characteristic step at the nanoparticle surface, the unique phenomenon captured by our analysis.

In contrast, the irreversible deformation at strain $\varepsilon \geq 0.242$ results in an additional SV peak at 3.8 Å due to formation of perfect dislocations (Fig. 3b) occurring after the stacking fault reaches the nanoparticle surface (Fig. 4). This event triggers the transformation of partial dislocations into perfect dislocations previously unrecognized in nanodeconfined Si volumes. Consequently, the SV peak at 3.8 Å becomes even more pronounced and higher during unloading (Fig. 3b). Increasing prominence of the 3.8 Å peak is justified by the observation that upon unloading, stacking fault anchoring at the surface facilitates evolution of the fault into perfect.

4. Conclusion

The reversible dislocation-driven plasticity we witnessed (Fig. 1, Fig. 3 and Fig. 4) is in accord with the experimental findings (Fig. 2) and in line with the reversibility of plastic deformation apparent during ultra-low load nanoindentation of bulk single crystal surfaces reviewed by Gerberich *et al.* [5,6]. While a concept of reversible plastic deformation and its experimental detection were discussed in the past [21-25], the reversible plasticity discerned in the Si nanospheres differs from the previously considered phenomena such as; collective motion of dislocation ensembles [22], nucleation-annihilation cycles at the boundaries of nanograins [23], evolution of stacking fault structures [24], the “Baushinger” effect in submicron single crystal films[29], and the “plastic shakedown” model [21].

Uniqueness of the observed reversible plasticity stems from the conditions of 3D nanoscale deconfinement leading to a shift from phase-transformation-dominated to dislocation-driven incipient plasticity evident from the PI-PO effect witnessed by the authors. Given the influence of dislocations on the functional properties of Si nanovolumes [26], controlled evolution of reversible dislocation structures in Si nanovolumes presents unique opportunities for developing tunable Si nanodevices with optoelectronic and biomedical applications [26,27]. Moreover, it became increasingly evident during this study that nanoscale deconfinement will play a critical role in production of nanoparticles and cluster-materials already gaining a prominent role in contemporary nanotechnology [28].

Acknowledgments

The authors gratefully acknowledge the CSC–IT Center for Science (Finland) for computation resources and the Ceramic Society of Japan for invaluable assistance.

References

[1] I. Zarudi, J. Zou, and L. C. Zhang, Appl. Phys. Lett., **82** (2003) 874.
[2] V. Domnich, Y. Gogotsi, and S. Dub, Appl. Phys. Lett., **76** (2000) 2214.
[3] D. Ge, A. M. Minor, E. A. Stach, and J. W. Morris, Philos. Mag., **86** (2006) 4069.
[4] J. E. Bradby, J. S. Williams, J. Wong-Leung, M. V. Swain, and P. Munroe, Appl. Phys. Lett., **77** (2000) 3749.
[5] W. W. Gerberich, W. M. Mook, C. R. Perrey, C. B. Carter, M. I. Baskes, R. Mukherjee, A. Gidwani, J. Heberlein, P. H. McMurry, and S. L. Girshick, J. Mech. Phys. Solids, **51** (2003) 979.
[6] W. W. Gerberich, W. M. Mook, M. J. Cordill, C. B. Carter, C. R. Perrey, J. Heberlein, and S. L. Girshick, Int. J. Plast., **21** (2005) 2391.
[7] F. H. Stillinger and T. A. Weber, Phys. Rev. B, **31** (1985) 5262.
[8] J. Godet, L. Pizzagalli, S. Brochard, and P. Beauchamp, Phys. Rev. B, **70** (2004) 054109.
[9] N. P. Rao, N. I. Tymiak, J. Blum, A. Neuman, H. J. Lee, S. L. Girshick, P. H. McMurry, and J. Heberlein, J Aerosol Sci., **29** (1998) 707.
[10] H. Hertz, J. Reine Angew. Math., **92** (1882) 156.
[11] P. Valentini, W. W. Gerberich, and T. Dumitrica, Phys. Rev. Lett., **99** (2007) 175701.
[12] Y. Mo, K. T. Turner, and I. Szlufarska, Nature, **457** (2009) 1116.
[13] W. W. Gerberich, J. C. Nelson, E. T. Lilleodden, P. Anderson, and J. T. Wyrobek, Acta Mater., **44** (1996) 3585.
[14] J. Li, K. J. Van Vliet, T. Zhu, S. Yip, and S. Suresh, Nature, **418** (2002) 307.
[15] J. K. Mason, A. C. Lund, and C. A. Schuh, Phys. Rev. B, **73** (2006).
[16] D. Chrobak, K. Nordlund, and R. Nowak, Phys. Rev. Lett., **98** (2007) 045502.
[17] R. Nowak, D. Chrobak, S. Nagao, D. Vodnick, M. Berg, A. Tukianen, and M. Pessa, Nature Nanotech., **4** (2009) 287.
[18] O. L. Warren, S. A. Downs, and T. J. Wyrobek, Z Metallkd., **95** (2004) 287.
[19] E. T. Lilleodden, J. A. Zimmerman, S. M. Foiles, and W. D. Nix, J. Mech. Phys. Solids, **51** (2003).
[20] J. A. Zimmerman, C. L. Kelchner, P. A. Klein, J. C. Hamilton, and S. M. Foiles, Phys. Rev. Lett., **87** (2001) 165507.
[21] G. L. W. Cross, A. Schirmeisen, P. Grutter, and U. Durig, Nature Materials, **5** (200) 370.
[22] M. W. Barsoum, T. Zhen, S. R. Kalidindi, M. Radovic, and A. Murugaiah, Nature Materials, **2** (2003) 107.
[23] V. Yamakov, D. Wolf, M. Salazar, S. R. Phillpot, and H. S. Gleiter, Acta Mater., **49** (2001) 2713.
[24] P.-R. Cha, D. J. Srolovitz, and K. T. Vanderlick, Acta Mater., **52** (2004) 3983.
[25] R. E. Miller, L. E. Shilkrot, and W. A. Curtin, Acta Mater., **52** (2004) 271.
[26] M. H. Nayfeh, and L. Mitas, Nanosilicon (ed. Kumar, V.) 1-78 (Elsevier, Amsterdam, 2008).
[27] N. O'Farrel, A. Houlton, and B. R. Horrocks, Int. J. Nanomedicine, **1** (2006) 451.
[28] S. Kan, T. Mokari, E. Rothenberg, and U. Banin, Nature Materials, **2** (2003) 155.

(Received: 23 March, 2012, Accepted: 10 April, 2012)

Transactions on GIGAKU ***1****(2012)01006/1-7*

Nanomaterials as Environmentally Compatible Next Generation Green Carbon Capture and Utilization Materials

Abdul Rahman Mohamed[*], Subhash Bhatia, Keat Teong Lee, Chee Yew Henry Foo,
Zhi Hua Lee, Nurul Aini Razali
Low Carbon Economy (LCE) Research Group, School of Chemical Engineering, Engineering Campus, Universiti Sains Malaysia, 14300 Nibong Tebal, Pulau Pinang, Malaysia.
chrahman@eng.usm.my

Researchers are striving to find a green solution towards the global warming issue. Looking into the significant aspects of sustainability and profitability, carbon dioxide (CO_2) capture and utilization will be a sustainable and cost-effective process route. In brief, this is a process where CO_2 will be selectively captured from the points of large emission sources, collected in a concentrated form during the regeneration process, and reused as a carbon feedstock in order to produce various valuable chemical products. The vast developments in the field of nanotechnology and green chemistry should be relatively cheap, environmental friendly and high efficiency by the CO_2 capture adsorbents and CO_2 conversion catalysts. Nanotechnology is a promising technology which utilizes materials at least one dimension sized from 1 to 100 nanometers in nano-sized regime. With such a quantum-realm scale, the adsorption and reaction activities will be greatly increased due to larger surface area, unique crystal structure, and mechanical effect for better reaction. In order to fulfill the concept of green chemistry, it is crucial to make the synthesis method with environmental benignancy besides to practice sustainable development, industry ecology, safety and waste minimization, improving heat and mass transfer limitation and life-cycle analysis in addition to the new approaches.

1. Introduction

Amongst greenhouse gases, carbon dioxide (CO_2) is the main contributor to global warming [1], because it has notably high emission compare to others greenhouse gases, such as methane, nitrous oxide, and hydrofluorocarbons. The strong liberation and accumulation of CO_2 in our planet is caused by the energy supply industry, transportation sector, and manufacturing industry. Scientists predicted that CO_2 level in the atmosphere should not exceed 450 ppm to prevent global warming from threatening the world [2]. However, the global CO_2 level is alarming at 383 ppm with a 2.2 ppm increment per year [3]. Consequently, CO_2 capture is an extremely crucial task at the moment. It is known that CO_2 has a molecular size 3.4Å and is a thermodynamically stable compound [4]. This inert property makes that CO_2 capture is a difficult task to be executed. Inversely, it also can be a cheap, nontoxic and abundant carbon feedstock for various valuable chemicals. Thus, development and integration of carbon capturing and their utilization processes in chemical industry for new energy production suggest to be one of the directions that researchers should look into the finite solution to stop accumulation of CO_2 in the atmosphere towards alleviation of global warming. Figure 1 shows the mapping of the concept where the CO_2 emitted is captured and regenerated for its re-utilization in the chemical production industry. Many valuable chemicals including methanol [4], carbonates [5], carbamates [6], dimethyl carbonate [7], cyclic carbonates [8,9], and synthetic gas [10] as well as formic acid and its derivatives [11] could actually be synthesized from CO_2. Profitably, low carbon economy is hoped to attract more investors to join the ranks and to cope with the environmental issue. With the target of protecting the environment, it is of paramount importance that the CO_2 capture and utilization processes are green processes. Thus, green chemistry principles should be concerned with process operations, identification and quantification of products, conversion, selectivity and productivities, catalyst and solvent losses, heat and mass transfer limitations, development and application of sustainable measures, incompability of safety and waste minimization [12].

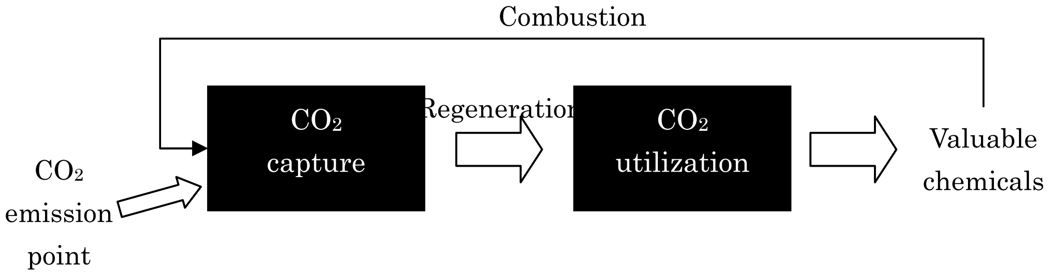

Fig. 1. Concept mapping of CO_2 capture and utilization

A nano-material can classify, when it possesses at least one dimension equivalent or less than 100 nm [12]. When such material has a nanoscale dimension, many addition properties appears. These unique properties will give a plausible enhancement in many chemical processes. In the present article, we reveal the current technology in CO_2 capture and CO_2 utilization to review on research works that have been performed in these two particular fields. In addition, it is mentioned that nanomaterials give extraordinary performance in the chemical processes and both challenges and potentials to become candidates for environmental compatible green materials in future.

For current CO_2 capture technology, recently, solvent stripping by amine solution or ammonia is the most widely used technology in capturing CO_2 from its emission points. This technology can achieve high CO_2 removal even at low CO_2 concentration. Absorber and stripper make up the major part of this process. The stripper is used to regenerate the saturated solvent from adsorber. Schematic diagram of the solvent stripping CO_2 capture is shown in Fig. 2. However, still many drawbacks are faced in such high energy consumption, solvent loss due to its low viscosity, and handling difficulties [15]. The CO_2 capture capacity (mol/kg solvent) is relatively low for large CO_2 emission source like power plants. Hence, a large absorber and stripper are needed in this condition.

Nowadays, in current CO_2 utilization, CO_2 is only being utilized in a few industries due to its inert and stable properties. Two common examples are in urea and salicylic acid synthesis. However, the researchers are looking into different perspective of CO_2 utilization so that the most threatening gas of this century can be removed in a more economical way. Some of the research directions include using solar energy for CO_2 conversion, developing value added CO_2 sequestration, using CO_2 as a mild oxidant [13].

2 Nanomaterials in CO_2 capture and utilization

2.1. CO_2 capture and utilization

Some potential nanomaterials for CO_2 capture were reported in the literature as shown in Table 1. Many research works were tried to synthesize sorbents in various types of nanostructure [13-22], such as nanoporous ‘molecular basket’, nanopods, and nanoparticles. Apart from that, some researches are trying to introduce functionality of carbon nanotubes (CNTs) in CO_2 adsorption [15,16]. However, such nanomaterial will have a higher cost of the production. For instance, CNT with specific structure is only available at extremely high price (US$ 5/g) compared to granular activated carbon which cost US$ 1/kg [15].

In recent decades for CO_2 utilization, the transformation of CO_2 to valuable chemicals and biofuel has attracted much attention. Researchers have been conducted on CO_2 hydrogenation, CO_2 cycloaddition to epoxides, CO_2 reduction under photo irradiation or electrolytic conditions. Table 2 summarizes the types of CO_2 utilizations with their reaction.

Various methods and catalysts have been used in order to obtain the very active catalyst with high CO_2 conversion [3]. Most of the catalysts obtained low conversion of CO_2 (<40%) and low selectivity of chemicals products (<80%). Thus, the exploration of superior design and fabrication of high performance nanocatalyst system for conversion of CO_2 to valuable chemicals is required for CO_2 removal in industrial and a beneficial investment for the plant developer.

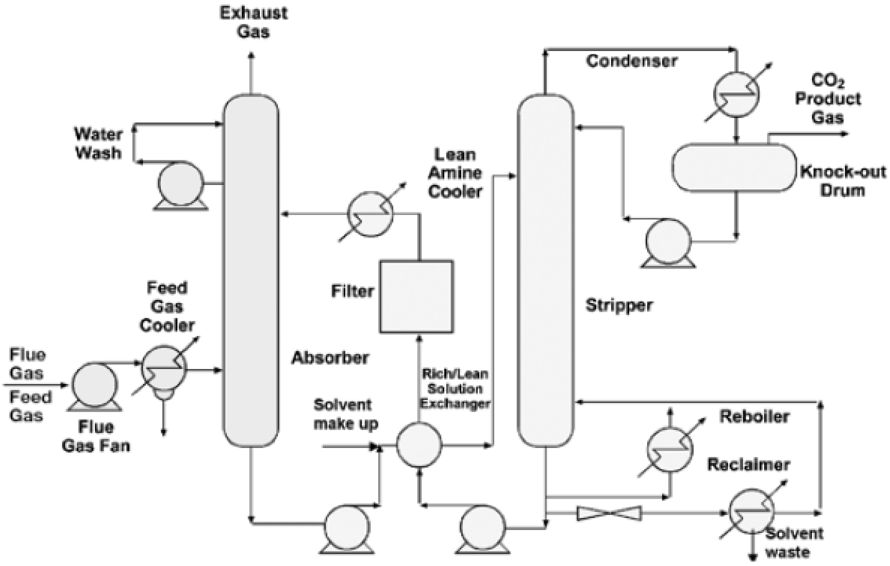

Fig. 2 Schematic diagram of solvent stripping CO_2 capture technology in industry [14].

Table 1 Nanometerials synthesized for CO_2 capture with the advantages

Nanosorbents	Advantages
Nanoporous MCM-41 'molecular basket' [15,16]	A synergetic effect on the adsorption of CO_2 by polyethylenimine (PEI) CO_2 condensed in a pore channel like a 'basket' form
Mesoporous MgO [17]	selective to CO_2 gas thermally stable regenerable.
Multiwalled CNT [18]	have higher capture capacity with same surface area with activated carbon or zeolite
Single-walled CNT [21]	
CaO Nanopods [19]	higher CO_2 capture capacity retaining >50% CO_2 absorption capacity after 50 CO_2 capture-and-release cycles
CaO-$MgAl_2O_4$ spinel nanoparticles [20]	Reduce decay problem of CaO, retain more than 115 capture-regenaration cycles
Nanocrystalline Li_2ZrO_3 particles [21]	Improved capture of CO_2 in a wide temperature range and improved kinetics of the regeneration

2.2 Green materials

One should always aware that a material will only be claimed potential when it is produced and assembled through green and environmentally responsible methodology. Green materials are defined as materials that are efficient and durable as their conventional counterparts. But, these do not pose a threat to people or the environment and provide other major benefits [22]. In this century, it is apparent that the full potential of as-prepared nanostructures will only be realized when nanomaterials are not only synthesized in large quantities with reproducible size, shape, structure, crystallinity, and composition but also prepared and assembled using green, environmentally responsible methodologies [23].

Table 2 Types of CO_2 utilizations with their reaction details.

Reaction	**Catalyst**	**Reaction Condition**	**Results (%)**
CO_2 reforming of CH_4 to synthesis gas [24-27]	- Metal oxide - Metal/Zeolite	773–973K 773 -1173K	CH_4 conversion: 59-92 CO_2 conversion: 54-94
CO_2 hydrogenation to methanol [28-31]	- Metal oxide - Metal/Zeolite	433-523 K, 8.0MPa	CO_2 conversion: 9-54 CH_3OH selectivity: 60- 92
Synthesis of cyclic carbonate from CO_2 and epoxide [32-35]	- Metal/mesoporous - Metal/Zeolite	293-393K, 0.5-2.0 MPa 283- 393 K, 2-3 MPa	Epoxide conversion: 6-98 Cyclic carbonate Selectivity: 90-97
Synthesis of DMC from CO_2 and methanol [7,36-38]	- Metal/zeolite	373-403K, 0.2-1.5 MPa	CH_3OH conversion: 3-10 DMC selectivity: 25-86

Especially, the latter point is the focus of the present review and the social significance associated with developing these types of techniques cannot be overemphasized. Green chemistry can be broadly defined as the invention of novel reactions that can maximize the desired products and minimize by-products, designing new synthetic schemes and apparatus that can simplify operations in chemical productions, and seeking greener solvents that are inherently environmentally and ecologically benign [39]. Specifically, many groups worldwide have worked on similar types of materials, we have made a deliberate effort to abide by the 12 principles that had been clearly defined in the publication of Green Chemistry. Theory and Practice in 1998 [22] listed below to provide a coherent vision for the emerging green chemistry movement. 1) Designing safer chemicals with desired function while minimizing their toxicity, 2) Safer solvents and auxiliaries, 3) Maximize energy efficiency as if possible to conduct synthetic process under ambient temperature and pressure, 4) Use of renewable feedstocks, 5) Reduce reaction derivatives, 6) Make use of selective catalytic reagents, 7) Design for degradation of chemical products so their function breakdown into innocuous degradation products and do not persist in the environment, 8) Real-time analysis for pollution prevention as in-process monitoring and control prior to the formation of hazardous substances and 9) Safer chemistry for accident prevention as substances used in chemical process should be chosen to minimize the potential for chemical accidents, including releases, explosions and fires.

For nanomaterials made of green materials the potentials can be given that green chemistry has been employed successfully in the preparation of highly functionalized nanomaterials proposed for a range of future applications. These materials are expected to (i) exhibit new size-dependent properties particularly in beneficial quantum realm, (ii) involving a multidisciplinary of material science approach and innovation with associated elemental and material compositions, including organics, inorganics and hybrid structures, and (iii) occupied a high degree of surface functionality. Apart from that, assessment of the potential toxicological and environmental effects of nanoscale materials before they are accepted as mature technologies presents an opportunity to minimize putative negative consequences from the outset and ultimately lead to the design of higher performance materials. Therefore, understanding the structure-function relationships that related specifically to nanomaterials could lead to new “design rules” for producing benign, high-performance nanoscale substances and toward greener synthetic methods for functionalized metal nanoparticles. Recently, a great deal of attentions have been paid to the development of greener synthetic methods involving innovative citrate reduction, direct synthesis of ligand stabilized nanoparticles, seeded growth and shape control of nanoparticles and alternative solvents for nanoparticles synthesis.

2.3 Some examples for green nanomaterials

Since the pioneered work for by J. Turkevich et al. in 1951 [40,41], they gave nearly monodisperse, water soluble gold clusters with diameters ranging from 7-100 nm. Although the synthesis predates green chemistry principles by several decades, it is a rather benign procedure, as the reagent pose little hazard. The preparation did not rely on organic solvents and few (if any) undesirable side products were generated in the course of the reaction. Revered for its simplicity, requiring only a metal salt, trisodium citrate, and water, it remained one of the most reliable methods of creating large metal nanoparticles [42]. For direct synthesis of ligand stabilized nanoparticles, a wide range of metal nanoclusters or nanoparticles stabilized by polymers and organic ligands have boosted the development of nanotechnology as one of the most important building blocks to construct nano-organized systems. The direct preparation of ligand-stabilized nanoparticles provided a simple route to functionalized materials, usually in a single-step, straight forward, imparting stability and chemical functionality to the nanoparticle products without post-synthetic modification [43].

Current research challenges are focused on selecting solvents, reaction conditions, and reagents to synthesis a target material, but one should not overlook the opportunity to adopt greener syntheses pathway by giving equal consideration to more benign reaction conditions (i.e., safer solvents and avoid toxic surfactants), overall yield and atom economy, and environmental issue of new nanoproducts. Additional aspects of metal nanoparticles in organic solvent such as their fabrication, morphology control, growth mechanism, stabilization, characterization, physical properties, and potential applications to be covered [44].

Focusing on seeded growth approaches for the synthesis of nanoparticles leads again to many different methods that have been published. On broad sense, nanoparticles having core diameters exceeding 5 nm can be grown from smaller seed particles through the epitaxial addition of metal atoms [43]. In addition, the use of well-defined seeds is crucial to obtain products with narrow size dispersity. Other reagents like surfactants may promote the formation of anisotroic materials or simply as surface passivants and stabilizing agents. Nevertheless, growth of such materials from monodisperse seeds allows the researcher to employ milder reaction conditions for the synthesis of materials, and the wide range of weaker reducing agents capable of reducing metal ions in a growth solution offers increased possibilities for designing greener syntheses.

Table 3 Some details of barriers faced in green nanoscience [45].

Barriers	Location in the innovation chain	Stakeholder
There are no clear design guidelines for researchers in initial discovery phases of green nanoscience	Discovery phase; link between academic research and industry	Universities
Green nanomaterials require new commercial production techniques, which increases the need for basic research, engineering research, and coordination of the two between the industrial and research communities;	Development and Production phase; Research phase; link between academic research and industry	Universities; Small and large industry
There is a lack of “deep bench” of scientists and engineers with experience developing green nanotechnology;	Development and production phase	Small and large industry
Toxicology and analysis protocols need to be developed and constantly updated to reflect advance in the science;	Research phase; link between academic research and industry	Universities, National Laboratories, Regulatory Agencies, Small and large industry
Regulatory uncertainty persists, and green nanotechnologies often face higher regulatory barriers than existing or conventional chemicals;	Commercialization phase	Regulatory Agencies, Small and large industry, Consumers
The end-market demand is unclear, especially since there are only a limited number of commercial grade products that can be compared to conventional materials in terms of performance	Commercialization phase	Small and large industry. Consumers, financing mechanisms

3. Challenges emerging with green nanoscience

The emerging field of green nanoscience faces considerable research challenges to achieve the maximum performance and benefit from nanotechnology while minimizing impact on human health and the environment. Several general barriers to overcome were listed below together with its location in the innovation chain and responsible stakeholder.

As the above listing of research challenges suggests, green nanosynthesis is in its early stages and further research is warranted to develop the approach and examine the breadth of its application. There are encouraging results that suggest that the green nanoscience framework can guide design, production, and application of greener nanomaterials across the range of compositions, sizes, shapes, and functionality. Further development and application of this framework to the design and production of a growing number of classes of nanoparticle materials will provide research opportunities and challenges for this community for the foreseeable future.

4. Conclusion

Fossil fuels will still the dominant source of energy for this century, in view of the immaturity of development of other energy resources. CO_2 capture in existing power plants can be classified into three categories: pre-combustion capture, oxy-combustion capture and post-combustion capture. Post-combustion capture has gained the major focused. It is looked as the most feasible approach while it can be easily retrofitted into the existing conventional coal power plant compared to other method. While other technologies are facing their limitations, CO_2 adsorption with dry-based materials has gained numerous attentions and in an evolution towards nanomaterials. To make this process become more economically feasible, CO_2 utilization in industry need to be explored and developed in a wider scope. It is ought to mention that the route of synthesis of the adsorbents need to be green as well in order to achieve a totally green CO_2 removal process.

Acknowledgemens

The authors would like to acknowledge for the financial supports given by (1) Long Term Research Grant (LRGS) (203 / PKT / 6723001) from Ministry of Higher Education (MOHE) Malaysia and (2) Research University Grant (1001/PJKIMIA/854001) from University Sains Malaysia (USM).

References

[1] O.T. Hui, Renewable and Sustainable Energy Reviews, **14** (2010) 2697.
[2] M.S.J. Hansen, P. Kharecha, D. Beerling, and R. Berner, V. Masson-Delmotte, M. Pagani, M. Raymo, D.L. Royer, and J. C. Zachos, Open Atmosphere Sci. J., **2** (2008) 217.
[3] P. Canadell, P. Ciais, T. Conway, C.B. Field, C.L. Quéré, R.A. Houghton, G. Marland, and M.R. Raupach, Carbon Budget 2007; Global Carbon Project 2008.
[4] J. Toyir, R. Miloua, N.E. Elkadri, M. Nawdali, H. Toufik, and F. Milouaet, Phys. Procedia, **2** (2009) 1075.
[5] J. George, Y. Patel, S.M. Pillai, and P. Munshi, J. Mol. Catal. A: Chem., **304** (2009) 1.
[6] N. McCann, D. Phan, D. Fernandes, and M. Maeder, Int. J. Greenhouse Gas Control, **5** (2011) 396.
[7] J. Bian, M. Xiao, S. Wang, X. Wang, Y. Lu, and Y. Meng, Chem. Eng. J., **147** (2009) 287.
[8] H. Xie, S. Li, and S. Zhang, J. Mol. Catal. A: Chem., **250** (2006) 30.
[9] L.F.Xiao, F.W. Li, J.J. Peng, and C.G. Xia, J. Mol. Catal. A: Chem., **253** (2006) 265.
[10] K.C. Mondal, V.R. Choudhary, and U.A. Joshi, Appl. Catal. A: Gen., **316** (2007) 47.
[11] A. Behr, G. Henze, L. Johnen, and S. Reyer, J. Mol. Catal. A: Chem., **287** (2008) 95.
[12] K. Savolainen, L. Pylkkäen, H. Norppa, G. Falck, H. Lindberg, and T. Tuomi, Safety Sci., **48** (2010) 957.
[13] C. Song, Catal. Today, **115** (2006) 2.
[14] B. Metz, O. Davidson, Hd. Coninck, M. Loos, and L. Mryer, Carbon Dioxide Capture and Storage Special Report, International Panel on Climate Change (2005).
[15] X. Xu, C. Song, J.M. Andresen, B.G. Miller, and A.W. Scaroni., Micropor. Mesopor. Mater., **62** (2003) 29.

[16] M.K. Aroua, W.M.A.W. Daud, C.Y. Yin, and D. Adinata, Sep. Purif. Technol., **62** (2008) 609.
[17] M. Bhagiyalakshmi, J.Y. Lee, and H.T. Jang, Int. J. Greenhouse Gas Control, **4** (2010) 51.
[18] F. Su, C. Lu, W. Cnen, H. Bai, and J.F. Hwang, Sci. Total Environ., **407** (2009) 3017.
[19] Z. Yang M. Zhao, N.H. Florin, and A.T. Harris, Ind. Eng. Chem. Res.,**48** (2009) 10765.
[20] L. Li, D.L. King, Z. Nie, X.S. Li, and C. Howard, Energy & Fuels. **24** (2010) 3698.
[21] R.B. Khomane, B.K. Sharma, S. Saha, and B.D. Kulkarni, Chem. Eng. Sci., **61** (2006) 3415.
[22] T.A. Paul and J.C. Warner, Green Chemistry: Theory and Practice: Oxford University Press, New York; 1998.
[23] Y. Mao, T.J. Park, F. Zhang, H. Zhou, and S.S. Wong, Small, **3** (2007) 1122.
[24] M. Nagai, K. Nakahira, Y. Ozawa, Y. Namiki, and Y. Suzuki, Chem. Eng. Sci., **62** (2007) 4998.
[25] J. Guo, J. Gao, B. Chen, Z. Hou, J. Fei, and H. Lou, Int. J. Hydrogen Energy, **34** (2009) 8905.
[26] J. Chen, Q. Wu, J. Zhang, and J. Zhang, Fuel. **87** (2008) 2901.
[27] R. Takahashi, S. Sato, T. Sodesawa, and S. Tomiyama, Appl. Catal. A: Gen., **286** (2005) 142.
[28] X.L. Liang, X. Dong, G.D. Lin, and H.B. Zhang, Appl. Catal. B: Environ., **88** (2009) 315.
[29] X. Guo, D. Mao, S. Wang, G. Wu, and G. Lu, Catal. Commun., **10** (2009) 1661.
[30] J. Słoczyński, R. Grabowski, P. Olszewski, A. Kozłowska, J. Stoch, and M. Lachowska, Appl. Catal. A: Gen., **310** (2006) 127.
[31] D. Lee, J.Y. Lee, and L.J. Sung, Sang-Eon Park J-SC, Kyu-Wan L, editors. Studies in Surface Science and Catalysis: Elsevier; 2004. p. 169-72.
[32] R. Srivastava, D. Srinivas, and P. Ratnasamy, J. Catal., **233** (2005) 1.
[33] X. Zhang, N. Zhao, W. Wei, and Y. Sun, Catal. Today, **115** (2006) 102.
[34] S. Udayakumar, M.K. Lee, H.L. Shim, S.W. Park, and D.W. Park, Catal. Commun., **10** (2009) 659.
[35] A. Ion, V. Parvulescu, P. Jacobs, D. de Vos, Appl. Catal. A: Gen., **363** (2009) 40.
[36] J. Bian, M. Xiao, S.J. Wang, Y.X. Lu, and Y.Z. Meng, Appl. Surf. Sci., **255** (2009) 7188.
[37] X.L. Wu, Y.Z. Meng, M. Xiao, and Y.X. Lu, J. Mol. Catal. A: Chem., **249** (2006) 93.
[38] Y. Zhang, D.N. Briggs, E. de Smit, and A.T. Bell, J. Catal., **251** (2007) 443.
[39] C.J. Li and B.M. Trost, Proc. Nat. Acad. Sci., **105** (2008) 13197.
[40] J. Turkevich, P.C. Stevenson, and J. Hillier, Discussions Faraday Soc., **11** (1951) 55.
[41] J. Kimling, M. Maier, B. Okenve, V. Kotaidis, H. Ballot, and A. Plech, J. Phys. Chem. B, **110** (2006) 15700.
[42] L. Pei, K. Mori, and M. Adachi, Langmuir, **20** (2004) 7837.
[43] N. Toshima, Macromol. Symp., **204** (2003) 219.
[44] S. Nath, S. Jana, M. Pradhan, and T. Pal, J. Colloid. Interf. Sci., **341** (2010) 333.
[45] K.J.M Matus, J.E. Hutchison, R. Peoples, S. Rung, and R.L. Tanguay, American Chemical Society's Green Chemistry Institute ® (ACS GCI). American Chemical Society’s Green Chemistry Institute® (ACS GCI); 2011.

(Received: 21 March, 2012, Accepted: 30 June, 2012)

Transactions on GIGAKU ***1****(2012)01007/1-8*

Nanomatrix Structure Formed for Natural Rubber

Seiichi Kawahara and Oraphin Chaikumpollert
Department of Materials Science and Technology, Nagaoka University of Technology,
1603-1 Kamitomioka-cho, Nagaoka 940-2188, Japan
**E-mail: kawahara@mst.nagaokaut.ac.jp*

Preparation of natural rubber with nanomatrix structure was made in latex stage by graft-copolymerization of styrene onto deproteinized natural rubber (DPNR) with tert-butyl hydroperoxide / tetraethylenepentamine as an initiator. The DPNR was prepared by enzymatic deproteinization and urea-deproteinization, respectively. Conversion and grafting efficiency of styrene and acrylonitrile were more than 90% under a suitable condition of the graft-copolymerization for both enzymatic DPNR and urea-DPNR. The morphology of the film specimens, prepared from graft-copolymers, was observed by transmission electron microscopy after staining the films with OsO_4. Natural rubber particle of about 0.5μm in diameter was dispersed in polystyrene matrix of less than 15 nm in thickness.

1. Introduction

"Nanomatrix structure" is a novel phase separated structure for a multi component system, which may provide outstanding mechanical, optical and electrical properties. It is defined to consist of dispersoid of a major component and matrix of a minor component, which is distinguished from ordinary island-matrix, cylinder, gyroid and lamellar structures for block- and graft-copolymers. The nanomatrix structure is anticipated to achieve both outstanding properties of the dispersoid and functional properties of the matrix.

The nanomatrix structure may be formed by covering particles with a nano-layer followed by coagulation of the resulting nano-layer-covered particles [1]. In this case, the particles are required to chemically link to the nano-layer, in order to stabilize the nanomatrix-structure in equilibrium state. Especially, in the case of natural rubber, the chemical linkages may be formed by gaft-copolymerization of a monomer onto rubber-particles in latex stage, since the particles in the latex are dispersed in water. However, the graft-copolymerization was prevented by side reactions of proteins [2-6], which covered the rubber particle [7]. Therefore, we have to remove the proteins from natural rubber to form the nanomatrix structure. As long as we use deproteinized natural rubber latex as a source, the side reaction may be suppressed to attain high conversion and high graft efficiency for the graft-copolymerization [8].

In the present work, an attempt to form nanomatrix structure is performed by graft-copolymerization of styrene onto deproteinized natural rubber in latex stage, in which the DPNR was prepared by enzymatic deproteinization and urea-deproteinization, respectively. Morphology of the products is observed by transmission electron microscopy. Mechanical properties of the products were related to morphology, which was dependent upon styrene unit contents.

2. Experiment

Natural rubber latex used in this study was commercial high ammonia latex. The incubation of natural rubber latex was made with 0.1 wt% urea in the presence of 1 wt% sodium dodecyl sulphate (SDS) at 30, 60, 90^{o}C, respectively The cream fraction was re-dispersed in 1 wt% SDS to make 30 %DRC latex and was washed twice by centrifugation. The natural rubber latex was also deproteinized by incubation of the latex with 0.04 wt% proteolytic enzyme (Kao, KP-3939) and 1 wt% SDS for 12 h at 32^{o}C followed by centrifugation. The cream fraction was re-dispersed in 1 wt% SDS to make 30 %DRC latex and was washed twice by centrifugation to prepare deproteinized natural rubber (DPNR) latex.

Graft-copolymerization of the urea-DPNR (U-DPNR) latex and enzymatic DPNR (E-DPNR) latex was carried out with styrene and acrylonitrile as a monomer, using *tert*-butyl hydroperoxide with tetraethylene pentamine as an initiator. The latices were charged with N_2 gas for 1 h at 30°C. The initiator of $3.3X10^{-2}$ mol/kg-rubber and monomer were added to the latex, respectively. The reaction was carried out by stirring the latex at about 400 rpm for 2 h at 30°C. The unreacted styrene was removed by using a rotary evaporator under reduced pressure. The as-prepared graft copolymer (gross polymer) was obtained by dipping the glass tube into the reacted latex and dried under reduced pressure at ambient temperature for more than a week. The gross polymer was extracted with acetone/2-butanone 3:1 mixture in a Soxhlet apparatus for 24 h under nitrogen atmosphere in the dark and dried under reduced pressure for about one week, in which the removal of almost all free-polystyrene, isolated from natural rubber, was completed by the extraction for 24 hours. Feed of monomer for the graft-copolymerization is shown in Table 1.

Measurement of nitrogen content of the rubbers was made by Kjeldahl method as described in RRIM Test Method B7. Rubber sample, mixed with catalyst mixture, i.e. potassium sulphate : copper sulphate : selenium in the weight ratio of 15:2:1, was digested with concentrated H_2SO_4. The resulting solution was distilled, and distillates were titrated with 0.05 M H_2SO_4 using methyl red as an indicator.

Ozonization was carried out by blowing an equimolar amount of ozone in ozonated oxygen through a 0.4 w/v% methylene chloride solution of the extracted graft-copolymer at –30°C. Reductive degradation of the resulting ozonide was performed by reaction with lithium aluminum hydride ($LiAlH_4$) in diethyl ether followed by decomposition of residual $LiAlH_4$ with water. After reductive degradation, grafted polystyrene, thus isolated from graft copolymer, was dissolved in a small amount of chloroform. The chloroform solution was centrifuged, and the polymer was precipitated with methanol.

Measurements of molecular weight and molecular weight distribution of the rubbers were made with a TOSOH GPC, consisting a TOSOH CCPD pump, a RI-8012 Differential Refractometer and UV-8011 UV detector. The measurement was made at 30°C and the flow rate of the mobile phase, THF, was 0.5 ml/min.

^{1}H-NMR measurements were carried out at 50°C by a JEOL EX-400 NMR spectrometer at the pulse repetition time of 7 sec.

The volume mean particle diameter was determined using a Coulter LS230 equipped with a small volume module.

Table 1 Feed of monomer for the graft-copolymerization

Rubber	Monomer	Feed of monomer (mol/kg-rubber)	Sample name
Enzymatic Deproteinized Natural Rubber	Styrene	0.5	E-DPNR-PS1
		1.0	E-DPNR-PS2
		1.5	E-DPNR-PS3
		2.0	E-DPNR-PS4
Urea Deproteinized Natural Rubber	Styrene	0.5	U-DPNR-PS1
		1.0	U-DPNR-PS2
		1.5	U-DPNR-PS3
		2.0	U-DPNR-PS4
Urea Deproteinized Natural Rubber	Acrylonitlire	1.0	U-DPNR-PAN1
		2.0	U-DPNR-PAN2
		3.0	U-DPNR-PAN3
		4.0	U-DPNR-PAN4
		5.0	U-DPNR-PAN5

Observation of morphology for the graft-copolymer was made with a transmission electron microscope (TEM), Hitachi H-800 at accelerating voltage of 120 kV. The ultra thin sections of the graft-copolymer were prepared by a Sovall Instruments MT6000 Ultra-microtome at a temperature lower than T_g of NR. The thin sections were stained by OsO_4 after annealing the blends at 80°C for 30 min.

3. Results and Discussion

(1) Removal of protein

Removal of proteins from natural rubber may be essentially concerned with methods of how to control interactions between the rubber and proteins in the latex stage, that is, chemical and physical interactions. The former is cleaved with proteolytic enzyme such as alkaline protease and the latter varied with denaturant such as urea. Thus, we investigated a change in the amount of proteins present in natural rubber after deproteinization under various conditions. Table 2 shows total nitrogen content, X, of natural rubber and rubbers coagulated from the latex after deproteinization with alkaline protease at 32°C for a day (E-DPNR) or incubation with 0.1 wt% urea at 30°C for an hour (U-DPNR). The total nitrogen content of natural rubber was significantly reduced by both the methods to about 1/20, reflecting that not only alkaline protease but also urea were effective to remove the proteins from the rubber. Since urea is well-known to change only conformation of the proteins but not cleave any chemical linkages, the removal of almost all proteins from natural rubber with urea may suggest that the proteins present in natural rubber are attached just on the surface of the rubber particles through physical interactions without any chemical linkages.

To prove the interactions between the rubber and proteins, temperature and time necessary to remove the proteins from natural rubber was investigated. Figure 1 shows the total nitrogen content of natural rubber treated with urea, as a function of time, *t*. At 30°C, the total nitrogen content decreased from 0.38 wt% to 0.022 wt% after incubation with urea for 10 min. Further decrease in the content progressed to 0.020 wt% for 60 min at 30°C. On the other hand, as the temperature of the incubation rose, the nitrogen content of natural rubber increased to about 0.025 wt%. The little bit increase in the nitrogen content may be attributed to less ability of urea to form hydrogen bonds between urea and the proteins at higher temperature. This demonstrates that most proteins, attached on the surface of the rubber particles, undergo a conformational change to detach themselves from the rubber particles with urea. Consequently, the temperature and time necessary to remove proteins from natural rubber with urea was determined to be room temperature and an hour, respectively.

Table 2 Nitrogen content of natural rubber

Specimens	Incubation time (minute)	Nitrogen content (wt%)
Natural rubber	-	0.38
U-DPNR	60	0.020
E-DPNR	720	0.017

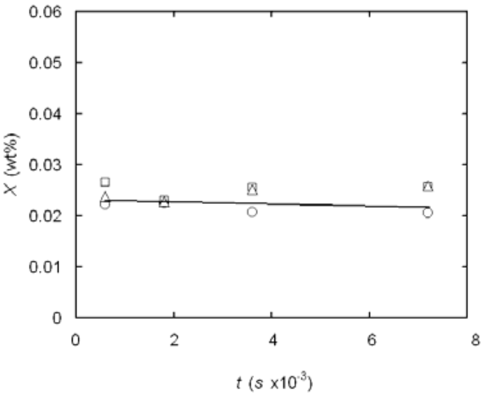

Fig. 1 Nitrogen content of urea-treated natural rubber at 30°C (○), 60°C (△) and 90°C (□) versus time for incubation.

(2) Graft-copolymerization

Styrene

Graft-copolymer was characterized through ^{1}H-NMR spectroscopy. Figure 2 shows a typical ^{1}H-NMR spectrum for the graft-copolymer, i.e. U-DPNR-PS3. Signals characteristic of *cis*-1,4-isoprene units appeared at 1.76, 2.10, and 5.13 ppm, which were assigned to methyl, methylene and unsaturated methyne protons of isoprene units, respectively. Broad signals around 6 - 7 ppm were assigned to phenyl proton of styrene units, whose intensity was dependent upon the feed of styrene as a monomer. Thus, we estimated a content of styrene units in the graft-copolymer and conversion of styrene from a ratio of signal intensities of phenyl to methyl protons and the feed of styrene. The estimated content of styrene units and conversion of styrene for U-DPNR-PS are shown in Fig. 3. The conversion of styrene was dependent upon the feed of styrene, in which a maximum was shown at styrene-feed of 1.5 mol/kg-rubber. In contrast, the content of styrene units of U-DPNR-PS increased monotonically, as the feed of styrene increased. These may suggest that a suitable feed of styrene is 1.5 mol/kg-rubber for the graft-copolymerization of U-DPNR with tert-butyl hydroperoxide of $3.3\mathrm{X}10^{-5}$ mol/g-rubber with tetraethylene pentamine at 30°C. In Fig. 3 are also shown the content of styrene units and conversion of styrene for E-DPNR-PS. The content of styrene units and conversion of styrene for E-DPNR-PS were dependent upon the feed of styrene, as in the case of U-DPNR-PS. Thus, it is possible to expect that the graft-copolymerization for U-DPNR may proceed in a similar way to E-DPNR.

We estimated a grafting efficiency for U-DPNR-PS and E-DPNR-PS. To estimate the grafting efficiency, free polystyrene, which was a mixture present in the graft-copolymer, was removed by extraction with acetone/2-butanone 3:1 mixture. The grafting efficiency, ν, was estimated as follows:

$$\nu = \frac{\text{Mole of polystyrene linked to natural rubber}}{\text{Mole of polystyrene produced during graft-copolymerization}}$$

The estimated value of grafting efficiency of styrene for U-DPNR-PS and E-DPNR-PS is shown in Fig. 4. The grafting efficiency was dependent upon the feed of styrene and a maximum was shown at 1.5 mol/kg-rubber feed of styrene. The feed of styrene at the maximum was a similar to that for the conversion of styrene. This may be attributed to a deactivation and chain transfer of the radicals due to less and large amount of styrene, respectively. At 1.5mol/kg-rubber feed of styrene for U-DPNR and E-DPNR, almost all polystyrene, thus produced, was proved to link up to the rubber molecule. This demonstrates that the reactivity of U-DPNR for graft-copolymerization with free-radical-initiator is the same as that of E-DPNR.

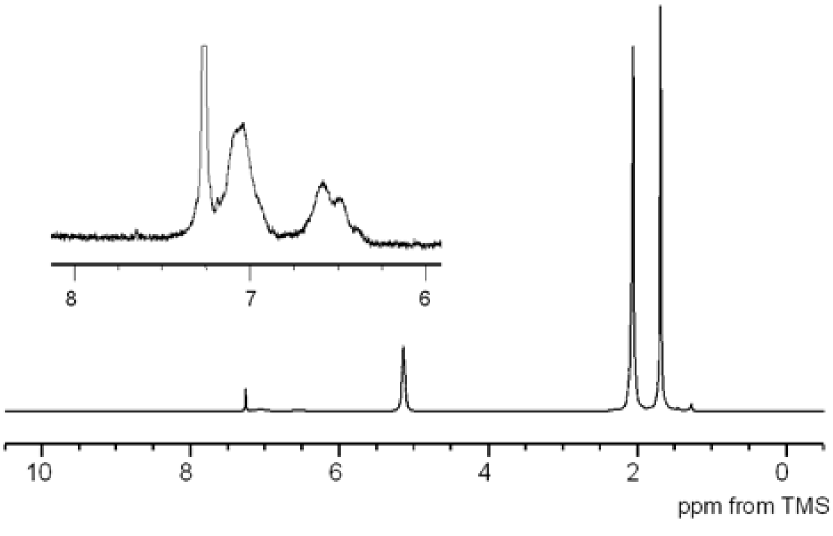

Fig. 2 Typical ^{1}H-NMR spectrum for U-DPNR-PS3.

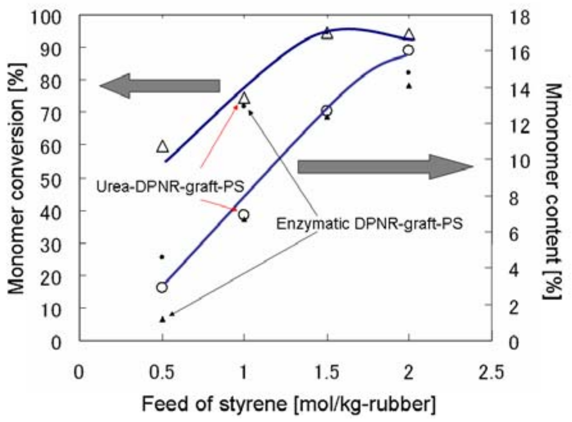

Fig. 3 Conversion and content of styrene for U-DPNR-PS and E-DPNR-PS.

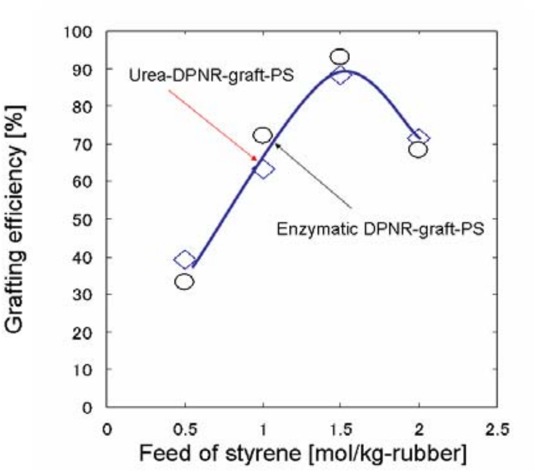

Fig. 4 Grafting efficiency for DPNR-St.

Acrylonitlire

Content of acrylonitlire units and conversion of acrylonitlire for U-DPNR-PAN are shown in Fig. 5. The conversion of acrylonitlire was dependent upon the feed of acrylonitlire, in which a maximum was shown at acrylonitlire-feed of 3.0 to 4.0 mol/kg-rubber. In contrast, the content of acrylonitlire units of U-DPNR-PAN increased monotonically up to 4.0 mol/kg-rubber, as the feed of acrylonitlire increased. These may suggest that a suitable feed of acrylonitlire is 4.0 mol/kg-rubber for the graft-copolymerization of acrylonitrile onto U-DPNR with tert-butyl hydroperoxide of $3.3X10^{-5}$ mol/g-rubber and tetraethylenepentamine at 303K.

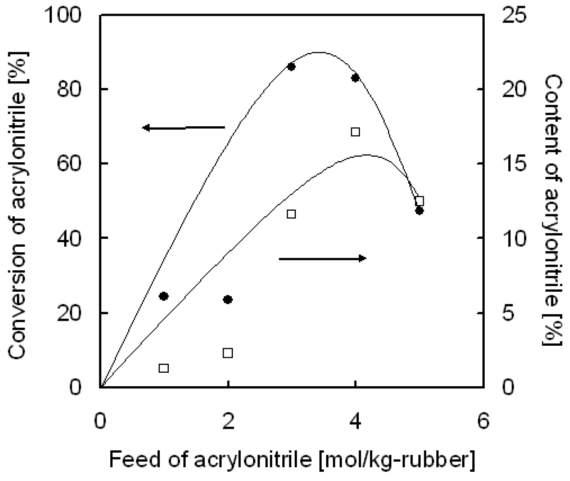

Fig. 5 Conversion (●) and content (□) of acrylonitlire for U-DPNR-PAN.

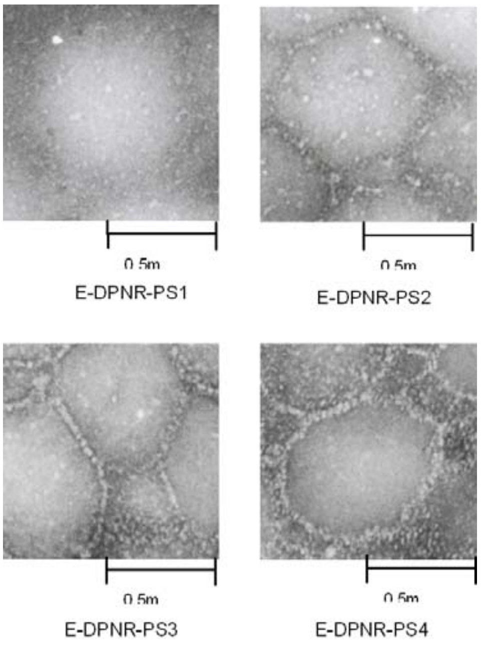

Fig. 6 TEM photographs for E-DPNR-PS1, E-DPNR-PS2, E-DPNR-PS3 and E-DPNR-PS4, respectively.

Morphology

TEM photographs for E-DPNR-PS1, E-DPNR-PS2, E-DPNR-PS3 and E-DPNR-PS4 are shown in Fig. 6, in which a gloomy domain is natural rubber and a bright domain is polystyrene. As for E-DPNR-PS1, little bright domain was scattered in the gloomy matrix. As the feed of polystyrene increased, the bright domain segregated together to cover the gloomy spheres. To characterize the gloomy spheres, we estimated an average diameter of gloomy sphere for E-DPNR-PS3 and E-DPNR-PS4, and these are tabulated in Table 3. The average diameter of gloomy sphere was similar to the volume mean particle diameter of the dispersoid present in natural rubber latex, which is about 0.7 μm in diameter. Since the film specimens were prepared by coagulation of the latex, the gloomy sphere, observed in the photograph, may be attributed to the dispersoid present in the latex. The thickness of the bright domain is also shown in Table 3. The thickness was about 15nm for E-DPNR-PS3, while it was about 25 nm for E-DPNR-PS4. This bright domain would be a matrix, that is, a continuous phase. To confirm the fact that polystyrene was the matrix, a volume fraction of polystyrene for E-DPNR-PS3 was estimated by image-analysis of the photograph. The estimated volume fraction of polystyrene was about 10 v/v% for E-DPNR-PS3, which corresponded to 11 v/v%, estimated from styrene unit content shown in Figure 3. This demonstrates that natural rubber particle of about 0.5 μm in diameter is dispersed in polystyrene matrix of about 15 nm in thickness. Since the grafting efficiency of styrene for E-DPNR-PS3 is more than 90mol%, as shown in Fig. 4, almost all polystyrene may link up to E-DPNR. Figure 7 shows TEM photograph for U-DPNR-PS3. The nano-matrix structure was also found for U-DPNR-PS3, as in the case of E-DPNR-PS3. The thickness of bright domain was about 15nm. Since the styrene content and grafting efficiency of styrene for U-DPNR-PS3 were about 12w/w% and 90%, respectively, the nano-matrix structure was proved to be formed for not only E-DPNR but also U-DPNR.

Table 4 Average diameter and average thickness for E-DPNR-PS3 and E-DPNR-PS4.

Specimen	*D* (μm)	*t* (nm)
E-DPNR-PS3	0.5	15
E-DPNR-PS4	0.6	25

D: average diameter
t : average thickness

Morphology of U-DPNR-PAN4 was also observed by TEM. Figure 8 shows TEM photographs for U-DPNR-PAN4, in which a gloomy domain is natural rubber and a bright domain is polyacrylonitrile. The natural rubber particle was covered with polyacrylonitlire to form nano-matrix structure, in which the thickness of polyacrylonitlire was less than 15 nm. This demonstrates that the

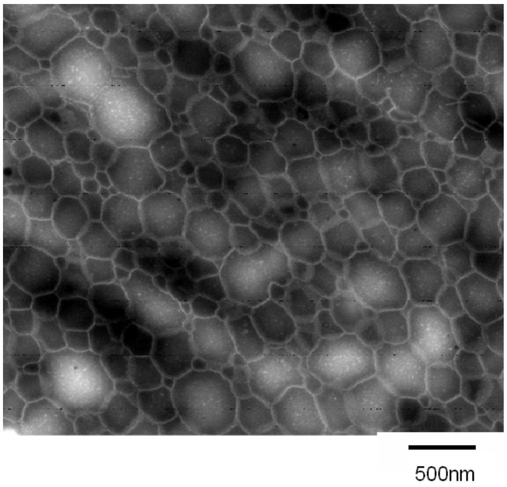

Fig. 7 TEM photograph for U-DPNR-PS3.

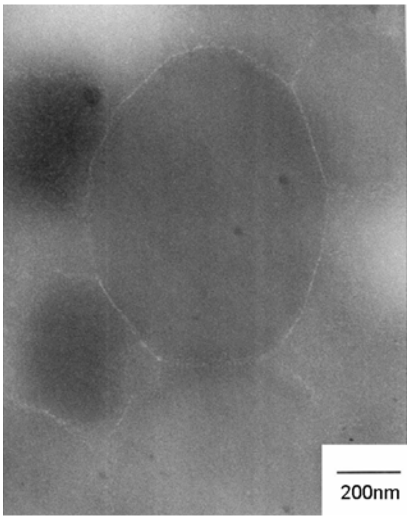

Fig. 8 TEM photograph for U-DPNR-PAN4.

nano-matrix structure is formed with not only styrene as a non-polar monomer but also acrylonitrile as a polar monomer.

Mechanical properties and oil resistance

Figure 9 shows stress-strain curves for unvulcanized graf-copolymers, that is, E-DPNR-PS1, E-DPNR-PS2, E-DPNR-PS3 and E-DPNR-PS4. A stress at strain of 1 increased as the styrene content increased, reflecting an increase in Young's modulus. On the other hand, the highest stress at break was shown for E-DPNR-PS3. This may be attributed to not only the nano-matrix structure but also the highest grafting efficiency. As the results, the nano-matrix structure was proved to be formed for E-DPNR-PS3.

Oil resistance of U-DPNR-PAN is shown in Fig. 10. The oil resistance for U-DPNR-PAN1, U-DPNR-PAN2 was identical to that for U-DPNR, itself. However, as the PAN content increased, i.e. for U-DPNR-PAN3, U-DPNR-PAN4, U-DPNR-PAN5, the oil resistance increased significantly. The abrupt increase in the oil resistance of U-DPNR-PAN may be attributed to the formation of nano-matrix structure. This may be distinguished from the oil resistance of U-DPNR/PAN blend, which consists of ordinary island-matrix morphology.

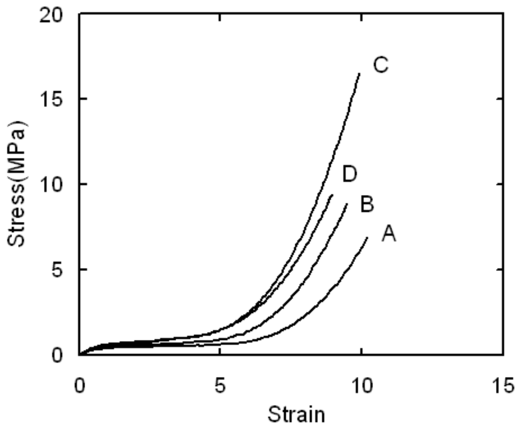

Fig. 9 Stress-Strain curve for unvulcanized E-DPNR-PS: A, E-DPNR-PS1; B, E-DPNR-PS2; C, E-DPNR-PS3; D, E-DPNR-PS4.

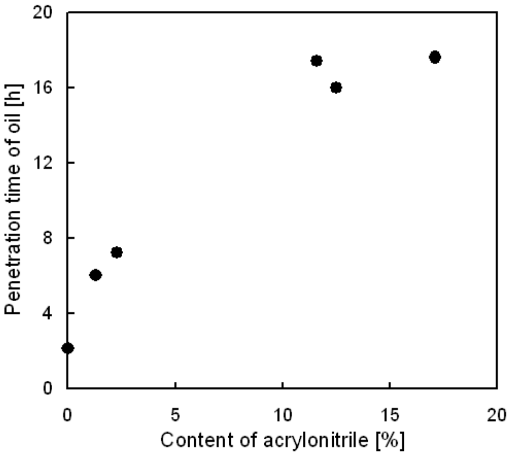

Fig. 10 Oil resistance of U-DPNR-PAN

4. Conclusion

Graft-copolymerization of deproteinized natural rubber was carried out with tert-butyl hydroperoxide / tetraethylenepentamine as an initiator. The highest conversion and grafting efficiency were achieved at styrene feed of 1.5mol/kg-rubber to be 98% and 93%, respectively. For E-DPNR-PS3, natural rubber particle of about 0.5μm in diameter was dispersed in polystyrene-matrix of about 15 nm in thickness. The stress at break for E-DPNR-PS3 was found to be the highest, due to not only nano-matrix of polystyrene but also the highest grafting efficiency. It is concluded that the nano-matrix structure, which results in outstanding mechanical properties, is formed by graft-copolymerization of styrene onto DPNR in latex stage. On the other hand, graft-copolymerization of acrylonitrile onto DPNR was also effective to increase the oil resistance at acrylonitrile feed of more than 3.0mol/kg-rubber.

Acknowledgments

This work was supported from the Grant-in-Aid for Scientific Research from the Ministry of Education, Science, Sports, Culture and Technology, Japan, and by Program for High Reliable Materials Design and Manufacturing in Nagaoka University of Technology.

References

[1] S. Kawahara, T. Kawazura, T. Sawada, and Y. Isono, Polymer, **44**, (2003) 4527.
[2] G. A. Jeffery, Trans. Fraday Soc., **38**, (1941) 384.
[3] G. F. Bloomfield, and P. M. Swift, J. Appl. Chem., 5 (1955) 605.
[4] P. W. Allen, and F. W. Merrett, J. Polym. Sci., 22 (1956) 193.
[5] E. G. Cockbain, T. D. Pendle, and D. T. Turner, J. Polym. Sci., 39 (1959) 419.
[6] H. Y. Erbil, J. Nat. Rubb. Res., 1 (1986) 234.
[7] C. C. Ho, T. Kondo, N. Muramatsu, H. Ohshima, J Coll. Interface Sci. 178 (1996) 442.
[8] Y. Fukushima, S. Kawahara, Y. Tanaka, J. Rubb. Res., 1 (1998) 154.

(Received: 16 May, 2012, Accepted: 30,June 2012)

*Transactions on GIGAKU **1**(2012)01008/1-4*

Mullite Formation in Presence of Y_2O_3 by Homogeneous Precipitation

José de Jesús Rocha Jiménez[1], J. Merced Martínez Rosales[1]
Keizo Uematsu[2], Satoshi Tanaka[2]and Satoshi Sugita[1]

1 Departamento de Química, Universidad de Guanajuato, México
Noria alta s/n Col Noria Alta CP.36050. Guanajuato, Gto, México
[2]Department of Materials Science and Technology, Nagaoka University of Technology,
1603-1 Kamitomioka-cho, Nagaoka 940-2188, Japan
**E-mail: stanaka@vos.nagaokaut.ac.jp*

A novel route to obtain mullite ceramics ($3Al_2O_3$-$2SiO_2$) with less energy consuming was proposed. As have been proved in previous works, yttria as a sintering additive promotes sintering of mullite phase via glassy phase. In this study, an yttria-doped mullite micro-composite powder was synthesized via the homogeneous precipitation technique and the subsequent mullitization reaction. Dense mullite ceramics with submicron grain size was obtained by micro-composite powder at 1450°C. Glassy phase retained on grain boundaries was reduced in mullite ceramics.

1. Introduction

Ceramic materials are extensively used around the world for wide applications. For example, at the moment ceramics are used in around 50% of material existing buildings worldwide and fast growing up market in technological applications. The environmental impacts associated with ceramic industry have become increasingly of importance. Usually, the manufacturing of ceramic materials employs highly energy intensive processes consuming natural resources, materials and energy; generating different types of environmental impacts. As the environmental concerns have increased, the need for environmental friendly ceramic processing is growing [1]. The special case is mullite ($3Al_2O_3$-$2SiO_2$) which is one of the most employed ceramics, because mullite phase is the only thermodynamically stable at high temperatures and ambient pressure. Its excellent properties at high temperature such as good mechanical strength, low thermal expansion coefficient, and high creep resistance make it an attractive ceramic material for high-temperature mechanical applications [2]. However, high temperatures (~1600°C) are required for the production of high density mullite ceramic materials. The higher energy consuming process is related to the last part of the process, sintering [3,4].

On previous works, it was possible to produce fine mullite powder (~0.2 μm) from a homogeneous precipitation technique, in which aluminum sulphate and fumed silica were used as raw materials [5]. On sintering of mullite ceramics, the addition of yttria powder 5wt% as a sintering aid to mullite powder reduce the sintering temperature to 1400°C [6]. However, when a large amount of yttria powder was added more, the large defects appeared as the large amounts of glassy phase concentrated at grain boundaries. The large defects in ceramic materials play a main role on the mechanical properties [7].

The objective of this study was to produce dense mullite ceramic materials with fine microstructure at lower temperature by using small quantities of yttria (2wt%) as additive for mullitization and sintering. An yttria-doped fine mullite powder was prepared from yttria-doped mullite precursor of pseudo-bohemite coated on silica. Preparing precursors with core shell type was supported in three facts: first, the reaction rate of mullite can be enhanced easily by reducing the distance between phases. Second, reducing the viscous glassy phase promotes the Al mass transport into silica rich phase [8]. Third, the use of yttria during sintering promotes densification through glassy phase sintering mechanisms. The reduction of temperature leads to reduction in waste energy, in other words, low impact environmental mullite ceramic materials.

2. Experimental

The preparation of pseudo-bohemite coated on fumed silica surface with and without yttria was made using aluminum sulphate, fumed silica (10-40 nm), and nanometric yttria (<50 nm) as starting materials. The entire process was divided in 2 steps. The first step, homogeneous precipitation was used, which had been reported in detail elsewhere [5]. The technique consists of preparing a well-dispersed aqueous suspension of fumed silica and/or yttria in ultrasonic water bath. Subsequently, by controlling pH ~4, a basic aluminum sulphate was precipitated on the fumed silica and yttria surfaces. After the precipitation was finished, the obtained precursor was ammonia neutralized in order to remove the sulphate ions. The neutralization was carried out at pH ~9.5, 70°C and 15 min. The final mullite precursor was pseudo-bohemite coated silica micro-composite with and without dopants, labeled as Al-Si and Al-Si-Y respectively. After neutralization, Al-Si and Al-Si-Y were heated dynamically at 5°C/min in a controlled electric furnace. To study the behavior of mullite reaction from precursor, both were heated at several temperatures until 1300°C.

After heat treatment, synthesized yttria-doped or non-doped mullite powder were ball milled for 24 h using ammonia poly-acrylate as dispersant, respectively. Green compact was formed by a conventional slip casting technique. Subsequently, the green compacts were sintered at 1400°C. SEM observations for powders and sintered materials were made, also a XRD test were made for phase analysis during heat treatment.

3. Results and Discussion

Figure 1 shows XRD patterns of the thermal evolution of precursors with and without dopant. On the left image, it can be seen that the precursor phase is pseudo-bohemite identified for the characteristic peaks at 26, 37, 48, and 63°, it also can be observed at 20° the wide amorphous silica peak. According to XRD, yttria effect on crystallinity is almost undetectably, being the doped sample less crystalline.

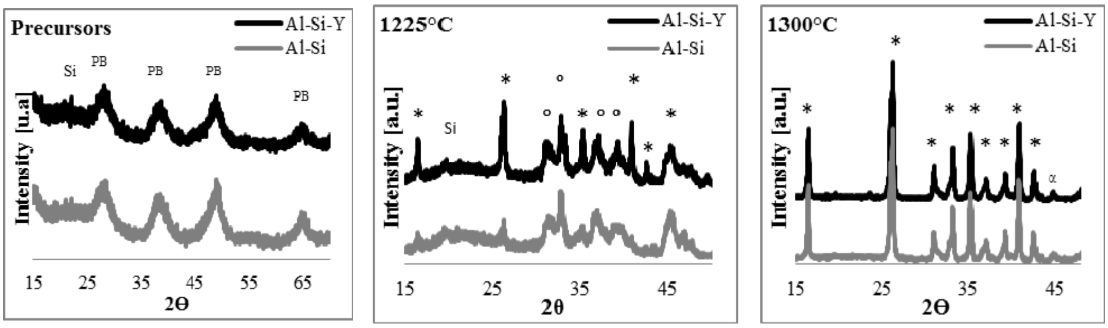

Fig. 1 XRD patterns of powders evolution before and after heat treatment. Si: SiO_2, PB: Pseudo-bohemite, °: cubic spinel and *****:Mullite.

During the heat treatment, mullite formation becomes perceptible. Yittria doped sample displayed more intense signals at 1225°C. This phenomenon is related to the increased Al mass transportation into silica by reduction of viscosity of the glassy phase, which was made by the formation of a transient glassy material Y-Al-Si-O [6]. The present phases identified on XRD coexisting during mullite formation were recognized as: Si-Al spinel, a mixture of (θ- δ) transition alumina and broad wide signal of amorphous silica.

The formation of mullite was almost completed at 1300°C for the doped sample, the broad peak of silica and alumina peaks were almost disappeared. Sample without yttria still has some trace of silica. In general, yttria accelerates the reaction velocity of mullite formation.

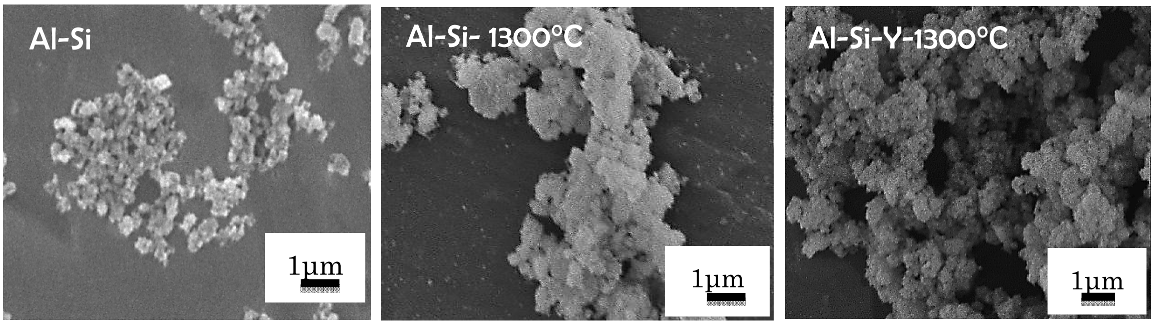

Fig. 2 SEM micrograph of (left) the pseudo-bohemite before heat treatment, heat treated powders (center) without dopant and (right) with 2wt% yttria.

Figure 2 shows SEM micrographs of morphology of precursor and their reaction to mullite powder after heat treatment at 1300°C. The precursor morphology consists of sub-micrometric primary nearly spherical particles. After heat treatment, the morphology of particles is retained and agglomerates consisting of submicron particles are observed. Based on observations, no noticeable differences on size or morphology were found between yttria doped or undoped material system. The enlarged size on particles was related to sintering.

Figure 3 presents the microstructures obtained from yttria doped and undoped material systems after sintering at low temperature ~1450°C during 2 h. Fig.3 (a) is related to the Al-Si system; the sample did not reach high density, and still porous. It is evident that the sintering processes such as neck forming and grain growth have being started. Usually, a high temperature above 1600°C for high density is necessary in undoped material system.

On doped system, at 1450°C, high density was reached as shown displaying fine microstructure (less than 0.5 µm in grain size) and without abnormal grain growth using small amounts of Y_2O_3 (2wt%) as sintering additive. Some pore still is observed between grain boundaries. The reduction porosity was favored by glassy phase sintering mechanisms occurring between grain boundaries. As the image presents, no accumulated glassy phase was observed between grain boundaries.

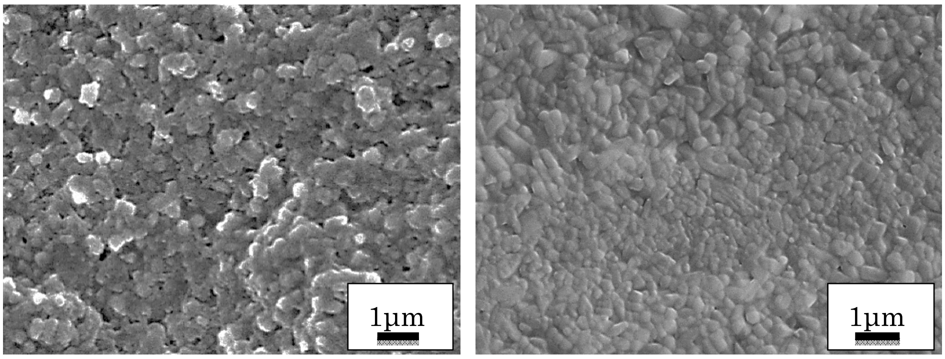

Fig. 3 SEM photo-micrograph of sintered materials heat treated at 1450°C. Left side undoped sample and right side doped sample.

The main difference between both microstructures was related to two different sintering processes. On the undoped sample, higher energy was required for densification since the densification mechanisms are governed by solid state sintering. For yttria doped mullite system, a transient viscous sintering mechanism related to the glassy phase existent between boundaries promotes high densification.

4. Conclusion

Less energy consuming mullite ceramic materials were prepared using yttria doped mullite micro-composite powders. The employ of small amounts of yttria (2wt%) as sintering additive provides clear benefits, such as: Sintering temperature 1450°C, being 150°C lower than normal mullite ceramic materials. Fine homogeneous microstructure (grain size ~0.5 μm) without abnormal grain growth related to low temperatures of sintering. Reduced defects associated to excessive glassy phase between grain boundaries. Increased mullite reaction rate promoted by low viscosity transient viscous phase sintering Al-Si-O-Y.

Acknowledgments

The authors thank to CONACyT for its financial assistance by providing a doctoral scholarship to one of us (J.J.R.J.)

References

[1] N. Tikul, P. Srichandr, J. Ceram. Soc. Jpn., **118** (2010) 887.
[2] I. A. Aksay, D. M. Dabbs, M. Sarikaya, J. Am. Ceram. Soc., **74** (1991) 2343.
[3] H. Schneider, J. Scheurer, B. Hildmann, J. Eur. Ceram. Soc., **28** (2008) 329.
[4] S. Somiya, Y. Hirata Am. Ceram. Soc. Bull., **70** (1991) 1624.
[5] S. Sugita, C. Contreras, J. Eur. Ceram. Soc., **18** (1998) 1145.
[6] P. Mechnich, H. Schneider, M. Schmücker, B. Saruhan, J. Am. Ceram. Soc., **81** (1998) 1931.
[7] S. Nakamura, S. Tanaka, Z. Kato, K. Uematsu, J. Am. Ceram. Soc., **92** (2009) 688.
[8] K. Wang, M. D. Sacks, J. Am. Ceram. Soc., 79 [1] (1996) 12.

(Received: 15 May, 2012, Accepted: 29 June, 2012)

Transactions on GIGAKU **1***(2012)01009/1-6*

Isolation and Characterization of *bzaA* and *bzaB* of *Sphingobium* sp. Strain SYK-6, Which Encode Aromatic Aldehydes Dehydrogenases with Different Substrate Preferences

Yuko Yamamoto, Daisuke Kasai, Naofumi Kamimura, Eiji Masai*
Department of Bioengineering, Nagaoka University of Technology,
1603-1 Kamitomioka, Nagaoka, Niigata 940-2188, Japan
**E-mail: emasai@vos.nagaokaut.ac.jp*

Conversion of vanillin and syringaldehyde to their corresponding acids is an essential step in the production of useful intermediate metabolites such as 2-pyrone-4,6-dicarboxylic acid (PDC). We isolated the aromatic aldehydes dehydrogenase genes, *bzaA* and *bzaB*, of *Sphingobium* sp. strain SYK-6, which showed approximately 30% identity at amino acid levels with vanillin dehydrogenase genes of *Pseudomonas* strains. Both genes were expressed in *Escherichia coli*, and the cell extract of *E. coli* carrying *bzaA* showed the oxidation activities toward a broad range of aromatic aldehydes, including syringaldehyde and vanillin. On the other hand, the gene product of *bzaB* was highly specific for *m*-anisaldehyde, and the oxidation activities toward syringaldehyde and vanillin were less than 16% of that toward *m*-anisaldehyde. Disruption of *bzaA* and *bzaB* in *Sphingobium* sp. strain SYK-6 had little effect on the growth of the mutant on syringaldehyde, suggesting that the contribution of these genes to the degradation of syringaldehyde in SYK-6 appeared to be insignificant. However, *bzaA* seemed to be a useful tool for bioprocesses converting lignin-derived aromatic aldehydes to industrially valuable intermediate metabolites.

1. Introduction

One of the practical utilizations of lignin, which is a major component of the plant cell wall, is the production of industrially valuable chemicals through a combination of chemical decomposition of lignin and microbial conversion. Since the chemical oxidation of lignin yields large amounts of vanillin and syringaldehyde, these lignin-derived aromatic aldehydes are thought to be effective starting compounds for the production of useful microbial metabolites, such as 2-pyrone-4,6-dicarboxylic acid (PDC) [1, 2]. PDC is an intermediate metabolite of the protocatechuate 4,5-cleavage pathway, and has been found to be useful in the production of biodegradable and high-functional polymers, for instance strong adhesives [3-5]. In order to convert vanillin and syringaldehyde to PDC, the conversion of these aldehydes to vanillate and syringate, respectively, is essential (Fig. 1). For this purpose, the vanillin dehydrogenase gene, *ligV*, was isolated from a lignin-derived aromatics degrader, *Sphingobium* sp. strain SYK-6 [1, 6]. The deduced amino acid sequence of *ligV* showed 50-55% identity with those of the known vanillin dehydrogenase genes of *Pseudomonas* strains. The gene product of *ligV* produced in *E. coli* showed the oxidation activities toward vanillin, benzaldehyde, protocatechualdehyde, *m*-anisaldehyde, and *p*-hydroxybenzaldehyde, but the activity toward syringaldehyde was less than 5% of that toward vanillin. Disruption of *ligV* in SYK-6 indicated that this gene is essential for normal growth of SYK-6 on vanillin. However, this disruption affected, to some extent, the ability of SYK-6 to grow on syringaldehyde, suggesting that another aromatic aldehydes dehydrogenase gene is responsible for the degradation of syringaldehyde.

In this study, we isolated and characterized the two different aromatic aldehydes dehydrogenase genes, *bzaA* and *bzaB*, from a cosmid clone pKTV3. pKTV3 was isolated as a cosmid clone, which conferred the ability to convert vanillin to vanillate on *Sphingomonas sanguinis* IAM 12578 [6].

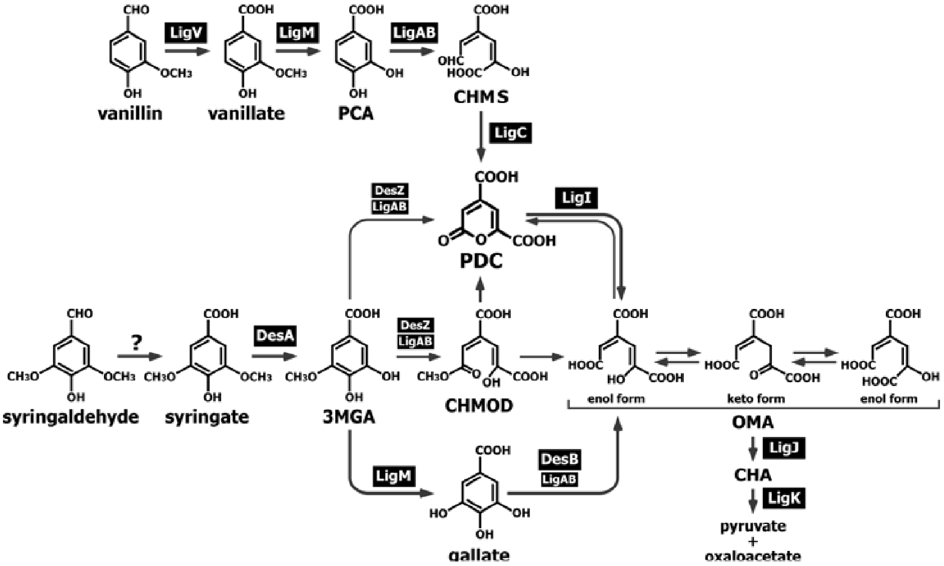

Fig. 1. Catabolic pathway of vanillin and syringaldehyde in *Sphingobium* sp. strain SYK-6. Enzymes: LigV, vanillin dehydrogenase; LigM, vanillate/3MGA *O*-demethylase; LigAB, PCA 4,5-dioxygenase; LigC, CHMS dehydrogenase; LigI, PDC hydrolase; LigJ, OMA hydratase; LigK, CHA aldolase; DesA, syringate *O*-demethylase; DesB, gallate dioxygenase; DesZ, 3MGA 3,4-dioxygenase. Compounds: PCA, protocatechuate; CHMS, 4-carboxy-2-hydroxymuconate-6-semialdehyde; PDC, 2-pyrone-4,6-dicarboxylate; OMA, 4-oxalomesaconate; CHA, 4-carboxy-4-hydroxy-2-oxoadipate; 3MGA, 3-*O*-methylgallate; CHMOD, 4-carboxy-2-hydroxy-6-methoxy-6-oxohexa-2,4-dienoate.

2. Experiment

Bacterial strains and culture conditions

Sphingobium sp. strain SYK-6 and its mutant derivatives were routinely grown at 30°C in Luria-Bertani (LB) medium or W minimal salt medium [7] containing 5 mM vanillin, 5 mM syringaldehyde, 10 mM vanillate, or 10 mM syringate. *Sphingomonas sanguinis* IAM 12578 [8] and the SYK-6 mutants were grown in LB medium. If necessary, 50 mg of kanamycin/liter, 300 mg of carbenicillin/liter, or 12.5 mg of tetracycline/liter were added to the cultures. *Escherichia coli* strains were grown in LB medium at 37°C. For cultures of cells carrying antibiotic resistance markers, the media for *E. coli* transformants were supplemented with 100 mg of ampicillin/liter, 25 mg of kanamycin/liter, or 12.5 mg tetracycline/liter.

Cloning and nucleotide sequencing of aromatic aldehydes dehydrogenase genes

A cosmid pKTV3 [6] was digested with various restriction enzymes, and each DNA fragment was subcloned into pBluescript II KS(+) or SK(+) [9]. Cells of *E. coli* JM109 [10] harboring subclones were grown in 10 ml of LB medium until the optical density at 600 nm (OD_{600}) of the culture reached 0.5. After the addition of 1 mM isopropyl-β-D-thiogalactopyranoside (IPTG), the culture was further incubated for 4 h. The cells were harvested by centrifugation (5,000 × *g*, 10 min), washed with 50 mM Tris-HCl buffer (pH 7.5), and resuspended in 1 ml of the same buffer. Cell suspensions (500 μl) were incubated with vanillin or syringaldehyde (1 mM) at 30°C for 24 h. After the incubation, cells were removed by centrifugation (15,000 × *g*, 15 min), and the supernatants were analysed by high-performance liquid chromatography (HPLC). Further subcloning was performed to clone the 3.1-kb BamHI-HindIII fragment carrying ORF1 (*bzaA*) from pKTVH8F carrying the 8.0-kb HindIII fragment in KS(+). Southern hybridization analysis of pKTV3 was done using the digoxigenin (DIG) system (Roche Diagnostic) to identify the DNA fragment, which carried the 5′

region of ORF2 (*bzaB*). The nucleotide sequences of *bzaA* and *bzaB* were determined by the dideoxy termination method with a CEQ 2000XL genetic analysis system (Beckman Coulter). Sequence analysis was performed with the GeneWorks program (Intelligenetics, Inc.). Homology searches were performed with the non-redundant protein sequence database using the BLAST program. Pairwise alignment was done with the EMBOSS alignment tool at the homepage of the European Bioinformatics Institute (http://www.ebi.ac.uk/Tools/psa/).

Disruption of bzaA and bzaB

The 1.0-kb BspHI fragment carrying the β-lactamase gene (*bla*) of pUC19 [10] was blunted, and ligated into the blunt-ended NdeI site of pUCV2 carrying the 3.1-kb SalI-XbaI fragment in pUC19 to disrupt *bzaA*. The 4.1-kb SalI-XbaI fragment of the resultant plasmid pADV2 was ligated into pK18*mobsacB* [11], and pADV2B was obtained. The 3.1-kb BamHI-HindIII fragment carrying *bzaB* was cloned into pK19*mobsacB* [11] to obtain pKBV3. The 0.8-kb StuI fragment of pKBV3 was replaced with the 1.9-kb SmaI fragment carrying the tetracycline resistance gene (*tet*) of pKRP12 [12], and pTDV3 was obtained. The 1.5-kb NaeI-StuI fragment of pUCV2 was replaced by the 1.0-kb BspHI fragment carrying *bla* to disrupt both *bzaA* and *bzaB*. The 2.6-kb SalI-XbaI fragment of the resulting pNSD23 was cloned into pK18*mobsacB* to generate pKDV23B. pADV2, pTDV3, and pKDV23 were individually introduced into SYK-6 cells by electroporation, and the candidates for *bzaA* mutant (SME044), *bzaB* mutant (SME045), and *bzaA bzaB* double mutant (SME046) were screened using the method described previously [13]. To examine the disruption in each gene, Southern hybridization analysis was performed. The total DNAs of candidates for SME044, SME045, and SME046 were digested with EcoRV, ApaI, and BamHI-HindIII, respectively. The 0.8-kb HincII-Eco47III fragment carrying *bzaA*, the 1.2-kb BspHI-EcoRV fragment carrying *bzaB*, the 1.0-kb BspHI fragment carrying *bla*, and the 1.9-kb HindIII fragment carrying *tet* were labelled with the DIG system and used as probes.

SYK-6 and its mutants were grown in LB medium (100 ml) until the OD_{600} of the culture reached 1.0. Cells were harvested by centrifugation (5,000 × *g*, 10 min), washed with 100 mM potassium phosphate buffer (pH 7.0), and resuspended in the same buffer. The cells were sonicated, and the cell lysate was centrifuged at 15,000 × *g* for 15 min. The resulting supernatant was used as cell extracts. Protein concentrations were determined using the Bradford method [14]. The oxidation activities of cell extracts for aromatic aldehydes were determined as descried below.

Expression of bzaA and bzaB in E. coli

The 1.7-kb BamHI-PstI fragment carrying *bzaA* and the 2.5-kb BglII-SalI fragment carrying *bzaB* were cloned into SK(+) and KS(+), respectively, to obtain pSKL2 and pBSV3. Cells of *E. coli* JM109 harboring pSKL2 or pBSV3 were grown in LB medium containing 100 mg ampicillin/liter at 37°C. Expressions of *bzaA* and *bzaB* were induced for 6 h and 8 h, respectively, by adding 1 mM IPTG when the OD_{600} of the culture reached 0.5. Cells were harvested by centrifugation and suspended in 100 mM potassium phosphate buffer (pH 7.0). The cell extracts were prepared similarly to the method mentioned above. Expressions of the genes were examined using sodium dodecyl sulphate-polyacrylamide gel electrophoresis (SDS-PAGE). Gels were stained with Coomasie brilliant blue.

Enzyme assay

Degradation of vanillin and syringaldehyde was periodically analysed with an Alliance 2690 separation module HPLC system equipped with a TSKgel ODS-80 column (6 by 150 mm; Tosoh). The mobile phase was a mixture of water (74.25%), acetonitrile (24.75%), and acetic acid (1%), and the flow rate was 1 ml/min. Vanillin and syringaldehyde were detected at 280 nm and 308 nm, respectively. The retention times of vanillin, syringaldehyde, vanillate, and syringate were 9.0, 9.0, 6.0, 5.9 min, respectively, by a photodiode array detector (Waters 2996).

Oxidation activities for aromatic aldehydes including vanillin and syringaldehyde were determined using a spectrophotometer (DU-7500, Beckman-Coulter). The decrease in absorbance at 364 nm derived from syringaldehyde (ε_{364} = 8,936 $M^{-1} cm^{-1}$, pH 7.0) was monitored in a reaction mixture containing 100 mM potassium phosphate buffer (pH 7.0), 0.5 mM NAD^+, 1.2 mM pyruvate, 1.0 U lactate dehydrogenase, 100 μM substrate, and a cell extract (100 μg of protein/ml of crude BzaA, 500 μg/ml of crude BzaB, and 500 μg/ml of cell extracts of SYK-6 and its mutants) at 30°C. To examine the substrate preference of BzaA and BzaB, the cell extracts were incubated with 100 μM of the following substrates as described above: benzaldehyde (ε_{293} = 1,270 M^{-1} cm^{-1}), *p*-hydroxybenzaldehyde (ε_{331} = 7,088 M^{-1} cm^{-1}), protocatechualdehyde (ε_{341} = 9,070 M^{-1} cm^{-1}), *m*-anisaldehyde (ε_{330} = 2,181 M^{-1} cm^{-1}), veratraldehyde (ε_{330} = 3,536 M^{-1} cm^{-1}), coniferyl aldehyde (ε_{410} = 3,330 M^{-1} cm^{-1}), or vanillin (ε_{346} = 8,697 M^{-1} cm^{-1}). One unit of enzyme activity was defined as the amount of activity that oxidized 1 μmol of aromatic aldehydes per 1 min. Specific activity was expressed in units per milligram of protein.

Nucleotide sequence accession number

The nucleotide sequence of *Sphingobium* sp. strain SYK-6 chromosome containing *bzaA* (SLG_27910) and *bzaB* (SLG_27920) were deposited in the DDBJ/EMBL/GenBank databases under accession number AP012222.

3. Results and Discussion

Isolation of aromatic aldehydes dehydrogenase genes from Sphingobium sp. strain SYK-6

Subcloning of pKTV3, which contained approximately 20-kb SalI fragments, showed that the 3.1-kb BamHI-HindIII fragment conferred the oxidation activity for syringaldehyde and vanillin on *E. coli* JM109. Nucleotide sequence of the 3.1-kb BamHI-HindIII fragment revealed an open reading frame (ORF), encoding a polypeptide of 472 amino acids (ORF1) and an incomplete ORF (ORF2), which are oriented convergently as shown in Fig. 2. The deduced amino acid sequence of ORF1 showed 31-35% identity with those of the vanillin dehydrogenase genes of *Pseudomonas putida* KT2440 [15], *Pseudomonas* sp. strain HR199 [16], *Pseudomonas fluorescence* AN103 [17], *P. putida* WCS358 [18], and *Sphingobium* sp. strain SYK-6 [6]. Therefore, this ORF appeared to encode aromatic aldehydes dehydrogenase and was designated *bzaA*. In order to obtain a full length of ORF2, Southern hybridization of pKTV3 was performed using the 0.5-kb BspHI-HindIII fragment carrying a part of ORF2 as a probe. This analysis showed that ORF2 was included in the 4.2-kb ApaI fragment. Nucleotide sequence of the 2.5-kb BglII-SalI fragment in the 4.2-kb ApaI fragment showed that ORF2 encodes a polypeptide of 489 amino acids (Fig. 2). The deduced amino acid sequence of ORF2 showed 27-34% identity with those of the vanillin dehydrogenase genes of *Pseudomonas* strains and SYK-6, and *bzaA*. Based on these similarities, ORF2 was designated *bzaB*.

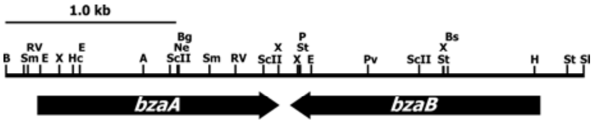

Fig. 2. Restriction map of the 3.4-kb BamHI-SalI fragment carrying *bzaA* and *bzaB*. Abbreviations: A, ApaI; B, BamHI; Bg, BglII; Bs, BspHI; E, EcoRI; H, HindIII; Hc, HincII; Ne, NaeI; P, PstI; Pv, PvuII; RV, EcoRV; ScII, SacII; Sl, SalI; Sm, SmaI; St, StuI; X, XhoI.

Enzymatic properties of BzaA and BzaB

Each of the *bzaA* and *bzaB* genes was expressed in *E. coli* JM109 under the control of *lac* promoter. SDS-PAGE showed the production of 45-kDa and 48-kDa proteins in cell extracts of *E. coli* JM109 harboring pSKL2 and pBSV3, which carried *bzaA* and *bzaB*, respectively. These values were close to the predicted molecular masses of the corresponding gene products calculated from the amino acid sequences.

Cell extracts (100 μg of protein/ml) of *E. coli* harboring pSKL2 or pBSV3 were incubated with 100 μM vanillin in the presence of NAD^+ or $NADP^+$ (500 μM) to determine the cofactor requirement. The vanillin dehydrogenase activities were dependent on NAD^+ or $NADP^+$. However, 2.3-fold higher activity of BzaA and 19-fold fold higher activity of BzaB were observed in the presence of NAD^+ than in the presence of $NADP^+$.

Substrate preferences of BzaA and BzaB were assessed with various aromatic aldehydes, including vanillin, syringaldehyde, benzaldehyde, *p*-hydroxybenzaldehyde, protocatechualdehyde, *m*-anisaldehyde, veratraldehyde, and coniferyl aldehyde. Crude BzaA enzyme showed a broad substrate preference exhibiting specific activities of 925, 627, 511, 473, 301, 261, and 225 mU/mg toward *p*-hydroxybenzaldehyde, coniferyl aldehyde, syringaldehyde, benzaldehyde, veratraldehyde, vanillin, and protocatechualdehyde, respectively (Fig. 3). On the other hand, BzaB was essentially specific for *m*-anisaldehyde. The activities of BzaB toward veratraldehyde, coniferyl aldehyde, benzaldehyde, syringaldehyde and vanillin were less than 16% of the activities of BzaB toward *m*-anisaldehyde (Fig. 3).

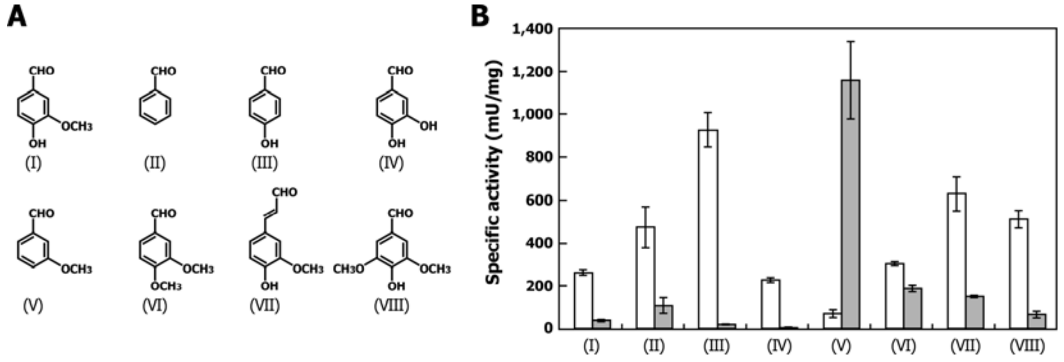

Fig. 3. (A) Chemical structures of aromatic aldehydes used in this study. Compounds: I, vanillin; II, benzaldehyde; III, *p*-hydroxybenzaldehyde; IV, protocatechualdehyde; V, *m*-anisaldehyde; VI, veratraldehyde; VII, coniferyl aldehyde; VIII, syringaldehyde. (B) Oxidation activities of BzaA and BzaB toward aromatic aldehydes. White and gray bars indicate the activities of BzaA and BzaB, respectively. The data are average ± standard deviations of three independent experiments.

Disruption of bzaA and bzaB in Sphingobium sp. strain SYK-6

In order to examine the roles of *bzaA* and *bzaB* in the degradation of syringaldehyde in *Sphingobium* sp. strain SYK-6, each of these genes in SYK-6 was disrupted by the insertion of the *bla* and *tet* gene, respectively, using a gene replacement technique. A *bzaA bzaB* double mutant was also constructed. Disruption of each gene was confirmed by Southern hybridization analysis. The *bzaA* mutant (SME044), *bzaB* mutant (SME045), and *bzaA bzaB* double mutant (SME046) grew on syringaldehyde at rates similar to that of the wild type, suggesting that these genes are not essential for the degradation of syringaldehyde in SYK-6. For further characterization of the mutants, the oxidation activities toward syringaldehyde and vanillin of cell extracts of SME044, SME045, and SME046 were evaluated. The activities of these three mutants for syringaldehyde and vanillin were almost the same as those of the wild type (Table 1). These results indicated that the contributions of both *bzaA* and *bzaB* to the degradation of syringaldehyde are minor in SYK-6.

Table 1. Oxidation activities of SYK-6 and its mutants toward vanillin and syringaldehyde

strains	Specific activity (mU/mg)	
	vanillin	syringaldehyde
SYK-6	129 ± 6.3	20.5 ± 2.8
DLV	20.1 ± 0.1	22.3 ± 0.2
SME044	152 ± 7.4	19.3 ± 2.5
SME045	100 ± 9.7	20.7 ± 3.0
SME046	152 ± 1.6	20.7 ± 2.7

4. Conclusion

Two novel aromatic aldehydes dehydrogenase genes, *bzaA* and *bzaB*, of *Sphingobium* sp. strain SYK-6 were isolated and characterized. The gene product of *bzaA* exhibited a broad substrate preference oxidizing syringaldehyde, vanillin, *p*-hydroxybenzaldehyde, and coniferyl aldehyde efficiently. This feature of BzaA appeared to be applicable to the bioprocesses converting syringaldehyde and vanillin to industrially valuable compounds such as PDC. Disruption of *bzaA* and *bzaB* suggested that these genes are insignificant to catabolism of syringaldehyde by *Sphingobium* sp. strain SYK-6. Our results may suggest the following two possibilities: i) there is a specific syringaldehyde dehydrogenase gene(s) in SYK-6. ii) there is no specific syringaldehyde dehydrogenase in SYK-6, and the sum of the activities of several aromatic aldehydes dehydrogenases with different substrate preferences enables SYK-6 to grow on syringaldehyde. Research is currently underway to identify the aromatic aldehydes dehydrogenase genes, which are actually involved in the syringaldehyde catabolism in SYK-6 by genome-wide analyses.

Acknowledgments

This work was supported in part by an Industrial Technology Research Grant from the New Energy and Industrial Technology Development Organization (NEDO) of Japan.

References

[1] E. Masai, Y. Katayama, and M. Fukuda, Biosci. Biotechnol. Biochem., **71** (2007) 1.

[2] Y. Otsuka, M. Nakamura, K. Shigehara, K. Sugimura, E. Masai, S. Ohara, and Y. Katayama, Appl. Microbiol. Biotechnol., **71** (2006) 608.

[3] Y. Hasegawa, K. Shikinaka, Y. Katayama, S. Kajita, E. Masai, M. Nakamura, Y. Otsuka, S. Ohara, and K. Shigehara, Sen'i Gakkaishi, **65** (2009) 359.

[4] M. Hishida, K. Shikinaka, Y. Katayama, S. Kajlta, E. Masai, M. Nakamura, Y. Otsuka, S. Ohara, and K. Shigehara, Polym. J., **41** (2009) 297.

[5] T. Michinobu, M. Bito, Y. Yamada, Y. Katayama, K. Noguchi, E. Masai, M. Nakamura, S. Ohara, and K. Shigehara, Bull. Chem. Soc. Jap, **80** (2007) 2436.

[6] E. Masai, Y. Yamamoto, T. Inoue, K. Takamura, H. Hara, D. Kasai, Y. Katayama, and M. Fukuda, Biosci. Biotechnol. Biochem., **71** (2007) 2487.

[7] X. Peng, T. Egashira, K. Hanashiro, E. Masai, S. Nishikawa, Y. Katayama, K. Kimbara, and M. Fukuda, Appl. Environ. Microbiol., **64** (1998) 2520.

[8] E. Yabuuchi, Y. Kosako, N. Fujiwara, T. Naka, I. Matsunaga, H. Ogura, and K. Kobayashi, Int. J. Syst. Evol. Microbiol., **52** (2002) 1485.

[9] J. M. Short, J. M. Fernandez, J. A. Sorge, and W. D. Huse, Nucleic Acids Res., **16** (1988) 7583.

[10] C. Yanisch-Perron, J. Vieira, and J. Messing, Gene, **33** (1985) 103.

[11] A. Schäfer, A. Tauch, W. Jäger, J. Kalinowski, G. Thierbach, and A. Pühler, Gene, **145** (1994) 69.

[12] K. S. Reece and G. J. Phillips, Gene, **165** (1995) 141.

[13] T. Abe, E. Masai, K. Miyauchi, Y. Katayama, and M. Fukuda, J. Bacteriol., **187** (2005) 2030.

[14] M. M. Bradford, Anal. Biochem., **72** (1976) 248.

[15] R. Plaggenborg, J. Overhage, A. Steinbüchel, and H. Priefert, Appl. Microbiol. Biotechnol., **61** (2003) 528.

[16] H. Priefert, J. Rabenhorst, and A. Steinbüchel, J. Bacteriol., **179** (1997) 2595.

[17] A. Narbad and M. J. Gasson, Microbiology., **144** (1998) 1397.

[18] V. Venturi, F. Zennaro, G. Degrassi, B. C. Okeke, and C. V. Bruschi, Microbiology, **144** (1998) 965.

(Received: 17 May, 2012, Accepted: 30 June, 2012)

Transactions on GIGAKU **1**(2012)01010/1-8

Development of an Appropriate Treatment Process for Wastewater from a Natural Rubber Processing Factory

Daisuke Tanikawa[1)]*, Takuya Yamashita[1)], Masashi Hatamoto[1)], Masao Fukuda[2)], Masanobu Takahashi[3)], Kazuaki Syutsubo[4)], Pairaya Kucivilize Choeisai[5)], Takashi Yamaguchi[1)]
[1)]Department of Environmental System Engineering, Nagaoka University of Technology,
1603-1 Kamitomioka, Nagaoka 940-2188, Japan
[2)]Department of Bioengineering, Nagaoka University of Technology,
1603-1 Kamitomioka, Nagaoka 940-2188, Japan
[3)]Department of Civil and Environmental Engineering, Tohoku University, 6-6-06 Aoba, Sendai 980-8579, Japan
[4)]Center for Regional Environmental Research, National Institute for Environmental Studies, 16-2 Onogawa, Tsukuba 305-8506, Japan
[5)]Department of Environmental Engineering, Faculty Engineering, KhonKaen University, KhonKaen 40002, Thailand
**E-mail: dtanikawa@vos.nagaokaut.ac.jp*

Natural-rubber latex wastewater containing a high concentration of sulfate was treated using a combined system consisting of a two stage reactors of up-flow anaerobic sludge blanket (UASB) and a down-flow hanging sponge (DHS) reactor for over 10 months. The system achieved a COD removal efficiency of 97.6 ± 1.1% at an organic loading rate (OLR) of 0.91 kgCOD/(m^3.d), where the influent of 10,200 ± 1,370 mgCOD/L was maintained at 11.1 days of the hydraulic retention time. The methane-producing and sulfate-reducing activity tests indicated that sulfate-reducing bacteria (SRB) was superior to methanogenis in the first stage reactor. However, methanogens were superior to SRB in the second stage of the UASB reactor. Microbial community analysis based on a 16S rRNA gene sequence revealed that many species of SRB, such as *Desulfomicrobium*, existed in the 1st UASB reactor. However, the ratio of SRB was decreased in the 2nd UASB reactor. Furthermore, for the treatment of the wastewater, the consumption of power by the two stage system was 93% less than that of the conventional lagoon system.

1. Introduction

The natural rubber industry is concentrated in the South-East Asia region, especially in Thailand, Indonesia, and Malaysia. In addition, more than 60 % of worldwide natural rubber production comes from these three countries [1]. Rubber latex, which is extracted from rubber trees, is used as a raw material for three intermediate forms of the rubber products: ribbed smoked sheets (RSS), which are used as a raw material for making vehicle tires and industrial rubber parts; technically specified rubber (TSR), which is used as a raw material for making high viscosity products such as belts; and concentrated latex, which is used as a raw material for making dipped products such as medical gloves. These three intermediate products are used in downstream rubber products industries [2, 3].

In a natural rubber processing factory, a large amount of wastewaters containing a high concentration of organic matter, nitrogen (especially, ammonia) and sulfate is discharged. This is because that a large amount of ammonia is used for the preservation of rubber latex and sulfuric acid is required for recovering rubber particles [3]. In South-East Asia, such wastewater is generally treated by conventional lagoon systems such as aerated lagoons, anaerobic lagoons, and facultative lagoons [3, 4]. However, these systems need long retention times and large treatment areas. In addition, these systems consume a large amount of power to aerate and discharge large amounts of excess sludge. These systems are also responsible for polluting the environment in many ways, such as through greenhouse gases (GHG, e.g., methane, carbon dioxide), malodor emissions, and groundwater pollution [3].

In a new process of wastewater treatment consisting of two stage reactors of an up-flow anaerobic sludge blanket (UASB) and a down-flow hanging sponge (DHS) reactor was developed. The UASB + DHS system exhibited high treatment performances, low excess sludge productions, low operational costs, and energy savings [5, 6]. Moreover, when the UASB + DHS system treated wastewater containing sulfate, the sulfide generated in the UASB reactor was promptly oxidized in the DHS reactor.

In the present study, an on-site pilot scale experiment was conducted in the Von Bundit natural rubber processing factory in Srat Thani, Thailand to develop an appropriate treatment process for wastewater from natural rubber latex waste by using a combined two-stage UASB and DHS system. The pilot plant was operated at the natural rubber processing factory for a period of more than 300 days. The performance of a conventional lagoon system and the developed system was evaluated and compared.

2. Experiment

(1) Two-stage system combined with UASB and DHS reactors

A schematic diagram of the developed system is given as Fig.1. The system consists of an acidification tank with 1180 L of working volume, the two stage UASB reactor was combined with 997 L of the first stage UASB and 597 L of the second stage UASB, and a DHS reactor with 195 L volume of sponge media. The UASB reactor and the DHS reactor were seeded with the sludge obtained from an anaerobic lagoon and an aerated lagoon at the factory, respectively.

Table 1 lists chemical characteristics of the concentrated latex wastewater. The concentrated latex wastewater discharged from the factory was received in the acidification tank and was later fed to the 1st UASB reactor as an influent. The pH of the influent was adjusted to 6.9–7.5 by addition of 2.5 N NaOH and a part of the UASB effluent obtained during the 1st UASB reactor was returned to the influent at a recirculation ratio of 2:1. The operational period was divided into ten separate periods (phase 1–7b) according to the organic loading rate (OLR) and the hydraulic retention time (HRT).

(2) Chemical analysis

Gas composition was measured by a gas chromatograph equipped with a thermal conductivity detector (GC-8A, Shimadzu). The solution pH was analyzed by using a pH meter (HM-20P, DKK). For sulfate analysis, the samples were filtered by 0.45 μm of glass fiber filter paper (GB-140, Advantec). Sulfate, chemical oxygen demand (COD) and sulphide were measured by Hach apparatus (DR890, Hach). Analysis of biochemical oxygen demand (BOD), suspended solids (SS), volatile suspended solids (VSS) and total nitrogen was conducted according to standard method, which was published by the Japan Sewage Works Association [7]. Volatile fatty acids (VFA) was determined by a gas chromatograph equipped with a flame ionization detector (GC-1700, Shimadzu).

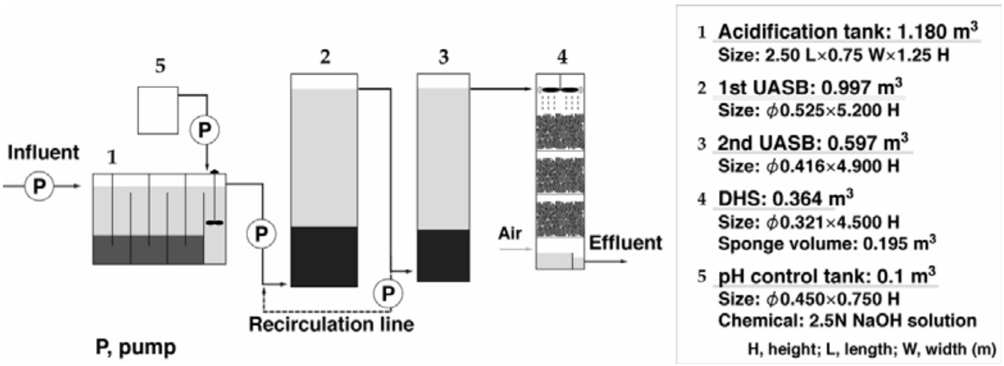

Fig. 1 Schematic diagram of the two-stage system

Table 1 Chemical characteristics of the concentrated latex waste water

Parameter	Average±SD*	Unit
pH	5.54±0.54	-
Total COD	9,710±2,600	mgCOD/L
Soluble COD	8220±2,020	mgCOD/L
Total BOD	8,670±2,750	mgBOD/L
Soluble BOD	7,310±2,320	mgBOD/L
Total VFA	4,460±1,290	mgCOD/L
Sulfate	1,430±490	mgS/L
Total Nitrogen	1,370±480	mgN/L
SS	1,780±1,260	mgSS/L
VSS	1,050±760	mgVSS/L

*: Standard deviation

(3) Microbial activity test

The methane producing activity (MPA) and sulfate reducing activity (SRA) of the retained sludge in the UASB reactor at 0 (as the seed), 87, 156, and 251 days were determined in duplicate. The test sludge was obtained from each stage of the UASB reactor having, a vertical height of 0.5 m. The sludge was disintegrated under anaerobic conditions and was used for the activity tests. Sodium acetate (2,000 mgCOD/L), sodium propionate (1,000 mgCOD/L), and H_2/CO_2 (80:20, v/v, 1.4 atm) were used as test substrates. All vials were incubated in a reciprocal shaker (radius = 4 cm) with 120 rpm at 35°C. In the SRA test, sodium sulfate (200 mgS/L) and chloroform solution (5 mg/L) were added as an electron acceptor and a methanogenic inhibitor, respectively. Detailed procedures for the activity tests are described elsewhere [8, 9].

(4) Microbial community analysis

Sludge samples obtained from each stage of the UASB reactor at 196 days were used for microbial community analysis. The DNA was extracted from the washed sludge using an ISOIL Beads Beating kit (Nippon gene), as described in the manufacturer’s instructions. The extracted DNA was used for amplification of bacterial and archaeal 16S rRNA gene fragments with primer pairs of EUB8F/150r [10, 11] and Arc109f/1500r [11, 12], respectively. Bacterial and archaeal 16S rRNA gene clone libraries were constructed using a TOPO TA cloning kit (Invitrogen). Classification and determination of the closest species of the obtained clones were performed using a classifier program of a ribosomal database project.

(5) Comparison between two stage system and conventional lagoon system in ~~at~~ the Natural Rubber factory

In the abovementioned factory, three types of wastewater were discharged, first type of wastewater stream was obtained from concentrated latex (latex) production, second type of wastewater stream was obtained from RSS production, and third type of wastewater stream was obtained from standard Thai rubber (STR) production. Fig. 2 shows the schematic diagram of the conventional lagoon system in the factory. Each wastewater stream was discharged from each production line and was treated separately. The conventional lagoon system consisted of anaerobic lagoonsfor RSS and STR wastewater treatment, aerated lagoons for latex wastewater treatment, a facultative lagoon, and a polishing lagoon for post treatment. To compare the both systems in the performance, influent and effluent water samples obtained from each lagoon were collected and the water quality was analyzed. Furthermore, some data concerning operational parameters such as power consumption, wastewater discharge volume, and excess sludge volume were collected to evaluate the performance of the two stage system developed.

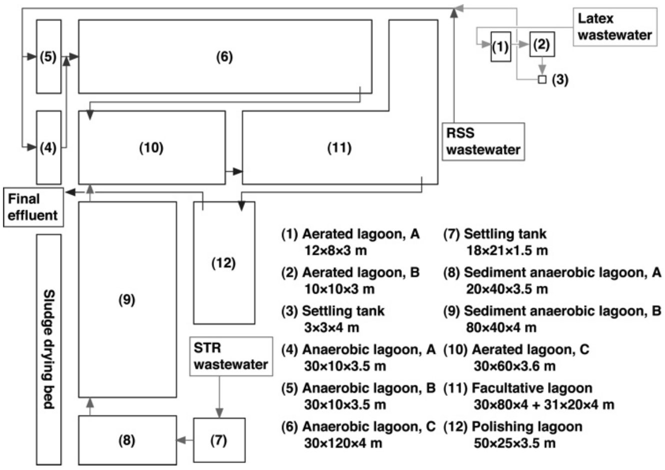

Fig.2 Schematic diagram of the conventional lagoon system at the factory

3. Results and Discussion

(1) Process performance of the developed system

Fig. 3 shows the time course of the OLR and total COD removal. In phase 1, the total COD removal efficiency was 89.9 ± 2.3% at 7.4 days of HRT with an OLR of 0.79 ± 0.04 kgCOD/(m^3.d) for the whole system (for only 1st UASB reactor, the total COD removal efficiency was 70.2 ± 4.4% at 1.4 days HRT with an OLR of 2.27 ± 0.08 kgCOD/(m^3.d)). In phase 2, the HRT was shortened to 3.7 days and the influent COD concentration was increased, which corresponded to an OLR of 10.0 ± 2.19 kgCOD/(m^3.d) for the 1st UASB reactor. The COD removal efficiency of the whole system decreased to 64.0%. Concurrently, a large amount of SS became more than 2,000 mg/L in the effluent of the 1st UASB reactor and then was washed out from the UASB reactor to the DHS reactor. This was caused by the overloading of the 1st UASB reactor, which inhibited the usual treatment processes. In phases 3a–4, the HRTs of both stages of the UASB reactor returned to the same as in phase 1, and the wastewater supply rate for the DHS reactor was adjusted in order to investigate the degradation of solid sulfur that had accumulated in the upper part of the DHS reactor. For the 1st UASB reactor (in phases 3a–3c), at an OLR of 5.59 ± 0.91 kgCOD/(m^3.d), the outflow of SS from the UASB reactor decreased. Though the total COD removal efficiency in the 1st UASB reactor was only 30.9 ± 13.7%, the total COD removal efficiency of the whole system was 91.5 ± 10.8%. This shows that the organic matter was successfully treated in the 2nd UASB reactor. In phases 4–7b, except for phase 6, when the COD concentration of the influent suddenly increased, the OLRs of the 1st UASB reactor were controlled to be 2.42 ± 0.41 kgCOD/(m^3.d). As a result, the total COD removal efficiency of the 1st UASB reactor increased and stabilized to 76.2 ± 0.7% in phase 7b.

Based on the experimental results described above, the maximum acceptable OLR of the 1st UASB reactor is approximately 5.8 kgCOD/(m^3.d) at phase 3c (i.e., ca. 1.6 kgCOD/(m^3.d) for the two-stage UASB reactor). The optimum OLR of the 1st UASB reactor is approximately 2.5 kgCOD/(m^3.d) (i.e., ca. 1.0 kgCOD/(m^3.d) for the two-stage UASB reactor) because a sufficient COD removal efficiency of 72.1 ± 3.9% was achieved in the 1st UASB reactor at phase 7a. This OLR was lower than the OLR of the other mesophilic UASB reactors treating in industrial wastewater [13]. This was because of the influence of the high concentration of hydrogen sulfide generated in 1st UASB reactor. As reported by Lens et al. [14], the methane production activity of granular sludge was inhibited by 50% with a concentration of 90–250 mgH_2S/L of hydrogen sulfide [15]. In the effluent of the 1st UASB reactor, the concentration of hydrogen sulfide was 130 ± 0.8 mgH_2S/L in phase 3c and 149 ± 30 mgH_2S/L in phase 7a.

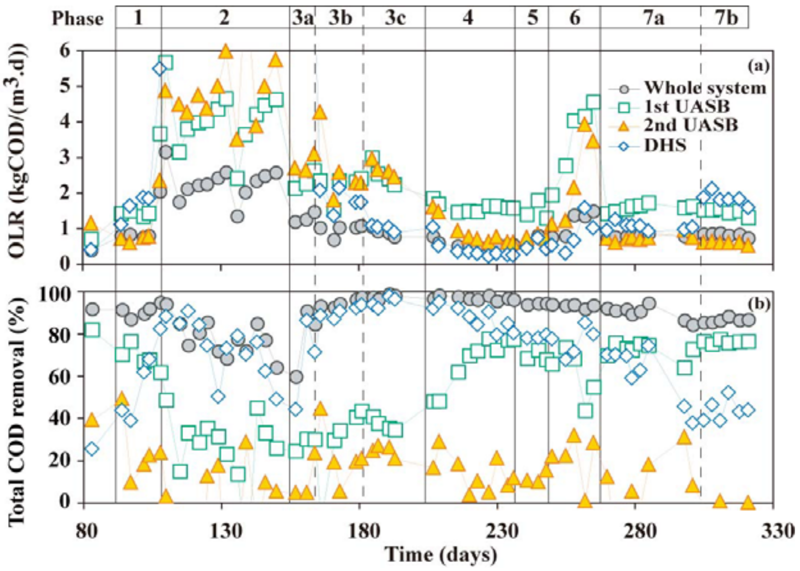

Fig.3 Time course of (a) organic loading rate and (b) total COD removal.

(2) Microbial activity of the retained sludge of the UASB reactor

Fig.4 shows the time course of MPA and SRA of the retained sludges of the two stages of the UASB reactor. The MPA of both retained sludges in the UASB reactor increased during reactor operation with an exception of H_2/CO_2-fed MPA (MPA–H_2). After 196 days, both acetate- and propionate-fed methanogens (MPA-Pro.) in the retained sludge for the 2nd UASB reactor were greater than that obtained in the 1st UASB reactor. Here, the ratio for the acetate was 1.61 in the 2nd UASB/1st UASB and that of the propionate was 1.81 on 251 days. This could be resulted by the low sulfate concentration in the influent in the 2nd UASB reactor. In regards to the SRA of the UASB retained sludges, the H_2/CO_2-fed SRA (SRA–H_2) was highest for both stages. Acetate- and propionate-fed SRAs in the retained sludge of the 1st UASB reactor were minimal. However, the acetate- and propionate-fed SRAs of the retained sludge in the 2nd UASB reactor were not detected at all.

For acetate and propionate utilization, MPA was higher than SRA for both UASB stages at 251days. On the other hand, hydrogen-utilizing SRA was higher than that for MPA. In addition, the SRA/MPA ratio for the first and second UASB stages were 5.72 and 6.63, respectively. These results indicated that hydrogen-utilizing sulfate-reducing bacteria (SRBs) acted as hydrogen scavengers in both stages of the UASB reactor.

(3) Microbial communities of the UASB retained sludge

Table 2 shows the microbial community compositions derived from the 16S rRNA gene base analysis of the retained sludges in the UASB reactor. *Proteobacteria* (39%) and *Firmicutes* (30%) in the 1st UASB reactor, and *Firmicutes* (23%), *Proteobacteria* (21%) and *Bacteroidetes* (12%) in the 2nd UASB reactor were the dominant phyla of bacteria. Among *Proteobacteria*, a lot of clones relating to the SRB *Desulfomicrobium* were detected. In addition, 17 clones of possible 95 clones were present in the 1st UASB reactor, which could have been due to the high concentration of sulfate.

Moreover, only *Euryarchaeota* were detected as archea in both UASB reactor stages. Among the clones, *Methanomethylovorans* and *Methanosaeta* dominated with more than 70% share in both UASB reactor stages. It was reported that *Methanomethylovorans* species existed in the retained sludge of methanol-fed UASB reactors and utilized methanol and dimethyl sulfide as catabolic substrates, however, H_2/CO_2 and acetate were not utilized [15, 16]. The existence of *Methanomethylovorans* in our reactors might be related to the high concentration of sulfate in the feed and the utilization of dimethyl sulfide. However, further research is needed to determine the role of *Methanomethylovorans* in our reactors.

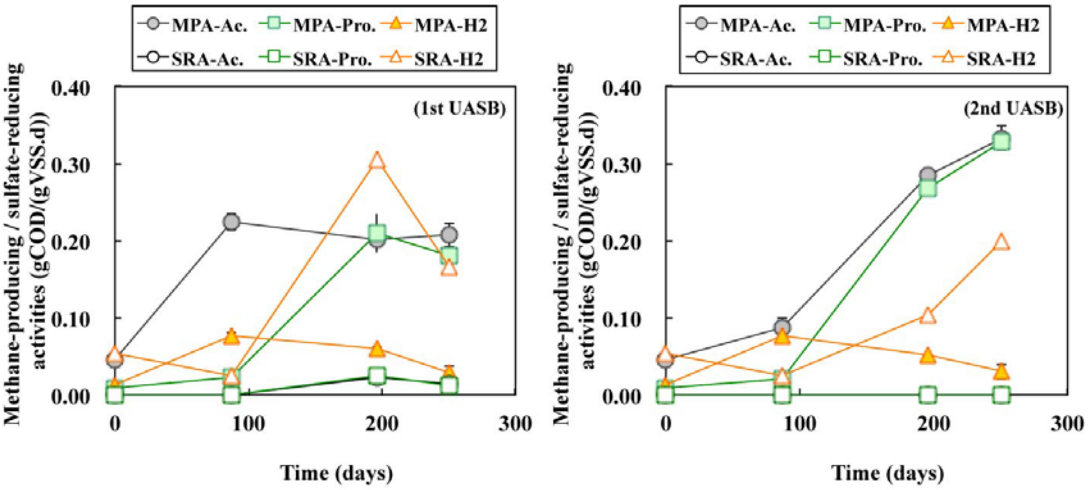

Fig.4 Time course of methane-producing/sulfate-reducing activities of the retained sludges of the first and second stages of the UASB reactor

Table 2 Microbial community compositions from 16S rRNA gene based analysis of retained sludges in the UASB reactor stages

Classification	No. of clone (% of total clones)	
	1st UASB	2nd UASB
Bacteria		
Actinobacteria		3 (3)
Armatimonadetes		1 (1)
Bacteroidetes	5 (5)	11 (12)
Chloroflexi	5 (5)	2 (2)
Firmicutes	29 (31)	22 (23)
Proteobacteria		
Desulfuromonadaceae	4 (4)	6 (6)
Desulfobacteraceae	15 (16)	10 (11)
Desulfomicrobiaceae	17 (18)	
other *proteobacteria*		4 (4)
Synergistetes		2 (2)
Verrucomicrobia	1 (1)	2 (2)
Uncultured bacteria	19 (20)	31 (33)
Total - Bacteria	95 (100)	94 (100)
Archaea		
Methanolobus	2 (4)	3 (7)
Methanomethylovorans	29 (62)	22 (49)
Methanosaeta	6 (13)	16 (35)
Methanosphaera		1 (2)
Methanosarcinales	3 (6)	
Uncultured archaea	7 (14)	4 (9)
Total - Archaea	47 (100)	46 (100)

(4) Comparison between the two stage system and conventional lagoon system

After evaluating the process performance for latex wastewater treatment, the two stage system was used to treat the RSS and STR wastewaters. Table 3 shows the chemical characteristics of each wastewater stream and the final effluent obtained from the both systems. For the purpose of comparison, the assumption was made that the two stage system would treat all three wastewater streams. The first stage of the UASB reactor would treat the latex wastewater, the second stage would be for both the RSS and STR wastewaters, and the DHS reactor would provide post-treatment. The two stage system achieved the Thai effluent standard for the 20 mg/L of BOD, 120 mgCOD/L of CODcr and 50 mg/L of SS and maintained a better process performance than those of the conventional lagoon system. Table 4 shows the power consumption of each treatment system. In the conventional system, the latex wastewater treatment consumed a large amount of powers because of the need for aeration. Also a large amount of excess sludges was discharged from the aerated lagoon. Furthermore, 20 t CO_2/d of methane gas was emitted from the anaerobic lagoons. Emission of methane gas was calculated from the COD removal in the anaerobic lagoons. On the other hand, the two stage system reduced 93% of the power consumption for the latex wastewater treatment, reduced the amount of excess sludge discharged by 90%, and reduced the GHG emissions from the aerated lagoons by 95% by recovering methane as an energy source. These results prove that the two stage system was suitable for the wastewater treatment in a natural rubber processing factory.

Table 3 Chemical characteristics of wastewater and final effluent of the two stage system and conventional system

Parameter	Wastewater (Average±SD*)			Final effuent(Average±SD*)		Unit
	Latex	RSS	STR	Developed	Conventional	
pH	5.54±0.54	7.34±0.44	7.77±0.41	7.43±0.67	7.79±0.08	-
BOD	8,670±2,750	435±238	509±226	9±27	46±18	mg/L
COD_{Cr}	9,730±2,600	1,070±421	1,080±492	113±35	112±20	
SS	1,780±1,260	651±677	261±116	13±9	50±14	

*: Standard deviation

Table 4 Power consumption and greenhouse gases emission of each wastewater treatment system

Source of effluent	Discharge (m^3/d)	Power consumption (kWh/m^3 effluent)		GHG emission (t CO_2/m^3 effluent)	
		Developed system	Conventional system	Developed system	Conventional system
Latex	75	0.38	5.83	0.45	14.69
RSS	500	0.06	0.00	0.03	1.70
STR	2000	0.01	0.00	0.01	9.81
Post treatment	2575	0.00	0.34	0.00	0.20
Total system	2575	0.04	0.51	0.03	8.57

4. Conclusion

In the present research, latex wastewater was treated using a two-stage UASB and DHS system, and the wastewater treatment performance was evaluated in long term process. During the experimental period, a COD removal efficiency of 97.6% was achieved under the operating conditions of 0.91 kgCOD/(m^3.d) of OLR and 11.1 days of HRT. The 1st UASB reactor removed organic matter while the producing methane and reducing sulfate, the 2nd UASB reactor produced methane, and the DHS reactor removed the remaining organic matter.

In terms of the microbial community in the stages of the UASB reactor, both the dimethyl sulfide-utilizing methanogen, *Methanomethylovorans*, and some SRBs such as *Desulfomicrobium* were detected because of the high concentration of sulfate. In both UASB stages, methanogen activity was higher than SRB activity for acetate and propionate. On the other hand, hydrogen-utilizing SRB activity was higher than methanogen. These results indicate that hydrogen-utilizing SRBs acted as hydrogen scavengers under a in both stages of the UASB reactor.

The results showed that the two stage system achieved better process performance than the conventional lagoon system. Furthermore, the former system reduced the power consumption for the latex wastewater treatment by 93%, excess sludge volume discharge from the aerated lagoon by 90%, and GHG emissions by 95% through recovery of methane as an energy source. These results proved that the developed system is suitable for wastewater treatment in a natural rubber processing factory.

Acknowledgments

This research was supported by the JST/JICA, SATREPS (Science and Technology Research Partnership for Sustainable Development), Japan. We wish to thank Von Bundit co., ltd. and their staff for installation and operation of the two stage system.

References

[1] M. Mohammadi, H. C. Man, M. A. Hassan, and P. L. Yee, African J. Biotech., **9** (2010) 6233.
[2] P. Takasakul and S.Tekasakul, J. Aerosol Res.,**21** (2006) 122.
[3] W. Jawjit, C. Kroeze, and S. Rattanapan, J. Cleaner Production, **18** (2010) 403.
[4] S. Chaiparapatand and S. Sdoodee, Resour.,Conserv.Recy., **51** (2007) 577.
[5] I. Machdar, Y. Sekiguchi, H. Sumino, A. Ohashi, and H. Harada, Wat. Sci. Tech., **42** (2000) 83.
[6] M. Tanduker, A. Ohashi, and H. Harada, Wat. Res.**41** (2007) 2697.
[7] Japan Sewage Works Association, Japanese standard methods for sewage and wastewater (1997) (in Japanese).
[8] K. Syutsubo, N. Shinthurat, A. Ohashi, and H. Harada, Wat. Sci. Tech., **43** (2001) 59.
[9] T. Yamaguchi, H. Harada, and I. C. Tseng, Proc. 8th Int. Conf. Anaerobic Digestion,**2** (1997) 362.
[10] L. Ovreas, L. Forney, F.L. Daae, and V. Torsvik, Appl. Environ. Microbiol., **63** (1997) 3367.
[11] D. J. Lane, 16S/23S rRNAsequencing, In E. Stackebrandt, and M. Goodfellow (ed), Nucleicacidtechniques in bacterialsystematics, JhonWileyand Sons, Inc., N. Y. (1991) 115-175.
[12] G. Regine, H. J. Peter, and L. Werner, Appl. Environ. Microbiol., **64** (2010) 960.
[13] S. V. Gali, K. Pradeep, and M. Indu, Water Res., **39** (2005) 154.
[14] P. N. L. Lens, A. Visser, A. J. Janssen, L. W. Hulshof Pol, and G. Lettinga, Critical review in Environ. Sci. and Technol.,**28** (1998) 41.
[15] B. Jiangand and N. S. Parshina, Syst. Eval. Microbiol., **55** (2005) 2465.
[16] B. P. Lomans, R. Maas, R. Luderer, H. J. M. Op den Camp, A. Pol., C. Van der Drift, and G. D. Vogels, Appl. Environ. Microbiol., **65** (1999) 3641.

(Received: 18 May, 2012, Accepted: 4 July, 2012)

Transactions on GIGAKU **1**(2012)01011/1-4

Biodegradation of Persistent Chlorinated Organophosphorus Flame Retardants by Microorganisms Newly Isolated from Soil – a short review

Yoshio Kera *, Shouji Takahashi, Katsumasa Abe
Department of Environmental Systems Engineering, Nagaoka University of Technology,
1603-1 Kamitomioka-cho, Nagaoka 940-2188, Japan
**E-mail: yoshkera@vos.nagaokaut.ac.jp*

The novel bacterial strains that can degrade trihaloalkyl phosphates, *Sphingobium* sp. TCM1 and *Sphingomonas* sp. TDK1, were isolated from soil by growth on persistent chlorinated organophosphorus (OP) flame retardants, tris(2-chloroethyl) phosphate (TCEP) or tris(1,3-dichloro-2-propyl) phosphate (TDCPP), as a sole phosphorus source, respectively. While *Sphingobium* sp. TCM1 and *Sphingomonas* sp. TDK1 degraded TCEP and TDCPP by hydrolyzing their phosphotriester bonds, both strains were not able to degrade 2-chloroethanol and 1,3-dichloro-2-propanol, which were hydrolysis products of TCEP and TDCPP, respectively. The two strains were able to degrade and assimilate not only the chlorinated OP flame retardants but also several other OP flame retardants and plasticizers and the strains possessed different substrate specificity for trialkyl phosphates.

1. Introduction

The chlorinated organophosphorus (OP) compounds, tris(2-chloroethyl) phosphate (TCEP) and tris(1,3-dichloro-2-propyl) phosphate (TDCPP), as shown in Fig. 1, are widely used as flame retardants mainly in a range of plastic foams, resins, and latexes and in the production of liquid unsaturated polyester resins, respectively [1]. Their widespread use has led to contamination of various environments [2-7]. Particularly, a higher contamination level was observed in leachates and raw water of waste disposal sites [8]. Furthermore, they were also detected in drinking water [1], because they were hard to eliminate not only in the environment but also in sewage treatment plants [9]. Many studies reported several toxic effects of the compounds. For example, TCEP was shown to cause adverse effects on brain, liver, and kidney and on the fertility of male rats and mice [1]. In addition, TCEP produced tumors at various organ sites [10], also was suspected to possess carcinogenicity [11] and was shown to inhibit the expression of cell cycle regulatory proteins, DNA synthesis, and cell numbers [12]. It was known that TDCPP exhibited genotoxicity in several *in vitro* assays conducted in prokaryotic and eukaryotic cells [13] and produced some indications of carcinogenicity [1].

Many bacteria and fungi that can degrade OP pesticides and insecticides, such as parathion and chlorpyrifos, have been discovered, isolated, and characterized [14-17]. In contrast, few studies have been conducted on microbial degradation of chlorinated OP flame retardants, despite their persistence and potentially nonnegligible toxicity. Thus far, there has been no report of the isolation of bacteria that can degrade TCEP and TDCPP.

In the present short review, we summarize our recent studies about the development of 2 enrichment bacterial cultures that can degrade rapidly both TCEP and TDCPP [18] and the isolation and identification of bacteria that can degrade the compounds from each enrichment culture [19].

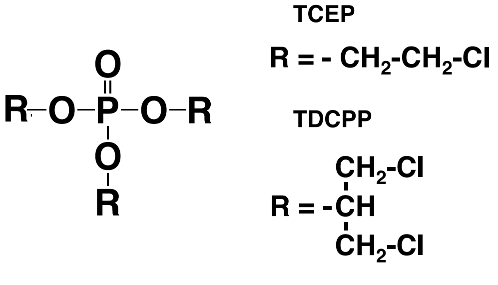

Fig. 1 Structures of tris(2-chloroethyl) phosphate (TCEP) and tris(1,3-dichloro-2-propyl) phosphate (TDCPP).

2. **Enrichment and Characterization of Chlorinated Organophosphate Esters-Degrading Mixed Bacterial Cultures [18]**

Chlorinated OP ester-degrading enrichment cultures were obtained using TCEP or TDCPP as the sole phosphorus source. The degradation activity of each culture was assayed by measuring the decrease of TCEP or TDCPP in each culture.

TCEP or TDCPP in cultures was extracted with an equal volume of ethyl acetate and analyzed using a GC-17A gas chromatograph equipped with a flame photometric detector with a phosphorus optical filter (Shimadzu, Japan). 2-Chloroethanol and 1,3-dichloro-2-propanol in cultures were extracted in the same manner and analyzed by a GCMS-QP2010 gas chromatograph mass spectrometer (Shimadzu). Chloride ion concentration in cultures was determined colorimetrically [20].

In cultures with 46 environmental samples, significant TCEP and TDCPP degradation was observed in 10 and 3 cultures, respectively, and successive subcultivation markedly increased their degradation rates. Stable enrichment culture 67E and 45D, obtained with TCEP and TDCPP, respectively, completely degraded 20 μM of the corresponding compounds within 6 h and also the other compounds, although the degradation rate of TCEP by 45D was relatively slow. We confirmed chloride ion generation in both degradation cases and the generation of 2-chloroethanol and 1,3-dichloro-2-propanol as metabolites of TCEP and TDCPP, respectively.

The 67E and 45D also showed dehalogenation ability toward 2-chloroethanol and 1,3-dichloro-2-propanol, respectively. Addition of inorganic phosphate did not significantly influence their abilities to degrade the chlorinated OP esters but markedly increased the dehalogenation ability, which was on a maximum level at 0.2 mM of inorganic phosphate and decreased at a higher concentration.

Denaturing gradient gel electrophoresis (DGGE) analysis, followed by 16S rRNA gene sequence analysis (135-160 bp) of prominent DGGE bands, showed that dominant bacteria in 67E were related to *Acidovora*x spp. and *Sphingomonas* spp. and those in 45D were *Acidovorax* spp., *Aquabacteriu*m spp., and *Sphingomonas* spp. This analysis indicated the relationship of the *Sphingomonas*- and *Acidovorax*-related bacteria with the cleavage of the phosphoester bond and dehalogenation, respectively, in both cultures.

3. Isolation and Identification of Persistent Chlorinated Organophosphorus Flame Retardant-Degrading Bacteria [19]

As described above, we demonstrated that TCEP and TDCPP were rapidly degraded in two enrichment bacterial cultures, named 67E and 45D, obtained by using TCEP and TDCPP as sole phosphorus sources [18]. We therefore attempted to isolate bacteria that can degrade the compounds from each enrichment culture. A single colony isolated from the enrichment culture 67E was named strain TCM1 and that from the 45D was named TDK1. The morphological and physiological characteristics of the both strains were similar to those of *Sphingomonas* spp., although the two strains were distinct from each other in physiological characteristics.

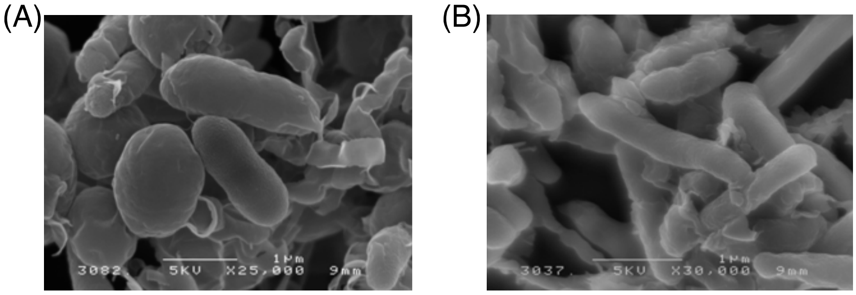

Fig. 2 SEM micrographs of *Sphingobium* sp. TCM1 (A) and *Sphingomonas* sp. TDK1 (B).

The nearly full-length 16S rRNA gene (approximately 1,500 bp) of TCM1 and TDK1 was analyzed and sequence homology searches were performed against the 16S rRNA gene sequence database at the DDBJ using the BLAST program (http://www.ddbj.nig.ac.jp/search/top-e.html). The similarity between the sequences of TCM1 and TDK1 was 93.4%. The strain TCM1 and TDK1 were grouped with the members belonging to the genera *Sphingobium* and *Sphingomonas*, respectively, showing that strains TCM1 and TDK1 are members of the respective genera. The SEM micrographs of *Sphingobium* sp. TCM1 and *Sphingomonas* sp. TDK1 are shown in Fig.2.

While *Sphingobium* sp. TCM1 and *Sphingomonas* sp. TDK1 degraded TCEP and TDCPP by hydrolyzing their phosphotriester bonds, both strains were not able to degrade the produced 2-chloroethanol and 1,3-dichloro-2-propanol, which were hydrolysis products of TCEP and TDCPP, respectively.

Both strains could grow on other trihaloalkyl phosphate like tris(2,3-dibromo propyl) phosphate (TBPP) and triaryl phosphates like triphenyl phosphate (TPP) and tricresyl phosphate (TCP) (Fig. 3). In addition, the strain TCM1 was able to grow moderately on tributyl phosphate (TBP) and slightly on trimethyl phosphate (TMP), tris(2-ethylhexyl) phosphate (TEHP), triethyl phosphate (TEP) and tris(2-butoxyethyl) phosphate (TBXP). However, the strain TDK1 was not able to grow on all of trialkyl phosphates tested. These results showed that the strains could degrade and assimilate not only the chlorinated OP flame retardants but also several other OP flame retardants and plasticizers. In addition, the strains showed different substrate specificity for trialkyl phosphates.

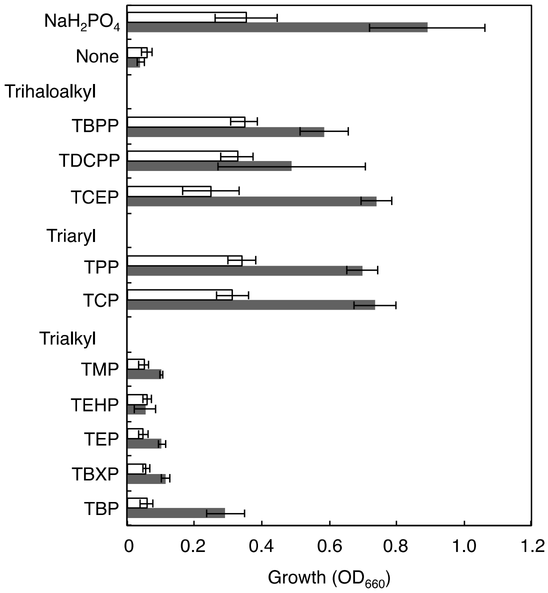

Fig. 3 Substrate specificity of strains TDK1 and TCM1. White and black bars show the growth of strains TDK1 and TCM1, respectively. Growth (OD_{660}) was measured after 96 h. Data represent mean ± standard deviation of three independent experiments. The initial OD_{660} of cultures was 0.05.

Acknowledgments

This work was supported in part by Grant-in-Aid for Scientific Research (B) from the Ministry of Education, Science, Sports, and Culture of Japan, and by Project to Form a Hub of Human Resources Development and New Industry Creation-Building a Sustainable Society through Highly Interactive Cooperative Educational Research with Pacific Rim Countries.

References

[1] World Health Organization, Environmental health criteria **209** (1998).
[2] Y. Kawagoshi, I. Fukunaga, and H. Itoh, J. Mater. Cycles Waste Manage., **1** (1999) 53.
[3] E. Fries, and W. Puttmann, J. Environ. Monit., **5** (2003) 346.
[4] J. A. Andresen, A. Grundmann, and K. Bester, Sci. Total Environ. **332** (2004) 155.
[5] A. Marklund, B. Andersson, and P. Haglund, J. Environ. Monit., **7** (2005) 814.
[6] H. M. Stapleton, S. Klosterhaus, S. Eagle, J. Fuh, J. D. Meeker, A. Blum, and T. F. Webster, Environ. Sci. Technol., **43** (2009) 7490.
[7] J. Regnery, and W. Püttmann., Clean Soil Air Water, **37** (2009) 334.
[8] Y. Kawagoshi, S. Nakamura, and I. Fukunaga, Chemosphere, **48** (2002) 219.
[9] J. Andresen, and K. Bester, Water Res., **40** (2006) 621.
[10] U.S. National Toxicology Program, Natl. Toxicol. Program Tech. Rep. Ser. **391** (1991) 1.
[11] H. B. Matthews, S. L. Eustis, and J. Haseman, Fundam. Appl. Toxicol. **20** (1993) 477.
[12] X. Ren, Y. J. Lee, H. J. Han, and I. S. Kim, Chemosphere, **74** (2008) 84.
[13] E. J. Søderlund, E. Dybing, J. A. Holme, J. K. Hongslo, E. Rivedal, T.Sanner, and S. D. Nelson,

Acta Pharmacol.Toxicol. **56** (1985) 20.
[14] F. M. Raushel, Curr. Opin. Microbiol., **5** (2002) 288.
[15] B. K. Singh, and A. Walker, FEMS Microbiol. Rev., **30** (2006) 428.
[16] B. K. Singh, Nat. Rev. Microbiol. **7** (2009) 156.
[17] K. Abe, S. Takahashi, and Y. Kera, In: Microbial Bioremediation of Non-metals; Current Research (Ed., A. -I. Koukkou), Caister Academic Press, Norfolk, (2011) 45.
[18] S. Takahashi, K. Kawashima, M. Kawasaki, J. Kamito, Y. Endo, K. Akatsu, S. Horino, R. H. Yamada, and Y. Kera, J. Biosc. Bioeng. **106** (2008) 27.
[19] S. Takahashi, I. Satake, I. Konuma, K. Kawashima, M. Kawasaki, S. Mori, J. Morino, J. Mori, H. Xu, K. Abe, R. H. Yamada, and Y. Kera, Appl. Environ. Microbiol., **76** (2010) 5292.
[20] A. M. Fauzi, D. J. Hardman, and A. T. Bull, Appl. Microbiol. Biotechnol., **46** (1996) 660.

(Received: 10 May, 2012, Accepted: 30 June, 2012)

Transactions on GIGAKU **1***(2012)01012/1-6*

Electrochemical Deposition of Cobalt on Mesoporous Silica Films

Motohiro Tagaya[1,*], Mitsuhiro Okuda[2], Sarah Ward Jones[2], Takaomi Kobayashi[1]
[1)]Department of Materials Science and Technology, Nagaoka University of Technology,
1603-1 Kamitomioka-cho, Nagaoka 940-2188, Japan
[2)]H.H. Wills Physics Laboratory, University of Bristol,
Tyndall Avenue, Bristol BS8 1TL, United Kingdom
**E-mail: tagaya@mst.nagaokaut.ac.jp*

Electrochemical deposition of cobalt (Co) particle on mesoporous silica (MPS) films formed on a Si wafer was examined. The MPS films were synthesized by a supramolecular templating method to exhibit the highly-ordered hexagonal structure and the surface area of 435 $m^2 \cdot$(g of silica)$^{-1}$ with the pore size of 5.0 nm. The deposited Co particles were successfully formed on the surfaces at the voltage of −1.5 (V vs. SCE); the cracks appeared on the film surface at the deposition time of 100 s and simultaneously nanoparticles were formed in the inside surface, and subsequently amorphous nanoparticles were homogeneously covered over the MPS surfaces at 300 s, whereas the flower-like structure was formed on the Si wafer. These results suggest the generation of initial Co deposition in the mesopores and the subsequent deposition processes were affected by the amorphous silica frameworks of MPS.

1. Introduction

The electrochemical deposition is known as an inexpensive and simple process for the formation of metallic materials [1,2]. Although it is considered that the electrochemical deposition can produce relatively thick metallic layers, recent developments have demonstrated that the deposition is able to make very thin metallic films and a wide range of nanostructured materials [3,4]. Thus, the investigation of the deposition process on the nanostructured materials is of great importance for designing the dissimilar interface.

Mesoporous silicas (MPSs) were prepared by the cooperative organization of surfactant and inorganic species, the synthesis, characterization and applications of the nanostructues have been investigated [5,6]. The MPSs prepared by supramolecular templating methods possess attractive features such as well-defined and controllable pore size, large surface area, and reactive surfaces [7,8]. The host–guest and guest–guest interactions based on the mesopore size can be controlled, and the host–guest complexes have been synthesized, and the possible applications have been reported so far [9–17]. Accordingly, the incorporation of functional species into the silica mesopore encompasses wide variety applications. Thus, the formation of the metal−MPS composites is of great importance for controlling the metal particles at the nanometer scales.

In this study, the MPS films with the pore diameter of 5.0 nm were prepared on a Si wafer by the supramolecular templating method, and the electrochemical deposition process of cobalt (Co) particles from the aqueous solution containing Co(II) sulfate hydrate and boric acid was investigated.

2. Experiment

Preparation of MPS Films

MPS films were synthesized according to the previous reports [12,18]. 2.0 g (13.1 mmol) of tetramethoxysilane (TMOS: Shinetsu Chemical Co., Ltd.), 472 μL of ultrapure water, and 100 μL of hydrochloric acid aqueous solution (HCl: Wako Co., Ltd.) (0.1 M) were vigorously stirred at 40°C for 60 min to generate condensation polymerization. Then, 534 mg (92 mmol) of poly(ethylene oxide)$_{20}$–poly(propylene oxide)$_{70}$–poly(ethylene oxide)$_{20}$ (P123: Sigma-Aldrich Co., Ltd., Mw=5800) was dissolved in 2.6 mL of ultrapure water and the solution was added into the siliceous solution at the molar ratio of TMOS:P123=1:7×10^{-3}, and then stirred at 40^{o}C for 15 min. The resulting solution was spin-coated on a glass substrate and naturally-oxidized silicon (Si) wafer (boron-doped p-type Si(100), Ryoukou Sangyou Co., Ltd.) at the rotate speed of 6000 rpm for 10 s, and then dried at 60^{o}C for 18 h. The template was removed by the calcination at 450 ^{o}C for 6 h under air.

Electrochemical Deposition of Co

The solution containing 0.1 M of Co(II) sulfate hydrate ($CoSO_4$: Aldrich Co., Ltd.) and 0.5 M of boric acid (H_3BO_3: Sigma-Aldrich Co., Ltd.) using ultrapure water was prepared. 60 ml of the solution was added into the electrochemical cell and then the dissolved oxygen molecules were removed by nitrogen bubbling for 15 min. In the working electrode (WE), an electrical contact was made to the back of the Si wafer using a GaIn eutectic and a piece of Cu foil as shown in Figure 1 (a). The wafer and contact were covered with Kapton tape except for a 6 mm diameter circle on the MPS film surface, giving an area of 0.28 cm^2 of the MPS film exposed to the solution. A standard three electrode electrochemical cell set-up with a saturated calomel electrode (SCE) as a reference electrode (RE) and a platinum foil counter electrode (CE) was used for the electrochemical deposition as shown in Figure 1 (b). A SP-150 potentiostat (Bio-Logic Co., Ltd.) controlled using EC-Lab Express software was used to control the potential and record the current by completely shielding the light reaching the electrode. The cyclic voltammetry curve was measured on the condition (scan rate: 50 mV/s, start potential: 0 (V vs SCE), first switching potential: −1.2 (V vs SCE), second switching potential: +1 (V vs SCE), final potential: 0 (V vs SCE)). The current measurement with the deposition time was conducted at the fixed voltage of −1.5 (V vs. SCE).

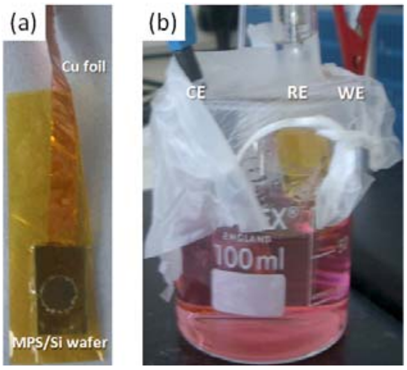

Fig. 1 Photographs of the experiment set-up for (a) WE made of the MPS on Si wafer with Cu foil and Kapton tape and (b) the standard three electrode cells with WE, RE and CE in the solution.

Characterization

X-ray diffraction (XRD) patterns were recorded on a X'Pert Pro MPD (PNAalytical Co., Ltd.) using monochromatized CuKα radiation. Infrared spectra were recorded on a fourier transform infrared spectrometer (FT-IR: PerkinElmer Inc., Spectrum GX) with an accumulation of 32 times and resolution of 2.0 cm^{-1}. Nitrogen adsorption isotherm was measured at 77K on a SA3100 instrument (BECHMAN COULTER Co., Ltd.). Prior to the measurement, the samples were degassed under vacuum at 393K for 4 h. The surface area was evaluated by the BET surface area, and the pore volume was calculated by the BET surface area and averaged pore size. The morphologies of the surfaces were observed using a field emission scanning electron microscopy (FE-SEM: Hitachi Co., Ltd., S-4500N). The MPS films on the glass substrates were applied for the XRD, FT-IR and nitrogen adsorption/desorption measurements, and those on the Si wafers were for the electrochemical experiments.

3. Results and Discussion

Figure 2 (A) shows the XRD patterns of the MPS films before and after the calcination and the illustration of possible mesoporous hexagonal structure. The peaks are indexed as (100), (110), (200) and (220) reflections of hexagonal structure as shown in Figure 2 (B), and the d_{100} values are 6.3 nm and 5.2 nm before and after the calcinations in Figure 2 (a, b). With the calcination, the diffractions were shifted to higher angles due to the contraction of the silica framework. The results suggest that the highly-ordered nanostructures are preserved with the calcination. FT-IR spectra indicated that the bands at around 1070 and 1225 cm^{-1} are originated from Si–O–Si asymmetric and symmetric stretching and the bands at around 795 and 960 cm^{-1} are assigned to the Si–OH stretching (data not shown). The bands at around 1480, 2854, and 2925 cm^{-1} which can be assigned to the C–H stretching and bending in the surfactant completely disappeared by the calcination, indicating the removal of the P123 surfactant. Therefore, the MPS with the hexagonal structure was successfully prepared by the supramolecular templating method.

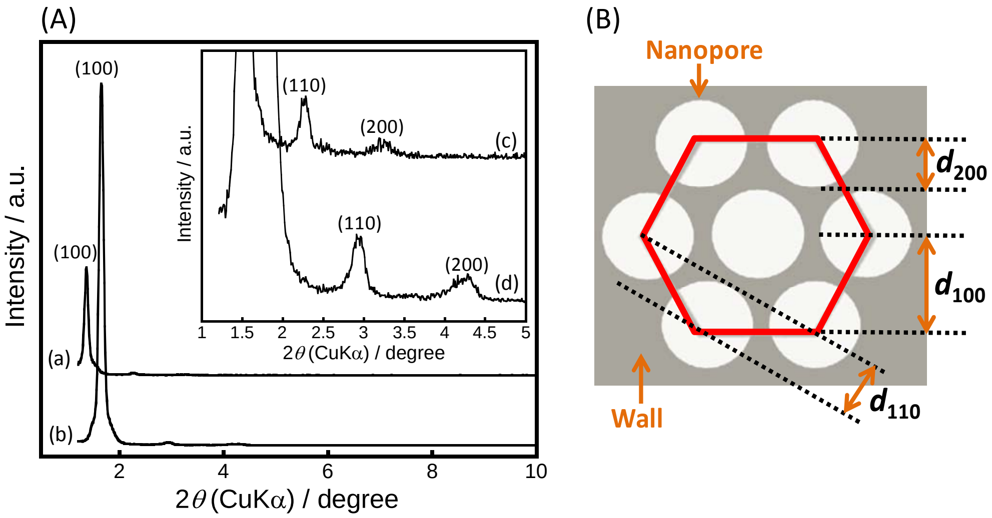

Fig. 2 (A): XRD patterns of the MPS films (a, c) before and (b, d) after the calcination and (inset) the magnified patterns at the lower angles. (B): Illustration of hexagonally-aligned mesoporus structure.

Figure 3 (a) shows the photograph of the MPS film after the calcination. The film thickness is 150−200 nm and exhibits high transparency. Figure 3 (b) shows the nitrogen adsorption isotherm of the MPS film and the pore size distribution. A hysteresis between the adsorption and desorption was observed, indicating the formation of mesopores. The isotherms indicated that the BET surface area, pore size and volume are 435 m^{2}·(g silica)$^{-1}$, 5.0 nm and 0.54 ml·g^{-1}. Taking into account the d_{100} value evaluated from the XRD pattern, the thickness of the silica pore wall is 0.2 nm.

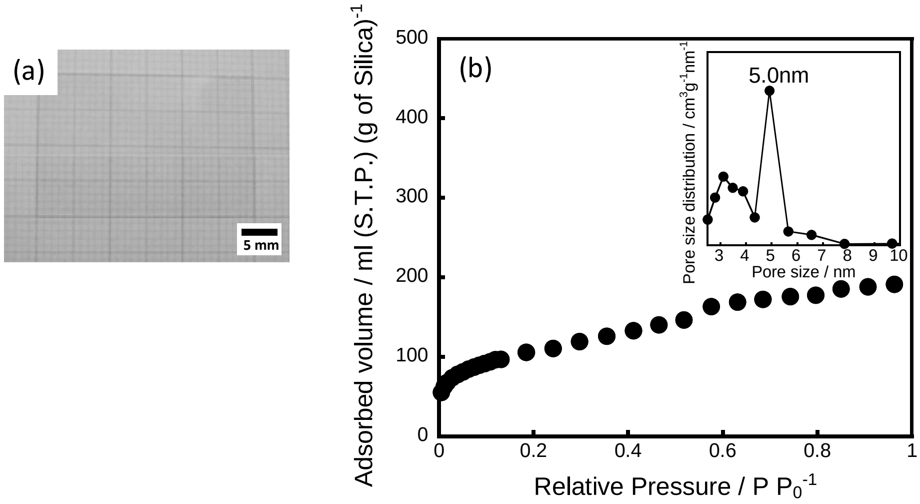

Fig. 3 (a) Photograph of the MPS film on a glass substrate and (b) the nitrogen adsorption isotherm and (inset) pore size distribution.

Figure 4 shows the CV curve of the MPS film on the Si wafer and the current changes with the deposition time in the preparative solution. In the CV curve in Figure 4 (a), the negative currents induce the Co deposition and hydrogen evolution, while the positive current peak at the peak of +0.4 (V vs. SCE) corresponds to the stripping (oxidation) of Co off the electrode.

When this negative potential is applied to WE, divalent metal ions of Co^{2+} surrounded by their hydration layers move towards the cathode and are reduced to the metal. The movement rate of ions in a given electric field E depends on two factors, namely, the mobility of the ions and the potential gradient across the WE and CE,

$$V_{+} = \mu_{+}\, dE/dx \qquad (1)$$

$$V_{-} = \mu_{-}\, dE/dx \qquad (2)$$

where the V_+ and V_- are the movement rates of Co cations and sulphate anions, respectively, and the μ_+ and μ_- are the mobilities of Co and sulphate ions, respectively. Here, the components $V_{\parallel}$ and $V_{\perp}$ of the metal ion movement rate (V_+), and the competition between them are the key parameters determining the resultant geometry after electrodeposition. During the electrodeposition process, Co^{2+} in $CoSO_4$ precursor are surrounded by a hydration shell. This hydration layer will effectively reduce the metal ion mobility, and the components of metal ion velocity become almost equal ($V_{\parallel} \approx V_{\perp}$) [26]. Therefore, the rate of reduction of metal ions would become equal in both directions, resulting in the homogeneous Co growth in the mesopores and on the film surfaces.

At the fixed voltage, the current signal changes with the time are measured as shown in Figure 4 (b), indicating the critical point at around 30 s. The saturated part of the current transient indicates the production of Co on the MPS film surfaces. This indicates the successful Co deposition on the MPS film surfaces.

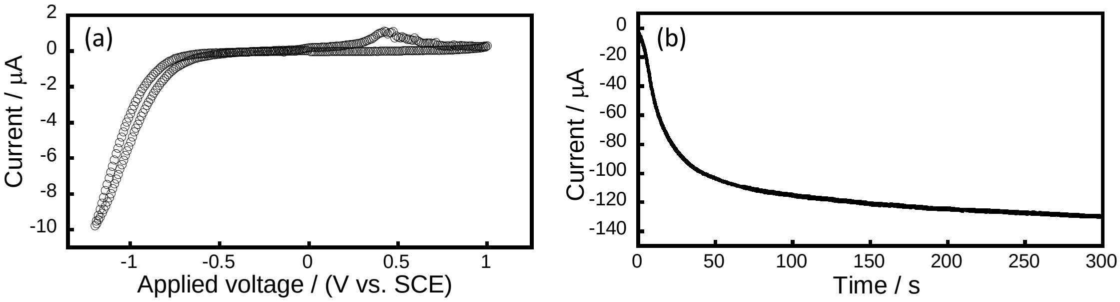

Fig. 4 CV curve of the MPS film on the Si wafer and the current changes with the deposition time at the fixed voltage of −1.5 (V vs. SCE).

Figure 5 shows the FE-SEM surface images of the MPS films and Si wafers after the deposition. Before the deposition, the MPS surface shows the significant flat surface at the several nanometer scales as shown in Figure 5 (a). At the deposition time of 100 s, the cracks at the width of 10−20 μm were clearly formed on the MPS surface. N_2 adsorption isotherm of the MPS film decreased with the deposition and didn't show the mesopores. These results indicate that the cracks are pressed up by the Co deposition into mesopores. It has been reported that the metal growth during electrodeposition in porous materials originates from the cathode surface at the bottom edge of the pore [26]. Thus, the high surface area and presence of sites with low coordination number in the MPS surfaces would afford energetically favorable sites for initiating metal adsorption during electrodeposition.

At the deposition time of 300 s, the cracks and particle-covered surfaces were clearly observed on the MPS surface and the average particle size is several ten nanometers, suggesting the formation of amorphous particles on the surfaces. At the deposition time of 900 s, the cracks and particle-aggregated surfaces were observed on the MPS surface and the aggregated particles with the diameter of several micrometer sizes were formed on the surface. From the XRD analysis at the 2θ range from 40° to 80°, the deposited particles were amorphous structure. At the deposition time of 900 s on the Si wafer, the flower-like particles were homogeneously formed on the surface and the morphology is clearly different from that on the MPS surface.

The electrodeposition is capable of depositing materials in extremely confined and ordered spaces which exist in porous media called template. Possin [19] has reported the fabrication of wires as small as 40 nm in diameter with a method involving electroplating into etched particle tracks in mica. Williams and Giordano [20] refined this technique and used it to routinely produce wires as small as 8.0 nm. Recent researches for the method were pioneered by Martin et al. [21−25], introduced template synthesis for the fabrication of one dimensional nanostructures (i.e. nanowires). This method entails using the nanoscopic pores in a host membrane as templates to prepare monodisperse nanoscopic ultra-fine structures of a desired material. The mesoporous templates can be used as an insulating host material which encompasses cylindrical pores with diameters in nanometer range. The template fabrication methods generally use prefabricated cylindrical nanopores in an inorganic solid material as templates. By filling the desirable metals into the mesopores, the functional nanocomposites with the predetermined diameter can be fabricated. In this study, the highly-ordered hexagonal structure would induce the outstanding cooperative phenomena that clearly differ from the bulk and even from their thin film counterparts. The smaller pore with the size of 5.0 nm that was homogeneously formed on the transparent film surface effectively affects the deposition process, and the nanocomposites will be applicable for the optical and electronic devices.

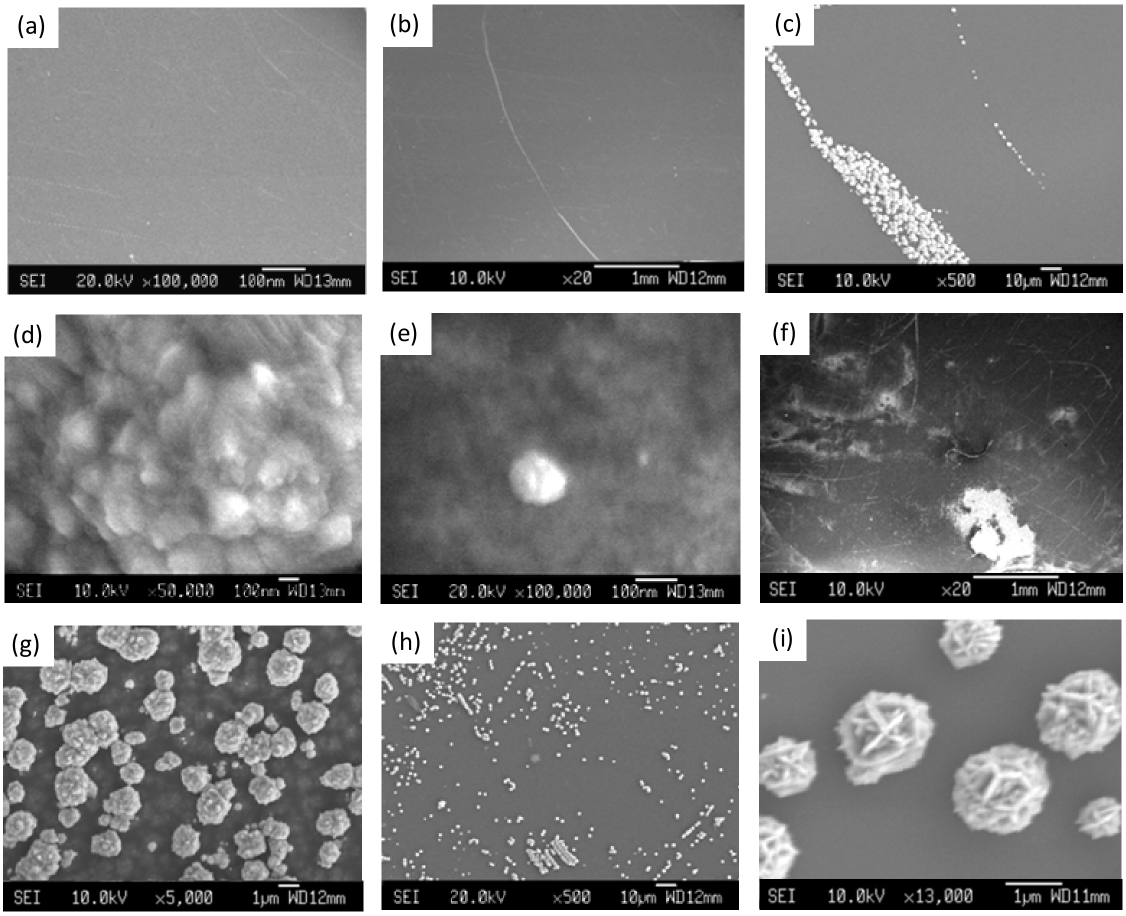

Fig. 5 FE-SEM surface images of the MPS films deposited for (a) 0 s, (b, c) 100 s, (d, e) 300 s, (f, g) 900 s and the (h, i) Si wafers deposited for 900 s.

4. Conclusion

Electrochemical deposition on MPS films formed on a Si wafer was investigated. The MPS films were synthesized by the supramolecular templating method to exhibit the highly-ordered hexagonal structure and surface area of 435 m^2·(g of silica)$^{-1}$. The deposited Co particles were successfully formed on the surfaces; the cracks were generated on the film at 100 s and subsequently the nanoparticles were homogeneously covered on the surface at 300 s, whereas the plate-like structure was formed on the Si wafer. Thus, the ordered structures induce the outstanding cooperative phenomena that clearly differ from the bulk. These results suggest the initial deposition in the mesopores and the subsequent deposition reflected by the framework amorphous silica wall surfaces of the MPS. Therefore, the deposited MPS films will be promising candidates for nanoscopic electrodes in applied electrochemistry and for various other fundamental studies.

Acknowledgments

This study was supported by a grant from the Japan Society for the Promotion of Science (JSPS). The authors thank Prof. Dr. Walther Schwarzacher and Prof. Dr. Natasa Vasiljevic for many helpful discussions and Dr. Stuart Bellamy and Mr. Fred Hale for providing the facilities of Nanoscience and Quantum Information (NSQI) at Bristol University.

References

[1] W. Schwarzacher, J. Phys.: Condens. Matter., **16** (2004) R859.
[2] W. Schwarzacher, Electrochem. Soc. Interf., **15** (2006) 32.
[3] U. Erb, Nanostructured Mater., **6** (1995)533.
[4] S. C. Tjong, and H. Chen, Mater. Sci. Eng., **R 45** (2004) 1.
[5] T. Yanagisawa, T. Shimizu, K. Kuroda, and C. Kato, Bull. Chem. Soc. Jpn., **63** (1990) 988.
[6] C. T. Kresge, M. E. Leonowicz, W. J. Roth, J. C. Vartuli, and J. S. Beck, Nature, **359** (1992) 710.
[7] R. I. Nooney, D. Thirunavukkarasu, Y. Chen, R. Josephs, and A.E. Ostafin, Chem. Mater., **14** (2002) 4721.
[8] M. Ogawa, K. Kato, and N. Shimura, Bull. Chem. Soc. Jpn., **82** (2009) 121.
[9] K. B. Yoon, Chem. Rev., **93** (1993) 321.
[10] K. Moller, and T. Bein, Chem. Mater., **10** (1998) 2950.
[11] M. Ogawa, Ann. Rep. (Sec. C), **94** (1998) 209.
[12] M.Ogawa, H. Ishikawa, and T. Kikuchi, J. Mater. Chem., **8** (1998) 1783.
[13] A. Stein, B. J. Melde, and R. C. Schroden, Adv. Mater., **12** (2000) 1403.
[14] B.J. Scott, G. Wirnsberger, and G. D. Stucky, Chem. Mater., **13** (2001) 3140.
[15] M. Ogawa, J. Photochem. Photobiol. C, Photochem. Rev., **3** (2002) 129.
[16] M. Tagaya, and M. Ogawa, Phys. Chem. Chem. Phys., **10** (2008) 6849.
[17] M. Tagaya, and M. Ogaawa, Chem. Lett., **35** (2006) 108.
[18] D. Zhao, Q. Huo, J. Feng, B. F. Chmelka, and G. D. Stucky, J. Am. Chem. Soc., **120** (1998) 6024.
[19] G. E. Possin, Review of Scientific Instruments, **41** (1970) 772.
[20] W. D. Williams, and N. Giordano, Review of Scientific Instruments, **55** (1984) 410.
[21] R. M. Penner, and C. R. Martin, Anal. Chem., **59** (1987) 2625.
[22] C. J. Brumlik, and C. R. Martin, J. Am. Chem. Soc., **113** (1991) 3174.
[23] C. R. Martin, Science, **266** (1994) 1961.
[24] C. R. Martin, Chem. Mater., **8** (1996) 1739.
[25] S. A. Sapp, B. B. Lakshmi, and C. R. Martin, Adv. Mater., **11** (1999) 402.
[26] T. N. Narayanan, M. M. Shaijumon, P. M. Ajayan, and M. R.Anantharaman, J. Phys. Chem. C, **112** (2008) 14281.

(Received: 26 April, 2012, Accepted: 18 June, 2012)

*Transactions on GIGAKU **1**(2012)01013/1-6*

Grafting Effects of Fe(III) on Photocatalytic Activities of WO_3 and $BiVO_4$ on Visible-Light Irradiation

Masami Nishikawa, Souta Hiura, Yasufumi Mitani, Yoshio Nosaka*
Department of Materials Science and Technology, Nagaoka University of Technology,
1603-1 Kamitomioka, Nagaoka 940-2188, Japan
**E-mail: nosaka@nagaokaut.ac.jp*

The grafting effects of Fe(III) on the photocatalytic activities of narrow bandgap ($\leq$ 2.5 eV) oxide semiconductors of WO_3 and $BiVO_4$ were examined. The photocatalytic activities measured on visible-light irradiation for both oxides were increased by grafting Fe ions. Moreover, it was revealed, by means of chemiluminescence photometry, that the electrons in the valence band transfer to the grafted Fe ions and then the energized Fe ions can reduce O_2 into H_2O_2. This charge transfer would suppress electron-hole recombination, leading to the raise of the photocatalytic activities of WO_3 and $BiVO_4$.

1. Introduction

Photocatalytic materials have been used in wide application such as air purification, water purification, anti-pollutant and anti-virus [1,2]. Photocatalytic reaction proceeds owing to holes and electrons generated in materials by absorbing light energy. The photogenerated holes have oxidation ability and the photogenerated electrons have reduction ability. To decompose pollutants of organic compounds by photocatalytic reaction, the oxidation potential of hole needs to be more positive than +1 V that is redox potential of general organic compounds. In addition, the redox potential of electrons needs to be more negative than that of oxygen (O_2/O_2^- or H_2O_2) because surplus electrons that are not consumed by reduction of oxygen would result in electron-hole recombination that is one of the factors in decreasing photocatalytic activity. The most suitable material for photocatalyst, which also meets these conditions, is TiO_2. The bandgaps of rutile and anatase type TiO_2 are 3.0 and 3.2 eV, respectively. The potentials of their conduction bands are negative enough to reduce oxygen into O_2^- by one-electron reduction and the potentials of their valence bands are much positive enough to decompose organic compounds. However, it is the serious problem that photocatalytic reaction proceeds only under ultraviolet (UV) light irradiation. The content ratio of UV light in solar spectrum is only 5 % and moreover those in fluorescent lights and white light emitting diodes are much less. To raise photocatalytic activity and use photocatalysts indoors, it is indispensable to develop their visible light responses. To achieve the purposes, narrowing of the bandgap of TiO_2 by doping elements such as N, S, and metal ions was reported to be effective [3-5]. Among them, N-doped TiO_2 showed high photocatalytic activity under visible light irradiation. It is considered that the level of orbitals assigned to N atoms would be formed above the level of valence band assigned to O atoms and accordingly the oxidation ability seems to be decreased. Recently, it was reported that the TiO_2 grafted by Fe (III) or Cu (II) ions showed higher photocatalytic activity under visible light irradiation than N-doped TiO_2 [6,7]. The Fe or Cu was considered to be amorphous FeOOH or CuO clusters, respectively. When the Fe or Cu grafted TiO_2 (Fe/TiO_2, Cu/TiO_2) was irradiated by visible light irradiation, electrons in the valence band of TiO_2 would be excited to grafted Fe or Cu ions. Thus it has been considered that the direct electron transfer from valence band of TiO_2 to Fe or Cu ions is the origin of visible light response [8,9].

Oxide semiconductors with narrow bandgap of $\leq$2.5 eV have a potential for visible-light-driven photocatalyst as well as TiO_2. In general, the quantum efficiency, however, is lowered due to high probability of electron-hole recombination with narrowing the bandgap. In the case of WO_3 whose bandgap is 2.5 eV, the valence band level is almost the same as

TiO_2, while the conduction band level is much lower than that of TiO_2 and then just able to reduce oxygen to H_2O_2 by two-electron reduction. Since the rate of two-electron reduction of oxygen would be low, resulting in the recombination of electron-hole [10], WO_3 alone was considered to show the low quantum efficiency under visible light irradiation. When Pt nanoparticles were deposited on the surface of WO_3, the photocatalytic activity was raised because the Pt nanoparticles play a role as a promoter of the two-electron reduction process [10]. Additionally, it was reported that the photocatalytic activity of WO_3 was increased by grafting Cu (II) and Fe (III) [7,8]. Unlike Pt nanoparticles, the Fe and Cu ions are desirable in aspects of cost and resources. However, especially, the reaction mechanisms of Fe(III) grafted WO_3 (Fe/WO_3) was not clear. $BiVO_4$ which is 2.4 eV bandgap in monoclinic form has also been reported for visible-light-driven photocatalyst for O_2 evolution by oxidation of H_2O [11], but, the photocatalytic activity in gas phase is not clear. Moreover, the grafting effects of Cu (II) and Fe (III) on photocatalytic activity of $BiVO_3$ have not be reported yet. Therefore, it is important to examine the grafting effects of Fe (III) on photocatalytic activities of WO_3 and $BiVO_4$ for practical applications.

In this paper, the grafting effects of Fe(III) on the photocatalytic activities of WO_3 and $BiVO_4$ were examined compared to TiO_2. Moreover, the photocatalytic reaction mechanism of Fe(III) grafted WO_3 and $BiVO_4$ (Fe/$BiVO_4$) was successfully elucidated using chemiluminescence photometry.

2. Experimental

Materials

Fe/TiO_2, Fe/WO_3 and Fe/$BiVO_4$ photocatalysts were prepared by impregnation method. 10 mL of distilled water was added to a mixture of $FeCl_3 \cdot 6H_2O$ and 1 g of TiO_2 (MT-150A, TAYCA), WO_3 (Nacalai Tesque) or $BiVO_4$ (Alfa Aesar), respectively. $FeCl_3 \cdot 6H_2O$ was weighted so that the weight fractions of Fe relative to each photocatalyst was 0.1wt%. Each mixed solution was heated at 90°C for 1 h under stirring. Then the solution was centrifuged and then the solid powder was sufficiently washed with distilled water. The obtained photocatalysts were dried at 110°C for 24 h.

Photocatalytic activity

The photocatalytic activity was measured for the decomposition of acetaldehyde as follows. Photocatalyst powder of 0.15 g was spread on a Petri dish of 4 cm diameter and then the dish was placed in the circulated reactor with a volume of 260 mL which was filled with mixed gas of $O_2/N_2=1:4$. The acetaldehyde gas of 50 μL and water of 10 μL were injected into the reactor. The dish placed in the reactor was irradiated by a set of LED (light emitting diode) of a wavelength of $\lambda=470$ nm at the intensity of 20 mW/cm^2, and the amount of generated CO_2 was monitored by a gas analyzer (LI-COR, LI-840) equipped in the circulation reactor system.

Luminol chemiluminescence probe methods

The generation of O_2^- was observed by using a luminol chemiluminescence probe method. [12] Photocatalyst of 15 mg was added in 0.01 M NaOH solution of 3.5 mL in a quartz cell (1 cm × 1 cm) and then the suspension was irradiated by a He-Cd laser (KIMMON, IK5652R-G) at $\lambda=442$ nm with 14 mW. After the irradiation, 50 μL of 7 mM luminol solution was immediately added in the suspension. The chemiluminescence intensity was measured using a Peltier-cooled photon-counter head (Hamamatsu Photonics, H7421). For the measurements of H_2O_2, the photocatalyst suspension was irradiated by the LED and then was kept in dark to eliminate O_2^-. 50 μL of 7 mM luminol solution was added in the suspension and then the suspension was kept in dark for 10 min. 50 μL of hemoglobin (Hb) solution was added in the suspension and then the chemiluminescence intensity was measured. To convert the chemiluminescence intensities to the absolute concentration of O_2^- and H_2O_2, the apparatus factor was calculated from the experiment where all luminol molecules are consumed for the reaction with an excess amount of H_2O_2. The integrated number of photons was proportional to the luminol concentration. From the slope, the observed chemiluminescence intensity can be converted to H_2O_2 concentration as mentioned in detail in the previous report [12].

3. Results and discussion

Figure 1 shows the amounts of CO_2 generated by the decomposition of gaseous acetaldehyde for TiO_2, Fe/TiO_2, WO_3, Fe/WO_3, $BiVO_4$ and Fe/$BiVO_4$ on the irradiation of visible light (470-nm LED) for 1 h. In the case of TiO_2, CO_2 generated by decomposition of acetaldehyde was not detected for the bare TiO_2. This was due to lack of interband excitation because the bandgap of rutile TiO_2 is 3.0 eV, corresponding to λ=413 nm. In contrast, the Fe/TiO_2 showed a decomposition ability of 80 ppm/h in CO_2 generation. This visible response was due to the direct charge transfer form valence band of TiO_2 to Fe^{3+} grafted on the TiO_2 surface as reported previously [9]. At the same time, acetaldehyde was oxidatively decomposed by holes in the valence band of TiO_2. In the case of WO_3, the bare WO_3 alone showed a decomposition ability of 170 ppm/h. This decomposition ability was due to interband excitation because the bandgap of WO_3 is 2.5 eV, corresponding to λ=496 nm. In the Fe/WO_3, the generation amount of CO_2 was increased to 209 ppm/h. In the previous report, the photocatalytic activity of Cu(II) grated WO_3 was also higher than the bare WO_3 [8]. It was considered that some electrons in conduction band from valence band would transfer to the grafted Cu^{2+}, leading to the raise of the photocatalytic activity because electron-hole recombination was suppressed. Based on this consideration, the Fe ions in Fe/WO_3 also would play an important role for charge separation. In the case of $BiVO_4$, the similar tendency to WO_3 was shown. The bare $BiVO_4$ alone showed a little decomposition ability of 3 ppm/h. Since the bandgap of $BiVO_4$ is 2.4 eV (λ=516 nm), interband excitation should occur. However, the decomposition ability was much smaller than WO_3. Therefore, it was considered that the probability of electron-hole recombination of the used $BiVO_4$ was high compared to WO_3. In the Fe/$BiVO_3$, the decomposition ability was largely increased to 49 ppm/h. The result indicates that the Fe ions in Fe/$BiVO_4$ also would play an important role for charge separation. Moreover, for the photocatalysts with little photocatalytic activity such as $BiVO_4$ under visible light irradiation, it was revealed that the grafting of Fe ions is more effective to increase their photocatalytic activities.

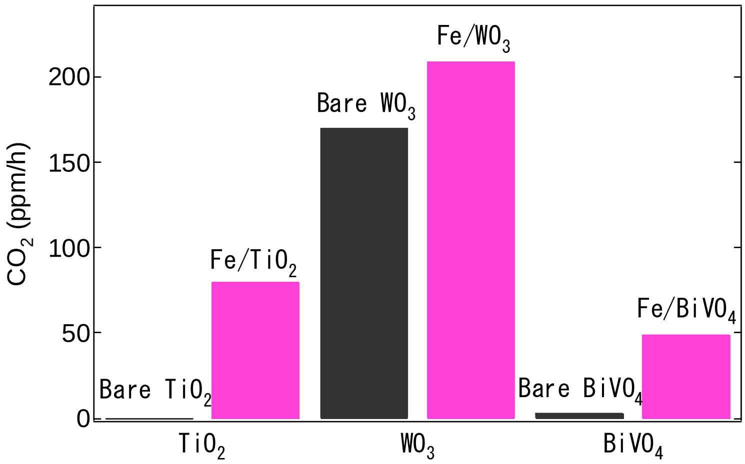

Fig. 1 The amounts of CO_2 generated for 1 h by the decomposition of gaseous acetaldehyde for photocatalysts under visible-light irradiation.

To elucidate the photocatalytic reaction mechanisms of Fe/WO_3 and Fe/$BiVO_4$, the abilities of their excited electrons were examined for the reduction of molecular oxygen. Reduction of oxygen is a key reaction because photocatalytic reactions cannot proceed when the photogenerated electrons do not react with oxygen which is the only molecule to be reduced in ambient atmosphere. In the Fe/TiO_2, it has been already confirmed by means of chemiluminescence photometry that the excited Fe^{2+} ions reduced oxygen into H_2O_2 by two-electron reduction [9]. Figure 2 shows the amounts of O_2^- and H_2O_2 generated by reduction of oxygen by excited electrons under visible light irradiation with the 442-nm He-Cd laser. In the bare WO_3, H_2O_2 was detected while O_2^- was not detected. This reason is that the conduction level of WO_3 is +0.55 V (vs. SHE at pH = 0), which is more positive than the redox potential of $(O_2,H^+)/ HO_2$, +0.46 V (vs. SHE at pH = 0) and is more negative than the redox potential of $(O_2,2H^+)/H_2O_2$, +0.695 V (vs. SHE at pH = 0). In the Fe/WO_3, the amount of generated H_2O_2 was increased. The redox potential of Fe^{3+}/Fe^{2+} is +0.77 V (vs. SHE at pH = 0), which is located under the conduction band of WO_3. It is possible that electrons transfer to the grafted Fe ions by direct electron transfer from valence band with interfacial charge transfer absorption or indirect charge transfer from valence band via conduction band (valence band → conduction band → Fe ions). In the case of the TiO_2, under visible light irradiation, the direct charge transfer form valence band of TiO_2 to grafted Fe ions occur and under UV light irradiation, some electrons excited in conduction band of TiO_2 by interband excitation transfer to grafted Fe ions [9]. From this report, it was concluded that the increase of H_2O_2 in Fe/WO_3 was due to the electrons excited to Fe ions as well as the Fe/TiO_2. In the case of the bare $BiVO_4$, O_2^- was mainly detected while H_2O_2 was not almost detected. The conduction band level of $BiVO_4$ is 0.0 V (vs. SHE at pH = 0), which is negative enough to reduce O_2 into O_2^-. In contrast, in the Fe/$BiVO_4$, the amount of O_2^- was decreased while that of H_2O_2 was increased. These results indicated that charge transfer to Fe ions would occur because excited Fe ions have only ability of two-electron reduction. The amount of H_2O_2 seems to be somewhat small. This indicates that generated H_2O_2 would be oxidized into H_2O by holes.

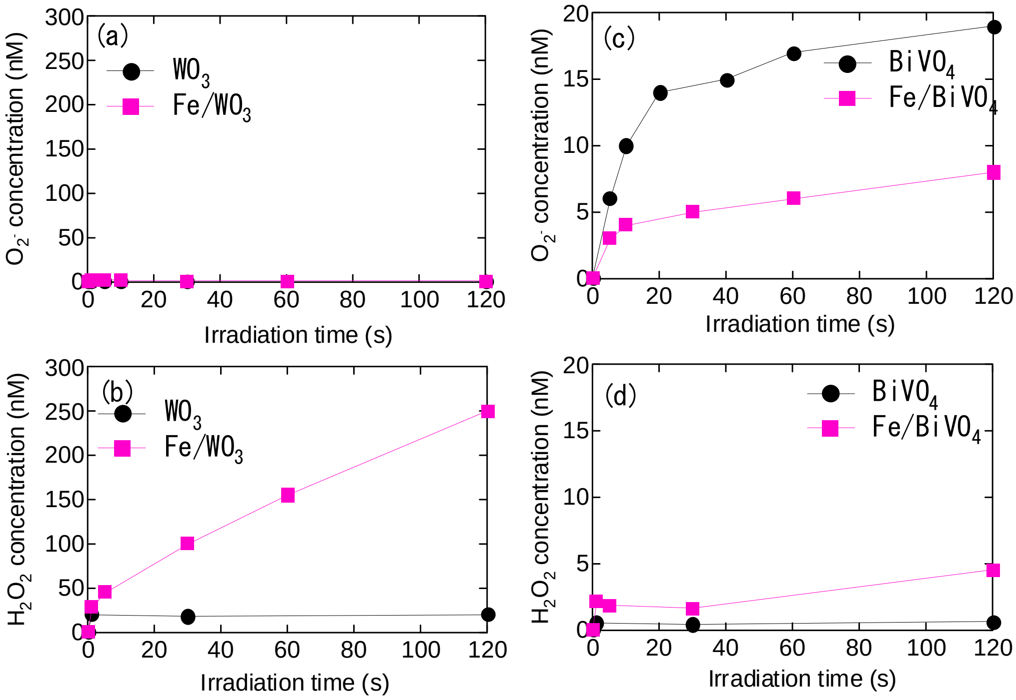

Fig. 2 The amounts of (a) O_2^- and (b) H_2O_2 generated for WO_3 and Fe/WO_3 photocatalysts and (c) O_2^- and (d) H_2O_2 generated for $BiVO_4$ and Fe/$BiVO_4$ photocatalysts as a function of the irradiation time at 442 nm.

Based on the results, the plausible reaction mechanisms of Fe/WO_3 and Fe/$BiVO_4$ photocatalysts were summarized in Fig. 3. Compared to WO_3, $BiVO_4$ has valence band positioned at more negative. Therefore, the oxidation ability of $BiVO_4$ against organic compounds such as acetaldehyde is low as seen in Fig. 1. In this case, the remained holes in valence band, which can not react with organic compounds, might diminish by recombination with electrons. When both photocatalysts of WO_3 and $BiVO_4$ are grafted Fe ions on their surface, electrons in their balance bands are photo-excited to the grafted Fe ions under visible light irradiation. In addition, in the case of $BiVO_4$, electrons are excited to their conduction band and then transfer to the Fe ions. Although it is not clear which electron transfer proceed, in either electron transfer processes, electrons transfer to the grafted Fe ions. By transfer of excited electrons to the grafted Fe ions, holes photo-generated in WO_3 or $BiVO_4$ and are separated from electrons, leading to a low probability of electron-hole recombination. Therefore, the photocatalytic activities of WO_3 and $BiVO_4$ were raised by grafting Fe ions. Since the Fe ions play an important role for charge separation, for the photocatalysts with little photocatalytic activity such as $BiVO_4$, it was considered that the grafting of Fe ions is more effective to increase their photocatalytic activities.

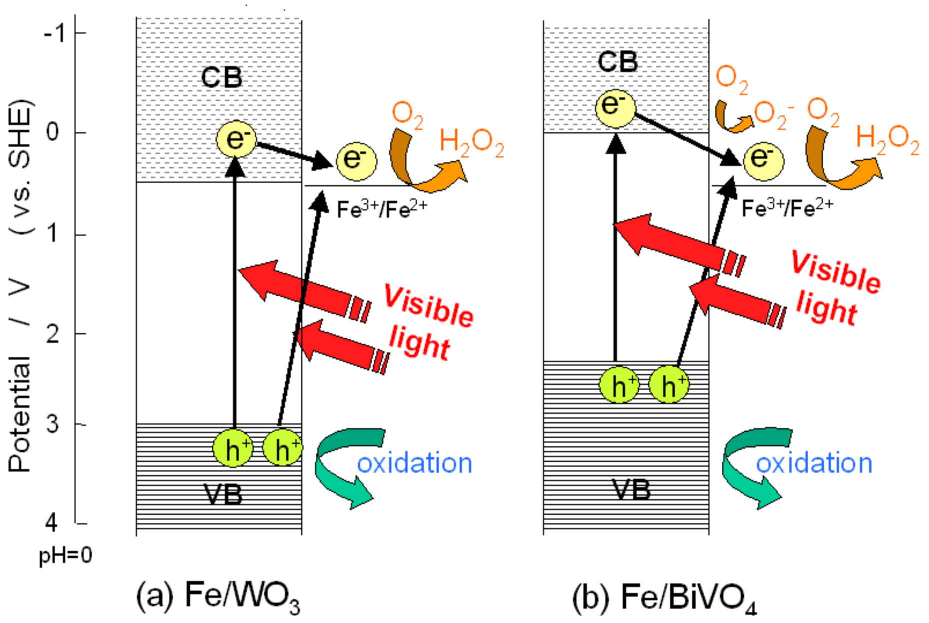

Fig. 3 The photocatalytic mechanisms of (a) Fe/WO_3 and (b) Fe/$BiVO_4$.

4. Conclusions

The grafting effects of Fe(III) on the photocatalytic activities of narrow bandgap oxide semiconductors of WO_3 and $BiVO_4$ were examined. The photocatalytic activities of both oxides were increased by grafting Fe ions. Especially, for the $BiVO_4$ of little photocatalytic activity, the grafting of Fe ions was revealed to be more effective to increase its photocatalytic activities. Moreover, the reductive ability of the excited electrons was successfully examined by means of chemiluminescence photometry. As a result, it was revealed that electrons transfer to the grafted Fe ions by visible light irradiation and the excited Fe ions (Fe^{2+}) have a reduction ability of oxygen into H_2O_2. This charge transfer to Fe ions on the surfaces of the photocatalysts would suppress electron-hole recombination because holes remain in the photocatalysts, which would be leading to the raise of the photocatalytic activity of WO_3 and $BiVO_4$.

References

[1] A. Fujishima, X. Zhang, and D. Tryk, Surf. Sci. Rep., **63** (2008) 515.

[2] M. Anpo and P.V. Kamat, Eds. *Environmentally Benign Photocatalysis- Application of Titanium Dioxide-based Materials*; Springer: New York, 2010.

[3] R. Asahi, T. Morikawa, T. Ohwaki, K. Aoki, and Y. Taga, Science, **293** (2001) 269.

[4] T. Umebayashi, T. Yamaki, H. Ito, and K. Asahi, Appl. Phys. Lett., **81** (2002) 454.

[5] Y. Murakami, B. Kasahara, and Y. Nosaka, Chem. Lett., **36** (2007) 330.

[6] H. Irie, K. Kamiya, T. Shibanuma, S. Miura, D.A. Tryk, T. Yokoyama, and K. Hashimoto, J. Phys. Chem. C, **113** (2009)10761.

[7] H. Yu, H. Irie, Y. Shimodaira, Y. Hosogi, Y. Kuroda, M. Miyauchi, and K. Hashimoto, J. Phys. Chem. C, **114** (2010) 16481.

[8] Y. Nosaka, S. Takahashi, H. Sakamoto, and A. Nosaka, J. Phys. Chem. C, **115** (2011) 21283.

[9] M. Nishikawa, Y. Mitani, and Y. Nosaka, J. Phys. Chem. C, **2011**, submitted.

[10] R. Abe, K. Sasaki, H. Kunioku, and B. Ohtani, J. Am. Chem. Soc., **130** (2008) 7780.

[11] A. Kudo, K. Omori, and H. Kato, J. Am. Chem. Soc., **121** (1999**)** 11459.

[12] T. Hirakawa and Nosaka, *J. Phys. Chem.* C, **112** (2008) 15818.

(Received: 14 May, 2012, Accepted: 19 June, 2012)

Transactions on GIGAKU **1***(2012)01014/1-8*

In Vitro Targeting of Cancer Cells with Luminescent Nanoporous Silica Spheres

Motohiro Tagaya[1,*], Junzo Tanaka[2], Nobutaka Hanagata[3], Toshiyuki Ikoma[2],
Taro Takemura[3], Kota Shiba[4], Takaomi Kobayashi[1]
[1)]Department of Materials Science and Technology, Nagaoka University of Technology,
1603-1 Kamitomioka-cho, Nagaoka 940-2188, Japan
[2)] Department of Metallurgy and Ceramics Science, Tokyo Institute of Technology,
O-okayama 2-12-1, Meguro-ku, Tokyo 152-8550, Japan
[3)] Nanotechnology Innovation Station, National Institute for Materials Science (NIMS),
1-2-1 Sengen, Tsukuba, Ibaraki 305-004, Japan
[4)] WPI Center for Materials Nanoarchitectonics, National Institute for Materials Science (NIMS)
Namiki 1-1, Tsukuba, Ibaraki 305-0044, Japan
**E-mail: tagaya@mst.nagaokaut.ac.jp*

The luminescent europium(III)-doped nanoporous silica spheres (Eu:NPS) were successfully synthesized by a supramolecular templating method. Folic acid (FA) as the targeting ligand for cancer cells was immobilized on the Eu:NPS surface through a mediation of 3-aminopropyltriethoxysilane (APTES). The ordered nanopores were preserved with the APTES and FA immobilization. The surface area decreased only with the APTES immobilization, and the FA was immobilized only on the outer surface of pores. The photoluminescence of the immobilized spheres showed the characteristic luminescence peak due to interactions between the FA and Eu^{3+}, and the luminescence can be detected by a fluorescent microscopy. The immobilized spheres were highly dispersed stably in the cell culture medium to bind specifically to cancer cells and exhibit the luminescence. Thus, the FA was successfully immobilized on the luminescent Eu:NPS spheres to exhibit the highly targeting ability to the cancer cells.

1. Introduction

The designing of superior targeting nanomaterials against specific cells is important for use in the biomedical science field. The targeting to cells by specific ligands or utilizing antibodies depends on the ability of the targeting reagents to bind selectively to the cell surface and to trigger subsequently receptor-mediated endocytosis [1]. The challenges for combining the imaging with targeting into one system are desired using a nanoparticle. However, the coupling of multifunctional groups in sufficient concentration on the particle surface is difficult because of the limited number of attachment sites.

Nanoporous silica (NPS) prepared by the supramolecular templating method possesses attractive features such as a well-defined and controllable pore size, large surface area, and reactive surface [2,3]. The large immobilization capacity for various functional molecules is one of the many attractive features of NPS, accompanied by controlling the nanostructural properties on a nanometer scale such as pore and particle sizes and framework structures [4-11]. The preparation of silica-based biohybrid and the NPS spheres having therapeutic or imaging properties for bio-functions have been recently reported [12-17]. The drug delivery systems that have been synthesized to combine the two-functional therapeutic and imaging moieties on the surfaces have been reported using a fluorescent dye covalently linked to the surface, making them visible by fluorescence microscopy [18,19]. If the external surface and silica framework in NPS are functionalized as the targeting and imaging, respectively, the internal pore surfaces can be used for therapeutic medicine. However, the combination of the functions (therapeutic, imaging and targeting) into one particle has not yet been investigated in detail.

In this study, folic acid (FA) molecules, which have been known as the targeting reagents for cancer cells [20], were covalently immobilized on luminescent Eu^{3+}-doped NPS (Eu:NPS) spheres by mediation of the 3-aminopropyltriethoxysilane (APTES) adlayer in Scheme 1 (a), and the targeting behavior of the spheres to the cancer cells was examined as compared with that to the normal cells (fibroblast cells) in Scheme 1 (b).

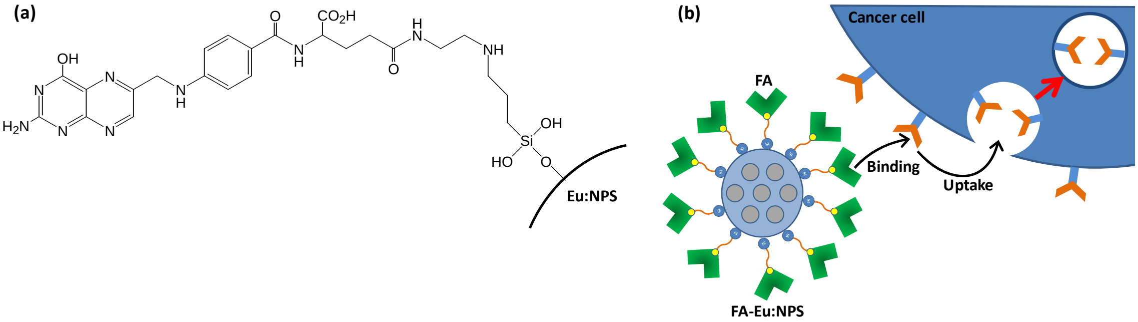

Scheme 1 Schemes of (a) the FA immobilization on Eu:NPS spheres and (b) the targeting of the FA-immobilized Eu:NPS to cancer cells through a receptor-mediated endocytosis.

2. Experiment

Synthesis of Eu:NPS. Eu: NPS spheres were synthesized according to our previous reports [14]. 1.0 g of CTAB, 225 g of ultrapure water and 3.5 mL of 2.0 M NaOH solution were stirred. Then, 5.515 mL of TEOS and 15 mL of Eu^{3+} aqueus solution containing 0.226 g, 0.452 g and 0.904 g of $EuCl_3{\cdot}6H_2O$ (Kanto Chemical Co., Ltd.) at the molar concentration of the Eu^{3+} to Si (Eu/Si) of 1/40, 1/20 and 1/10 were stirred at 80°C for 2 h. The solution was filtered, and the resulting solids were washed, vaccuumed for 4 h, and calcined at 550°C for 4 h, which were abriviated as 2.5-Eu:NPS, 5.0-Eu:NPS and 10.0-Eu:NPS for the Eu/Si of 1/40, 1/20, 1/10, respectivly.

As reference smples, Eu_2O_3 was synthesized by the calcination of the $EuCl_3{\cdot}6H_2O$, which was identified with ICDD-ICSD 00-034-0072. The Eu^{3+} in ethanol at the concentaration of 16.5 mM was fabricated by the dissolution of $EuCl_3{\cdot}6H_2O$.

Immobilization of FA. The APTES immobilization was conducted by stirring Eu:NPS (250 mg) with HCl (12 mL), APTES (0.78 mL) and ethanol (5 mL) at 37.5°C. The FA immobilization was conducted by stirring the APTES-modified Eu:NPS (APTES-Eu:NPS, 150 mg) with 50 mM phosphate buffered saline (PBS: pH=7.2, 25 mL), dimethyl sulfoxide (12 mL), and the folate N-hydroxysuccinimidyl ester (NHS-FA) synthesized at the different initial concentrations based on our previous reports [14]. The resulting materials with the immobilized FA amounts of 39, 61, 83, 206 and 858 μmol·(g of APTES-Eu:NPS)$^{-1}$ were abbreviated as FA**1**-, FA**2**-, FA**3**-, FA**4**- and FA**5**-Eu:NPS, respectively.

Characterization of Nanostructures. The doped amount of Eu^{3+} was determined by the inductively coupled plasma optical emission spectrometer (ICP-OES: Leeman Labs, INC U.S.A., Prodigy ICP). Nitrogen adsorption and desorption isotherms were measured at 77K on a SA3100 instrument (BECHMAN COULTER Co., Ltd.). Prior to the measurement, the samples were degassed under vacuum at 393K for 4 h. The surface area was evaluated by the BET surface area, and the pore volume was calculated by the BET surface area and averaged pore size. X-ray diffraction (XRD) patterns were recorded on a X'Pert Pro MPD (PNAalytical Co., Ltd.) using monochromatized CuKα radiation.

Characterization of Luminescence Properties. Luminescence properties were evaluated by photoluminescence spectroscopy and microscopy. The excitation and luminescence spectra were recorded on a FluoroMax-4 spectrophotometer (Horiba Co., Ltd.) with the monitored luminescence at 611 nm and excitation wavelength at 464 nm under room temperature (atmosphere: air, excitation-slit/detection-slit: 2 nm/2 nm, measure time: 0.1 s, step width: 1.0 nm, sample weight: 150 mg, light cut filter on the detection side: $\lambda_{cut} < 515$ nm). The luminescence intensities centered at the top of 590 nm and 611 nm, which are abbreviated as I_{590} and I_{611}, were calculated by the integrated intensity areas in the ranges of 580−600 nm (assigned to $^5D_0 \rightarrow {}^7F_1$) and 600−640 nm (assigned to $^5D_0 \rightarrow {}^7F_1$) based on the Voigt-function fitting at the peak tops, and the ratio of I_{611} to I_{590} (I_{611}/I_{590}) was also calculated. The luminescence intensity centered at the top of 611 nm abbreviated as I_{611} was also calculated by the integrated intensity based on the Voigt-function fitting at the peak top in the range of 600–640 nm. The microscope images were observed by a luminescence microscope (Nikon Co., Ltd., BX-50; excitation wavelength: 380–420 nm, exposure time: 1500 ms, sensitivity: 20). The decay kinetics, which can be explained with an exponential function, was measured on a wavelength at 394 nm from a Xe flash lump (Horiba Co., Ltd., Fluoromax-TCSPC), and the decay of the luminescence intensity was detected on a wavelength at 611 nm. The measured decay was recorded by a numerical fitting to an exponential function based on the Eq. (1), and was repeatedly measured ten times.

$$I(t) = I(0)\exp(-t/\tau) \tag{1}$$

where the $I(t)$ and $I(0)$ are the luminescence intensity at time (t) and starting point ($t = 0$), and the τ is luminescence life time in the decay process, which consequently provided the I (0) and correlation factor (R^2) of 20021 ± 85 cps and 0.9992 for 2.5-Eu:MPS, 101307 ± 727 cps and 0.9978 for 5.0-Eu:NPS, 7024 ± 19 cps and 0.9978 for 10.0-Eu:NPS, 19434 ± 67 cps and 0.9997 for Eu_2O_3 and 22639 ± 125 cps and 0.9998 for Eu^{3+} in ethanol. The quantum efficiency was recorded on a FP-8500 (Nihondenshi Co., Ltd.) with an integrating sphere (diameter: 60 mm) equipment. The efficiency is defined as the ratio of photons absorbed from the excitation wavelength (464 nm) to photons emitted at 611 nm.

Cell Culture and Fabrication of Cell Suspensions. Fibroblast NIH3T3 (RCB1862) and Hela cancer (RCB0007) cells as cell lines provided by Riken BioResource Center were separately cultured in a plastic cell culture flask with an area of 75 cm^2 (BD Bioscience, USA) containing 15 mL of the fetal bovine serum (FBS: SAFC Bioscience Co., Ltd., product number: 12603C, lot no. 6D0975) dispersed into Dulbecco's minimum essential medium (DMEM: Invitrogen Co., Ltd.) at 10 vol% (10% FBS/DMEM). The cells were incubated at 37°C in a humidified atmosphere of 5% CO_2, and subcultured every 7 days using 1 mL of the trypsin-EDTA. After being washed with 15 mL of phosphate buffer saline (PBS: SEIMI Co., Ltd.) and treated with 1 mL of the trypsin-EDTA for 10 min at 37°C, the cells were dispersed in 15 mL of PBS, separated by centrifugation (2000 rpm, 2 min), and dispersed in 15 mL of 10% FBS/DMEM. The centrifugation and dispersion were carried out twice. The number of cells in the suspension was counted and adjusted at the seeding density of 2.72×10^4 cells·mL^{-1}.

Evaluation of Cell Viability. The fibroblast cell suspension was cultured on a commercially-available 96-well cell culture plate (Greiner Bio-one Co., Ltd., bottom area: 0.34 cm^2/well, product number: 655180) at the area density of 8000 cells/cm^2. At the culture time of 12 h, the cultured fibroblast cells were adhered on the plate and had fibrous morphology in Figure 1 (a), and showed no luminescence as shown in Figure 1 (b). Then, 100 μL of the FA-Eu:NPS in 10% FBS/DMEM (concentration: 100 μg/mL) was added into the cell surfaces and additionally cultured for 48 h. The cell viability was evaluated by WST-8 method [21]. 10 μL of the Cell Counting Kit-8 solution (Chemical-Dojin Co., Ltd., product number: 343-07623) was added and stored for 3 h at 37°C in a humidified atmosphere of 5% CO_2. The absorbance at 450 nm of the resulting solution was measured by a photospectrometer (Power Scan ®HT, DS Pharma Biomedical Co., Ltd.). The background absorbance as the 10% FBS/DMEM was subtracted and the average value for five samples (n=5) was calculated. The absorbance maximum of the samples is fitted to be 100 %.

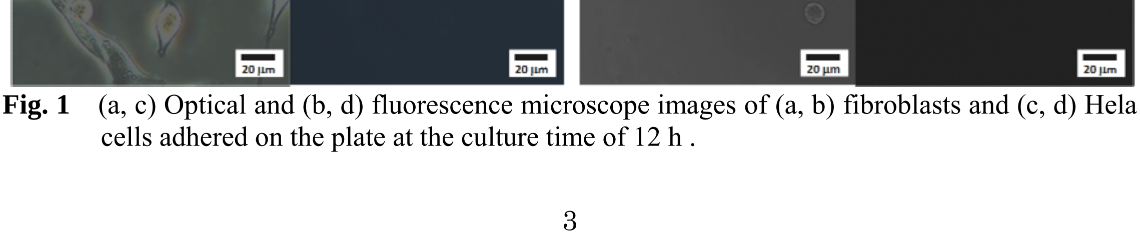

Fig. 1 (a, c) Optical and (b, d) fluorescence microscope images of (a, b) fibroblasts and (c, d) Hela cells adhered on the plate at the culture time of 12 h .

Specific Staining of the Cells. The Hela cell suspension was cultured on both the commercially-available 96-well cell culture plate and the 35 mm tissue culture dish (BD Falcon™ Co., Ltd.) at the area density of 8000 cells/cm^2. At the culture time of 12 h, the cultured fibroblast cells were adhered on the culture plate and had round shape in Fig. 1 (c), and showed no luminescence as shown in Fig. 1 (d). Then, 100 μL and 1 mL of the FA-Eu:NPS in 10% FBS/DMEM (concentration: 100 μg/mL) were added into the adhered cells on the plate and dish, respectively.

The cells on the plate were cultured for 1, 2, 3, 4, 5, and 6 days. After the culture, the cells were washed two times with 100 μL of PBS and then the luminescence intensity was measured by a photospectrometer (Power Scan ®HT, DS Pharma Biomedical Co., Ltd.). On the other hand, the cells on the dish were culture for 2 days. The cultured cells were washed two times with 1 mL of PBS and then the cellular nuclei was stained at room temperature with 100 μL of 4',6-diamino-2-phenylindole (DAPI: Invitrogen™ Co., Ltd.) which was diluted 15 times into PBS. The samples in the dye solution were then incubated in the dark for 60 min, and washed three times with 1 mL of PBS. The cells in the PBS were covered and sealed with a glass to prevent evaporation during the observation by the fluorescence microscope.

3. Results and Discussion

Nanostructure of Eu:NPS. Table 1 shows the ICP-OES analytical values of the Eu molar concentration to Si (Eu/Si) and the nanopore properties (S_{BET} and V) evaluated by the N_2 adsorption and desorption isotherms. The Eu and Si concentrations in the dissolved solution contains 1.93 ± 0.02 ppm and 12.82 ± 0.17 ppm for 2.5-Eu:NPS, 2.84 ± 0.04 ppm and 9.72 ± 0.13 ppm for 5.0-Eu:NPS, and 5.03 ± 0.04 ppm and 9.12 ± 0.11 ppm for 10.0-Eu:NPS. It is indicated that the Eu/Si values by the ICP-OES analysis are similar to those estimated by the initial solution compositions.

The isotherms indicated that the BET surface area and volume are 758 m^2·(g silica)$^{-1}$ and 0.68 ml·g^{-1} for NPS, 576 m^2·(g silica)$^{-1}$ and 0.48 ml·g^{-1} for 2.5-Eu:NPS, 557 m^2·(g silica)$^{-1}$ and 0.55 ml·g^{-1} for 5.0-Eu:NPS, and 523 m^2·(g silica)$^{-1}$ and 0.79 ml·g^{-1} for 10.0-Eu:NPS, indicating the reduced surface area with the Eu^{3+}-doping.

The peaks of the XRD patterns are indexed as (100), (110), (200) and (220) reflections of a hexagonal structure (data not shown), suggesting that the highly-ordered arrangements are preserved with the doping. In the wide-angles, there are no detectable diffractions of the Eu_2O_3 crystalline phase. These results significantly correspond to our previous reports [14].

Table 1 ICP-OES analytical values of the Eu molar concentration to Si (Eu/Si), the nanopore properties (S_{BET} and V) evaluated by the N_2 adsorption and desorption isotherms, the luminescence lifetime and the quantum efficiency the Eu:NPS.

	ICP-OES	**N_2 adsorption/desorption isotherm**		**Luminescence lifetime**	**Quantum efficiency**
Sample	Eu/Si (mol %)	S_{BET} (m^2 (g of Eu:Silica)$^{-1}$)	V (ml (g of Eu:NPS)$^{-1}$)	τ (ms)	Φ (%)
NPS	–	758	0.68	–	–
2.5-EuNPS	2.78 ± 1.23	576	0.48	1.234 ± 0.012	6.51
5.0-EuNPS	5.40 ± 2.11	557	0.55	1.052 ± 0.016	8.67
10.0-EuNPS	10.19 ± 3.54	523	0.79	0.826 ± 0.004	3.91

Luminescence Properties of Eu:NPS. Figure 2 shows the typical excitation and photoluminescence spectra of 5.0-Eu:NPS and FA-Eu:NPS. The excitation spectra of 5.0-Eu:NPS consists of several narrow peaks, which are located at around 361, 375, 380, 394, 412, and 465 nm, and the spectral shapes were almost same as the Eu_2O_3 and Eu^{3+} in ethanol. The peaks are attributed to f–f transitions within the $4f^6$ electron configuration [22], indicating the reflection of the electronic transitions of Eu^{3+} irrespective of host matrix.

The luminescence spectrum showed the narrow peaks assigned to the f–f transitions of the Eu^{3+}, due to the shielding of the 4f orbitals by the outer $5s^2$ and $5p^6$ orbitals [22]. All the observed peaks correspond to the transitions from the metastable orbital singlet state $^5D_0$ to spin–orbital states of ^7F_J ($J = 0, 1, 2, 4$) of Eu^{3+} [23], which indicates the characteristic transitions from the $^5D_0$ to $^7F_0$ at 577 nm, $^7F_1$ at 585 nm, 590 nm and 595 nm, $^7F_2$ at 611 nm, $^7F_3$ at 646 nm and $^7F_4$ at 700 nm. The spectral shapes were clearly different from the Eu_2O_3 and Eu^{3+} in ethanol, indicating the different relaxation process of the Eu^{3+} depending on the host matrix. The luminescence of the Eu^{3+} doped into the silica framework is predominantly attributed to $^5D_0 \rightarrow {}^7F_1$ and $^5D_0 \rightarrow {}^7F_2$, and the $^5D_0 \rightarrow {}^7F_2$ intensity significantly depends on the site environment of Eu^{3+} [24]. The I_{611} (due to $^5D_0$-$^7F_2$ transition) is 3.5 times larger than the I_{590} (due to $^5D_0$-$^7F_1$ transition), and the I_{611}/I_{590} is constant irrespective of the Eu/Si, and corresponds to the spectral shapes of the Eu^{3+} located in low symmetry sites [25]. The Eu^{3+} is present in an environment of a low symmetry in the silica framework structure, and the structural environment enhanced the $^5D_0 \rightarrow {}^7F_2$ transition. Therefore, the Eu^{3+} concentration as well as the silica framework structure affected the efficient luminescence of Eu^{3+}, and the highly-efficient luminescence was observed at the Eu/Si of 5.0 mol%.

In order to understand the luminescence relaxation process, the decay kinetics of the excited states was investigated as shown in Table 1. The decay kinetics was significantly fitted with an exponential function. The decay kinetics of the Eu_2O_3 and Eu^{3+} in ethanol turned out to be very fast at 0.211 ± 0.001 ms and 0.279 ± 0.003 ms [14], indicating the effective quenching through a non-radiative phonon in the oxide and solution states. The Eu^{3+} doped in the silica framework is much longer life time as compared with that in the oxide, solution, and $Eu(Phen)_3{}^{3+}$-doped in nanoporous silica film (0.330 ms) [26], suggesting the effective host matrix of the silica framework for the efficient luminescence and relaxation. Although the increase in the Eu^{3+} concentration enhanced the cross relaxation among the neighboring Eu^{3+} ions to shorten the life time, the silica framework induced the longer life time of the Eu^{3+}. The relationship between the Eu^{3+} concentration and the life time clearly reveals a negative correlation, indicating the mono-dispersion of the Eu^{3+} ions in the silica frameworks.

The integral luminescence intensity is in the order of 5.0-Eu:NPS > 2.5-Eu:NPS > 10.0-Eu:NPS, suggesting the occurrence of concentration quenching of the 10.0-Eu:NPS. Furthermore, the quantum efficiency is also in the order of 5.0-Eu:NPS > 2.5-Eu:NPS > 10.0-Eu:NPS as shown in Table 1. Thus, the 5.0-Eu:NPS shows the highly-efficient luminescence was used for the following experiment.

FA Immobilization on Eu:NPS. The FA was effectively immobilized on the APTES-Eu:NPS to give yellow-colored products, and the immobilized amount was controlled by the initial concentration. The XRD patterns clearly revealed the hexagonal structure with the APTES and FA immobilizations. In the N_2 adsorption and desorption isotherms, a hysteresis between the adsorption and desorption was observed The FA immobilization with covalent bonding on the Eu:NPS was successfully achieved, and the ordered nanopores were preserved by the immobilization [14]. Taking into account the molecular sizes, the pore size of Eu:NPS (ca. 2.5 nm) is large enough to accommodate the APTES, whereas the FA cannot be incorporated into the nanopore, indicating the FA immobilization only on the external surfaces.

The excitation and luminescence spectra of FA**5**-Eu:NPS in Fig. 2. With the APTES and FA immobilization, the charge-transfer band at 240 nm in the excitation spectra (detected emission at 611 nm) increased as shown in Fig. 2 (a), which was located at the short-wavelength as compared to that of the other oxides [25], suggesting the interaction of the O atoms of APTES with the near-surface Eu^{3+} ions. The luminescence spectral shapes clearly depended on the FA amount. The peaks in the APTES-Eu:NPS correspond to the transitions from the metastable orbital singlet state of $^5D_0$ to the spin–orbital states of ^7F_J ($J = 0, 1, 2, 3$) [23], which indicates the transitions from the $^5D_0$ to $^7F_0$ at 577 nm, $^7F_1$ at 590 nm, $^7F_2$ at 611 nm and $^7F_3$ at 700 nm, and the luminescence intensity is 0.2 times weaker than that of the Eu:NPS. With the increase in the FA amount, the broad luminescence peak at around 550 nm was enhanced. Taking into account no luminescence of the neat FA and NHS-FA, the spectral change would be attributed to the excitation of the conjugation band between the FA molecules and near-surface Eu^{3+} ions, implying the effective charge transfer transition. The luminescence of the Eu^{3+} doped in the silica framework was predominantly attributed to $^5D_0 \rightarrow {}^7F_1$ and $^5D_0 \rightarrow {}^7F_2$, and the $^5D_0 \rightarrow {}^7F_2$ intensity depended on the site environment of Eu^{3+} [24]. The ratio of the $^5D_0 \rightarrow {}^7F_2$ to $^5D_0 \rightarrow {}^7F_1$ luminescence intensities was almost constant with the immobilization. The integral luminescence intensity and the I_{550}/I_{611} were clearly changed, and these values were maximum at the FA amount of 60.3 μmol·(g of APTES-Eu:NPS)$^{-1}$ (FA**2**-Eu:NPS) and 83.0 μmol·(g of APTES-Eu:NPS)$^{-1}$ (FA**2**-Eu:NPS), respectively. The decrease with the much higher increase in the FA amount would be attributed to the radiationless deactivation by the interactions among the FA molecules. Therefore, the FA immobilization effectively induced the characteristic luminescence by the band due to the chelete complex (i.e. FA–Eu^{3+}), suggesting the importance of controlling of the Eu^{3+} concentration as well as the interactions among the FA molecules.

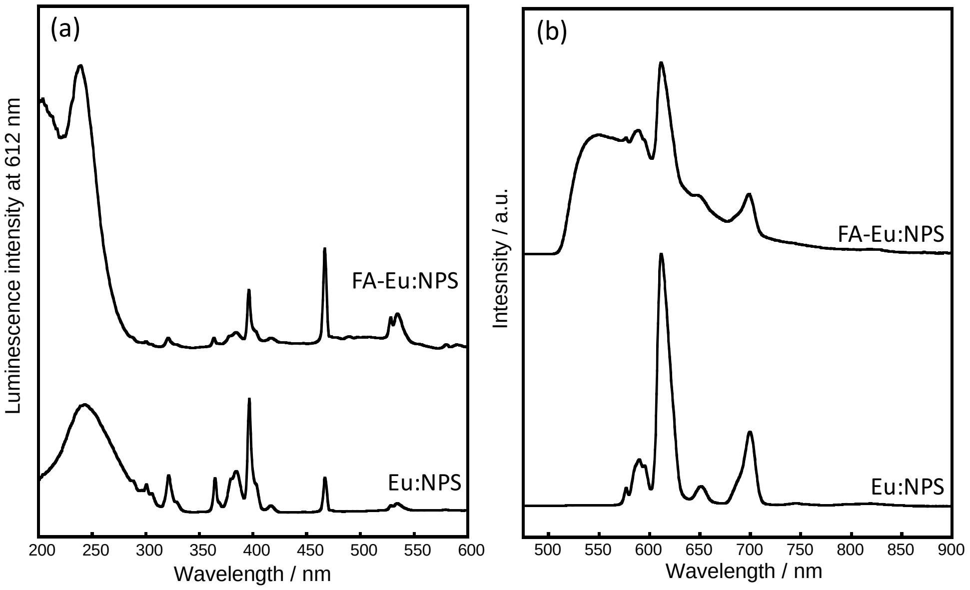

Fig. 2 (a) Excitation and (b) photoluminescence spectra of Eu:NPS and FA-Eu:NPS.

Figure 3 shows the cell viability of the fibroblasts cultured in the Eu:NPS, APTES-Eu:NPS, and FA-Eu:NPS dispersed in 10%FBS/DMEM at the additional culture time of 48 h. The cells remained attached to the plate and maintained their normal morphology as compared with the morphology in Fig. 1 (a). The cell viability in the APTES-Eu:NPS shows the lowest viability due to the influence of activated amino groups, and that of Eu:NPS also shows the lower viability due to the oxygen atom in silanol group. With increasing the FA immobilized amount, the cell viability significantly increased. This indicated that the amino group was deactivated with the FA immobilization and the FA molecules were functionalized on the surfaces to exhibit the good cytocompatibility, and FA**5**-Eu:NPS shows the highest viability.

Figure 4 (a) shows the luminescence intensity changes of the Hela cells targeted by the FA-Eu:NPS with the different FA immobilization amount. The luminescence intensity from the Hela cells gradually increase with the culture time, and was irrespective of the FA immobilization amount, suggesting that the Hela cells realize the FA ligand at the lower immobilization amount and uptake the FA-Eu:NPS for the initial 12 h. On the other hand, no luminescence was observed from the fibroblast cells.

Figure 4 (b–e) shows the optical and fluorescence microscope images of the fibroblast and Hela cells staining with DAPI and FA**5**-Eu:NPS at the additional culture time of 48 h. The optical and fluorescence microscope images show the blue luminescence from the cellular nuclei due to the DAPI staining. No binding and uptake by the fibroblasts in Fig. 4 (b, c) and the significant binding and uptake by the Hela cells in Fig. 4 (d, e) were clearly observed. The fluorescent image of the Hela cells indicates the presence of luminescent particles located around the nucleu. With an increase of the particle concentration, the number of red-emitting particles in the cells increased. Thus, the FA-Eu:NPS was found to be effectively taken up only by the Hela cells. Here, the particle size is important for the uptake efficiency; 100 nm particles were studied as compared to about 400 nm particles, and a smaller particle size may lead to enhanced nonspecific cellular uptake. For amorphous silica, toxicity tends to be inversely related to particle size, and a particle size below 100 nm has actually been found to induce cytotoxicity [27]. In this study, the particle size is 300 nm, which would affect the efficient uptake. The detailed nanopartile design and imaging techniques will be reported by our group soon.

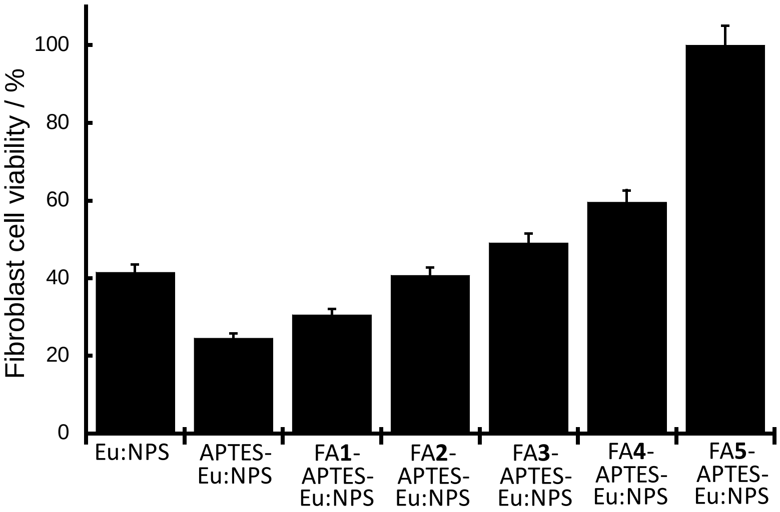

Fig. 3 Cell viability of the fibroblasts cultured in the 10%FBS/DMEM containing Eu:NPS, APTES-Eu:NPS, and FA-Eu:NPS at the additional culture time of 48 h.

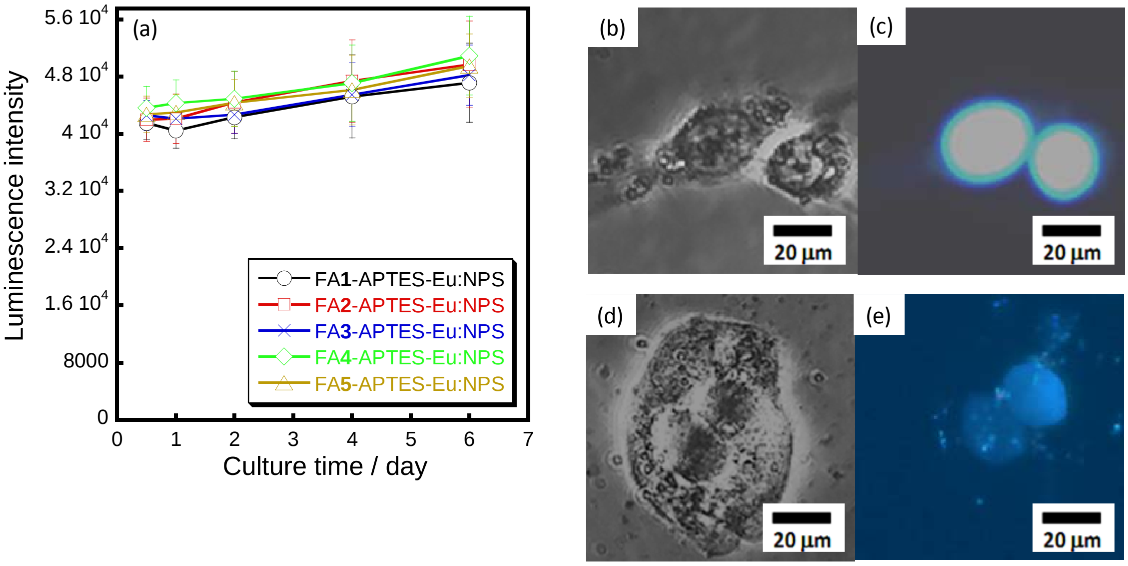

Fig. 4 (a) Luminescence intensity changes of the Hela cells targeted by the FA-Eu:NPS with the culture time, and (b, d) optical and (c, e) fluorescence microscope images of (b, c) fibroblast and (d, e) Hela cells staining with DAPI and FA**5**-Eu:NPS at the additional culture time of 48 h.

4. Conclusion

In conclusion, FA was successfully immobilized on the luminescent Eu:NPS spheres by mediation of the APTES adlayer. The ordered nanostructures were preserved by the immobilizations. The FA–APTES–Eu:NPS showed the characteristic luminescence due to the interactions between FA and Eu^{3+}, suggesting the importance of controlling the interactions among the FA molecules on the surfaces. The immobilized spheres were highly dispersed stably in the cell culture medium to bind specifically to cancer cells and exhibit the luminescence without cytotoxicity for fibroblasts. Thus, the FA was successfully immobilized on the luminescent Eu:NPS spheres to exhibit the highly targeting ability to the cancer cells.

Acknowledgment

This study was supported by a grant from the Japan Society for the Promotion of Science (JSPS).

References

[1] L. Brandon-Peppas and J. O. Blanchette, Adv. Drug Delivery Rev., **56** (2004) 1649.
[2] T. Yanagisawa, T. Shimizu, K. Kuroda and C. Kato, Bull. Chem. Soc. Jpn., **63** (1990) 988.
[3] C. T. Kresge, M. E. Leonowicz, W. J. Roth, J. C. Vartuli and J. S. Beck, Nature, **359** (1992) 710.
[4] K. B. Yoon, Chem. Rev., **93** (1993) 321.
[5] K. Moller and T. Bein, T. Chem. Mater., **10** (1998) 2950.
[6] M. Ogawa, Ann Rep (Sec C), **94** (1998) 209.
[7] A. Stein, B. J. Melde and R. C. Schroden, Adv. Mater., **12** (2000) 1403.
[8] B. J. Scott, G. Wirnsberger and G. D. Stucky, Chem. Mater., **13** (2001) 3140.
[9] H. Furukawa, T. Watanabe and K. Kuroda, Chem. Comm. (2001) 2002.
[10] M. Ogawa, J. Photochem. Photobiol., C Photochem. Rev. **3** (2002) 129.
[11] (a) M. Tagaya and M. Ogaawa, Chem. Lett., **35** (2006) 108; (b) M. Tagaya and M. Ogawa, Phys. Chem. Chem. Phys., **10** (2008) 6849.
[12] J. L. Vivero-Escoto, I. I. Slowing, C. W. Wu and V. S. Y. Lin, J. Am. Chem. Soc., **131** (2009) 3462.
[13] M. Okuda, M. Takeguchi, Y. Zhu, A. Hashimoto, N. Ogawa, M. Tagaya, S. Chen, N. Hanagata and T. Ikoma, Surf. Interf. Sci., **42** (2010) 1548.
[14] (a) M. Tagaya, T. Ikoma, T. Yoshioka, T. Motozuka, F. Minami and J. Tanaka, Mater. Lett., **65** (2011) 2287; (b) M. Tagaya, T. Ikoma, T. Yoshioka, S. Motozuka, Z. Xu, J. Colloid and Interf. Sci., **363** (2011) 456; (c) M. Tagaya, T. Ikoma, T. Yoshioka, Z. Xu and J. Tanaka, Chem. Commun., **47** (2011) 8430.
[15] J. M. Rosenholm, A. Meinander, E. Peuhu, R. Niemi, J. E. Eriksson, C. Sahlgren and M. Lindn, ACS Nano, **3** (2009) 197.
[16] (a) E. Ruiz-Hitzky, P. Aranda, M. Darder and M. Ogawa, Chem. Soc. Rev., **40** (2011) 801; (b) N. Nassif and J. Livage, Chem. Soc. Rev., **40** (2011) 849.
[17] V. Sokolova and M. Epple, Nanoscale, **3** (2011) 1957.
[18] Y. Zhu, T. Ikoma, N. Hanagata and S. Kaskel, Small, **6** (2010) 471.
[19] X. Kang, S. Huang, P. Yang, P. an Ma, D. Yanga and J. Lin, Dalton Trans., **40** (2011) 1873.
[20] J. F. Kukowska-Latallo, K. A. Candido, Z. Y. Cao, S. S. Nigavekar, I. J. Majoros, T. P. Thomas, L. P. Balogh, M. K. Khan and J. R. Baker, Cancer Res., **65** (2005) 5317.
[21] H. Tominaga, M. Ishiyama, F. Ohseto, K. Sasamoto, T. Hmamoto, K. Suzuki and M. Watanave, Anal. Commun., **36** (1999) 47.
[22] W. Chen, R. Sammynaiken and Y. Huang, J. Appl. Phys., **88** (2000) 1424.
[23] N. Wan, J. Xu, T. Lin, X. Zhang and L. Xu, Appl. Phys. Lett., **92** (2008) 201109.
[24] E. J. Nassar, K. J. Ciuffi, S. J. L. Ribeiro and Y. Messaddeq, Mat. Res., **6** (2003) 557.
[25] M. A. Zaitoun, T. Kim and C. T. Lin, J. Phys. Chem. B, **102** (1998) 1122.
[26] S-J. Seo, D. Zhao, K. Suh, J. H. Shin and B-S. Bae, J. Lumin., **128** (2008) 565.
[27] K. O. Yu, C. M. Grabinski, A. M. Schrand, R. C. Murdock, W. Wang, B. Gu, J. J. Schlager, S. M. Hussain, J. Nanopart. Res., **11** (2009) 15.

(Received: 26 April, 2012, Accepted: 31 May, 2012)

Transactions on GIGAKU **1**(2012)01015/1-6

Effect of Flow Channel on Specific Surface Area of Steam-Activated Carbon Material from Coffee Bean Wastes

Hiroe Toda[1], Ikumi Toda[1*], Hiroki Tanikawa[1], Tomokazu Takahata[1], Shigeo Ohshio[1], Hiroki Akasaka[1], Shuji Himeno[2], Toshinori Kokubu[3], Hidetoshi. Saitoh[1]
[1)]Department of Materials Science and Technology, Nagaoka University of Technology,
[2)]Department of Civil and Environmental Engineering, Nagaoka University of Technology
1603-1 Kamitomioka-cho, Nagaoka 940-2188, Japan
[3)]Department of Chemical Science and Engineering, Miyakonojo National College of Technology
473-1, Yoshio, Miyakonojo, Miyazaki 885-8567, Japan
**E-mail: ikumi_toda@mst.nagaokaut.ac.jp*

The effect of a flow channel on specific surface area of steam-activated carbons was investigated for activated carbons fabricated from coffee bean wastes. The specific surface areas of the activated carbons fabricated at steam-activation temperatures of 700, 775, and 825°C for 6 h were 98, 937, and 656 m^2/g, respectively. To examine relationship between specific surface area and other properties of activated carbons materials for crystalline and spongelike morphological structures, X-ray diffraction (XRD) analysis and cross sectional scanning electron microscopy (SEM) were performed for the activation at each temperature. The former analysis showed that the interlayer space d_{002} and crystallite size L_c of the graphite structure had no change with the activation temperature. The SEM images showed that the spongelike structure changed with the activation temperature. These results indicated that controlling the flow channel was important in the attributed spongelike structure for the fabrication of activated carbons with a high specific surface area.

1. Introduction

Recently, mass disposal of agricultural waste has become a seriously environmental problem. To solve this problem, technologies for recycling agricultural waste as a biomass resource have been studied [1]. One of the recycling technologies is to produce activated carbon from biomass wastes as reusable products. There have been many reports on the production of activated carbons that are used as absorbent materials for removing hazardous compounds [2-4], as a canister to control gasoline vapor [5], as electrodes in electric double-layer capacitors [6,7], and as hydrogen storage materials [8-10]. The utilization of biomass resources has a number of advantages, such as the production of functional materials at a low cost and the reduction of environmental impact.

Coffee bean waste is a biomass resource that is discarded in large quantities [11], Coffee is a promising raw material for the fabrication of activated carbon, because it contains plant tissues. It was reported that coffee bean waste formed a spongelike structure consisting of micrometer-size ordered voids during the roasting process [12]. The surface area of such structure was increased upon chemical activation, resulting in the production of activated carbon. Boonamnuayvitaya *et al.* reported the preparation of a mesoporous carbon material from coffee bean waste with a specific surface area of 914 m^2/g and a pore volume of 1.01 cm^3/g by zinc chloride ($ZnCl_2$) impregnation coupled with activation by carbon dioxide [13]. Activated carbons fabricated by chemical activation using hydrogen phosphate (H_3PO_4) were reported by Baquero *et al* [14]. These materials had a specific surface area of 1402 m^2/g and a pore volume of 1.25 cm^3/g.

When activated carbons are used as an adsorbent to small molecules such as hydrogen, a higher specific surface area is generally required [9]. The pores of activated carbons are classified by their diameter d as micro-pores ($d < 2$ nm), mesopores ($2 < d < 50$ nm), and macropores ($d > 50$ nm) [15]. The specific surface area changes with the development of these pores, which is related to changes in the resulting graphite structure on activated carbons. Takahata *et al.* [16] reported the relationship between specific surface area and the structure of graphite on activated carbon. They found that the specific surface area increased with decreasing graphite crystalline size L_c and increasing graphene sheet interlayer spacing d_{002} from the analysis of patterns of activated carbons. Additionally, Toda *et al.* [17] reported that the change in the specific surface area of activated carbon materials was dominated by their micro-pore structures. They calculated the micro-pore volume as a proportion of the total pore volume for activated carbons and found that the micro-pore volume was accounted for the majority of total pore volume. These reports suggested that the graphite structure is related to the development of the micro-pore structure. On the other hand, to utilize the micro-pores of activated carbons for gas adsorption, it was necessary that the micro-pores were exposed on the surface of the materials. David *et al.* proposed a pore structure model for activated carbons [18]. According to its pore structure model, the meso-pores and macro-pores in the activated carbons acted as flow channels for the adsorbent into the micro-pores. Thus, it was considered that the gas adsorption ability of activated carbons depended on the micro-pore volume. For the fabrication of activated carbons with high specific surface area from coffee bean waste, it is important to investigate the relationship between activation temperature and the graphite structure and flow channels on activated carbons. In the present work, activated carbons with flow channels were fabricated from waste coffee beans in steam activation. The relationship between the specific surface area, flow channels and the graphite crystallite structure of activated carbons was investigated.

2. Experiments

Activated carbons were fabricated by steam-activation. The coffee bean wastes were used as raw material, which drinking contents have been removed. Before the steam-activation process, the coffee bean waste was dried in an oven at 120°C for 24 h to remove moisture. Steam-activation was performed by a two-step process involving carbonization and activation. In the carbonization process, the coffee bean waste was placed into a SiC crucible, where it was heated at 200ºC for 2 h to remove moisture from coffee bean waste, then at 600ºC for 24 h with a heating rate of 5ºC/min, carbonization was carried out. After the carbonization, the carbon materials were placed in an SUS container whose bottom was composed of a mesh, which was placed in a steam superheater (Dai-Ichi High Frequency Co., Ltd.). The steam-activation process was performed at 700, 775, or 825ºC for 6 h with a 50 g/min flow of steam.

Specific surface area of the activated carbons was estimated by the analysis of N_2 adsorption isotherm profiles on the samples at 77 K. The isotherm profiles were obtained by a Micrometrics Gemini V2375 automatic surface area analyzer (Shimadzu Corp.). Before the N_2 adsorption measurements, absorbed gases were removed by heating at 200ºC for 1 h under vacuum pressure (10^{-1} Pa). After that, the balance pressure at each pressure was measured for the sample. Here, the relative pressure was defined as the ratio of the balance pressure to the pressure of the saturated vapor at 77 K. The specific surface area S_{BET} was calculated using the Brunauer-Emmett-Teller (BET) model [19]. The crystallite structures of the activated carbons were determined by the θ-2θ method using XRD. An MO3XHF MXP3 diffractometer (Mac Science) with a Cu Kα (1.54 Å) X-ray source, a current of 40 mA, and a voltage of 40 kV was used for the XRD analysis. The detector angle and scanning speed were 0.02 °/step and 2.00 °/min, respectively. XRD patterns were measured in the range of 2θ=4-80°. The interlayer spacing d_{002} and average crystallite size L_c of the activated carbons were calculated by Bragg's equation and Scherrer's equation using the obtained XRD patterns.

The flow channels in particles of the activated carbons were observed by scanning electron microscopy (SEM) (JSM-6700F, JEOL). To obtain smooth cross-section surfaces before SEM observations, polishing was performed by the following process. First, each activated carbon was embedded in epoxide resin (G2, Gatan). Second, to harden the epoxide resin, the sample with the epoxy was heated on a hot plate at 125ºC for 30 min. Finally, the cross section of the activated carbon was polished by an ion beam using a cross-section polisher (SM-09010, JEOL). SEM observation was performed in the secondary image (SEI) mode at an accelerating voltage of 3 kV and an irradiation current of 8 μA.

3. Results and Discussion

The specific surface area of the activated carbons increased from 98 to 937 m^2/g upon increasing the activation temperature from 700 to 775°C. However, when the temperature was increased from 775 to 825°C, the specific surface area decreased from 937 to 656 m^2/g. From these results, it was confirmed that the specific surface area of the activated carbons was changed with the activation temperature. The change in the specific surface area suggested that the activation temperature changed the graphite crystallite structure and flow channels of the activated carbons. The change in the morphological structure of the activated carbons produced at the activation temperature was evaluated from the XRD patterns. Figure 1 shows the XRD patterns of the activated carbons. The broad peak at $2\theta = 24°$ corresponded to the (002) plane of hexagonal graphite assigned by ICDD card No. 00-056-0159. The broader peak at 44° can be assigned to the (100) or (101) plane. This peak was assigned to the (10) plane [20], because neither of the above planes could be clearly discriminated. Since the peaks in the diffraction patterns were broad, the graphite clusters in the porous carbon were small and the order of the graphene layers was short. To understand the change in the graphite crystallite structure, the average interlayer spacing d_{002} and average crystallite size L_c was calculated from the diffraction patterns, where d_{002} for graphite was calculated using Bragg's equation with a peak at 24°. The value of d_{002} for the activated carbons slightly decreased from 0.377 to 0.373 nm with increasing the activation temperature from 700 to 825°C, as shown in Fig. 2. The average crystallite diameter L_c in the 002 direction was calculated using Scherrer's equation. The crystallite size L_c was reduced from 1.26 to 1.16 with an increase of the activation temperature from 700 to 825°C. These decreases in d_{002} and L_c were very small in compared with the change in specific surface area. These results indicated that the graphite crystallite structure of activated carbon was not affected by the activation temperature. Furthermore, the results suggested that the specific surface area was not affected by the graphite crystallite structure on steam activated carbons made from waste coffee beans.

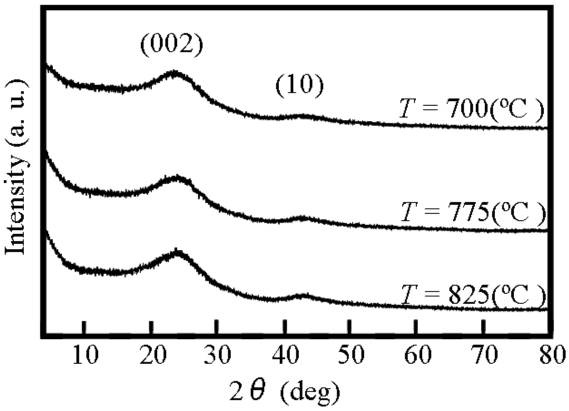

Fig. 1 XRD patterns of activated carbons prepared from coffee bean wastes.

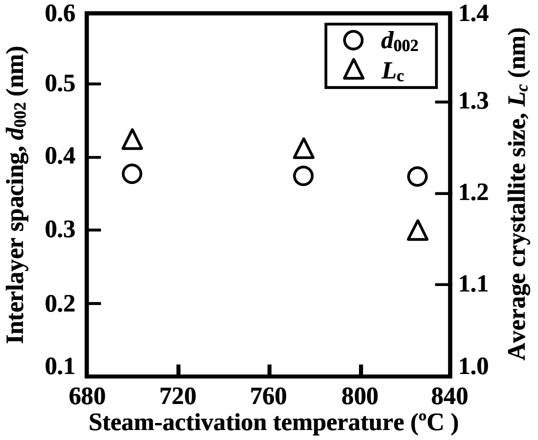

Fig. 2 Relationships between interlayer spacing or average crystallite size and activation temperature on activated carbons.

Figures 3 and 4 show cross-sectional SEM images of the activated carbon particles. The comparatively dark areas in the SEM images corresponded to epoxy resin, and the brighter areas were to the activated carbons having particle forms with about 100 μm. From the SEM images, we confirmed that the activated carbons have a spongelike structure consisting of cells (arrow A in Figs. 3(a), 3(b), and 3(c)) and partition walls (arrow B in Figs. 3(a), 3(b), and 3(c)). Furthermore, pores having about 40 nm also developed inside the partition walls of the spongelike structure as shown in Figs. 4(a) 4(b), and 4(c). The spongelike strucuture appeared to change with increasing activation temperature. Consequently, to evaluate the change in the spongelike structure caused by the increase in activation temperature, the partition wall thickness D_T and the average diameter of pores inside the partition walls D_p were measured from the SEM images. Figure 5 shows the relationship of between D_T or D_p and steam-activation temperature on activated carbons. The values of D_T decreased from 4.8 to 2.2 μm with increasing the activation temperature from 700 to 775°C and then increased slightly to 2.4 μm at 825°C. For D_p the values decreased from 19.2 to 15.3 nm with increasing steam-activation temperature from 700 to 775°C and then drastically increased to 59.2 nm at 825°C. The diameter of the pores inside the partition walls decreased with increasing the steam-activation temperature. These results suggested that the increase of the specific surface area from 700 to 775°C was related to the thickness of the partition walls. In addition, they suggest that the decrease in the specific surface area from 775 to 825°C was related to the increased diameter of pores inside the partition walls.

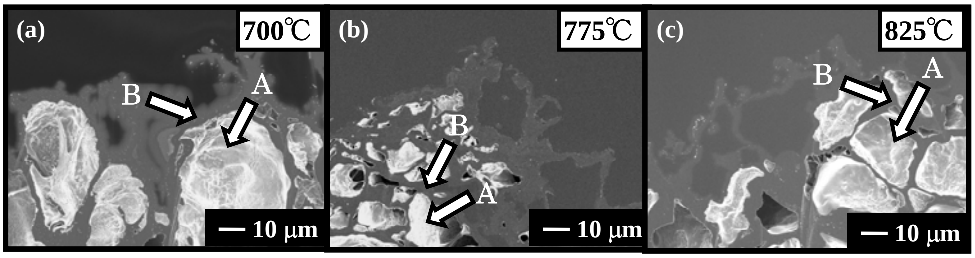

Fig. 3 Cross-sectional SEM images of spongelike structure in activated carbons after steam activation

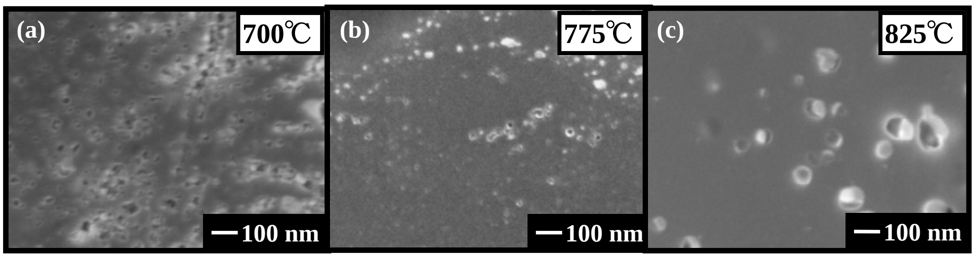

Fig. 4 Cross-sectional SEM images of partition walls of the spongelike structure in activated carbons after steam activation

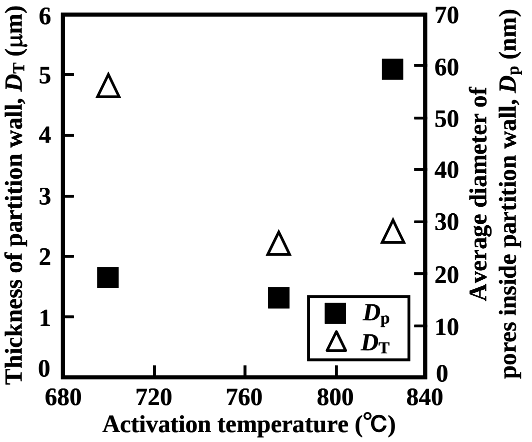

Fig. 5 Relationships between thickness of partition wall or average diameter of pores inside partition wall and activation temperature on activated carbons.

The differences in the specific surface area of the activated carbons prepared from coffee waste seemed to be related to the formation of flow channels led to the exposure of micro-pores. To obtain activated carbons with a high specific surface area, the development of flow channels might be necessary to allow gases to reach the micro-pores. The analysis of the crystalline structure indicated that the specific surface area was changed with increasing activation temperature, whereas no graphite crystallite structures was changed as shown in Fig. 2. This suggested that the formation of flow channels affected the specific surface area of activated carbons. As shown in Fig. 5, D_T decreased and specific surface area increased between 700 and 775ºC. This suggested that the exposure of micro-pores was caused by gasification of the walls of cells. Consequently, it was considered that the specific surface area was increased because the cell-like macro-pores were functionalized by the flow channels. On the other hand, between 775 and 825ºC, few changed in the partition wall thickness was observed with the steam-activation temperature, and the specific surface area decreased with increasing D_p. These changes showed that the micro-pore structure was destroyed by linkaging pores. As a result, the specific surface area decreased with the growth of flow channels inside the partition walls at 825ºC.

4. Conclusion

Activated carbons were fabricated from coffee bean waste through steam activation process at different steam-activated temperatures. To investigate the relationship between steam-activation temperatures and the properties of the activated carbons, the spongelike and graphite crystallite structure were measured. Between 700 and 775ºC, the specific surface area increased owing to the formation of flow channels, which was attributed to the increased thickness of the partition walls. In contrast, the specific surface area decreased above 775ºC owing to the decreased average diameter of pores inside the partition walls. These results indicated that the formation of flow channels mainly determined the specific surface area and that the flow channels in the activated carbons could fabricate the spongelike sturucture depending on the steam-activation temperature.

References

[1] A. Bota, K. Laszlo, L. G. Nagy, G. Subklew, H. Schlimper, and M. J. Schwuger, Adsorption, **3** (1997) 81.

[2] S. Nagano, H. Tamon, T. Adzumi, K. Nakagawa, and T. Suzuki, Carbon, **38** (2000) 915.

[3] S. Karagoz, T. Tay, S. Ucar, and M. Erdem, Bioresour. Technol., **99** (2008) 6214.

[4] E. Ekinci, T. Budinova, F. Yardim, N. Petrov, M. Razvigorova, and V. Minkova, Fuel Process. Technol., **77-78** (2002) 437.

[5] U. Mohr, Filtr. Sep., **34** (1997) 1016.

[6] M. Toyoda, Y. Tani, and Y. Soneda, Carbon, **42** (2004) 2833.

[7] K. Kinoshita, “Carbon: Electrochemical and Physicochemical Properties,” Wiley-Interscience, New York (1988) 294.

[8] R. Strobel, L. Jorissen, T. Schliermann, V. Trapp, W. Schutz, K. Bohmhammel, G. Wolf, and J. Garche, J. Power Sources, **84** (1999) 221.

[9] B. Panella, M. Hirsher, and S. Roth, Carbon, 43 (2005) 2209.

[10] A. Anson, J. Jagiello, J. B. Parra, M. L. Sanjun, A. M. Benito, W. K. Maser, and M. T. Martinez, J. Phys. Chem. B, **108** (2004) 15820.

[11] V. Boonamnuayvitaya, C. Chaiya, W. Tanthapanichakoon, and S. Jarudilokkul, Sep. Purif. Technol., **35** (2004) 11.

[12] T. Nakabayashi, and K. Suzuki, J. Food Sci. Tech., **33** (1986) 779.

[13] V. Boonamnuayvitaya, S. Sae-ung, and W. Tanthapanichakoon, Sep. Purif. Technol., **42** (2005)159.

[14] M. C. Baquero, L. Giraldo, J. C. Moreno, F. Suarez-Garcia, A. Martinez-Alonso, and J. M. D. Tascon, J. Anal. Appl. Pyrol., **70** (2003) 779.

[15] IUPAC, Manual of Symbols and Terminology (1972).

[16] T. Takahata, I. Toda, H. Ono, S. Ohshio, H. Akasaka, S. Himeno, T. Kokubu, and H. Saitoh,

Jpn. J. Appl. Phys. **48** (2008) 117001-1.
[17] I. Toda, H. Ono, T. Takahata, S. Ohshio, H. Akasaka, S. Himeno, T. Kokubu, and H. Saitoh, J. Sol. Mech. Mater. Eng., **3** (2009) 1306.
[18] E. David, J. Mater. Proc. Tech., **162-163** (2005) 169.
[19] S. Brunauer, P. H. Emmett, and E. Teller, J. Am. Chem. Soc., **60** (1938) 309.
[20] B. E. Warren, J. Chem. Phys., **2** (1934) 551.

(Received: 23 March, 2012, Accepted: 30 June, 2012)

Transactions on GIGAKU **1***(2012)01016/1-4*

Hydrogen Storage Property of Activated Carbon Fabricated with Lignin

Ikumi Toda[1]*, Hiroe Toda[1], Shigeo Ohshio[1], Hiroki Akasaka[1], Shuji Himeno[1],
Manami Nakaishi[2], Hidetoshi Saitoh[1]
[1]Nagaoka University of Technology, 1603-1, Kamitomioka, Nagaoka, Niigata 940-2188, Japan,
[2]Harima Chemicals, 671-4, Noguchichomizuashi, Kakogawa, Hyogo 675-4, Japan
**E-mail: ikumi_toda@mst.nagaokaut.ac.jp*

The micro-pore structure and hydrogen storage property at 298 and 77K of activated carbons fabricated with lignin through KOH activation were investigated. The specific surface area of activated carbons decreased 2290 to 1140 m^2/g as the carbonization temperature increased from 400 to 800°C in the carbonization process. The micro-pore volume of activated carbons also decreased from 1.49 to 0.48 cm^3/g as the carbonization temperature increased. The pore size of activated carbons was distributed around 0.8 and 1.1 nm in the micro-pore range. These results suggest that the micro-pore structure of activated carbons is affected by carbonization temperature in the carbonization process on KOH activation. The stored hydrogen content of activated carbons at 298K was 0.59wt% under 8.9 MPa. At 77K, the stored hydrogen content of activated carbons was 6.9wt% under 8.7 MPa. The fabrication of hydrogen storage materials from lignin was achieved. The results suggest that activated carbons fabricated from lignin have micro-pore structures which influence the stored hydrogen content.

1. Introduction

Environmental destruction has increased the urgency to develop technologies for the recycling of various materials. The disposal of biomass waste from agricultural activities is an environmental problem. One of the solutions to this problem is to produce functional and reusable materials from biomass resources. Activated carbons fabricated from biomass resource have been studied for use as functional materials. In particular, some activated carbons with nano-meter size pores, i.e., micropores, offer high performance because of their high specific surface areas. These activated carbon materials are prepared from various raw materials such as coal [1], palm shell [2], coffee waste [3], and rice husks [4]. Such activated carbon materials are widely used because of their high adsorption properties [5]. These approaches have been applied to hydrogen storage materials [6] and adsorbent materials for gases [7,8].

From recent reports, it is apparent that various carbon materials made from carbon nanotubes [9], graphite nanofibers [10], and activated carbons are capable of storing hydrogen and have been considered for the next generation of energy systems. For example, porous carbons with a specific surface area of 3220 m^2/g is capable of storing hydrogen of 1.3wt.% at room temperature [11]. The reports suggest the influence of specific surface area on the hydrogen storage efficiency of the micro-pores. In activated carbons fabricated from biomass recourses, it was reported that activated carbons with micro-pores in the pore structure were fabricated from lignin [12]. Lignin is product as of a residual material in the manufacture process of cellulose pulps. Some researchers have used potassium hydroxide (KOH) for the activation [13,14]. The micro-pore structure found in activated carbons fabricated with lignin following KOH activation is expected to be utilized as hydrogen storage materials.

In this study, activated carbons were fabricated through the KOH activation method and their micro-pore structure and hydrogen storage property were investigated.

2. Experiment

The samples of activated carbons were fabricated by the alkali activation method with KOH as an activation agent. Lignin of raw materials was dried at 100°C for 24 h. The sample preparation was performed by two processes of carbonization and activation. In the carbonization process, lignin was firstly carbonized at 400, 550, and 800°C for 3 h. The carbonized sample and KOH were mixed with a ratio of 5: 1 by weight. Then, the carbonized sample was treated by a heating process at 850℃ for 2 h.

The pore characteristics, specific surface area, pore size distribution, and pore volume were estimated by analyses of N_2 adsorption isotherm profiles at 77K for activated carbons. Isotherm profiles were obtained using Belsorp-max (BEL JAPAN Co.). Before N_2 adsorption measurements, absorbed gases were baked out at 200°C, for 10 h under vacuum pressure. The specific surface area (S_{BET}) and total pore volume (V_{total}) were calculated on the basis of the Brunauer-Emmett-Teller (BET) model [15]. The micro-pore size distribution and micro-pore volume (V_{micro}) were analyzed by the micro-pore (MP) –method [16].

The stored hydrogen content in activated carbons was measured using a volumetric analysis defined by the JIS H7201 "Method of determining the PCT relation of hydrogen absorbing alloys". Prior to the analysis, powder samples with a desired weight (0.2 g) were inserted into a pressure vessel. In the pressure vessel, the sample was degassed under 10^{-2} torr at 423K for 1 h and was maintained at 77 and 298K using a cryostat in the hydrogen pressure range of 0-12 MPa.

3. Results and Discussion

Figure 1 shows N_2 isotherms of carbonized samples fabricated with lignin. The N_2 adsorption isotherms of all carbonized samples are attributed to the type-III [17], indicating that the carbonized samples are non-porous materials. Figure 2 shows N_2 isotherms of activated carbons fabricated with lignin. The N_2 adsorption volumes of all activated carbons were increased considerably at $P/P_0 < 0.1$. At P/P_0=0.99, the N_2 adsorption volumes of the activated carbon decreased from 1277 to 396 cm^3/g as the carbonization temperature increased from 400 to 800°C. The adsorption isotherms of all activated carbons indicated the type-I [17], indicating that the activated carbons fabricated with lignin has micro-pore structure. Therefore, these results suggest that the development of pore structure in activated carbons fabricated from lignin was affected by carbonization temperature in the carbonization process.

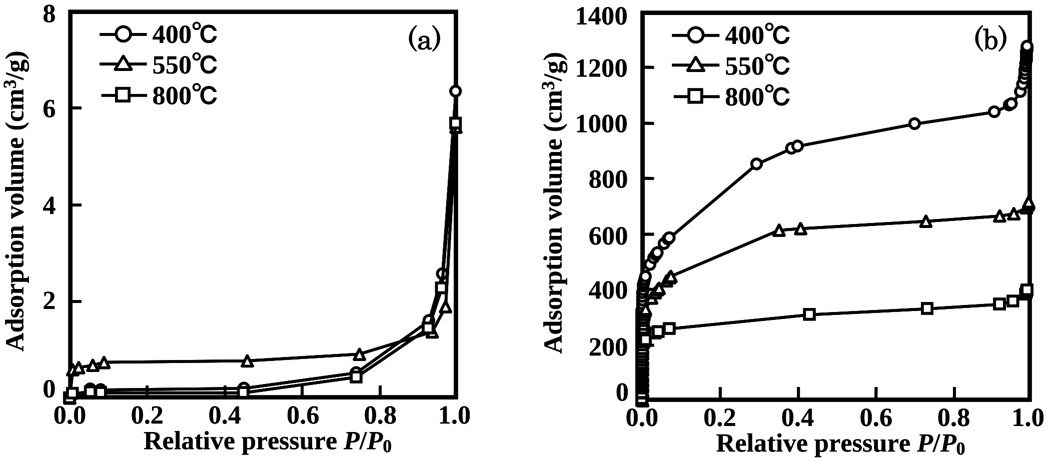

Fig. 1 Nitrogen adsorption isotherms of (a) carbonized samples and (b) activated carbons.

Table 1 shows the pore-characteristics of the carbonized samples and activated carbons. The S_{BET} of carbonized samples fabricated at 400, 550, and 800°C were 0.1, 3.0, and 0.4 m^2/g, respectively. The S_{BET} of activated carbons decreased from 2290 to 1140 m^2/g as the carbonization temperature increased from 400 to 800°C. The V_{total} of carbonized samples fabricated at 400, 550, and 800°C were 8.9×10^{-3}, 7.3×10^{-3}, and 7.8×10^{-3} cm^3/g, respectively. The V_{total} of activated carbons decreased from 1.97 to 0.61 cm^3/g as the carbonization temperature increased from 400 to 800^{o}C.

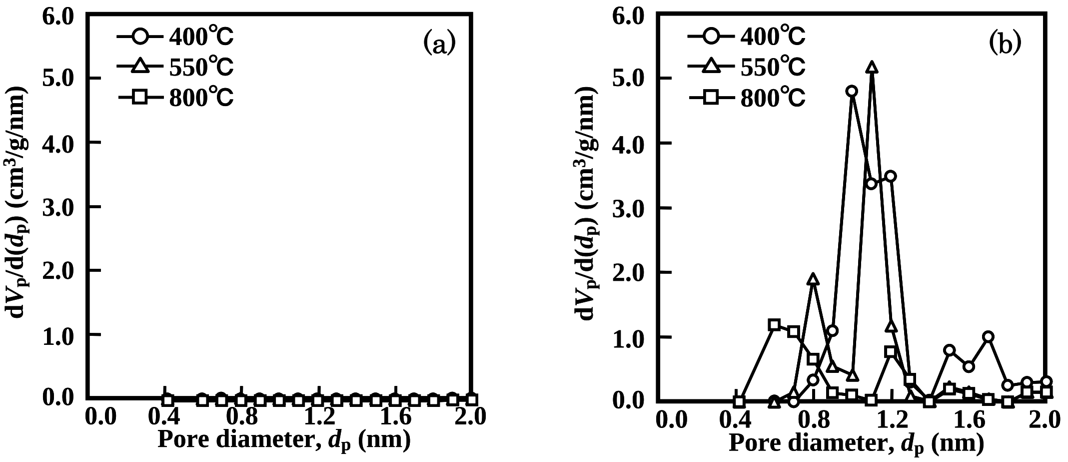

Fig. 2 Pore size distributions of carbonized samples (a) and activated carbon (b) in range of micro-pore.

Table 1 Pore-characteristics of carbonized samples and activated carbons

Temperature (℃)	Carbonized sample		Activated carbon		
	S_{BET} (m^2/g)	V_{total} (cm^3/g)	S_{BET} (m^2/g)	V_{total} (cm^3/g)	V_{micro} (cm^3/g)
400	0.1	8.9×10^{-3}	2290	1.97	1.49
550	3.0	7.3×10^{-3}	1740	1.10	0.99
800	0.4	7.8×10^{-3}	1140	0.61	0.48

Figure 2 shows the pore size distribution of carbonized samples and activated carbons in the range of micro-pore. The micro-pore volume of activated carbons decreased from 1.49 to 0.48 cm^3/g as the carbonization temperature increased from 400 to 800^{o}C. The existence of micro-pores was not seen in the carbonized samples. On the other hands, it is observed on the sample of activated carbons fabricated with the carbonized sample. The typical pore size was recognized at approximately 0.8 nm to 1.1 nm, indicating that the micro-pore structure of activated carbons was developed by KOH activation. Therefore, these results indicate that the micro-pore structure in activated carbons fabricated from lignin was affected by carbonization temperature in the carbonization process.

Figure 3 shows the hydrogen storage property of activated carbons which were fabricated from the samples carbonized at 400^{o}C. At 298K, the stored hydrogen content of the activated carbons increased as the equilibrium pressure of hydrogen increased. The stored hydrogen content of the activated carbon at 298K was 0.59wt% at 8.9 MPa. At 77K, the stored hydrogen content of the activated carbon was increased considerably as the equilibrium pressure of hydrogen increased. The stored hydrogen content of the activated carbon at 77K was 6.9wt% at 8.7 MPa. The hysteresis of stored contents was observed at 298 and 77K. These hystereses at 298 and 77K indicate that a chemical sorption also slightly occurred by effect of KOH activation. There results suggest that the micro-pore of activated carbons may effectively act as the hydrogen adsorption site at 77K.

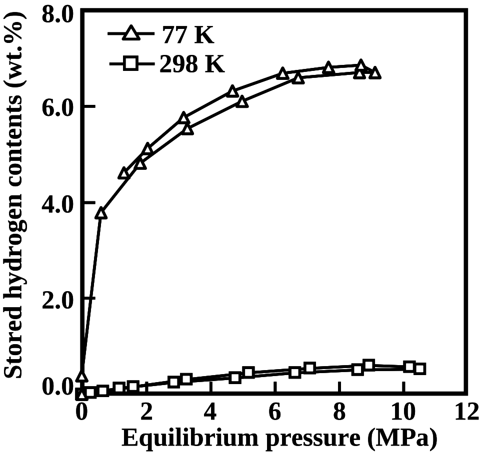

Fig. 3 Hydrogen storage properties at 298 and 77K of activated carbons with a specific surface area of 2290 m^2/g.

4. Conclusion

Activated carbons were fabricated from lignin by KOH activation. The micro-pore structure and hydrogen storage property of activated carbons were investigated. The pore size of activated carbons distributed at approximately 0.8 nm to 1.1 nm. The specific surface are and micro-pore volume of activated carbons decreased as the carbonization temperature increased. The specific surface area and micro-pore volume at carbonized temperature 400^{o}C reached 2290 m^2/g and 1.49 cm^3/g, respectively. The maximum stored hydrogen contents at the specific surface area of 2290 m^2/g were 0.59 wt% at 298K and 6.9wt% at 77K.

References

[1] J. Hayashi, T. Horikawa, K. Muroyama and V.G. Gomes, Microporous and Mesoporous Mater., **55** (2002) , 63.

[2] I. A.W. Tan, A. L. Ahmad and B. H. Hameed, Bioresour. Tech., **100** (2009) 1494.

[3] J. V. Nabais, P. Carrott, M. M. L. R. Carrott, V. Luz and A. L. Ortiz, Bioresour. Tech., **99** (2008) 7224.

[4] N. Yalcin and V. Sevinc, Carbon, **38** (2000) 1943.

[5] A. Amaya, N. Medero, N. Tancredi, H. Silva and C. Deiana, Bioresour. Tech., **98** (2007) 1635.

[6] M. Conte, P. P. Prosini and S. Passerini, Mater. Sci. Eng., **B108** (2004) 2.

[7] E. Diaz, S. Ordonez, A. Vega and J. Coca, Microporous and Mesoporous Mater., **82** (2005) 173.

[8] T. Qiang, Z. Zhigang, Z. Wenpei and C. Zidong, Fuel, **84** (2005) 461.

[9] H. Takagi, H. Hatori, Y. Yamada, S. Matsuo and M. Shiraishi, J. Alloys Comp., **385** (2004) 257.

[10] E. David, J. Mater. Proc. Tech., **162-163** (2005) 169.

[11] Y. Kojima, Y. Kawai, A. Koiwai, N. Suzuki, T. Haga, T. Hioki and K. Tange: J. Alloys and Comp., **421** (2006) 204.

[12] J. Hayashi, A. Kazehaya, K. Muroyama, A.P. Watkinson, Carbon **38** (2000) 1873.

[13] Y. Zou, B-X. Han, Adsorp. Sci. Technol., **19** (2001) 59.

[14] L. Khezami, A. Chetouani, B. Taouk, R. Capart, Powder Technol. **157** (2005) 48.

[15] S. Brunauer, P. H. Emmett, E. Teller, J. Amer. Chem. Soc, **60** (1938) 309.

[16] R. S. Mikhail, S. Brunauer, E. E. Bodor, J. Colloid and Interface Sci., **26** (1968) 45.

[17] S. Brunauer, L.S. Deming, W.E. Deming, E. Teller, J. Amer. Chem. Soc., **62** (1940) 1723.

(Received: 23 March, 2012, Accepted: 30 June, 2012)

Transactions on GIGAKU ***1****(2012)01017/1-6*

Recent Progress in Laser Patterning of Crystals in Glasses

Takayuki Komatsu*, Futoshi Suzuki, Kazuki Ogawa, Tsuyoshi Honma
Department of Materials Science and Technology, Nagaoka University of Technology,
1603-1 Kamitomioka-cho, Nagaoka 940-2188, Japan
**E-mail: komatsu@mst.nagaokaut.ac.jp*

This paper reviews shortly the laser patterning of crystals in oxide glasses, in particular, two-dimensional planar crystals of nonlinear optical β-BaB_2O_4 and ferroelastic β’-$Gd_2(MoO_4)_3$. By scanning Yb:YVO_4 fiber lasers (wavelength: 1080 nm) continuously with a small step (e.g., 0.5 μm) between laser irradiated areas, planar β-BaB_2O_4 and β’-$Gd_2(MoO_4)_3$ crystals are patterned successfully on the glass surface, and a preferential growth orientation is confirmed from linearly polarized micro-Raman scattering spectrum and second harmonic intensity measurements. It is found that the crystal growth direction is perpendicular to the laser scanning direction. This relation, i.e., the perpendicular relation, is different from the behavior in discrete crystal line patterning, where the crystal growth direction is consistent with the laser scanning direction. The laser-induced crystallization has a potential for the patterning of epitaxial crystals on the glass surface.

1. Introduction

Glass is important and key materials in advanced technologies. But, of course, it is impossible to take out all kinds of functional properties in glass itself as similar to other kinds of materials. In particular, as glass has random structure with inversion symmetry in atomic arrangements, in principle, active properties arising from anisotropic atomic arrangements such as second-order optical nonlinearity and ferroelectricity are not expected in glass. If such active functional properties are added to glasses, new glass-related materials with various functions would be possible for practical applications. One of the effective methods for fabrication of such active glasses is to develop new functional glass-crystal hybrid materials, i.e., functional glass-ceramics or crystallized glasses. Crystallization of glass proceeds through two steps of nucleation process and crystal growth process, and usually glass-ceramics containing active crystals are fabricated by heat treatment in an electric furnace.

Recently, laser-induced crystallization in glass has received much attention, because in which active crystals are patterned only in spatially selected part. So far, dots and lines consisting of crystals have been patterned in glasses by laser irradiations, i.e., zero-dimensional dot and one-dimensional line patterning [1-11]. From a viewpoint of practical device applications for laser-patterned crystals, it is of interest and importance to pattern two-dimensional planar crystals [12-14]. In this review, we report mainly the patterning of two-dimensional planar crystals of β-BaB_2O_4 (β-BBO) and β’-$Gd_2(MoO_4)_3$ on the glass surface.

2. Experiment

Two glasses with the compositions of $8Sm_2O_3$-$42BaO$-$50B_2O_3$ (mol%) for the pattering of β-BBO and $3Sm_2O_3$-$18.25Gd_2O_3$-$63.75MoO_3$-$15B_2O_3$ (mol%) for the patterning of β’-$Gd_2(MoO_4)_3$ were prepared using a conventional melt quenching technique. Glass transition, T_g, and crystallization peak, T_p, temperatures were determined using differential thermal analysis (DTA) at a heating rate of 10 K/min. The quenched glasses were annealed at T_g for 30 min to release internal stresses. Glasses were mechanically polished to a mirror finish with CeO_2 powders. The glass surface was irradiated by continuous wave (cw) Yb:YVO_4 fiber laser with a wavelength of λ=1080 nm using objective lens (magnification: 50 times, numerical aperture: NA=0.8). The plate-shaped glasses were put on the stage and mechanically moved during laser irradiations to construct two-dimensional planar crystals. Laser-irradiated parts were observed with a polarization optical microscope (POM) and a confocal scanning laser microscope (CSLM) (Olympus-OLS 3000). The crystalline phase in the laser-irradiated part was examined from micro-Raman scattering spectrum measurements (Tokyo Instruments Co., Nanofinder; Ar^+ laser with λ= 488 nm). Second harmonic generations (SHGs) were measured with a Maker fringe technique, in which a Q-switched Nd:YAG (yttrium aluminum garnet) laser with λ=1064 nm was used as the incident light and second harmonic (SH) light (λ=532 nm) was detected.

For the laser pattering, the rare-earth atom heat (REAH) processing has been used, in which lasers such as cw Yb:YVO_4 fiber laser are irradiated onto glasses with some amounts of Sm^{3+}. Irradiated lasers are absorbed by Sm^{3+} ions in glass through *f-f* transitions, and absorbed energies are transferred to thermal energies through non-radiative relaxation process (electron-phonon couplings). And thus surroundings of RE ions are heated locally, consequently inducing effectively structural modifications such as crystallization in glass [5]. In Fig. 1, the schematic model for the laser-induced local heating mechanism in Sm^{3+} ion containing glasses is shown. The equipment for the laser-induced crystallization constructed in our study is shown in Fig. 2.

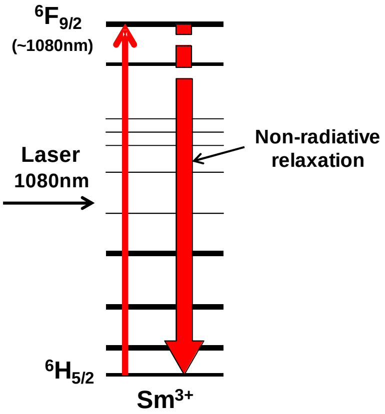

Fig. 1 Non-radiative relaxation process in the *f-f* transition in Sm^{3+} ion.

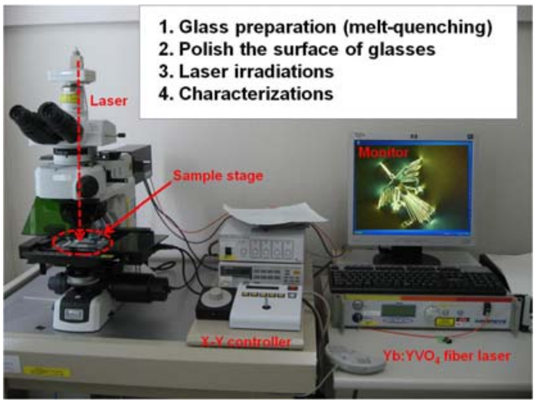

Fig. 2 Equipment for the patterning of crystals in glass constructed in our lab.

3. Results and Discussion

(1) Patterning of β-BaB_2O_4

The values of the glass transition and the crystallization peak temperatures for $8Sm_2O_3$-$42BaO$-$50B_2O_3$ glass prepared were determined to be T_g=566°C and T_p=681°C, respectively. It was determined from an optical absorption spectrum that the optical absorption coefficient (α: at room temperature) at λ=1080 nm for the glass is α=10.1 cm^{-1}. The crystalline phase formed by heat treatments in an electric furnace was identified to be only the β-BaB_2O_4 crystalline phase (ICDD# 85-0914) [3,14-16]. In the previous paper [3], discrete lines consisting of highly oriented (single-like) β-BBO crystals have been patterned on the glass surface of $10Sm_2O_3$-$40BaO$-$50B_2O_3$ and $10Dy_2O_3$-$45BaO$-$55B_2O_3$ by irradiations of cw Nd:YAG laser with λ=1064 nm. Because phenomena taking place in the laser-irradiated region in glass depend on laser irradiation conditions (laser type, power, scanning speed) and properties of a given glass, it would be necessary to confirm the quality of β-BBO crystal lines patterned by cw Yb:YVO_4 fiber laser (λ=1080 nm) in the present glass. The CSLM photograph for the discrete line patterned by cw Yb:YVO_4 fiber laser irradiations with a laser power of P=0.80 W and a laser scanning speed S=4 μm/s is shown in Fig. 3. The bump with a height of 0.4 μm and a width of 5 μm is observed in the laser-irradiated part. The azimuthal dependence of SHG signals for the discrete line is shown in Fig. 4, in which the measurements were carried out in the configuration of H-H. The notation of H-H means that the linearly polarized electric field of the incident laser is parallel to the electric field of SH waves in the measurements. Furthermore, the rotation angles of 0^o and 180^o correspond to the configuration that the polarized electric field of the incident laser is parallel to the line growth direction. The maximum SH intensities are observed at the rotation angles of ~0^o and ~180^o, the minimum intensities are located at ~90^o and 270^o. These profiles indicate the high orientation of β-BBO crystals in the discrete line patterned by cw Yb:YVO$_4$ fiber laser irradiations. It was also confirmed from the linearly polarized micro-Raman scattering spectra that the growth direction of β-BBO crystals along laser scanning direction is the *c*-axis [14].

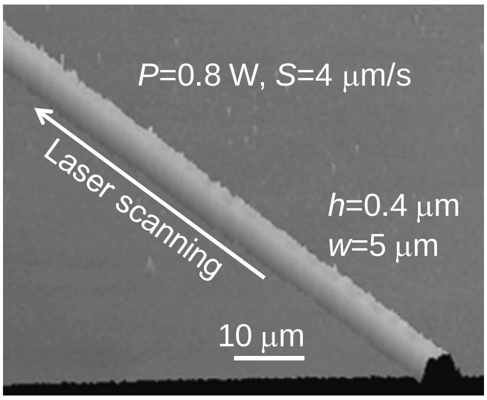

Fig. 3 CSLM photograph for the sample obtained by laser irradiations. The laser power and scanning speed were *P*=0.8 W and *S*=4 μm/s, respectively.

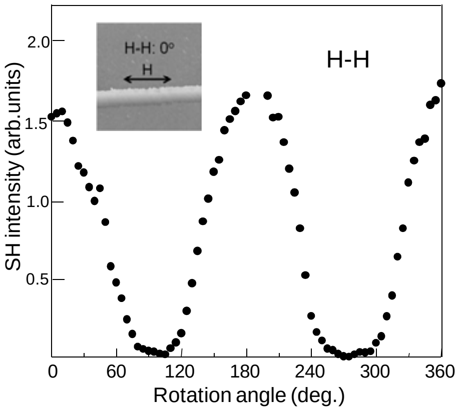

Fig. 4 Azimuthal dependence of SH intensities for the discrete line patterned by laser iradiations (Fig. 3).

The idea for the patterning of planar β-BBO crystals by laser irradiations is to irradiate lasers with small steps between laser irradiated areas [12-14]. That is, a forthcoming (next) laser irradiation is overlapped to the former (before) laser-irradiated part. The laser scanning was repeated with a step of 0.5 μm between the lines using the condition of *P*=0.8 W and *S*=8 μm/s, and the CSLM photograph for the sample obtained is shown in Fig. 5. It is found that the surface of the overlapped laser-irradiated part is smooth, suggesting the well overlapping of laser-irradiated parts.

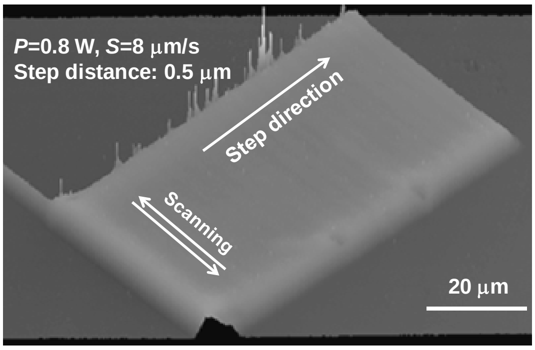

Fig. 5 CSLM photographs for the sample obtained by laser irradiations. The laser scanning direction and step direction are shown in the figure.

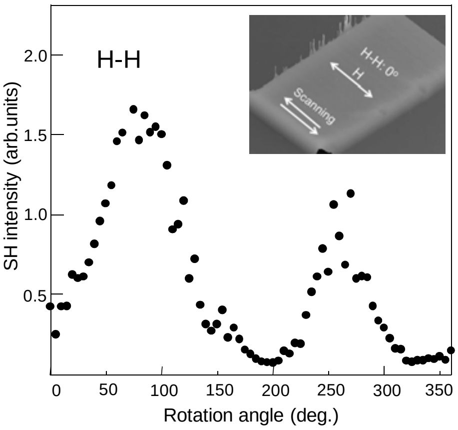

Fig. 6 Azimuthal dependence of SH intensities for the two-dimensional planar β-BBO crystals obtained by laser irradiations (Fig. 5).

The azimuthal dependence of SHG signals for the overlapped laser-irradiated part was measured, and the result is shown in Fig. 6. The measurements were carried out in the configuration of H-H as similar to the case of the discrete line shown in Fig. 3. The maximum SH intensities are observed at the rotation angles of ~90° and ~270°, and the minimum intensities are located at 0° and ~180°. These results are largely different from those observed for the discrete line shown in Fig. 4. Furthermore, the appearance of the two-fold angular dependence shown in Fig. 6 demonstrates that β-BBO crystals in the overlapped laser-irradiated part with a step of 0.5 μm are highly oriented [14].

The linearly polarized micro-Raman scattering spectra at room temperature for the two-dimensional planar β-BBO crystals were measured. The results suggest that β-BBO crystals in the overlapped laser-irradiated part are highly oriented and the *c*-axis direction of β-BBO crystals is perpendicular to the laser scanning direction or parallel to the laser step direction. In order to examine the orientation of β-BBO crystals in the overlapped laser-irradiated part more in detail, two-dimensional micro-Raman scattering spectra (imaging) were measured at room temperature. The results are shown in Fig. 7. In this experiment, the intensity of the peak at 637 cm^{-1} is focused, and the white color means the strong intensity of the Raman peak at 637 cm^{-1}. It is seen that the intensity of the white color is small in the initial laser-irradiated part (discrete line) and also in the overlapped (repeated) laser-irradiated part of about 10 μm at the beginning (near the discrete line). However, it is found that the intensity of the white color increases gradually and becomes almost constant with increasing step distance. These results indicate that the orientation of β-BBO crystals changes gradually [14].

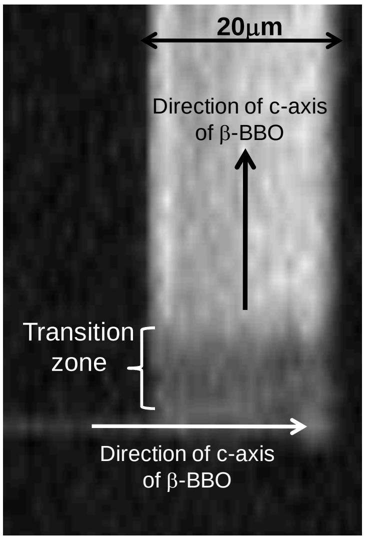

Fig. 7 Two-dimensional micro-Raman scattering spectra (imaging) at room temperature. The intensity of the peak at 637 cm^{-1} is focused, and the white color means the strong intensity of the Raman peak at 637 cm^{-1}.

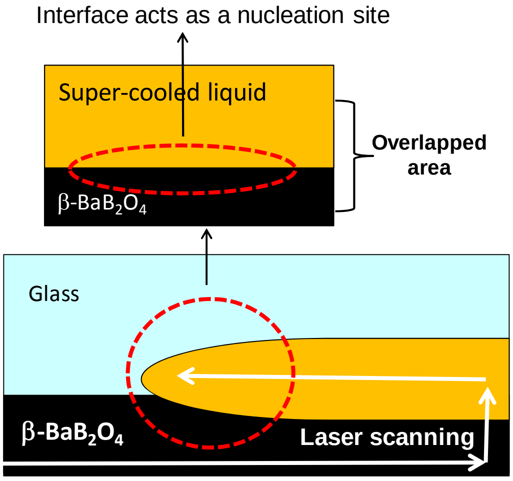

Fig. 8 Schematic model for the crystal growth in the laser overlapped region for the two-dimensional planar β-BBO crystals obtained by laser irradiations (Fig. 7).

The melting temperature of β-BBO crystals is known to be 1095°C. At this moment, the temperature of the laser-irradiated region (Yb:YVO_4 laser (λ=1080 nm), *P*=0.8 W and *S*=8 μm/s) is not measured, but it is obvious that the temperature is higher than the crystallization temperature (T_p=681°C) of $8Sm_2O_3$-42BaO-$50B_2O_3$ (mol%) glass examined in this study. As can be seen in Fig. 5, any damage such as melting or ablation is not observed at the surface of the overlapped laser-irradiated part, and thus, it is expected that the temperature would not be higher than the melting temperature (1095°C) of β-BBO crystals. In the overlapped laser-irradiated part, therefore, it is considered that initial β-BBO crystals patterned by laser irradiations are not melted, but melt (i.e., super-cooled liquid) is created at the side (i.e., the glass part) of initial β-BBO crystals. Considering the c-axis direction of β-BBO crystals in the overlapped laser-irradiated part, it is concluded that the interface between the initial β-BBO crystals and melt might have an important role for the growth and orientation of new (forthcoming) β-BBO crystals. In other words, the initial β-BBO crystals might act as nucleation sites for the growth of new β-BBO crystals.

(2) Patterning of β'-$Gd_2(MoO_4)_3$

The patterning of two-dimensional planar β'-$Gd_2(MoO_4)_3$ crystals with a high orientation has been succeeded [13]. This crystal shows a unique morphology in the line patterned by laser irradiations [7,13]. The POM photograph (top view) for the sample obtained by cw Yb:YVO_4 fiber laser irradiations with a laser power of P=1.2 W and a laser scanning speed of S=5 μm/s is shown in Fig. 9, indicating that a periodic structural change with different refractive indices is formed along the laser scanning direction. The periodic structural change shown in Fig. 9 has been proposed to call "self-organized periodic domains". Considering the width (~4 μm) of laser-patterned lines, the laser scanning was repeated with the pitch (step) of 0.7 μm between the lines, and the POM photograph for such a sample is shown in Fig. 10. A unique pattern is obtained, and its morphology is largely different from the discrete line (Fig. 9). That is, periodic domain structures with the bright and dark regions do not appear along the laser scanning direction, but are created to the direction perpendicular to the laser scanning direction [13].

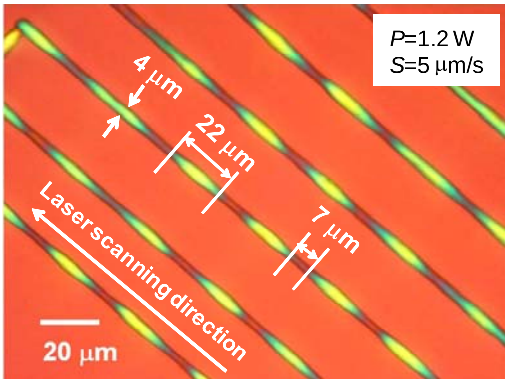

Fig. 9 POM photograph (top view) for the sample obtained by cw Yb:YVO_4 fiber laser irradiations with P=1.2 W and S=5 μm/s.

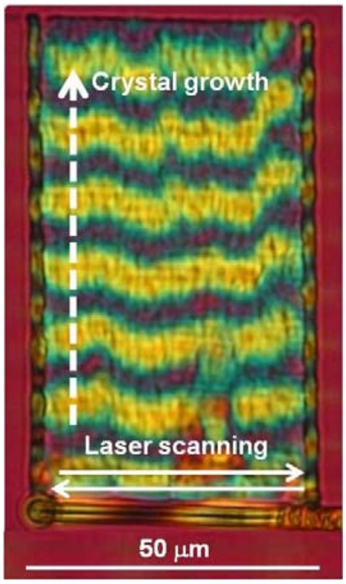

Fig.10 POM photograph for the sample obtained by cw Yb:YVO_4 fiber laser irradiations with a pitch of 0.7 μm between lines.

It was confirmed from micro-Raman scattering spectra that crystals patterned by laser irradiations with a pitch of 0.7 μm consist of the ferroelastic β'-$(Sm,Gd)_2(MoO_4)_3$ crystalline phase. In order to examine the periodic domain structure shown in Fig. 10 more in detail, two-dimensional micro-Raman scattering spectra (imaging of the shift from the peak position of 845 cm^{-1}) were measured at room temperature for laser-patterned crystals as similar to the case of two-dimensional β-BBO crystals (Fig. 7). The degradation of color depending on the domain structure was clearly observed, indicating that the antisymmetric Mo-O stretching vibrations in $(MoO_4)^{2-}$ tetrahedra in β'-$(Sm,Gd)_2(MoO_4)_3$ crystals patterned by laser irradiations change periodically depending on the domain structure. It was also found that the SH intensity changes depending on the rotation angle in the Azimuthal dependence curve. These results indicate that ferroelastic β'-$(Sm,Gd)_2(MoO_4)_3$ crystals in the two-dimensional planar region are oriented and their crystal growth directions are perpendicular to the laser scanning direction [13].

4. Conclusion

The laser-induced crystallization method was applied to pattern two-dimensional planar β-BaB_2O_4 and β'-$Gd_2(MoO_4)_3$ crystals on the glass surface. By scanning Yb:YVO_4 fiber lasers (wavelength: 1080 nm) continuously with a small step (e.g., 0.5 μm) between laser irradiated areas, highly oriented planar crystals were patterned successfully. In both crystals, the crystal growth direction is perpendicular to the laser scanning direction. Two-dimensional $LiNbO_3$ crystals were also patterned successfully on the surface of CuO-Li_2O-Nb_2O_5-B_2O_3-SiO_2 glasses [12]. It is required to examine more in detail about the orientation of crystals and the possibility of the so-called epitaxial crystal growth**.** The laser-induced crystallization method presented here was first developed in Nagaoka University of Technology, and from the point of view of "GIGAKU" (the policy and target in Nagaoka), further studies and applications of this technique are strongly required for the progress in materials science and technology.

Acknowledgments

This work was supported from the Grant-in-Aid for Scientific Research from the Ministry of Education, Science, Sports, Culture and Technology, Japan (No. 23246114), and by Program for High Reliable Materials Design and Manufacturing in Nagaoka University of Technology.

References

[1] R. Sato, Y. Benino, T. Fujiwara, and T. Komatsu, J. Non-Cryst. Solids, **289** (2001) 228.
[2] T. Honma, Y. Benino, T. Fujiwara, T. Komatsu, and R. Sato, Appl. Phys. Lett., **82** (2003) 892.
[3] T. Honma, Y. Benino, T. Fujiwara, T. Komatsu, and R. Sato, Apply. Phys. Lett., **83** (2003) 2796.
[4] T. Honma, Y. Benino, T. Fujiwara, and T. Komatsu, Apply. Phys. Lett., **88** (2006) 231105.
[5] T. Komatsu, R. Ihara, T. Honma, Y. Benino, R. Sato, H.G. Kim, and T. Fujiwara, J. Am. Ceram. Soc., **90** (2007) 699.
[6] M. Kusatsugu, M. Kanno, T. Honma, and T. Komatsu, J. Solid State Chem., **181** (2008) 1176.
[7] Y. Tsukada, T. Honma, and T. Komatsu, Appl. Phys. Lett., **94** (2009) 059901.
[8] A. Stone, M. Sakakura, Y. Shimotsuma, G. Stone, P. Gupta, K. Miura, K. Hirao, V. Dierolf, and H. Jain, J. Non-Cryst. Solids, **356** (2010) 3059.
[9] F. Suzuki, T. Honma, and T. Komatsu, J. Solid State Chem., **183** (2010) 909.
[10] K. Kioka, T. Honma, and T. Komatsu, Opt. Mater., **33** (2011) 1203.
[11] T. Komatsu, K. Koshiba, and T. Honma, J. Solid State Chem., **184** (2011) 411.
[12] T. Honma and T. Komatsu, Opt. Express **18** (2010) 8019.
[13] F. Suzuki, T. Honma, and T. Komatsu, Mater. Chem. Phys., **125** (2011) 377.
[14] F. Suzuki, K. Ogawa, T. Honma, and T. Komatsu, J. Solid State Chem., **185** (2011) 130.
[15] H. Tanaka, T. Honma, Y. Benino, T. Fujiwara, and T. Komatsu, J. Phys. Chem. Solids, **64** (2003) 1179.
[16] T. Honma, Y. Benino, T. Fujiwara, R. Sato, and T. Komatsu, J. Phys. Chem. Solids, **65** (2004) 1705.

(Received: 28 March, 2012, Accepted: 20 April, 2012)

Transaction on GIGAKU ***1*** *(2012) 01018/1-6*

Condensation Control of Nanoscale Polymer Aggregates by Using Atomic Force Microscope Tip

Akira Kawai
Department of Electrical Engineering, Nagaoka University of Technology
1603-1 Kamitomioka, Nagaoka, Niigata 940-2188, Japan
E-mail, kawai@nagaokaut.ac.jp

This paper reviews shortly condensation behavior of polymer aggregate in side-wall of resist pattern characterized by using atomic force microscope (AFM). Various hardening process, thermal heating and EB irradiation, are performed on the resist pattern after the pattern development. The condensation of polymer aggregates in the side-wall is clearly imaged. By the hardening treatments, condensation of polymer aggregate is accelerated. The interaction force among polymer aggregates can be analyzed based on Derjaguin approximation. The condensation structure of polymer aggregate accompanying with aggregate vacancy is also discussed.

1. Introduction

In recent years, condensation control of polymer aggregate has become important in order to improve line edge roughness (LER) in a side-wall of resist pattern [1]. The atomic force microscope (AFM) system has proven to be a versatile instrument for imaging minute structure of condensed matter [2]. Recently, present authors have already proposed the novel principle for direct analysis method of resist pattern adhesion, that is, direct peeling method by using AFM tip (DPAT) [3-6]. By the DPAT method, quantitative analysis of cohesive properties of resist pattern has been conducted. In this paper, by using the AFM, the condensation of polymer aggregate in side–wall of resist pattern is characterized. Particularly, the special attention is paid to the dependency of hardening processes.

2. Experiment

2.1. Resist material and line pattern fabrication

The KrF excimer laser resist, chemically amplified type, consisting of hydroxystyrene as a base polymer was used. The resist film was coated onto a Si(100) wafer by a spinning method. The native oxide layer was removed by dipping into HF aqueous solution prior to spin coating of the resist film. The pre-baking treatment was carried out at 100℃ for 1 min on a proximity hot plate. The silane-coupling treatment with hexamethyl-disilazane (HMDS) was performed at 80℃ for 60 s. The line patterns of 130 nm width were imaged to the resist film by using an KrF excimer laser stepper. After the pattern exposure, the resist films were baked at 100℃ for 1 min. Then, the resist films were developed by dipping into tetramethyl-ammoniumhydroxide (TMAH) 2.38 % aqueous solution for 60 s. Subsequently, the resist patterns were rinsed in the deionized water for 30 s and dried by the spin method. As the hardening processes, heat treatment and EB irradiation were performed. The heat treatment was performed at 150℃ for 5 min in the ambient condition. The charge density of EB irradiation was approximately 5 μ C/cm^2 with the acceleration voltage of 50 kV.

2.2. Condensation analysis with AFM

A commercially available AFM, integrated with a microtip, was used for the condensation analysis. As a tip used for the investigation, a conical tip mounted on the cantilever apex was used

(Fig.1). The radius of curvature of the tip apex was approximately 8 nm. The tip was made of a Si_3N_4 film. The tips with exposure to the HMDS vapor were prepared. The calibration measurements of the spring constant correlated well with the manufacturer's given value of k=0.44 N/m.

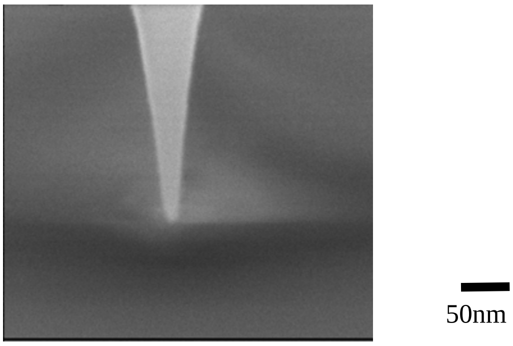

Fig. 1 SEM photograph of apex of AFM tip used for the investigation.

With the invention of the AFM, we have been equipped in good time with the appropriate tools to understand the cohesive properties of condensed matter on a nanometer scale. Figure 2 shows a schematic explanation of side-wall imaging by the DPAT method. Prior to the side-wall observation, the line resist pattern was imaged by the AFM in the non-contact mode. The tip traversed the line pattern by moving the piezo stage under the scanning control. By directly applying load to the top corner of the resist pattern with the AFM tip, the line pattern adhering on the substrate can be collapsed easily (Fig.2a). After the pattern collapse, the side-wall of resist pattern can be imaged easily as shown in Fig.2b. When the adhesion strength between the resist pattern and the substrate is relatively large, a certain residue of resist remains on the substrate. The measurement of DPAT method is described in detail in our previous reports [3-6].

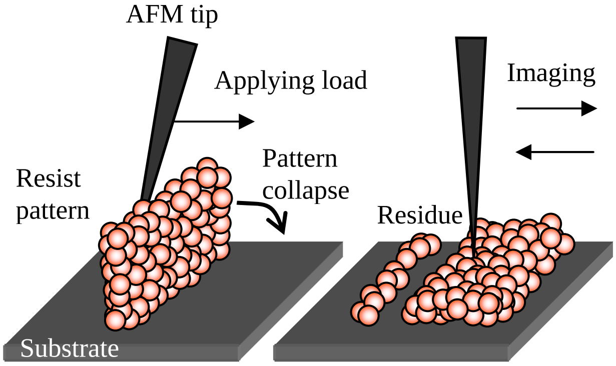

(a) Pattern collapse (b) Side-wall imaging

Fig. 2 Side-wall imaging by the DPAT method.

3. Results and Discussion

3.1. Condensation structure of polymer aggregate in side-wall

Figures 3a to 3c show the side-wall images of the resist pattern after the DPAT process. The resist pattern can be collapsed easily without any damages. The square area marked in each side-wall image is magnified in order to analyze condensation of polymer aggregates precisely.

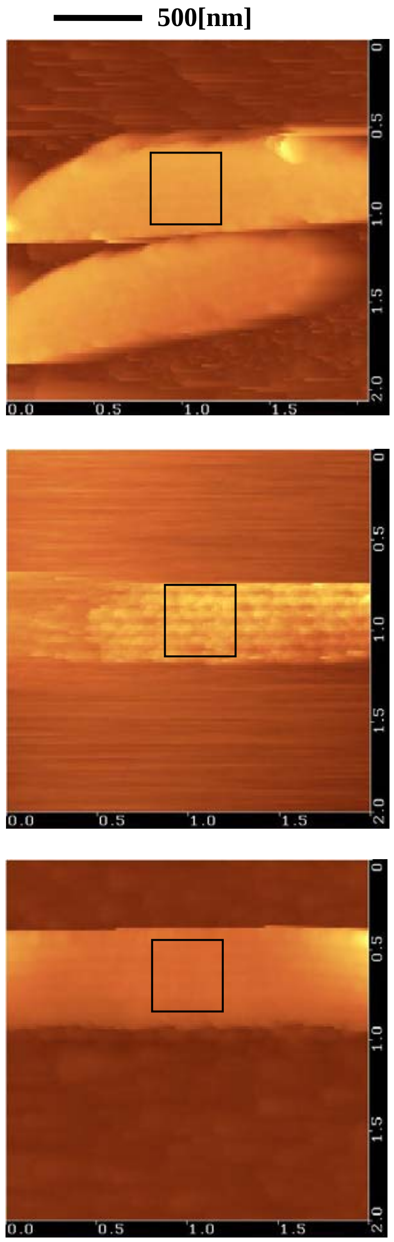

(a) Non-treatment
(after pattern development)

(b) Heat treatment

(c) EB irradiation

Fig. 3 AFM image of side-wall of resist pattern performed with bake and EB hardening treatment.

Figure 4 shows the side-wall images, surface topological profile and condensation structure model for each treatment. In the AFM images, roughened surface images in side-wall due to condensation of polymer aggregates can be clearly observed. In the case of the non-treatment (Fig.4a), the size of each polymer aggregate is approximately 20 nm. In the case of the heat treatment (Fig.4b), the large aggregate composed with many aggregates can be observed. Moreover, polymer aggregate becomes large due to condensation acceleration by the EB irradiation and the aggregate size is approximately 60 nm (Fig.4c). The polymer aggregate smaller than 10 nm size could not be resolved, because the limitation is caused by tip-sample convolution. The condensation model of polymer aggregate was discussed by Bug [7]. In this study, the condensation property of polymer aggregate is analyzed based on Derjaguin approximation in the following section.

(a) Non-treatment (after pattern development)

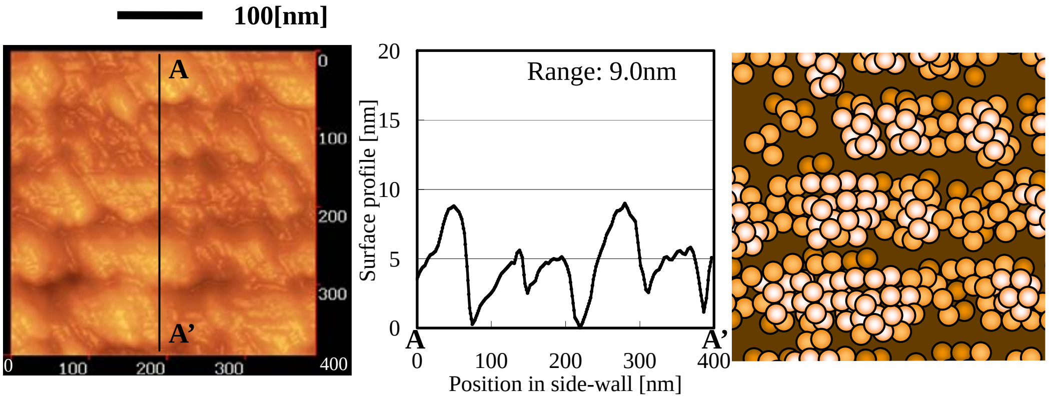

(b) Heat treatment

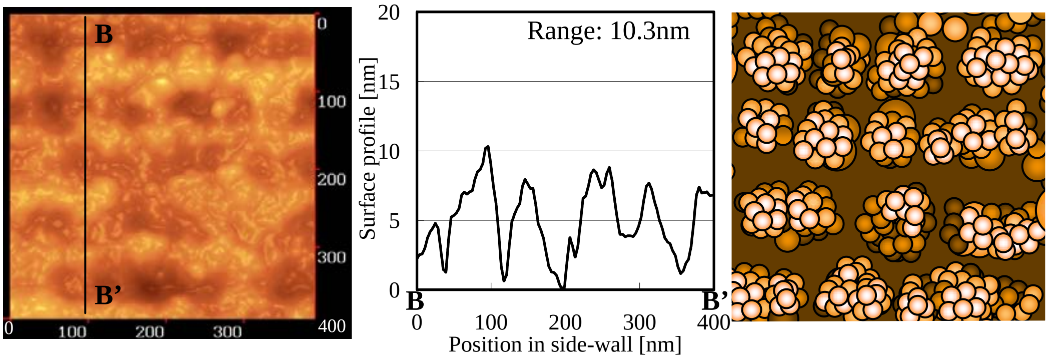

(c) EB irradiation

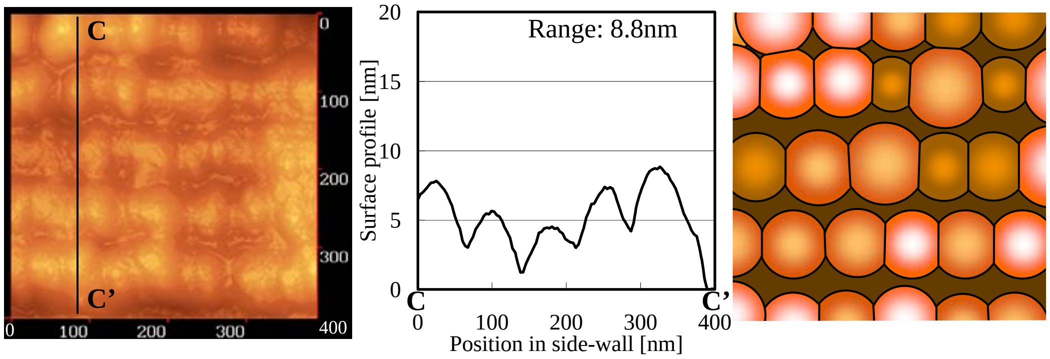

(AFM image of side-wall) (Surface topological profile) (Condensation structure model)

Fig. 4 Condensation of polymer aggregate in side-wall of resist pattern.

3.2. Condensation structure of polymer aggregate

In general, the size of micro condensed matter contributes strongly to surface roughness of solid material[1,8]. The size of polymer aggregate can be regarded as the representative value which reflects the condensation properties in side-wall of resist pattern. Figure 5 shows schematic explanation of condensation behavior of polymer aggregate based on Derjaguin approximation.

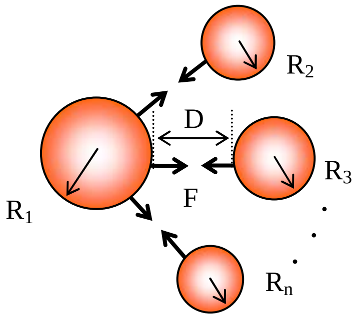

Fig. 5 Interaction force model between two spheres based on Derjaguin approximation.

As shown in Fig.5, based on Derjaguin approximation, a sum of interaction force F acting among some micro spheres (radius: R_1, R_2, ···, R_n) can be expressed as follows.

$$F = \frac{A}{6D^2}\sum_n \frac{R_1 R_n}{R_1 + R_n}, \qquad (1)$$

where symbols A and D represent Hamaker constant and interaction length between two spheres. The simple simulation result of interaction force is shown in Fig.6. It seems reasonable to suppose that the interaction force decreases with decreasing size of polymer aggregates. However, when the interaction length is less than 10 nm, the interaction force increases rapidly. Therefore, it can be explained that the small size aggregate is more likely to condense around the large size one, as shown in Fig.4b. This theory provides a very simple but direct approach to understand condensation of polymer aggregate.

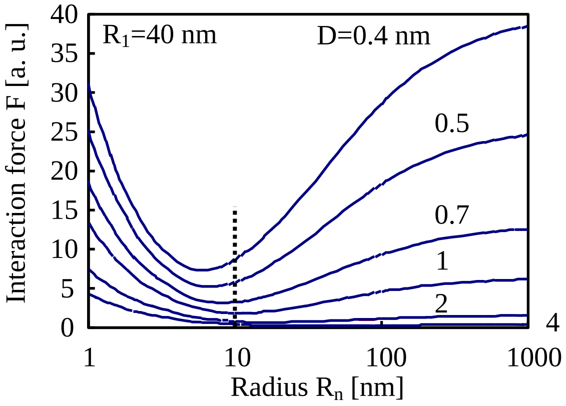

Fig. 6 Dependency of interaction force on spherical radius.

Meanwhile, the present author found out the vacancy of polymer aggregate formed in the resist pattern [6]. In most cases, the vacancy size is approximately 60nm. It is entirely fair to say that a vacancy of polymer aggregate is formed during the condensation processes. In Fig.7, the condensation models of polymer aggregate accompanying some vacancies are illustrated. We can be fairly certain to discuss that these condensed model are effective to study the formation mechanisms of roughened side-wall of resist pattern.

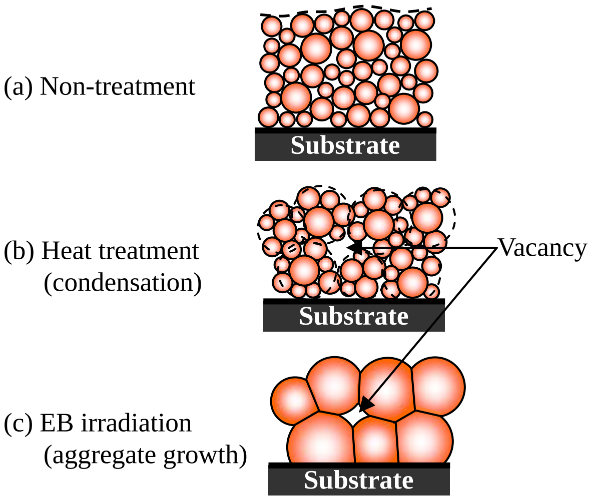

Fig. 7 Condensation model of polymer aggregate by hardening treatment (cross sectional view)

4. Conclusion

Condensation properties of polymer aggregate in side-wall are characterized by the DPAT techniques. By the hardening of resist pattern, condensation structure of polymer aggregate is drastically changed. The condensation model of polymer aggregate can be constructed based on Derjaguin approximation.

Acknowledgements

This work was supported from the Grant-in-Aid for Scientific Research from the Ministry of Education, Science, Sports, Culture and Technology, Japan, and by Program for High Reliable Materials Design and Manufacturing in Nagaoka University of Technology.

References

[1] T. Yoshimura, H. Shiraishi, J. Yamamoto and Shinji Okazaki, *Appl. Phys. Lett.*, **63** (1993) 764.
[2] G. Binnig, C. F. Quate and Ch. Gerber, *Phys. Rev. Lett.*, **56** (1986) 930.
[3] A. Kawai and Y. Kawakami, *Ext. Abstr. 44th Spring Meet. Japan Society of Applied Physics and Related Societies*, Chiba, March, (1997) p.576.
[4] A. Kawai, *Proc. SPIE's 24th Inter. Symp. Microlithography*, Santa Clara, **3677** (1999) p565.
[5] A. Kawai and N. Moriike, *Microelectronic Engineering*, **57-58** (2001) 683.
[6] A. Kawai, *J. Photopolymer Sci. Technol.*, **15** (2002) 371.
[7] A. L. R. Bug, M. E. Cates, A. A. Safran and T. A. Witten, *J. Chem. Phys.*, **87** (1987) 1824.
[8] J. N. Israelachvili, "*Intermolecular and surface force*", 2nd Edition, Academic press (1997) p326.

(Received: 29 May, 2012, Accepted: 12 June, 2012)

Transaction on GIGAKU **1** *(2012) 01019/1-6*

Intensity of Singularity Analysis for Three-dimensional Two-phase Transversely Isotropic Piezoelectric Bonded Joints

Md. Shahidul Islam[1,*], Hideo KOGUCHI[2]
[1)]Graduate school of Nagaoka University of Technology,
[2)]Department of Mechanical Engineering, Nagaoka University of Technology,
1603-1 Kamitomioka-machi, Nagaoka 940-2188, Japan
**E-mail: shahidul@stn.nagaokaut.ac.jp*

Stress singularity frequently occurs at a vertex in an interface of joints due to a discontinuity of materials. The stress singularity fields are one of the main factors responsible for debonding under mechanical or thermal loading. The stress distribution near the vertex in the interface of joints is very important to maintain the reliability of joints. However, the intensity of singularity for 3D transversely isotropic piezoelectric bi-material joints has not been made clear until now. In this paper, intensity of singularity in transversely isotropic piezoelectric dissimilar material joints is analyzed. The stress and electric displacement distributions on an interface and the intensity of singularity for stress and electric displacement are investigated using BEM. From the numerical results, it is shown that the intensity of stress singularity increases and the intensity of electric displacement singularity decreases with the increase of material thickness in joint.

1. Introduction

In recent years, intelligent or smart structures and systems have drawn more and more attention. Piezoelectric materials have been extensively used as transducers and sensors due to their intrinsic direct and converge piezoelectric effects that take place between electric field and mechanical deformation. Piezoelectric materials are playing a key role as active components in many fields of engineering and technology such as electronics, laser, microwave infrared, navigation and biology [1]. Mechanical stress occurs in piezoelectric material for any electric input. The stress concentrations caused by mechanical or electric loads may lead to crack initiation and extension, and sometimes the stress concentrations may be high enough to debond the material parts. Industrial products such as electronic devices and heat endurance parts are composed of dissimilar materials. A mismatch of material properties causes a failure at the free edge of joints, because a stress concentration occurs along the free edge of interface especially at the vertex of joint [2]. When two materials are joined, a free-edge stress singularity usually develops at the intersection of the interface and the free surface. Stress singularity is related to debond and delamination at interface of the bonded joints. The stress distributions around the vertex were determined using a boundary element method (BEM). Koguchi [3] determined the intensity of singularity by fitting the stress profile obtained from BEM analysis with a least squares method. Constabel et al.[4] proposed a method to compute their singularity exponents and the associated angular singular functions. Recently Hwu [5] and Ikeda et al.[6] proposed the solution of singular stress field and its SIFs of an interfacial corner of a 2D dissimilar piezoelectric material joints using extended Stroh formalism. At present, no clear picture exists of the problem of intensity of singularity for 3D two-phase transversely isotropic piezoelectric dissimilar material joints. Therefore, the purpose of this study is to analyze the intensity of singularity in transversely isotropic piezoelectric dissimilar material joints.

2. Formula of Analysis

In the absence of body forces and free charges, the governing equations of three-dimensional piezoelectric materials are expressed as follows:

$$\sigma_{ij,j} = 0 \qquad D_{i,i} = 0 \tag{1}$$

where σ_{ij} and D_i are stress tensor and electric displacement vector, respectively. These equations are the elastic equilibrium equations and Gauss's law of electrostatics, respectively. The constitutive relations for piezoelectric material are expressed as follows:

$$\sigma_{ij} = c_{ijkl}\varepsilon_{kl} - e_{kij}E_k \qquad D_i = e_{ikl}\varepsilon_{kl} + \chi_{ik}E_k \tag{2}$$

where ε_{kl} is the strain tensor which is the mechanical field variables, E_k is electric field, c_{ijkl} is the elastic constant, e_{kij} (e_{ikl}) and χ_{ik} are the piezoelectric constant and electric permittivity (dielectric constant), respectively.

The elastic strain-displacement and electric field-potential equations are expressed as follows:

$$\varepsilon_{ij} = \frac{1}{2}\left(u_{j,i} + u_{i,j}\right) \qquad E_i = -\phi_{,i} \tag{3}$$

where u_i and ϕ are the elastic displacement and electric potential, respectively.

According to Ding et al.[1], the fundamental solutions of the governing differential equations for the transversely isotropic piezoelectric material are shown as follows:

$$u = \sum_{i=1}^{3}\frac{\partial \psi_i}{\partial x} - \frac{\partial \psi_o}{\partial y} \qquad v = \sum_{i=1}^{3}\frac{\partial \psi_i}{\partial y} + \frac{\partial \psi_o}{\partial x} \qquad \left(s_1 \neq s_2 \neq s_3 \neq s_1\right)$$

$$w = \sum_{i=1}^{3}\alpha_{i1}\frac{\partial \psi_i}{\partial z_i} \qquad \phi = \sum_{i=1}^{3}\alpha_{i2}\frac{\partial \psi_i}{\partial z_i} \tag{4}$$

where, s_1, s_2, and s_3 are the three roots of the characteristic equation, which is related to the following equation.

$$as^6 - bs^4 + cs^2 - d = 0 \tag{5}$$

In three roots of Eq. (5), s_1 is assumed to be a positive real number, s_2 and s_3 are either positive real number or a pair of conjugate complex roots with positive real parts.

Function ψ_i in equation (4) for an infinite piezoelectric material is given as follows:

$$\psi_o = 0 \quad and \quad \psi_i = A_i sign(z - z_o)\ln\left(\bar{R}_{ii} + s_i\left|z - z_o\right|\right) \qquad (i = 1,\ 2,\ 3) \tag{6}$$

The expressions of stress and electric displacement are obtained in terms of the function ψ_i as below.

$$\sigma_{xx} = -\left(c_{11} - c_{12}\right)\frac{\partial^2 \psi_o}{\partial x \partial y} + \sum_{i=1}^{3}\left[\xi_i \frac{\partial^2}{\partial z_i^2} + \left(c_{11} - c_{12}\right)\frac{\partial^2}{\partial x^2}\right]\psi_i$$

$$\sigma_{yy} = \left(c_{11} - c_{12}\right)\frac{\partial^2 \psi_o}{\partial x \partial y} + \sum_{i=1}^{3}\left[\xi_i \frac{\partial^2}{\partial z_i^2} + \left(c_{11} - c_{12}\right)\frac{\partial^2}{\partial y^2}\right]\psi_i$$

$$\sigma_{zz} = \sum_{i=1}^{3}\vartheta_{i1}\frac{\partial^2 \psi_i}{\partial z_i^2} \qquad \tau_{xy} = c_{66}\left(\frac{\partial^2 \psi_o}{\partial z_o^2} + 2\frac{\partial^2 \psi_o}{\partial x^2}\right) + 2c_{66}\sum_{i=1}^{3}\frac{\partial^2 \psi_i}{\partial x \partial y}$$

$$\tau_{xz} = -\omega_{o1}\frac{\partial^2 \psi_o}{\partial y \partial z_i} + \sum_{i=1}^{3}\omega_{i1}\frac{\partial^2 \psi_i}{\partial x \partial z_i} \qquad \tau_{yz} = \omega_{o1}\frac{\partial^2 \psi_o}{\partial x \partial z_i} + \sum_{i=1}^{3}\omega_{i1}\frac{\partial^2 \psi_i}{\partial y \partial z_i}$$

$$D_x = -\omega_{o2}\frac{\partial^2 \psi_o}{\partial y \partial z_i} + \sum_{i=1}^{3}\omega_{i2}\frac{\partial^2 \psi_i}{\partial x \partial z_i} \qquad D_y = \omega_{o2}\frac{\partial^2 \psi_o}{\partial x \partial z_i} + \sum_{i=1}^{3}\omega_{i2}\frac{\partial^2 \psi_i}{\partial y \partial z_i}$$

$$D_z = \sum_{i=1}^{3}\vartheta_{i2}\frac{\partial^2 \psi_i}{\partial z_i^2} \tag{7}$$

where $\xi_i = \left(c_{13}\alpha_{i1} + e_{31}\alpha_{i2}\right)s_i - c_{12}$ $\qquad \omega_{o1} = c_{44}s_o$ $\qquad \omega_{o2} = e_{15}s_o$

$$\omega_{i1} = c_{44}\left(s_i + \alpha_{i1}\right) + e_{15}\alpha_{i2} \qquad \omega_{i2} = e_{15}\left(s_i + \alpha_{i1}\right) - \chi_{11}\alpha_{i2}$$

$$\vartheta_{i1} = \left(c_{33}\alpha_{i1} + e_{33}\alpha_{i2}\right)s_i - c_{13} \qquad \vartheta_{i2} = \left(e_{33}\alpha_{i1} - \chi_{33}\alpha_{i2}\right)s_i - e_{31}$$

$$\alpha_{i1} = \frac{c_{11}\chi_{11} - m_3 s_i^2 + c_{44}\chi_{33}s_i^4}{\left(m_1 - m_2 s_i^2\right)s_i} \qquad \alpha_{i2} = \frac{c_{11}e_{15} - m_4 s_i^2 + c_{44}e_{33}s_i^4}{\left(m_1 - m_2 s_i^2\right)s_i}$$

Another stress and electric displacement are derived for two domain.

3. Boundary Integral Equation

Based on the Somigliana equation, the boundary integral formulation is expressed as follows:

$$\mathbf{C}(d)\mathbf{u}(d) = \int_{\Gamma} \mathbf{U}^{*}(d,x)\mathbf{t}(x)d\Gamma - \int_{\Gamma} \mathbf{T}^{*}(d,x)\mathbf{u}(x)d\Gamma \tag{8}$$

where **C** is the coefficient matrix, which depends on shape of the boundary Γ, and the general displacement vector **u**, and surface traction vector **t** are as follows:

$$\mathbf{u} = \{u \quad v \quad w \quad -\phi\}^{T}, \qquad \mathbf{t} = \{t_x \quad t_y \quad t_z \quad -\omega\}^{T}$$

and two matrices $\mathbf{U}^{*}$ and $\mathbf{T}^{*}$ composed of fundamental solution are:

$$\mathbf{U}^{*} = \begin{bmatrix} u_{11}^{*} & u_{12}^{*} & u_{13}^{*} & \phi_{1}^{*} \\ u_{21}^{*} & u_{22}^{*} & u_{23}^{*} & \phi_{2}^{*} \\ u_{31}^{*} & u_{32}^{*} & u_{33}^{*} & \phi_{3}^{*} \\ u_{41}^{*} & u_{42}^{*} & u_{43}^{*} & \phi_{4}^{*} \end{bmatrix}, \qquad \mathbf{T}^{*} = \begin{bmatrix} t_{11}^{*} & t_{12}^{*} & t_{13}^{*} & \omega_{1}^{*} \\ t_{21}^{*} & t_{22}^{*} & t_{23}^{*} & \omega_{2}^{*} \\ t_{31}^{*} & t_{32}^{*} & t_{33}^{*} & \omega_{3}^{*} \\ t_{41}^{*} & t_{42}^{*} & t_{43}^{*} & \omega_{4}^{*} \end{bmatrix}$$

where u_{ij}^{*} and t_{ij}^{*} (i, j = 1, 2, 3) are displacements and surface tractions, respectively at a field point x in the j coordinate direction due to a unit load acting in the x_i directions at a load point d, u_{4j}^{*} and t_{4j}^{*} (j = 1, 2, 3) are displacement components and surface tractions, respectively, at a field point x in the j coordinate direction due to a unit electric charge at d. ϕ_{i}^{*} and ω_{i}^{*} (i = 1, 2, 3) are electric potentials and surface charges, respectively, at a field point x due to a unit load acting in the x_i directions at a load point d, and ϕ_{4}^{*} and ω_{4}^{*} are electric potential and surface charge respectively at a field point x due to a unit electric charge at d.

If the boundary is discretized with an eight-node isoparametric quadratic element, then the boundary integral equation is written as follows

$$\mathbf{C}(d)\mathbf{u}(d) + \sum_{e\in\Gamma}\sum_{i=1}^{8}\int_{-1}^{1}\int_{-1}^{1}\mathbf{T}^{*}\mathbf{u}_{i}N_{i}\,|J|\,d\zeta d\eta = \sum_{e\in\Gamma}\sum_{i=1}^{8}\int_{-1}^{1}\int_{-1}^{1}\mathbf{U}^{*}\mathbf{t}_{i}N_{i}\,|J|\,d\zeta d\eta \tag{9}$$

where N_i is the shape function, J is Jacobian matrix, $\mathbf{u}_i$ and $\mathbf{t}_i$ represent the displacement and surface traction at node, and **C** is the coefficient matrix.

4. Eigenequation

An eigenequation based on the finite element method (FEM) was used to analyze the singularity at the singular point in a 3D dissimilar material joint. In the formulation of FEM, a spherical coordinate system with the origin at a singular point is introduced, and displacement within a sphere of radius r_0 in the singular field is expressed using the characteristic root p, which is related to the order of singularity. The surface of the sphere is divided into mesh.

The eigenequation was formulated for determining the order of stress singularity as follows:

$$\left(p^{2}[\mathbf{A}] + p[\mathbf{B}] + [\mathbf{C}]\right)\{\mathbf{U}\} = \{0\} \tag{10}$$

where

$$\{\mathbf{U}\} = \{u_r \quad u_\theta \quad u_\phi \quad \psi\}^{T},$$

$$[\mathbf{A}] = \sum_{S}\left([\mathbf{k}_a - \mathbf{k}_{sa}]\right), \quad [\mathbf{B}] = \sum_{S}\left([\mathbf{k}_b - \mathbf{k}_{sb}]\right), \text{ and } \quad [\mathbf{C}] = \sum_{S}\left([\mathbf{k}_c - \mathbf{k}_{sc}]\right).$$

Here, *p* represents the characteristic root, which is related to the order of singularity, λ, as $\lambda = 1-p$. [**A**], [**B**] and [**C**] are matrices composed of material properties, and {**U**} represents the elastic displacement and electric potential vector.

5. Result and Discussion

Figure 1(a) represents a model for 3D piezoelectric bonded structure used in the present analysis. The displacement and electric potential in the *z*-direction on the bottom in the model is fixed. The model is subjected to a uniform tension (1 MPa) and electric displacement (1 C/m^2) whose poling direction is parallel to the *z*-axis. Figure 1(b) represents the geometry of a typical case where a singular stress state occurs at the point o. The region surrounding the singular point is divided into a number of quadratic elements with a summit o, with each element being located in spherical co-ordinates *r*, θ, and ϕ by its nodes 1 to 8.

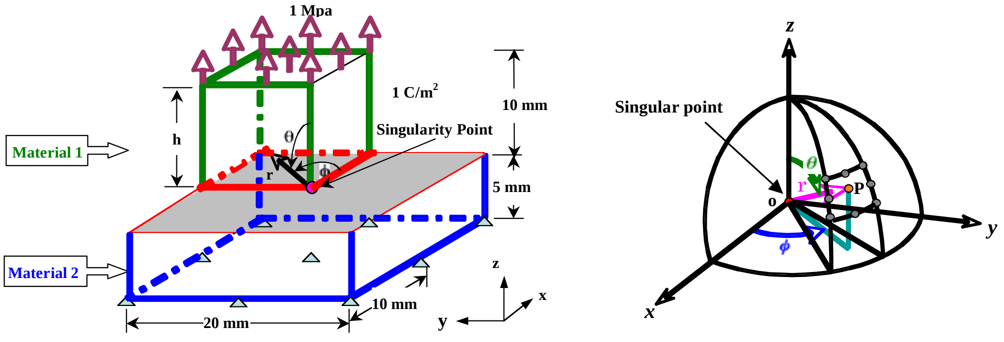

(a) Model of analysis (b) Element geometry and natural co-ordinate

Fig. 1 Model of analysis for two-phase piezoelectric bonded joint

Table1 Material properties of piezoelectric materials

Material	Elastic Constant, 10^{10} N/m^2					Piezoelectric Constant, C/m^2			Dielectric Constant, 10^{-10}C/Vm	
	c_{11}	c_{12}	c_{13}	c_{33}	c_{44}	e_{31}	e_{33}	e_{15}	χ_{11}	χ_{33}
PZT-4	12.6	7.78	7.43	11.5	2.56	-5.20	15.1	12.7	64.63	56.22
PZT-5H	12.6	5.50	5.30	11.7	3.53	-6.50	23.3	17.0	151.0	130.0

The model of three-dimensional two-phase transversely isotropic bonded joints and the distribution of nodal displacement are shown in Fig. 2. This figure is plotted, when 1MPa tensile load is applied on the upper material and 1 C/m^2 charge. And the elastic constants of lower material are 100 times larger than that of the upper material.

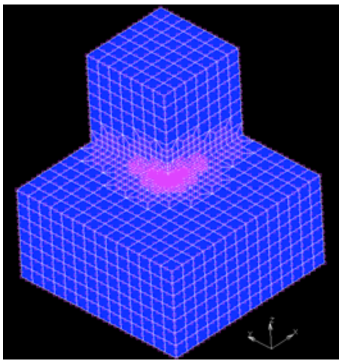

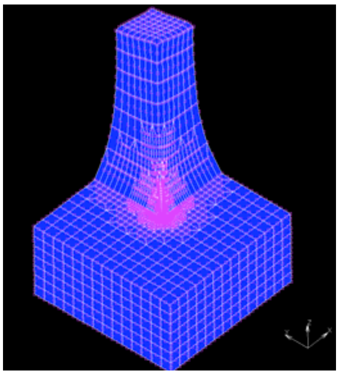

Fig. 2 Two-phase piezoelectric bonded joints and distribution of nodal displacement

The order of singularity, λ, at the vertex for the above model is calculated by eigenanalysis method. Solving eigenequation yields many roots p and eigenvectors are obtained. However, if the root p is within the range of $0 < p < 1$, this fact indicates that the stress field has singularity. The values of the order of singularity at the singularity corner are 0.582, 0.315, 0.178, and 0.079.

The stress distribution at the vertex in a singular field is expressed for spherical coordinate system as follows:

$$\sigma_{ij}\left(r,\theta,\phi\right)=K_{1ij}f_{1ij}(\theta,\phi)r^{-\lambda_{vertex}}+K_{2ij}f_{2ij}(\theta,\phi) \qquad (11)$$

where r is the distance from the vertex, λ_{vertex} is the order of stress singularity, K_{kij} (k = 1, 2) is the intensity of stress singularity, $f_{kij}(\theta, \phi)$ (k = 1, 2) is the angular function for stress component, σ_{ij}. Similarly, the electric displacement distribution at the vertex in a singular field is expressed for spherical coordinate system as follows:

$$D_i\left(r,\theta,\phi\right)=M_{1i}l_{1i}(\theta,\phi)r^{-\lambda_{vertex}}+M_{2i}l_{2i}(\theta,\phi) \qquad (12)$$

where M_{ki} (k = 1, 2) is the intensity of electric displacement singularity, $l_{ki}(\theta, \phi)$ (k = 1, 2) is the angular function for electric displacement component, D_i.

The distributions of stress and electric displacement in the singular field for the two-phase piezoelectric bonded structure are obtained using boundary element method. Figure 3 demonstrates the distributions of stresses, $\sigma_{\theta\theta}$, $\sigma_{r\theta}$, $\sigma_{\phi\theta}$ and electric displacement, D_θ against radial distance, r, on the interface of piezoelectric bonded joint. The plots for stresses, $\sigma_{\theta\theta}$, $\sigma_{r\theta}$ and electric displacement, D_θ are parallel in log-log graph. The red line indicates the line for $Ar^{-\lambda\, vertex}$, where A is a constant, λ_{vertex} (=0.582) represents the order of singularity at the vertex. The slope of all the curves is in good agreement with the result of eigenanalysis. Therefore, the power law singularity governs the stress and electric displacement field near the vertex. All figures show that the stress and electric displacement is larger at the vertex of the interface. Therefore, there is a possibility to debond and delamination at the corner of the bonded joint.

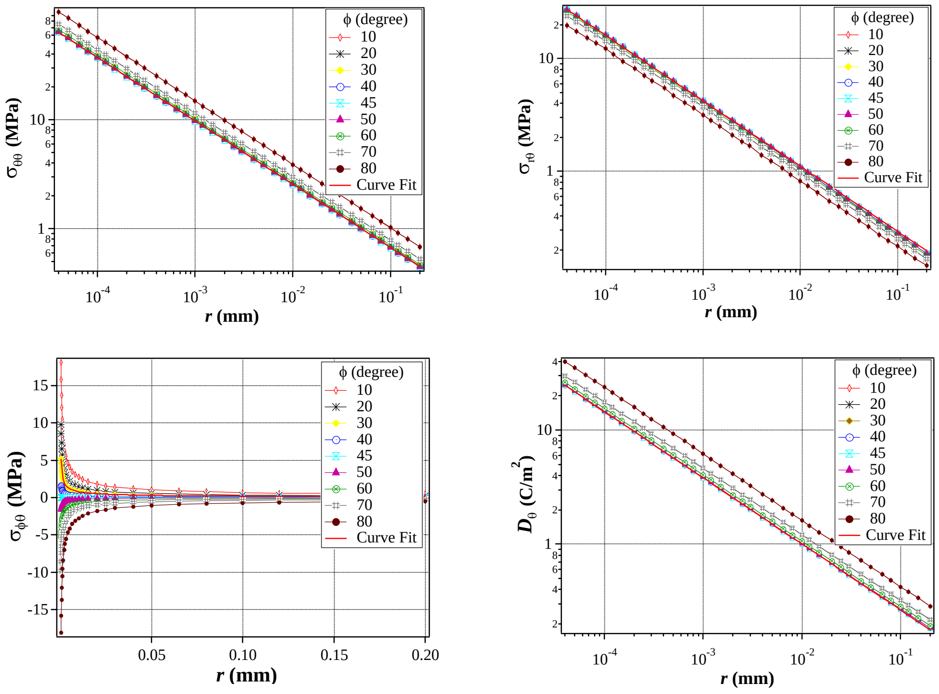

Fig. 3 Distributions of stress and electric displacement against radial distance, *r*

Figure 4 shows a relationship between the intensities of singularity for stress and electric displacement and the thickness of upper material, *h*. The intensities of singularity are calculated by fitting the stress and electric displacement curves with the help of the result of eigenanalysis. The boundary condition in BEM analysis as shown in Fig. 1(a) is agreed with the first value of the order of stress singularity. Therefore, the first value of the order of stress singularity at the vertex is used in intensities of singularity calculation. The intensity of stress singularity increases with thickness of upper material, but the intensity of singularity for electric displacement decreases with the thickness.

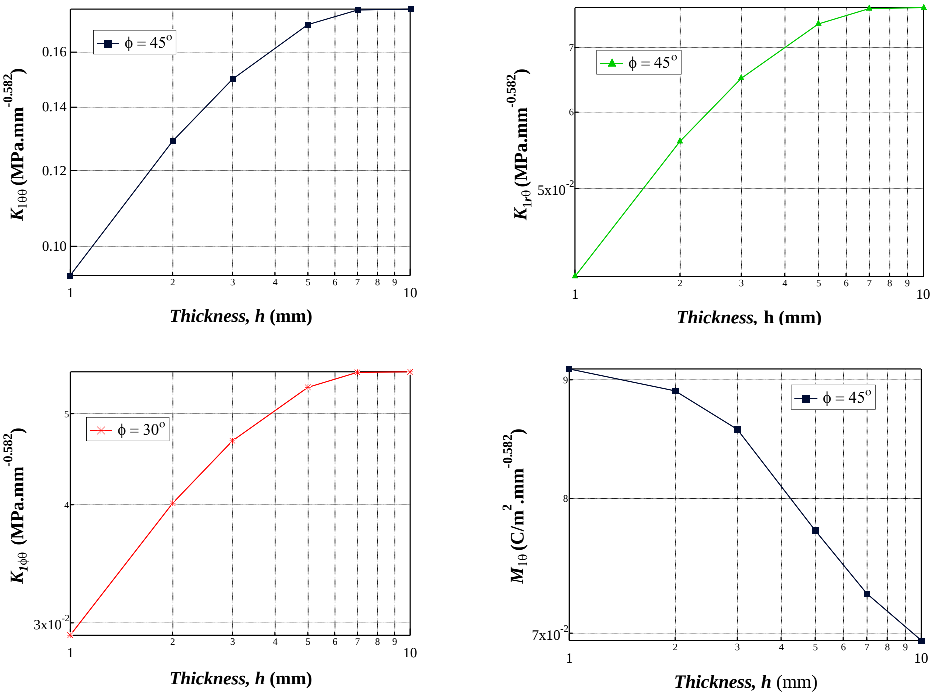

Fig. 4 Distribution of intensity of singularity against thickness, *h*

6. Conclusion

In this paper, the intensity of singularity that characterizes a singular field at a vertex in 3D dissimilar material joints was investigated using a boundary element analysis. The distributions of stress and electric displacement with respect to radial distance were calculated. The stress and electric displacement have a larger value at the vertex. The intensities of singularity were calculated by fitting the stress and electric displacement curves with the help of the result of eigenanalysis at the vertex. The intensity of stress singularity increases with the thickness of upper material, but the intensity of singularity for electric displacement decreases with the thickness, because the effect of charge for thin material is larger than that for the thick material.

References

[1] H. Ding and B. Chen, Int. J. Solids Struct., **34(23)** (1997) 3041.
[2] W. Attaporn and H. Koguchi, CMES, **39(3)** (2009) 237.
[3] H. Koguchi, Trans. JSME, **A72(724)** (2006) 2058.
[4] M. Constabel, M. Dauge, and Y. Lafranche, Comput. Meth. Appl. Mech. Eng., **190** (2001) 2111.
[5] C. Hwu, Int. J. Solids Struct., **45** (2008) 4460.
[6] T. Ikeda, H. Hirai, and M. Abe, Proceedings of the ASME, **InterPACK** (2011) 1.

(Received: 23 March, 2012, Accepted: 20 April, 2012)

*Transactions on GIGAKU **1**(2012)01020/1-5*

Evaluation of Internal Coarse Defects in Alumina Powder Compact and Ceramics

Satoshi Tanaka*, Keizo Uematsu
Department of Materials Science and Technology, Nagaoka University of Technology,
1603-1 Kamitomioka-cho, Nagaoka 940-2188, Japan
**E-mail: stanaka@vos.nagaokaut.ac.jp*

The internal coarse defects in alumina ceramics and powder compact before and after firing were observed by using the micro-focus x-ray computed tomography (micro CT) and the optical microscopy. We studied the effectiveness of micro CT by comparing with images in the powder compact by the optical microscopy. Furthermore, the relationships between powder compact and ceramics was examined. CT images show the large pores among and in granules as well as images taken by the optical microscopy. However, the external shapes of compressed granules were clearly observed by the optical microscopy. In ceramics, lots of ark cracks were detected well in micro CT images, whereas only shadows of coarse defects were observed in the optical microscopy. Many large defects were derived from interstices between granules and dimples in granules. Some large defects which were present in green compact and survived the densification process of sintering.

1. Introduction

Coarse defects are present in ceramics, reducing the mechanical property and reliability. New optical microscopy successfully revealed their characteristics for the first time, allowing a direct comparison between the characteristics of coarse defects and the mechanical properties of ceramics [1-11]. Very good agreement was noted among the simulated strength and its distribution, and those determined by direct measurement [12-14]. Clearly, the formation mechanism of these coarse defects must be understood in detail for drastic improvement of properties and reliability in ceramics. A study with an optical microscope revealed that these coarse defects are formed from non-uniformity in the powder compact of alumina powder during sintering, or densification process. Non-uniformity over a certain degree appeared to be transformed into coarse defects in ceramics. Recently, the micro-focus x-ray computed tomography (micro CT) has made a great progress and has started to be used to analyze internal structure in dental materials, etc [15,16]. The micro CT is a useful tool for non-destructive visualization of bone and tooth structures, and is expected for ceramic materials. The objective of this study is to examine the internal coarse defects in alumina powder compact before and after firing using micro-focus x-ray computed tomography (micro CT), and compare the micro CT images obtained with the optical microscopy.

2. Experiment

The alumina powder compact and ceramics (Alumina Referceram, AL-1) were used for observation. The alumina powder compact was formed by dry-pressing method using spray-dried granules (Fig.1). The relative density of alumina ceramics was ~ 98%. The powder compact and alumina ceramics were cut to a cubic 1mm x 1mm x 1mm on an each side. The samples were observed by micro focus x-ray computed tomography (micro CT) (SkyScan 1172) with a voltage of 40-100kV and a current 100-250 µA. It is possible to detect internal pores larger than 0.85 µm. Obtained image data was analyzed using 2D/3D software (SkyScan CTAn).

For observation by the optical microscopy, the samples were sliced and polished to 100 µm thick. Powder compact was made transparent with an adequate immersion liquid. The methylene iodide has a refractive index 1.74, which is almost the same with that of alumina. The internal microstructure was observed with an optical microscope in transmission mode (Olympus BX51).

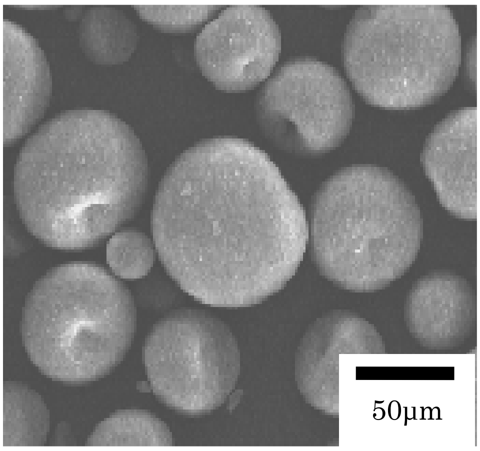

Fig. 1 SEM micrograph for alumina granules used in this study

After firing, thinned ceramics with 100 µm was observed directly with an optical microscope in transmission mode. Coarse defects in the ceramics were characterized in detail with SEM after the specimen was polished down to the depth of the defects.

3. Results and Discussion

(1) Internal structure of powder compacts

Figure 2 shows the internal structures of the alumina powder compact taken by the micro CT. Figure 3 shows the image taken by the optical microscopy. Both figures show circular shape of granules, some coarse defects between granules, and dimples inside of granules as a black spot. The trace of granules and dimple inside granules are very clearly observed in the optical micrograph (Fig. 3), whereas the morphology of coarse defects in micro CT images is ambiguous. In micro CT, the large pore which has zero density, are easily detected due to difference of adsorption of x-ray between particles and pore. However, fine pores among the primary particles and the interstices of deformed granules are not found, since they have similar density each other. This is a reason why the shapes of granules are confused in micro CT images.

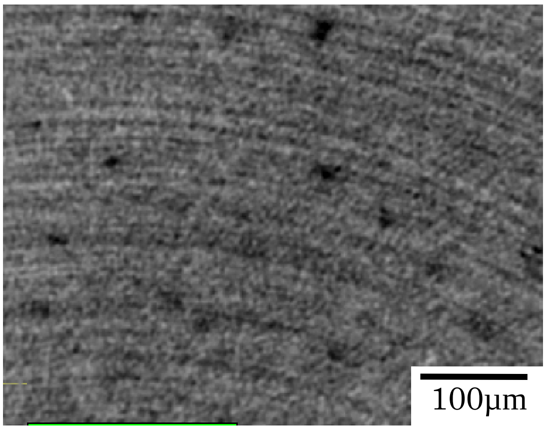

Fig. 2 Internal microstructure of powder compact taken by the micro CT

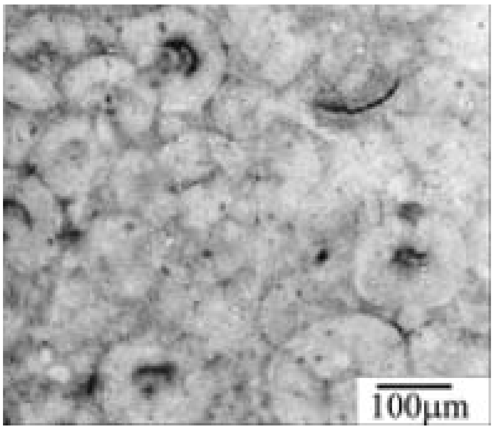

Fig. 3 Internal microstructure taken by the optical microscopy

(2) Coarse defects in alumina ceramics

Figure 4 shows the internal structures of the alumina ceramics taken by the micro CT. There are lots of large defects with several 10 µm to 100 µm in length. The coarse defects distributes homogeneously in ceramics. Shape of coarse defects is not spherical but crack type. This result suggests that interstices among granules and dimple in granules remain even after firing.

Figure 5 shows the structure of alumina ceramics taken by the optical microscopy Fig. 5(a) and the SEM micrograph (Fig. 5(b)) of an extremely large crack found at center of the optical micrograph. Sample thickness is around 100 µm. Many dark spots are noted in ceramics in Fig. 5(a), which correspond to pores. The biggest one appears to be developed from dimple of a granule. This black region was observed by SEM in detail (Fig. 5(b)). This crack is a trace of dimple left in ceramics after sintering. This crack is also detected in micro CT. The results show that the size of crack is clear in the optical microscopy, but the detail of each crack is cloudy.

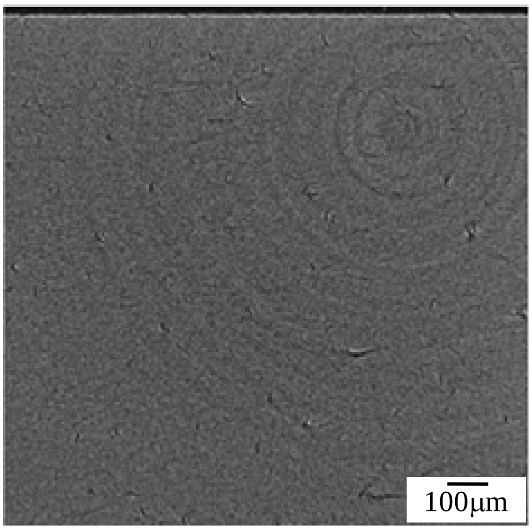

Fig. 4 Internal microstructure of alumina ceramics taken by the micro CT

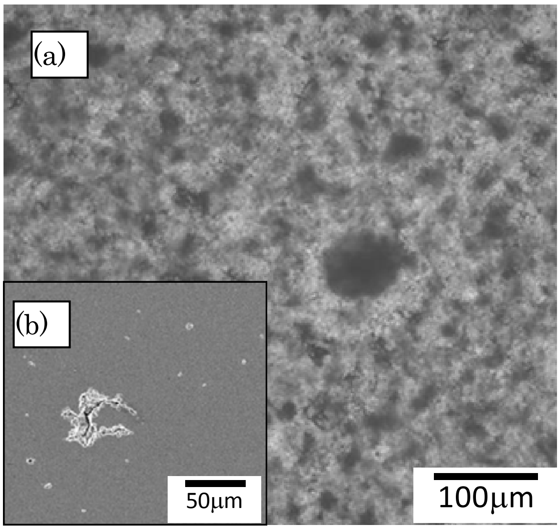

Fig. 5 Internal microstructure of alumina ceramics taken by optical microscopy (a), and SEM micrograph of a coarse defect appeared by polishing at same position(b).

(3) Various defects in alumina ceramics

Figure 6 shows various coarse defects in alumina ceramics and each detailed images taken by micro CT. The coarse defects with about 60 µm (Fig. 6(a)) is at triple points of granules. In Fig. 6(b), there is a circular defect with 30 µm, which is derived from dimples of granules. Finer defects with <10 µm can be observed.

4. Conclusion

The internal coarse defects in alumina ceramics and powder compact were characterized by micro-focus x-ray computed tomography (micro CT) and the usual optical microscopy with thinned sample. The large pores among and/or in granules in the powder compact was observed by micro CT. However, the external shapes of compressed granules were ambiguous compared to the optical microscopy. In ceramics, lots of cracks were detected well in micro CT. The origins of many large defects were discussed from each shape of coarse defects. Interstices between granules and dimples in granules in powder compact are left in ceramics after sintering.

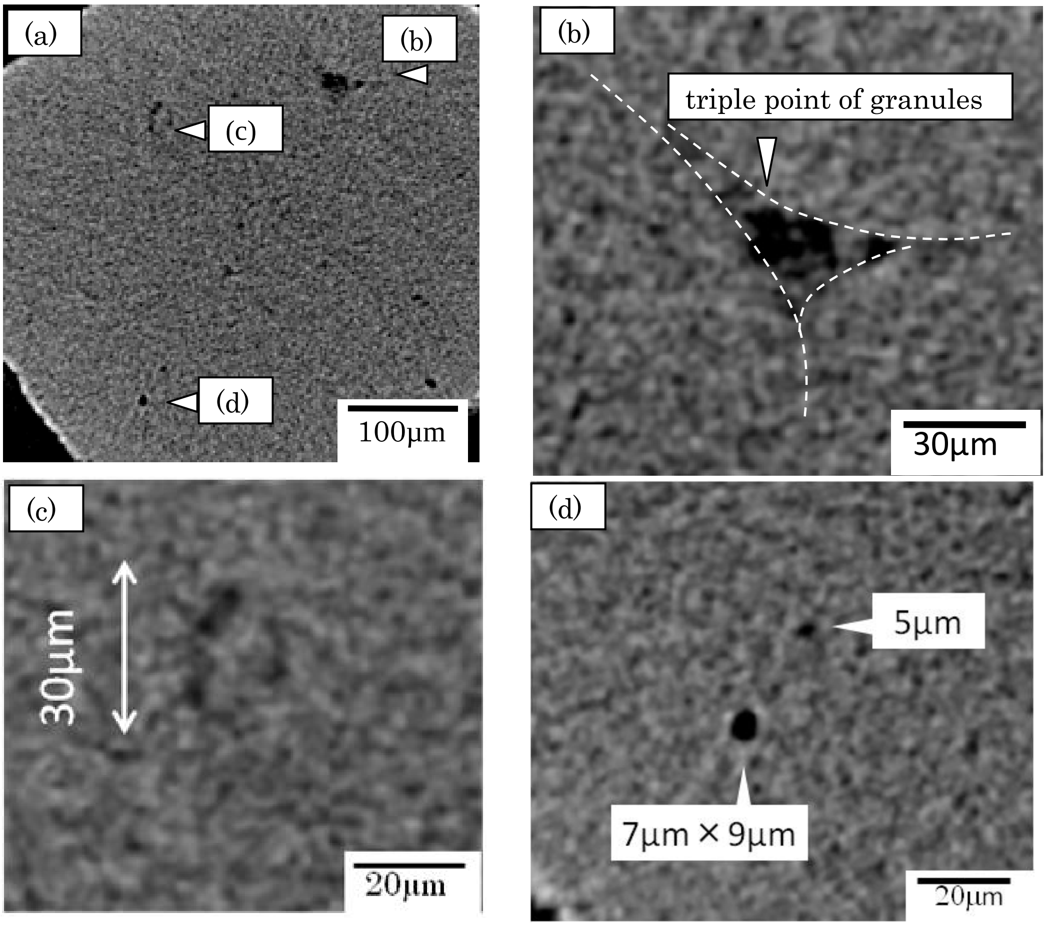

Fig. 6 Various coarse defects of alumina ceramics taken by micro CT (a), (b) three points between granules, (c) dimple of granules and (d)fine pores in alumina ceramics.

Acknowledgments

This work was supported by Program for High Reliable Materials Design and Manufacturing in Nagaoka University of Technology. The authors thanks to Prof. Komatsu, Prof. Kamado and Prof. Nakayama for observation of micro-focus x-ray computed tomography.

References

[1] F. F. Lange, J.Am.Ceram.Soc., **72** (1989) 3.
[2] F. F. Lange, J.Am.Ceram.Soc., **66** (1983) 396.
[3] K. Uematsu, J-Y. Kim, Z. Kato, N. Uchida and K. Saito, J.Ceram.Soc.Japan, **98** (1990) 515.
[4] K. Uematsu, J-Y.Kim, M.Miyashita, N.Uchida and K. Saito, J.Am.Ceram.Soc., **73** (1990) 2555.
[5] K. Uematsu, M. Miyashita, J-Y. Kim, Z. Kato and N. Uchida, J.Am.Ceram.Soc., **74** (1991) 2170.
[6] K. Uematsu, M. Miyashita, J-Y. Kim and N. Uchida, J.Am.Ceram.Soc., **75** (1992) 1016.
[7] J-Y. Kim M. Miyashita and N. Uchida, J.Am.Ceram.Soc., **27** (1992) 6609.
[8] M. Miyashita, J-Y. Kim, Z. Kato, N. Uchida and K. Uematsu, J.Ceram.Soc.Japan., **100** (1992) 1357.
[9] K.Uematsu, Powder Technology, **88** (1996) 291.
[10] N. Shinohara, M. Okumiya, T. Hotta, K. Nakahira, M. Naito and K. Uematsu, J. Mater. Sci., **34** (1999) 4271.
[11] K.Sato, S. Tanaka, N. Uchida and K. Uematsu, J. Ceram.Soc.Japan, **111** (2003) 525.

[12] Y. Zhang, M. Inoue, N. Uchida and K. Uematsu, J. Mater. Res., **14** (1999) 3370.
[13] S. Nakamura, S. Tanaka, Z. Kato and K. Uematsu, J.Am.Ceram.Soc., **92** (2009) 688.
[14] S. Nakamura, S. Tanaka, R. Furushima, K.Sato and K. Uematsu, J.Ceram.Soc.Japan, **117** (2009) 742.
[15] T. Hayakawa, H. Mishima, I. Yokota, T. Sakae, Y. Kozawa and K. Nemotoet, Dental Materials Journal, **19** (2000) 87.
[16] T. Nakamura, K. Wakabayashi, Y. Kawamura, S. Kinuta, Y. Mutobe and H. Yatani, Dental Materials Journal, **26** (2007) 598.

(Received: 1 June, 2012, Accepted: 12 June, 2012)

Transactions on GIGAKU **1**(2012)01021/1-6

Ultrasound Effect of Interpenetrated Hydrogels Having Hydrogen Bonding Networks in Poly(Vinylalcohol)/Poly(2-Hydroxyethyl Methacrylate) by Using FT-IR Spectroscopy

Kazuki Nakasone, Venegas S. Josue Addiel, Motohiro Tagaya, Takaomi Kobayashi*
Department of Material Science and Technology, Nagaoka University of Technology
1603-1 Kamitomioka, Nagaoka, Niigata 940-2188, Japan
**E-mail: takaomi@nagaokaut.ac.jp*

In hydrogels made of interpenetrated polyvinylalcohol (PVA) and poly 2-hydroxyethyl methacrylate (PHEMA), ultrasound (US) influenced to change breaking ability of hydrogen bonds between both polymers. When the PHEMA content in the interpenetrating hydrogel was changed from 10wt% to 20wt%, the IR band intensity of the OH stretching band at 3400 cm^{-1} was decreased by the exposure of US at the frequency of 43 kHz and output power of 8.5 W. This result indicated that the hydrogen bonding both PHEMA and PVA segments were broken by the US. The loose penetration in the 10wt% hydrogels could be easily influenced by the US exposure for breaking hydrogen bondings, which loosely formed the interpenetration between PHEMA and PVA.

1. Introduction

Ultrasound (US) treatment is known as a non-conventional and environmentally clean technology for some industrial uses. For mechanical engineering, cleaning industries, and health diagnosis, the US has been used to promote both physical and chemical processes. Therefore, US technology has become attractive to chemists and chemical engineers for various purposes in areas as diverse as electrochemistry, food technology, synthetic chemistry, materials science, and nanotechnology [1,2]. Therefore, most works related to US are advancing. The origin of such sonication effects on heterogeneous processes is known. Among them, it was reported that US influenced strongly on breaking hydrogen bonding between poly acrylic acid (PAA) and Al_2O_3 in aqueous slurry solution [3]. The US absorption caused a significant decrease in the slurry viscosity, because of the evidence supported by breaking the hydrogen bond networks in the aqueous slurries due to US stress. According to the reported researches, it was established that the US led to change breaking ability of hydrogen bonds of aqueous polymers of acrylic acid and *N*-isopropyl acrylamide [4].

On the other hand, interpenetrating polymer network (IPN) is a polymer comprising two or more networks which are interlaced on a polymer scale but not covalent bonded to each other. These networks are entangled in such a way that they are connected and cannot be pulled apart, but not bonded to each other by any chemical bond [5,6]. It was reported that PVA with interpenetrating PAA, Poly 2-hyroxyethyl methacrylate (PHEMA) was prepared by UV radiation method for polymer electrolyte membrane [7,8]. These kinds of IPN type hydrogels were cross-linked by hydrogen bond. Therefore, we expected to control their hydrogen bonding networks by using US stimuli since these kinds of work in hydrophilic polymer gels containing water were not well known in view points of ultrasound effects. In this study, the PVA/PHEMA hydrogels were cross-linked by both hydrogen bond and entangled polymer chains (Scheme 1), and applied for the purpose of examination of US effect on the hydrogen bonding networks of IPN hydrogels.

2. Experiment

2.1. Materials

The experimental procedure of preparation of IPN hydrogel of PVA and PHEMA is as follows. The 87.0~89.0 mol% hydrolyzed PVA (DP=1700) was purchased from Kuraray, Ltd.. 2-hydroxyethyl methacrylate (HEMA) and Ammonium persulfate (APS) were purchased from

Nacalai Tesque, Inc. All chemicals were used without further purification.

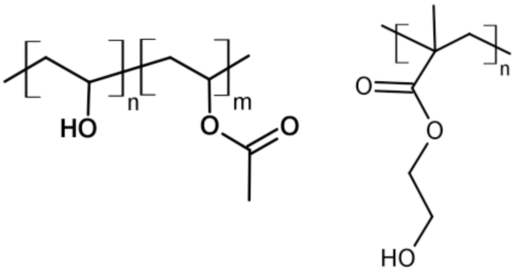

(a) PVA (b) PHEMA

Scheme 1 Chemical structures of (a) PVA and (b) poly HEMA for IPN hydrogels

2.2. Synthesis of interpenetrating hydrogels

Interpenetrated PVA/PHEMA hydrogels were prepared as following procedure (Figure 1). Aqueous solution of 10wt% PVA was mixed with 10 or 20wt% of HEMA having 1wt% APS used as initiator of HEMA polymerization. The mixture solution was spread in vial (35 mm diameter and 65 mm height) and kept at 50°C for 12 h under nitrogen atmosphere. The resultant white solid (in Figure 1) was well washed with excess of distilled water in order to remove the HEMA monomer from the hydrogel block. Here, the polymers of PVA/PHEMA prepared from 10wt% and 20wt% of HEMA concentration were abbreviated as PVA90PHEMA10 and PVA80PHEMA20, respectively.

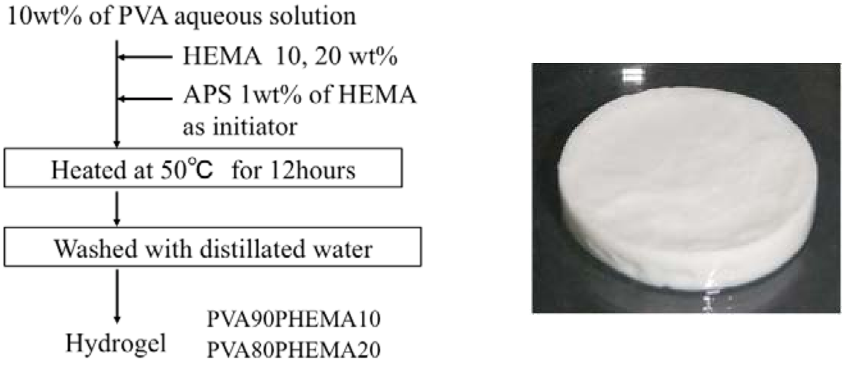

Fig. 1 Preparation procedure of IPN PVA/PHEMA hydrogels (left side) and photograph of PVA90PHEMA10 (right side).

2.3. Measurement of US effect on PVA/PHEMA hydrogels

The US equipment used in the present work was a sonoreactor (HSR-305R, Honda Electronics Co., Ltd.) that was connected with amplifier (HSA4012, NF Corporation) and Multi function synthesizer (WF1943B, NF Corporation) passing through matching box. As shown in Figure 2, the US was exposed to the sample hydrogel sandwiched by CaF_2 window plates (31.5 mm diameter and 1.5 mm thickness) at 25°C for 10 min. The input power of the US to the transducer was 50 W at 43 kHz and the exposed power into the water bath was 8.5 W, which was evaluated with calorimetric method.

As shown in Figure 1, the white hydrogels were obtained after polymerization. To obtain information of the chemical changes in the hydrogels, Fourier transform infrared (FT-IR) spectra of the hydrogels were recorded on a FT-IR spectrophotometer (FT-IR/4100, JAS.CO) in transmission mode in two CaF_2 windows (Pier Optics Co., Ltd.). For the preparation of the sample solutions, firstly, about 1 mg of the hydrogel sliced was put on the CaF_2 window and then 0.1 μl of water were slowly dropped to the gel surface. The transparent solution was left to rest for one hour and then the hydrogel was covered with another CaF_2 plate. The edges of the CaF_2 windows were sealed using teflon tape in order to prevent water penetration through the US exposure in the water bath. The FT-IR spectra were measured in transmittance mode before and after the US exposure was done for 5 min and 10 min.

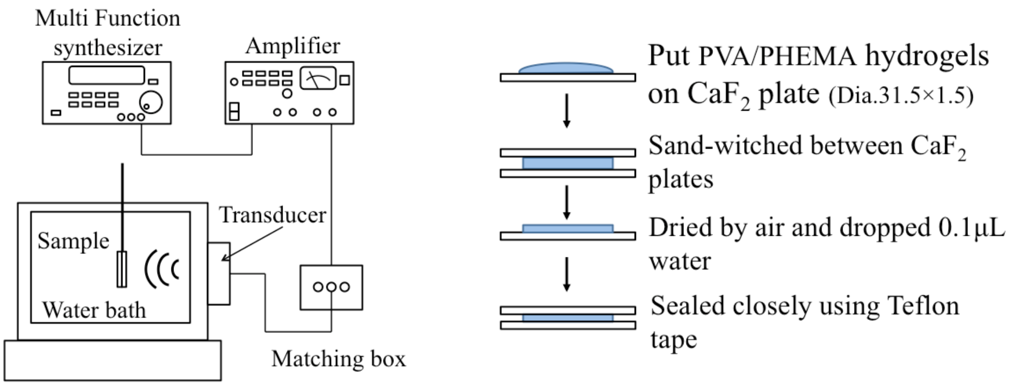

Fig. 2 Scheme showing the experimental setting for the measurement of US exposure to PVA/PHEMA hydrogel in US water bath and preparation of hydrogels for FT-IR measurement

3. Results and Discussion

Before investigation of US effect, the viscoelastic properties of the PVA90PHEMA10 and PVA80PHEMA20 were examined. Figure 3 shows the relationship between strain (%) and storage and loss elastic modulus (GPa) for the IPN hydrogels. The comparison in both hydrogels suggested that the viscoelastic data of the PVA80PHEMA20 included highly entangled polymer chains, which implied formation of rigid networks. Actually, the water contents of the PVA90PHEMA10 and PVA80PHEMA20 were 380% and 320%, respectively. This demonstrated that higher PHEMA content decreased hydrophilicity of the hydrogels.

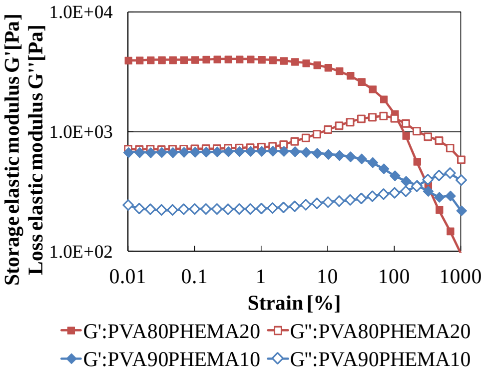

Fig. 3 Viscoelastic behaviors (G' and G'') of the IPN PVA/PHEMA hydrogels

Figure 4 shows the FT-IR spectra of PVA90PHEMA10 and PVA80PHEMA10. The spectra were measured after 5 or 10 min exposure of US for the hydrogels sandwiched with CaF_2 plates. These indicated that the band intensities of hydrogen bonded OH stretching at around 3400 cm^{-1} and C=O stretching at around 1730 cm^{-1} were decreased after the US exposure with depending on US irradiation time. The peak attributed to H_2O at around 2150 cm^{-1} was shifted toward low wavenumber. Herein, the spectral band in 2000-2300 cm^{-1} resulted in hydrogen bonding of water to the hydrogels. For the PVA90PHEMA10, the hydrogen bonding band shifted from 2160 cm^{-1} to 2100 cm^{-1} with the increase of the US exposure time. Additionally, the OH stretching appeared at

3100 cm^{-1} was changed in the intensity. Namely, the IR intensity at 3100 cm^{-1} was intense when the exposure time was increased to 10 min. These spectral changes indicated that free H_2O were generated by US exposure. However, the PVA80PHEMA20 showed less change of the spectra when the US was similarly exposed. Slight change of the hydrogen band of water was shifted toward 2110 cm^{-1} from meaning the 2120 cm^{-1}. Also, the OH stretching band at 3100 cm^{-1} showed no change even though US was exposed. This meant that the interpenetration of the PHEMA segments highly bound with the PVA segments as the PVA80PHEMA20 hydrogel and regulated water mobility in the hydrogel.

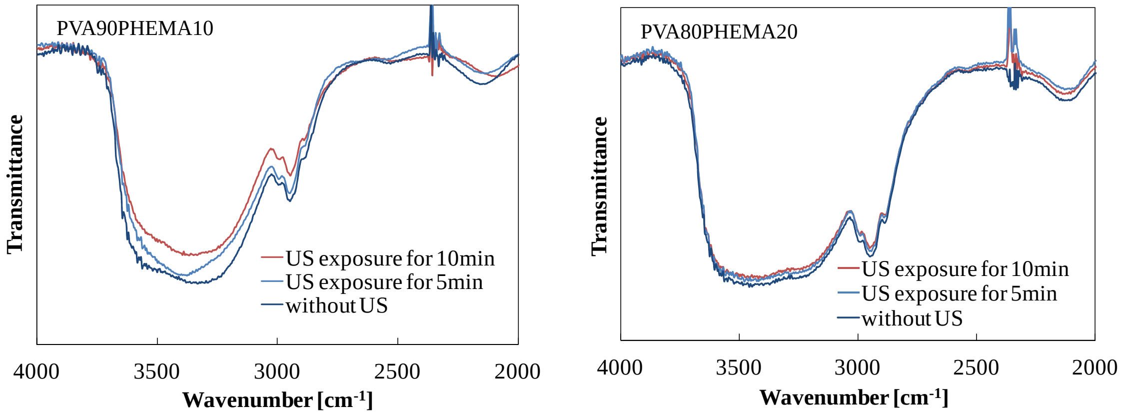

Fig. 4 FT-IR spectra of the IPN PVA/PHEMA hydrogels swelling by water at the different US exposure times.

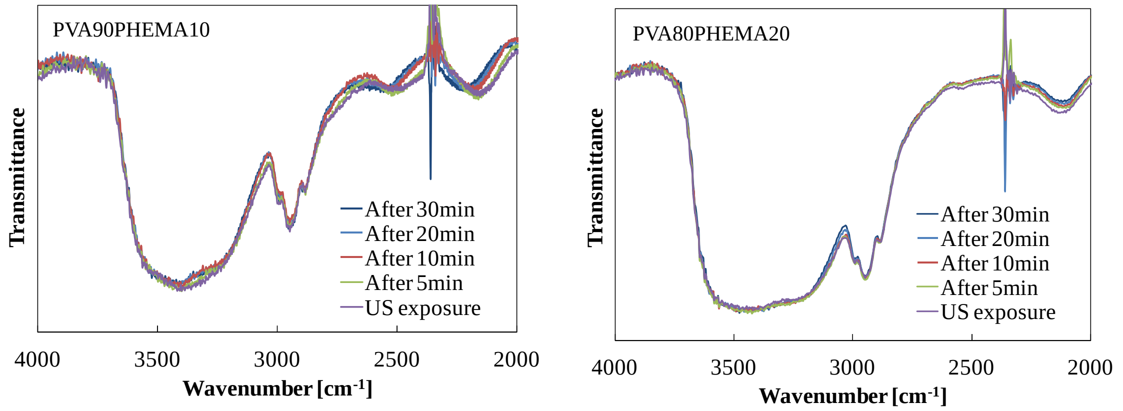

Fig. 5 FT-IR spectral changes of the IPN PVA/PHEMA hydrogels swelling after stopping US exposure.

As shown in Figure 5 for the FT-IR spectra measured after the US stopping water band near 2100 cm^{-1} changed to show higher wavenumber shift. Here, the exposure time of the US was 10 min. Their FT-IR spectra of the PVA90PHEMA10 after stopping US exposure showed that peak at around 2150 cm^{-1} was shifted toward 2200 cm^{-1} with increasing time, but the OH band about 3400 cm^{-1} was changed insignificantly (Figure 6). It was evidenced that the hydrogen bonds related with water were broken by US exposure and recovered with stopping US exposure. On the other hands, there was insignificant change of the FT-IR spectra of PVA80PHEMA20 which showed rigid IPN gel networks as indicated in Figure 3. For the viscoelastic data in PVA80PHEMA20, it was reasonable to consider that the highly entangled polymer chains seemed to restrict the US action for breaking hydrogen bonds networks. Therefore, water release from gel microenvironment might be weaker than that of the PVA90PHEMA10 showing loosed IPN networks.

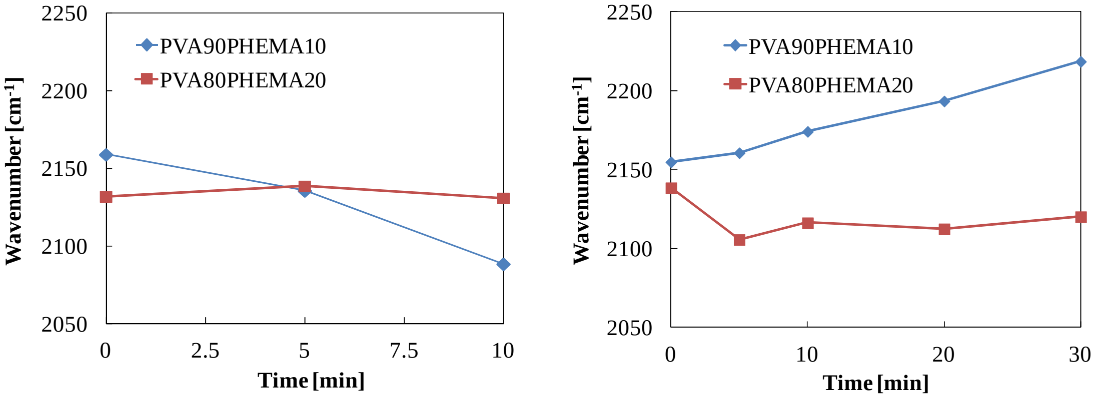

Fig. 6 FT-IR spectra of the IPN PVA/PHEMA hydrogels swelling by water.

It is very interesting to know the ultrasound effect on the change in the FAT-IR spectra of PVA and PHEMA with water. In order to consider the spectral change, we measured FT-IR spectra for aqueous PVA as well as the IPN hydrogels. As presented in Figure 7a, the aqueous PVA demonstrated quietly different change in the OH band when the US was exposed. The US action enhanced OH stretching at 3100 cm^{-1}. This indicated the US effected on the mobility of the stretching band for the PVA polymer chains, which were not restricted by IPN networks. It seemed to be breakage of hydrogen bonds with water to release from the polymer microenvironment. As shown for the PHEMA-water system in Figure 7b, the IR band intensity at 3400 cm^{-1} was less enhanced rather than that of the PVA-water system. This meant that similar effect was happened in the PHEMA. It was interesting to note that the maximum wavenumber for the OH stretching was different in PVA and PHEMA with 3400 cm^{-1} and 3500-3600 cm^{-1}, respectively.

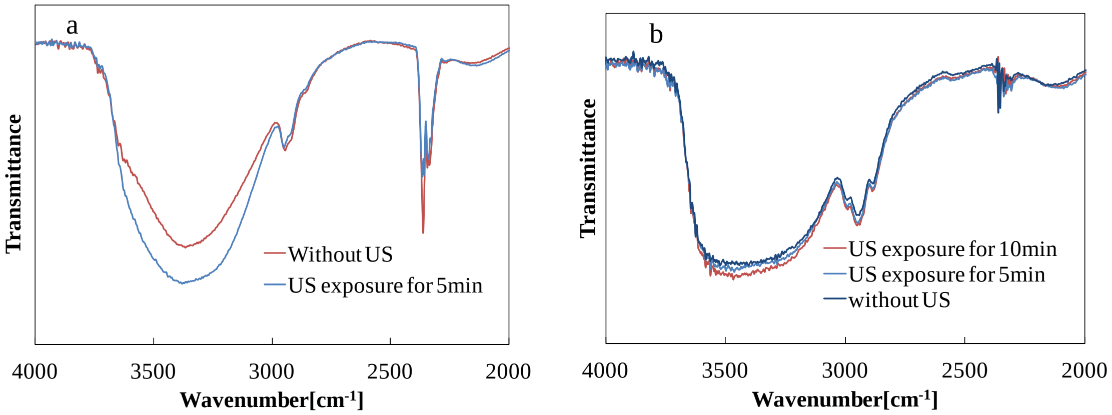

Fig. 7 Comparison of FT-IR spectra of (a) aqueous PVA and (b) swelled PHEMA with and without the US exposure.

As reported by Kitano et al. [9] with determination of a Fourier self-deconvolution of the original O-H stretching bands of water molecules, the bulk water systems of polyethylene glycol-aqueous solutions showed that the characteristics of water were determined by the analysis of the band for a water cluster. For example, the O-H stretching of pure water into five Gaussian components were assigned at 3620, 3500, 3390, and 3215 cm^{-1} to a free water, water molecules whose hydrogen bonds are partly broken, fully hydrogen-bonded water molecules uncorrelated (not in-phase), and fully hydrogen-bonded water molecules correlated (in-phase, both donation of the protons and acceptance of the protons with both of the electron lone pairs). Therefore the 3400 cm^{-1} in PVA assigned with fully hydrogen-bonded water molecules and the 3600 cm^{-1} band with free water molecules. Thus the

US exposure made partially free water from the polymer microenvironment of IPN networks.

4. Conclusion

The IPN hydrogels made of PVA and PHEMA were used for investigation of the US effect. As influenced to change breaking ability of hydrogen bonds between both polymers, the results clearly showed in FT-IR spectra that interpenetrated hydrogen bonds in PVA/PHEMA were broken by the exposure of the US at 43 kHz and 8.5 W. In the case of PVA90PHEMA10, FT-IR spectra for hydrogen bonds around 3400 cm^{-1} were changed for the intensity of the OH stretching band by US exposure. This meant that the US broke the hydrogen bands of the OH groups of the interpenetrated PHEMA and PVA, and water molecules interacted with the hydrogel. The less change in the PVA80PHEMA20 was observed by the US exposure. The tight interpenetration of the PHEMA and PVA segments caused that low mobility of the hydrogel responded to the less effect of the ultrasound for the water penetration into the matrix. These evidences were shown that the tendency depended on the component of interpenetration of PVA and PHEMA for the formation of free water molecules left from the IPN hydrogels.

References

[1] K.S. Suslick and G.J. Price, Annu. Rev. Mater. Sci. **29** (1999) 295.

[2] T.J. Mason, Sonochemistry: The Uses of Ultrasound in Chemistry, The Royal Society of Chemistry, 1990, p. 132.

[3] N.L. Ngoc and T. Kobayashi, Ultrason. Sonochem., **17** (2010) 186.

[4] N.L. Ngoc and T. Kobayashi, Ultrason. Sonochem., **18** (2011) 1185.

[5] L.H. Sperling, Interpenetrating Polymer Networks, American Chemical Society, 1994, p.3–38

[6] Y. Osada and K. Kajiwara, Gels Handbook, NTS, 1997, p. 63

[7] J.M. Yang, H.Z. Wang, and C.C. Yang, J. Membr. Sci., **322** (2008) 74.

[8] J.M. Yang, C.Y. Chiang, H.Z. Wang, and C.C. Yang, J. Membr. Sci., **341** (2009) 186.

[9] H. Kitano, K. Ichikawa, M. Ide, M. Fukuda, and W. Mizuno, Langmuir, **17** (2001) 1889.

(Received: 18 April, 2012, Accepted: 18 June, 2012)

Transactions on GIGAKU ***1*** *(2012)01022/1-6*

Crack Self-Repairing of Nano-Metal/Al_2O_3 Hybrid Materials

Makoto Nanko[1], Daisuke Maruoka[2], Pham Vu Hai[3] and Nguyen Dang Thuy[3]
[1]*Nagaoka University of Technology,*
[2]*Graduate School of Engineering, Nagaoka University of Technology,*
(Kamitomioka, Nagaoka, Niigata, 940-2188, Japan, Email: nanko@mech.nagaokaut.ac.jp)
[3]*Hanoi University of Science and Technology*
(1 Dai Co Viet Road, Hanoi, Vietnam)

This paper reviews shortly the crack-repairing of Al_2O_3 based hybrid materials dispersed with nano-sized metallic particles. Al_2O_3 dispersed with nano-Ni particles and nano-Co particles shows crack-repairing function. The crack-repairing of these systems is caused by the formation of the oxide product formed by the outward diffusion of cations. Doping of Si and Y into Al_2O_3 matrix is discussed on crack-repairing and high-temperature oxidation of Al_2O_3 dispersed with nano-Ni particles. On the other hand, no crack-repairing was observed in Al_2O_3 dispersed with Mo.

1. Introduction

Al_2O_3-based ceramics have been used in structural applications. However they have some disadvantages such as low fracture toughness, surface crack sensitivity for decreasing fracture strength. Al_2O_3 based composites with nano-sized metallic particles (referred as to metal/Al_2O_3) are expected as structural materials with high mechanical strength, high hardness and excellent thermal and chemical stability [1-19]. As well some of metal/Al_2O_3 have any other useful and unique functions, which can be adapted in structural components. For example, dispersion of nano-Fe, Co or Ni results in magnetism into Al_2O_3 based-ceramics.

Ando and his colleges have discovered the crack-repairing in some ceramic composites dispersed with SiC particles or whiskers by a thermal oxidation [20-25]. In high-temperature applications of those structural ceramics, crack-repairing takes place autonomously. Crack-repairing via heat treatment was observed in monolithic Al_2O_3 [26, 27], crack-repairing of those composites is available for larger cracks and by treatment at lower temperature than the monolithic Al_2O_3. The crack- repairing of those composites is caused by filling surface cracks with the oxidation product by high-temperature oxidation of the dispersoid. Crack-filling by the oxidation product decreases stress concentration to surface crack. Surface cracks do not behave as the fracture origin. The mechanical strength will be recovered up to the level of the virgin materials without surface cracks. The similar phenomenon of crack- repairing was observed in NiAl/Al_2O_3 [28], but not in TiC/Al_2O_3 [29].

Our research group has discovered newly crack-repairing of nano-Ni/Al_2O_3 [30, 31]. The systematic studies of crack-repairing of the Al_2O_3-based composites are necessary for understanding the mechanism of the crack-repairing of the Al_2O_3-based composites and to design the composites with faster crack-repairing and better mechanical properties. In the present paper, crack-repairing of those composites is discussed as well as high-temperature oxidation in order to understand the kinetic mechanism of the crack-repairing.

2. Experiments

Al_2O_3-based materials dispersed with 5 vol% Ni, Co or Mo were prepared in the present study. A slurry consisting of a commercial Al_2O_3 (average particle size: 0.4 μm, purity: 99.99%) and nickel or cobalt nitrate for nano-Ni or Co/Al_2O_3 was produced with distilled water. In the case of nano-Mo/Al_2O_3, molybdenum trioxide powder (average particle size: 0.7 μm) was mixed with the Al_2O_3 powder by ball-milling. Those bulk specimens were sintered by using pulsed electric current sintering at 1400°C under 40 MPa in uni-axial pressure during holding time of 5 min in vacuum.

Vickers hardness was measured with loading in 1.9 N. Fracture toughness was evaluated by using the IF method by using Niihara's equation [32].

Three Vickers indentations with loading at 49 and 490 N for 10 s were conducted into a sample to possess 12 cracks. The cracks introduced were semi-circular with approximately 350 μm in depth and 200 μm in length. Samples introduced cracks were heat-treated at temperature ranging from 600 to 1300°C for 1-48 h in air. Nano-Ni/Al_2O_3 were cut 3×4×26 mm and polished until mirror finish. The 3-point bending test at room temperature was conducted to as-cracked samples and ones oxidized at 1200°C for 6 h in air. The crosshead speed was 0.5 mm/min. Samples were evaluated by using scanning electron microscopy (SEM) for microstructure and X-ray diffraction for phase identification.

3. Results and Discussion

(1) Mechanical properties of nano-metal/ceramic hybrid materials

Table 1 lists mechanical properties of various nano-metal/Al_2O_3. Nano-metal/Al_2O_3 has excellent mechanical properties as high as or higher than 500 MPa and 5 $MPam^{0.5}$.

Table.1 Mechanical properties of various nano-metal/ceramic hybrid materials

Sample	nano-Ni/Al_2O_3	nano-Co/Al_2O_3	nano-Mo/Al_2O_3
Grain Size: Al_2O_3/ Metal [μm]	1.1/ 0.3	1.1/ 0.3	1.1/ 0.3
Vickers Hardness [GPa]	17.1	16.1	19.9
Fracture Toughness [$MPam^{0.5}$]	5.83	5.81	4.64
Bending Strength [MPa]	497	710	490

(2) Crack-Repairing of nano-metal/ceramic hybrid materials

Figure 1 shows the SEM images on the surface of various Al_2O_3-based hybrid materials with surface cracks before/after a thermal oxidation process. Figure 2 shows bending strength of various Al_2O_3-based hybrid materials. Surface cracks on nano-Ni/Al_2O_3 and nano-Co/Al_2O_3 disappear after heat treatment at 1200°C for 6 h in air. The values of bending strength in nano-Ni/Al_2O_3 and nano-Co/Al_2O_3 were recovered by thermal oxidation process. XRD reveals that MAl_2O_4 spinel (M = Ni or Co) was formed on the surface during high-temperature oxidation. Removing surface Ni particles by nitrate acid, $NiAl_2O_4$ was developed on the surface of nano-Ni/Al_2O_3. Those facts mean that the spinel phase was formed by the oxidation of Ni/Co dispersoid with Al_2O_3 matrix and partially by outward diffusion of Ni/Co ions during heat treatment. In the case of nano-Mo/Al_2O_3, the surface cracks disappear via heat treatment at 700°C for 6 h in air. However, the value of bending strength of nano-Mo/Al_2O_3 with surface cracks was not increased after heat treatment. In this materials system, oxidation products, $Al_2(MoO_4)_3$ covered only the surface of nano-Mo/Al_2O_3, not in the inside of the cracks.

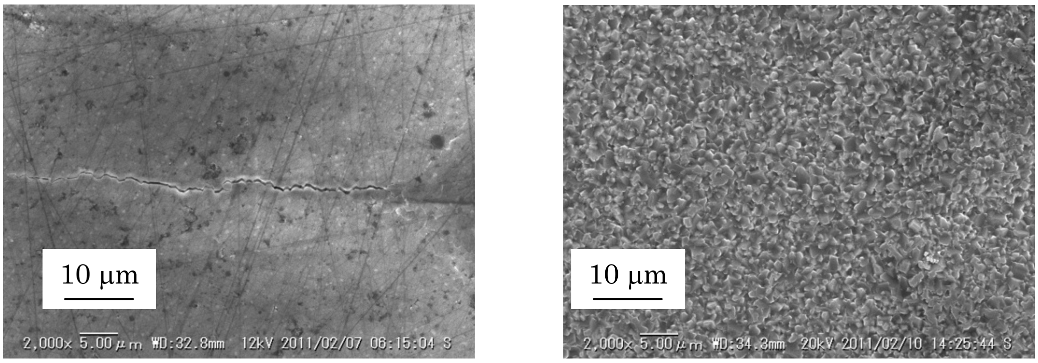

(a) nano-Ni/Al_2O_3

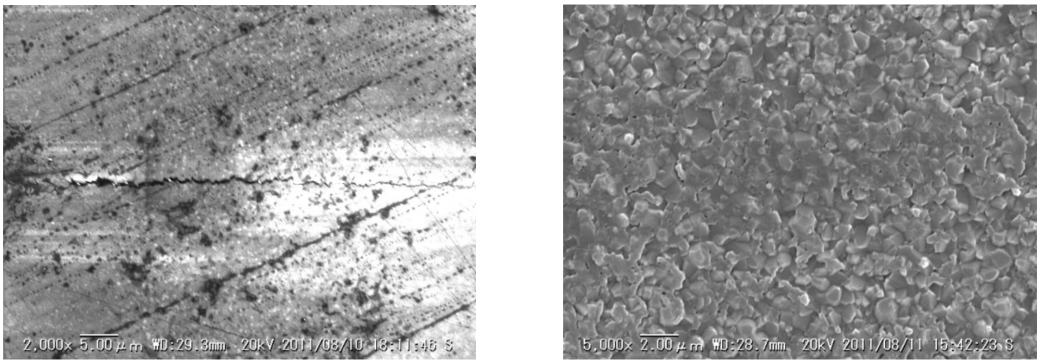

(b) nano-Co/Al_2O_3

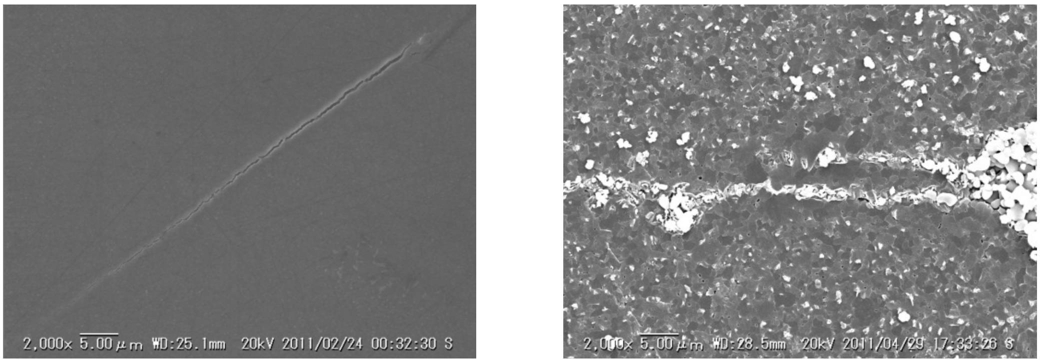

(c) nano-Mo/Al_2O_3

Fig. 1 SEM images on the surface of various Al_2O_3-based hybrid materials with surface cracks before/after a thermal oxidation process. (a) nano-Ni/Al_2O_3 (heat treatment at 1200°C for 6 h in air), (b) nano-Co/Al_2O_3 (heat treatment at 1200°C for 6 h in air), and (c) nano-Mo/Al_2O_3 (heat treatment at 700°C for 6 h in air). The left and right ones show as-cracked and as-heat treated ones, respectively.

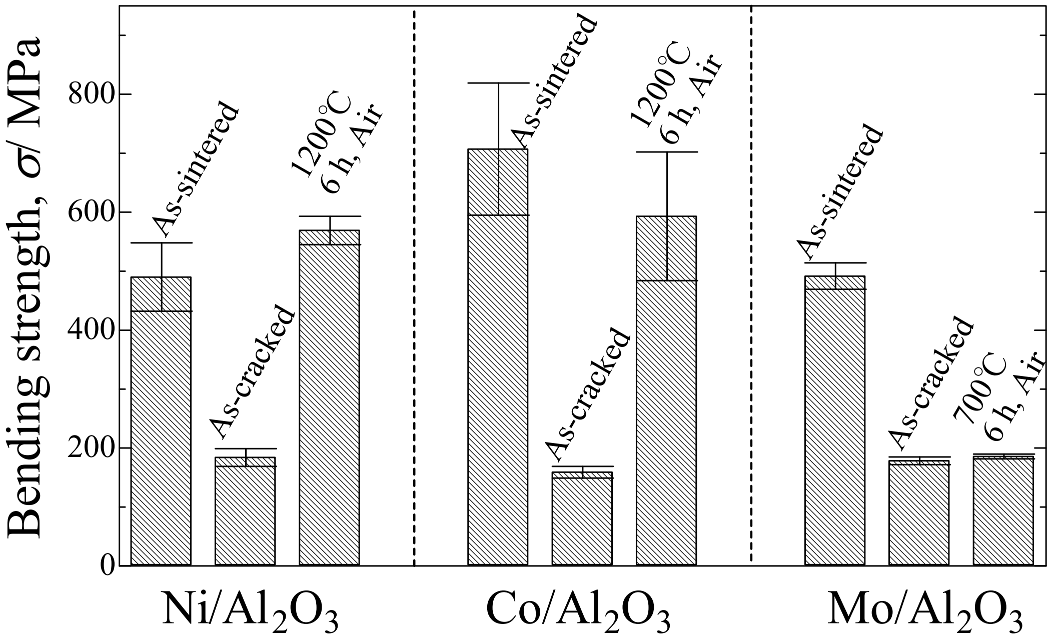

Fig.2 Bending strength of various Al_2O_3-based hybrid materials.

(3) Relationship between high-temperature oxidation and crack-repairing of nano-metal/ceramic hybrid materials

Some nano-metal/Al_2O_3 hybrid materials show the crack-repairing function to recover the mechanical strength degraded by surface cracks. Because the crack-repairing process was an oxidation process at high-temperatures, degradation of the nano-metal/Al_2O_3 hybrid materials should take place. High-temperature oxidation of nano-metal/Al_2O_3 hybrid materials is an oxidation of nano-metallic particles in the Al_2O_3 matrix from the surface of the hybrid materials. Thickness of the oxidized zone was increased in the parabolic manner in the cases of nano-Ni/Al_2O_3 and nano-Co/Al_2O_3. Comparison between oxidation rate and crack-repairing rate is useful for understanding life time of nano-metal/Al_2O_3 hybrid materials.

Figure 3 shows thickness of the oxidized zone and ratio of crack-disappearance as a function of oxidation time in nano-Ni/Al_2O_3 at 1200ºC. Crack-repairing of nano-Ni/Al_2O_3 occurs after the growth of oxidized zone. In fact, recovery of bending strength is completed for 1 h at 1200ºC in nano-Ni/Al_2O_3. Degradation of nano-Ni/Al_2O_3 by heat treatment for crack-repairing is negligible. As well, doping Y and Si into nano-Ni/Al_2O_3 can decrease growth rate of the oxidized zone and gives no significant change in ratio of crack-disappearance by thermal oxidation process [33, 34]. As shown in Fig. 3, thickness of the oxidized zone on Y-doped one is half of the un-doped one. On the other hand, crack-disappearance of Y-doped one is comparable with un-doped one.

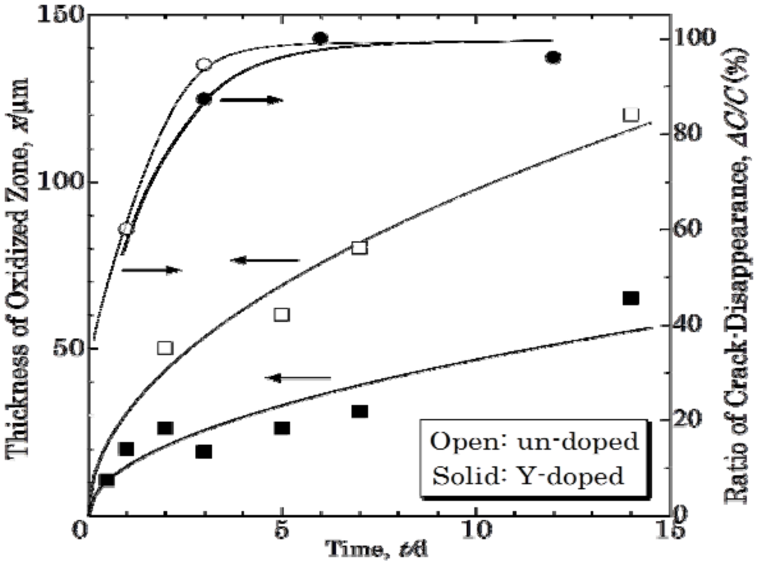

Fig.3 Thickness of the oxidized zone and ratio of crack-disappearance as a function of oxidation time in nano-Ni/Al_2O_3 at 1200ºC

4. Conclusion

Crack-repairing in nano-metal/Al_2O_3 hybrid materials was reported in the present paper. With respect to nano-Ni/Al_2O_3 and nano-Co/Al_2O_3, surface semi-circular cracks with approximately 350 μm in length and 200 μm in depth can be repaired via heat treatment at 1200ºC for 1 h in air as the bending strength was recovered as high as the virgin samples. The surface cracks were filled with the oxidation product, MAl_2O_4 (M = Ni or Co), which is formed by both of oxidation of surface Ni particles and reaction of Al_2O_3 with Ni ions diffused from the inside of the sample. During the heat treatment for crack-repairing, nano-Ni/Al_2O_3 was oxidized from the surface. The oxidation depth was much smaller than the crack size. However, nano-Mo/Al_2O_3 does not have crack-repairing function via a thermal oxidation. Surface of nano-Mo/Al_2O_3 was covered by the oxidation product, $Al_2(MoO_4)_3$, but the cracks was not filled by the product.

Acknowledgments

This work was supported partially from the Grant-in-Aid for Scientific Research from the Ministry of Education, Science, Sports, Culture and Technology, Japan by Program for High Reliable Materials Design and Manufacturing in Nagaoka University of Technology.

References

[1] H. Awaji: *Strength of Ceramic Materials*, (Corona Pub., 2001) pp. 6-8.
[2] K. Niihara: J. Ceram. Soc. Jpn., 99 (2000) 974-982.
[3] M. Nawa, T. Sekino and K. Niihara: J. Jpn. Soc. Powder Powder Metall., 39 (1992) 484-487.
[4] T. Sekino, T. Nakajima and K. Niihara: J. Am. Ceram. Soc., 80 (1997) 1139-1148.
[5] T.Sekino, A. Nakahira, M. Nawa and K. Niihara: J. Jpn. Soc. Powder. Powder. Metall., 38 (1991) 14-18.
[6] T. Matsunaga, U. Leela-Adisorn, Y. Kobayashi, S. M. Choi and H. Awaji: J. Ceram. Soc. Jpn., 113 (2005) 123-125.
[7] T. Isobe, K. Daimon, T. Sato, T. Matsubara, Y. Hikichi and T. Ota: Ceram. Int., 34 (2008) 213-217.
[8] X. Yao, Z. Huang, L. Chen, D. Jiang, S. Tan, D. Michel, G. Wang, L. Mazerolles and J. L. Pastol: Matt. Lett., 59 (2005) 2314-2318.

[9] B. S. Kim, T. Sekino, T. Nakayama, M. Wada, J. S. Lee and K. Niihara: Mat. Res. Innovat., 7 (2003) 57-61.

[10] T. Sekino and K. Niihara: J. Mater. Sci., 32 (1997) 3943-3949.

[11] M. Nawa, T. Sekino and K. Niihara: J. Mater. Sci., 29 (1994) 3185-3192.

[12] L. A. Diaz, A. F. Valdes, A. M. Espino and R. Torrecillas; J. Euro. Ceram. Soc., 23 (2003) 2829-2834,.

[13] W. P. Tai and T. Watanabe: J. Mater. Sci., 33 (1998) 5795-5801.

[14] W. P. Tai, Y. S. Kim and J. G. Kim: Mater. Chem. Phys., 82 (2003) 396-400.

[15] J. Li, X. Ni and G. Wang: J. Alloy. Comp. 440 (2007) 349-356.

[16] X. Shi, Y. Pan and J. Guo: Ceram. Intl., 33 (2007) 1509-1513.

[17] S. N. Hosseini, F. Karimzadeh and M. H. Enayati: Adv. powder Tech., (2011) in press.

[18] Z. Jiang and W. E. Rhine: Chem. Mater., 6 (1994) 1080-1086.

[19] A. Nakahira and K. Niihara: J. Ceram. Soc. Jpn., 100 (1992) 448-453.

[20] M. C. Chu, S. Sato, Y. Kobayashi and K. Ando: Fatig. Fract. Eng. Mater. Struct., 18 (1995) 1019-1029.

[21] K. Houjou, K. Ando, S. P. Liu and S. Sato: J. Euro. Ceram. Soc.. 24 (2004) 2329-2338.

[22] S. K. Lee, M. Ono, W. Nakao, K. Takahashi and K. Ando:, J. Euro. Ceram. Soc., 25 (2005) 3495-3502.

[23] W. Nakao, K. Takahashi and K. Ando, Self-healing of surface crack in structural ceramics, in: S. K. Ghosh(Eds.), Self-healing Materials, Fundamentals, Design Strategies, and Applications, WILEY-VCH, Weinheim, 2009, pp. 183-217.

[24] K. Takahashi, M. Yokouchi, S. K. Lee and K. Ando: J. Am. Ceram. Soc., 86 (2003) 2143-2147.

[25] T. Osada, W. Nakao, K. Takahashi, K. Ando and S. Saito: J. Euro. Ceram. Soc., 27 (2007) 3261-3267.

[26] F. F. Lange and T. K. Gurta, J. Am. Ceram. Soc., 53 (1970) 420-421.

[27] Y. Matsuo, T. Ogasawara, S. Kimura, S. Sato and E. Yasuda: J. Ceram. Soc. Jpn., 99 (1991) 384-389.

[28] O. Abe, Y. Ohwa and Y. Kuranobu, J. Euro. Ceram. Soc., 26 (2005) 689-695.

[29] L. Jun, Z. X. Zheng, H. F. Ding, Z. H. Jin, Fatigue Fract Engng Mater Struct., 27 (2004) 89-97.

[30] A. L. Salas-Villasenor, J. Lemus-Ruiz, M. Nanko and D. Maruoka:,Adv. Mat. Res., 68 (2009) 34-43.

[31] D. Maruoka and M. Nanko: Adv. Mat. Res., 89-91 (2010) 365-370.

[32] K. Niihara: Ceramics Japan, 20 (1985) 12-18.

[32] D. Maruoka and M. Nanko, *Mater. Trans.*,**51** (2010) 1570-1573.

[33] M. Nanko, D. Maruoka and Y. Sato, *Intl. J. Appl. Ceram. Technol.*, 9 (2012) 172-177.

(Received: 16 May, 2012, Accepted: 5 June, 2012)

Transactions on GIGAKU **1**(2012)01023/1-6

Development of Oxygen Sensors Exploiting Hot Spots in $GdBa_2Cu_3O_{7-\delta}$-based Composite Ceramic Rods

Tomoichiro Okamoto, Yuichiro Kuroki, Masasuke Takata[*]
Department of Electrical Engineering, Nagaoka University of Technology,
1603-1 Kamitomioka, Nagaoka 940-2188, Japan
**E-mail: Takata@vos.nagaokaut.ac.jp*

A hot spot, which is a local area glowing orange, appears in a $LnBa_2Cu_3O_{7-\delta}$ (Ln: rare earth element) ceramic rod when a voltage exceeding a certain value is applied to the rod at room temperature. The electrical current running through the hot spot depends strongly on the oxygen partial pressure in ambient atmosphere, which acts as an oxygen sensor without the need for any heating system. The $GdBa_2Cu_3O_{7-\delta}$ rod tends to melt and break by a sustained presence of the hot spot in a high P_{O_2} (~100 kPa). The composite rods containing dispersed high melting point materials such as $BaAl_2O_4$, $BaZrO_3$ and Gd_2BaCuO_5 show a remarkable high durability in the high P_{O_2}. In a low P_{O_2} (< 0.02 kPa), the current decreases to almost zero and the hot spot disappears, resulting in an insensitive rod to oxygen. The composite rods with dispersed CuO detects oxygen even in $P_{O_2} < 0.002$ kPa. The response time is improved by forming Gd_2BaCuO_5 core in $GdBa_2Cu_3O_{7-\delta}$ rod. The results suggest that the performance of hot spot oxygen sensors is improved by using composite materials.

1. Introduction

$LnBa_2Cu_3O_{7-\delta}$ (Ln: rare earth element), which is well known as the high-Tc superconductor, is a typical nonstoichiometric oxide. Oxygen deficiency δ increases with increasing temperature above 400°C [1]. The carrier density decreases with increasing δ, which results in a steep increase in the resistivity [2-4]. In other words, the material shows a positive temperature coefficient of resistivity (PTCR).

The present authors observed the phenomenon that a local area of a $LnBa_2Cu_3O_{7-\delta}$ ceramic rod glows orange once a voltage exceeding a certain value is applied at room temperature as shown in Fig. 1 [5]. The visible glowing area was named a hot spot. The hot spot moves to the negative electrode with the velocity of a few mm/min. The appearance of the hot spot is related to the PTCR characteristic [5-7]. The movement of the hot spot is considered to be caused by the diffusion of oxide ions in the electric field over the hot spot [5-6]. The temperature of the hot spot in air is about 900°C which is almost the same as its sintering temperature [6,8]. The heat treatment using the hot spot can be used as an improvement technique for its transport critical current density [8].

The current running through the rod decreases abruptly when the hot spot appears, and remains constant with increasing voltage [6-9]. This is possible because the size of the hot spot with high resistivity increases linearly with increasing voltage [5-7]. The rod with the hot spot can be used as a constant-current generator without any active component. The current is sensitive to the gas flow

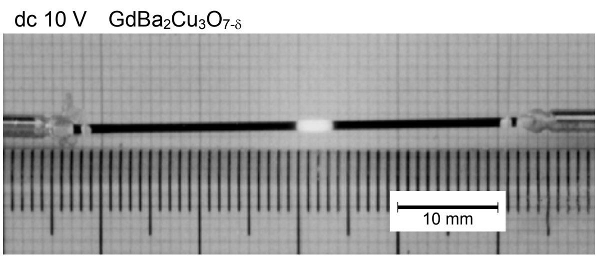

Fig. 1. Photograph of a hot spot appearing on a $GdBa_2Cu_3O_{7-\delta}$ ceramic rod. A dc voltage of 10 V was applied to the rod at room temperature in air.

around the rod, and the rod can be used as a high sensitive gas flow sensor [10]. Since the current vibrates in the form of damped sinusoidal oscillation under low oxygen partial pressure, the rod can be used as a new type of sine wave oscillator [11].

The current after the appearance of the hot spot depends on the oxygen partial pressure in ambient atmosphere, which acts as an oxygen sensor without the need for any heating system [6,10]. This paper reviews shortly the progress in the development of the oxygen sensors exploiting the hot spots appearing in $GdBa_2Cu_3O_{7-\delta}$ (Gd-123) -based composite ceramic rods.

2. General Features of Hot Spot Oxygen Sensor

Figure 2 shows current-voltage characteristics in various Po_2 for Gd-123 ceramic rod prepared by conventional solid state reaction [6]. The current increases linearly with increasing voltage in low voltage region. When the voltage reaches a certain value, the current abruptly decreases and a hot spot appears in the rod. After that the current remains constant with increasing voltage and depends strongly on Po_2. This result means that the oxygen concentration in environment can be evaluated from the current value, which is the principle of the hot spot oxygen sensor [6,10].

Figure 3 shows the oxygen partial pressure dependence of current through the rod with the hot spot. The relationship between the logarithmic current and the logarithmic Po_2 well agrees with a dotted straight line with a slope of 1/6.

When the oxygen content (7-δ) of $LnBa_2Cu_3O_{7-\delta}$ is higher than 6.2, the sample behaves like an oxygen excess (metal deficit) oxide [12]. If the $LnBa_2Cu_3O_{7-\delta}$ is kept at high temperature and the Po_2 is raised, the sample absorbs oxygen that dissociates into holes and oxide ions. The overall reaction is expressed as

$$O_2 = 2\,O_i'' + 4\,h^{\cdot} \qquad (1)$$

where O_i'' is an interstitial divalent oxide ion and $h^{\cdot}$ is a hole. Therefore, the $LnBa_2Cu_3O_{7-\delta}$ essentially has a *p* -type conduction since the excess oxygen plays the role of acceptor. The mass action law for equation (1) is

$$K = \frac{[O_i'']^2\ [h^{\cdot}]^4}{[O_2]} \qquad (2)$$

where K is the equilibrium constant, and $[O_i'']$, $[h^{\cdot}]$ and $[O_2]$ represent the concentrations of

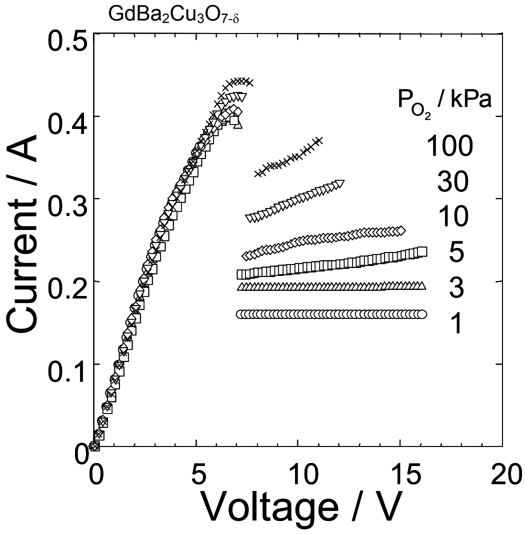

Fig. 2. Current-voltage characteristics in various Po_2 [6].

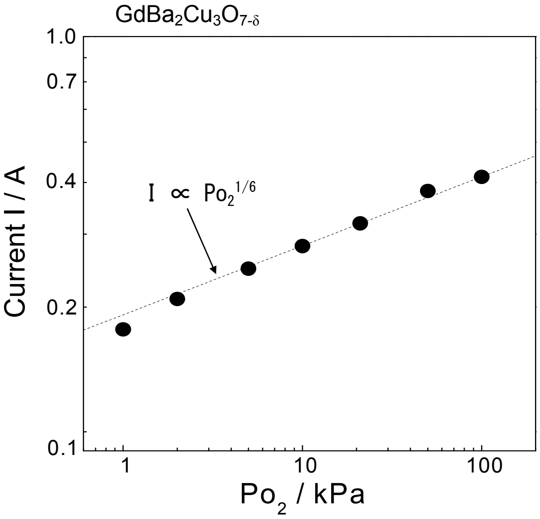

Fig. 3. Oxygen partial pressure dependence of current through the rod with the hot spot.

interstitial oxide ion, hole and oxygen ($=P\mathrm{o}_2$), respectively. When the formation of defects represented by equation (2) is predominant, the insertion of the relation $2[\mathrm{O}_i'']=[h^{\cdot}]$ into equation (2) yields

$$[h^{\cdot}] \propto P\mathrm{o}_2^{\ 1/6} \tag{3}$$

Since the conductivity σ is proportional to $[h^{\cdot}]$, the current is proportional to $P\mathrm{o}_2^{\ 1/6}$.

3. Improvement of durability in high $P\mathrm{o}_2$

To enable the practical use of the hot spot oxygen sensor, the durability of the sensing rods is important. The Gd-123 rod tends to be molten and broken by a sustained presence of the hot spot in a high $P\mathrm{o}_2$. The authors have found that the Gd-123-based composite rods with dispersed $BaAl_2O_4$ [13], $BaZrO_3$ [14] and Gd_2BaCuO_5 (Gd-211) [15] shows remarkable improvement in the durability.

Figure 4 shows the withstanding electric power in air for the various composite rods. For the rod with $BaAl_2O_4$, with increasing $BaAl_2O_4$ content, the power increases significantly until the content increases to 20 vol%, slightly increases at the contents between 20 and 40 vol%, and decreases gradually when the content exceeds 40 vol%. The results suggest the appropriate amount of $BaAl_2O_4$ is around 20 vol%. From the same way of the evaluation, suitable amount for $BaZrO_3$ and Gd-211 are found to be 30 and 7 vol%, respectively.

To evaluate the durability in high $P\mathrm{o}_2$, the presence of hot spot has been sustained under O_2 atmosphere where the condition is the most stressful for the rod because the temperature of the hot spot increases with increasing $P\mathrm{o}_2$ [6]. The currents through the various composite rods with hot spots are shown in Fig. 5. For Gd-123 rod, the current increases irregularly. After approximately 1 h, the rod breaks with melting at the hot spot. Local parts in the hot spot, particularly the grain boundaries, may become partially melting due to local deviation from the ideal composition [16]. The presence of partial melt is considered to be the cause of the breaking at the hot spot. As seen in Fig. 5, the currents through the composite rods increase gradually and the rods do not easily break, reflecting a high durability in the high $P\mathrm{o}_2$. Compared with the $BaAl_2O_4$-dispersed and

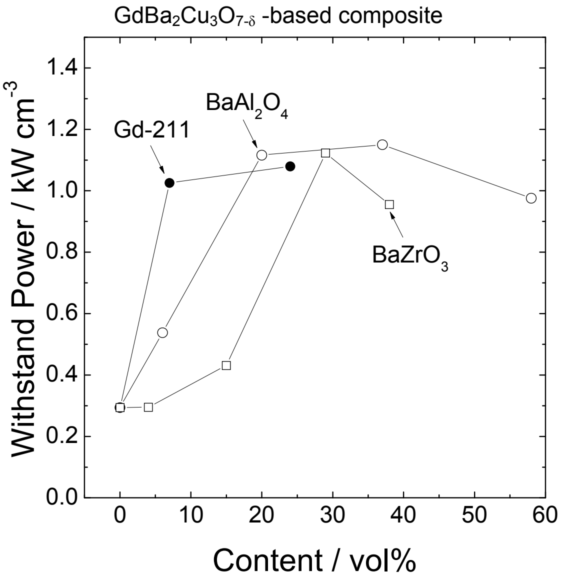

Fig. 4. Withstand electric power for various $GdBa_2Cu_3O_{7-\delta}$ –based composite ceramic rods with dispersed $BaAl_2O_4$, $BaZrO_3$ and Gd-211.

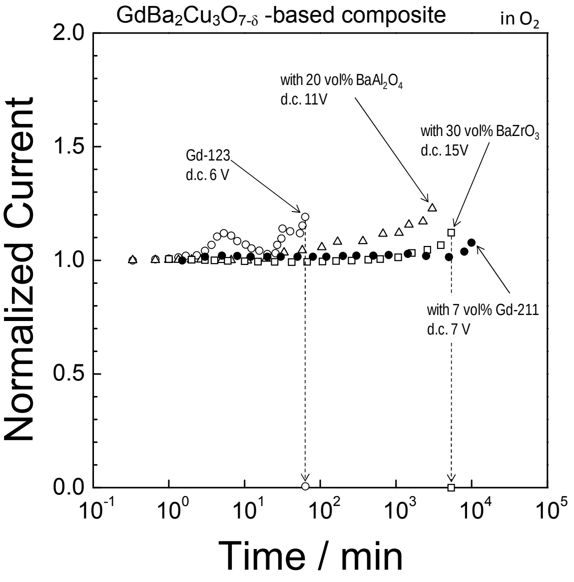

Fig. 5. Change in the current in O_2 atmosphere for various $GdBa_2Cu_3O_{7-\delta}$ –based composite ceramic rods with dispersed $BaAl_2O_4$, $BaZrO_3$ and Gd-211.

$BaZrO_3$-dispersed composites, the Gd-211-dispersed one shows higher durability, suggesting a promising material for the application in the high Po_2.

4. Improvement of durability in low $\boldsymbol{Po_2}$

Figure 6 shows oxygen sensing characteristics of (a) Gd-123 rod and (b) the composite rods containing 15 vol% of dispersed CuO [17]. For the Gd-123 rod, the current running through the rod with the hot spot decreases quickly when the atmosphere is changed from air to low Po_2 in the range of 1–0.03 kPa and subsequently increases gradually, showing overshoot of current. When the atmosphere is changed to air, the current increases abruptly, shows a steep peak, and then return to the initial value. When the atmosphere is changed to Po_2=0.02 kPa, the current becomes almost zero and the hot spot disappears in the rod. Then the current does not return to the initial value when the atmosphere is returned to air.

For the composite rod containing 15 vol% CuO, the current shows overshoot when the atmosphere is changed from air to Po_2=1–0.2 kPa. In contrast, the overshoot is not observed in Po_2=0.02–0.002 kPa. The rod keeps the current of tens of milliamperes even in Po_2=0.002 kPa, and the current returns to the initial value when the atmosphere is returned to air.

Figure 7 summarizes the oxygen partial pressure dependence of current for the rods containing various amount of CuO. For the rods containing CuO≤11 vol%, the currents become too low to maintain the hot spot in the rod at ~0.02 kPa. On the other hand, the rods containing 15 -52 vol% CuO have a sensitivity to oxygen even in Po_2<0.002 kPa.

The temperature of the hot spot decreases with increasing content of CuO [17]. With decreasing temperature, the diffusion of oxygen in the hot spot decreases and the overshoot of current is suppressed. As a consequence, the hot spot is retained in the rod and the sensing oxygen in the very low Po_2 is achieved.

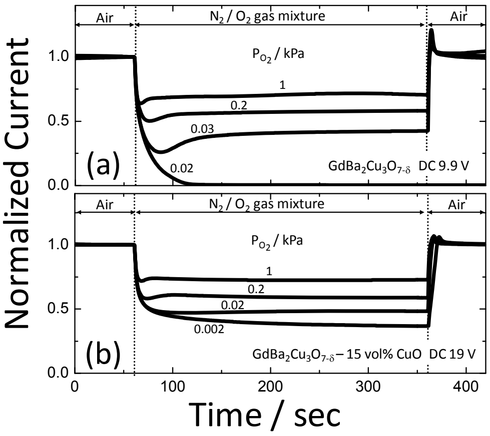

Fig. 6. Oxygen sensing characteristics for (a) $GdBa_2Cu_3O_{7-\delta}$ rod, and (b) the composite rods containing 15 vol% CuO.

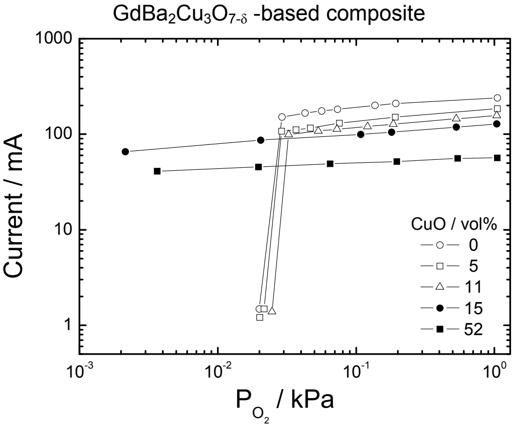

Fig. 7. Oxygen partial pressure dependences of currents for the composite rods containing various amount of CuO.

5. Improvement of response in low $\boldsymbol{Po_2}$

The response time of hot spot oxygen sensor has been improved by forming Gd-211 core in Gd-123 rod [18]. The composite rod with the core is prepared by dipping a Gd-211 rod into the Gd-123 slurry followed by sintering at 950°C. Figure 8 shows SEM images and EDS elemental maps of Gd for the cross section of the rods. In the elemental maps, the white area indicates a high concentration of Gd. The Gd is uniformly distributed in the rods without the core (b). In the rod with the core (d), the concentration of Gd in the core is higher than that in the coat, indicating that the core is Gd-211 and the coat is Gd-123. The average thickness of the Gd-123 coat is 21 μm.

The response time ($t_{0.9}$) is defined as the time taken for the ratio (i - i_0) / (i_∞ - i_0) to reach 0.9 after the change of the atmosphere from air to N_2+O_2 gas mixture as shown in Fig. 9, where i_0 is the initial current, and i_∞ is the final current measured after 300 s from the change in atmosphere. The response times as a function of Po_2 for various rods are shown in Fig. 10. It is found that, response time of oxygen sensor for the rod with the core is approximately 4 s shorter than those without the core at Po_2 of 0.2 kPa. The Gd-123 as a medium for oxygen sensing exists uniformly in all part of the rods without the core. On the other hand, the presence of Gd-123 is confined in the coat on the Gd-211 core. Therefore, length of the oxygen diffusion, which strongly affects the response, is assumed to be shorter in the rod with the core than those without the core [19].

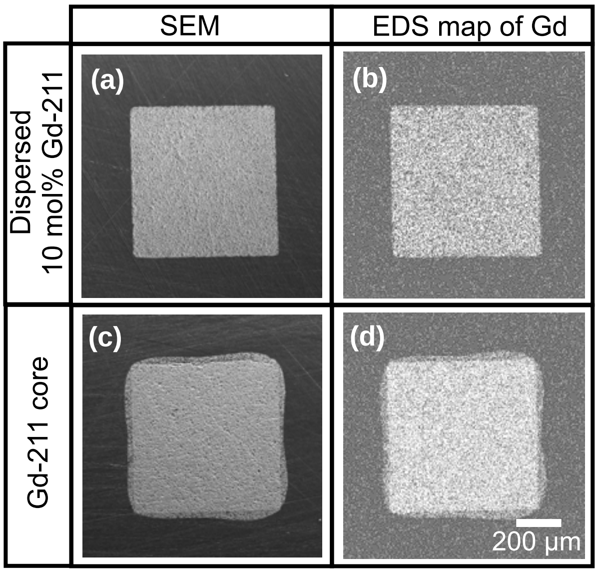

Fig. 8. SEM images and EDS elemental maps of Gd for the cross section of the rods: (a, b) Gd-123 with dispersed 10 mol% Gd-211 and (c, d) Gd-123 with Gd-211 core.

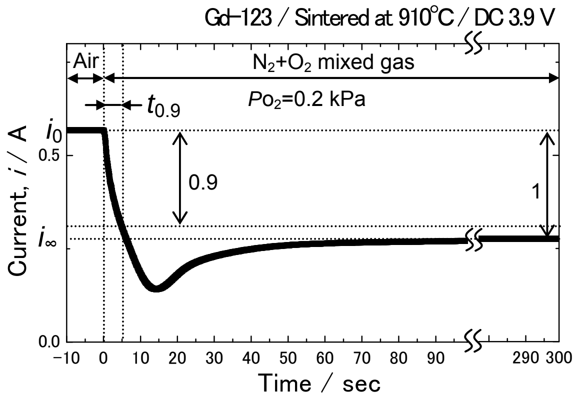

Fig. 9. Oxygen sensing characteristics for $GdBa_2Cu_3O_{7-\delta}$ rod.

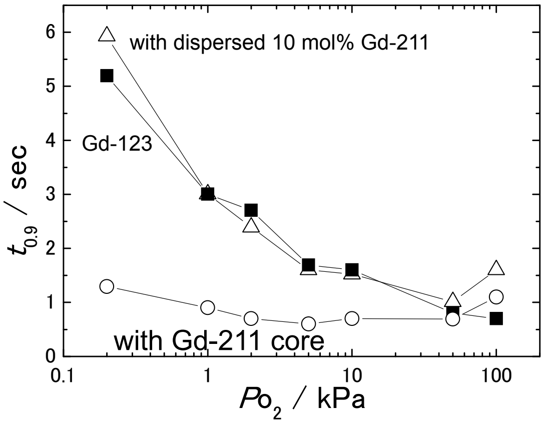

Fig. 10. Response time ($t_{0.9}$) for rods with various structures as a function of the Po_2.

6. Conclusion

The progress in the development of the hot spot oxygen sensor was reviewed. Though the $GdBa_2Cu_3O_{7-\delta}$ rod tends to melt and break by a sustained presence of the hot spot in a high Po_2, the $GdBa_2Cu_3O_{7-\delta}$ composite rods with dispersed high melting point materials, especially Gd_2BaCuO_5, show higher durability. In a low Po_2 $GdBa_2Cu_3O_{7-\delta}$ rod becomes insensitive to oxygen in Po_2<0.02 kPa, while the composite rods containing appropriate amount of CuO can detect oxygen even in Po_2<0.002 kPa. The response time of the oxygen sensor using a composite $GdBa_2Cu_3O_{7-\delta}$ rod with Gd_2BaCuO_5 core is shorter than that without the core. The results suggest that the performance of hot spot oxygen sensors is improved by using composite materials.

Acknowledgments

This work was supported from the Grant-in-Aid for Scientific Research from the Ministry of Education, Science, Sports, Culture and Technology, Japan, and by Program for High Reliable Materials Design and Manufacturing in Nagaoka University of Technology..

References

[1] K. Kishio, J. Shimoyama, T. Hasegawa, K. Kitazawa and K. Fueki, Jpn. J. Appl. Phys., **26** (1987) L1228.

[2] V.A.M. Brabers, W.J.M.de Jonge, L.A. Bosch, C.v.d. Steen, A.M.W.de Groote, A.A. Verheyen and C.W.H.M. Vennix, , Mater. Res. Bull., **23** (1988) 197.

[3] A.T. Fiory, M. Gurvitch, R.J. Cava and G.P. Espinosa, Phys. Rev. B, **36** (1987) 7262.

[4] T.K. Chaki and M. Rubinstein, Phys. Rev. B, **36** (1987) 7259.

[5] T. Okamoto, B. Huybrechts and M. Takata, Jpn. J. Appl. Phys., **33** (1994) L1212.

[6] M. Takata, Y. Noguchi, Y. Kurihara, T. Okamoto and B. Huybrechts, Bull. Mater. Sci., **22** (1999) 593.

[7] H. Sunatori, T. Okamoto and M. Takata, J. Ceram. Soc. Japan, **111** (2003) 217.

[8] Y. Kurihara, Y. Noguchi and M. Takata, Key Eng. Mater., **157-158** (1999) 127.

[9] Y. Kurihara, T. Okamoto, B. Huybrechts and M. Takata, J. Mater. Res., **11** (1996) 549.

[10] K. Kikuchi, M. Kanzaki, T. Neda, T. Kondo and M. Takata, Jpn. J. Appl. Phys., **34** (1995) L1311.

[11] Y. Ibaraki, T. Okamoto and M. Takata, Trans. Mater. Res. Soc. Jpn., **26** (2001) 23.

[12] K. Kakinuma and K. Fueki, Phys. Rev. *B*., **56** (1997) 3494.

[13] T. Okamoto and M. Takata, J. Ceram. Soc. Japan, **112** (2004) S567.

[14] Y. Tsutai, T. Okamoto, A. Kawamoto and M. Takata, J. Ceram. Soc. Japan, **112** (2004) S599.

[15] T. Okamoto, K. Iihama and M. Takata, Adv. Mater. Res., **11-12**, (2006) 137.

[16] R.S. Roth, K.L. Davis and J.R. Dennis, Adv. Ceram. Mater., **2** (1987) 295.

[17] K. Iihama, Y. Kuroki, T. Okamoto and M. Takata, Current Appl. Phys., **9** (2009) S167.

[18] S. Fujihara, Y. Kuroki, T. Okamoto and M. Takata, Key Eng. Mate., **445** (2010) 213.

[19] S. Fujihara, Y. Kuroki, T. Okamoto, and M. Takata, Inst. Phys. Conf. Series: Mater. Sci. and Eng., **18** (2011) 212004.

(Received: 31 May, 2012, Accepted: 7 June, 2012)

Transactions on GIGAKU ***1****(2012)01024/1-6*

TEM Observation of Carbon-Coated $Li_3V_2(PO_4)_3$ Glass-Ceramic Powders and Their High Rate Battery Performance

Kenta Nagamine, Keiichiro Oh-ishi, Tsuyoshi Honma, Takayuki Komatsu*
Department of Materials Science and Technology, Nagaoka University of Technology,
1603-1 Kamitomioka-cho, Nagaoka 940-2188, Japan
**E-mail: komatsu@mst.nagaokaut.ac.jp*

The morphology of carbon-coated $Li_3V_2(PO_4)_3$ crystals synthesized via glass-ceramic processing (the base glass composition: $37.5Li_2O$-$25V_2O_5$-$37.5P_2O_5$ (mol%)) was clarified from high resolution transmission electron microscope (HRTEM) observations and their high rate battery performance was examined. Glucose was added to the precursor glass powders as a reducing agent of vanadium ions (V^{4+}, V^{5+} $\rightarrow V^{3+}$) and a source of carbon coating, and two different techniques of hand mixing in a mortar and ball-milling mixing were applied. HRTEM observations indicate that a sintering of glass powders prepared by a ball-milling mixing is prevented by dispersed carbons on the surface of the primary glass particles, although the coating state of carbon on the surface of glass-ceramic powders is not homogeneous. The glass-ceramics with a carbon coating (a ball-milling mixing) synthesized by a heat treatment at 700°C for 30 min in $7\%H_2$/Ar atmosphere showed a discharged capacity of 109 $mAhg^{-1}$ in the range of 3.0-4.3 V and a good cycle performance at a high rate of 5C. The present study suggests that the glass-ceramic processing is a novel method for the synthesis of $Li_3V_2(PO_4)_3$ crystals with good lithium ion battery performance.

1. Introduction

Lithium ion secondary batteries have been widely used as energy sources of laptop-type personal computers, mobile phones, and so on, because of advantages such as portability and high energy densities. $LiCoO_2$, which is a usual cathode material in commercially available lithium ion secondary batteries, has critical disadvantages such as an extraction of oxygen in the charged state, high cost of cobalt, and its toxicity. These problems prohibit its use in large-scale devices such as electronic vehicles. Instead, lithium transition metal phosphates such as $LiFePO_4$ [1], $Li_3V_2(PO_4)_3$ [2], and $LiVOPO_4$ [3] have been proposed as potential cathode materials for lithium ion batteries over a decade. A framework consisting of phosphate network has effects that prevent the extraction of oxygen and that improve a cycle performance as a battery. Especially monoclinic $Li_3V_2(PO_4)_3$ crystals exhibit excellent electrochemical performances such as the highest theoretical capacity of 197 $mAhg^{-1}$ in phosphate cathodes reported and high-potentials of 3.60, 3.65, 4.10 V (for V^{4+}/V^{3+}) and 4.55 V (for V^{5+}/V^{4+}). These features ensure that $Li_3V_2(PO_4)_3$ can replace $LiCoO_2$ as practical battery cathode. On the other hand, phosphate materials have poor electronic conductivities, which limit charge-discharge rates for lithium ion batteries. This problem has been considered to be solved by carbon coating, particle size reduction, control of interface, and so on.

Recently, our group has reported the glass-ceramics processing as a synthesizing method for cathode materials of lithium ion secondary batteries and succeeded in synthesizing $LiFePO_4$ [4,5], $LiMn_xFe_{1-x}PO_4$ [6], and $LiVOPO_4$ [3]. The glass-ceramic technique has some advantages such as simple fabrication process, high-speed synthesis, no requirement of high cost reagent, and so on. These advantages are preferable to practical applications in lithium ion secondary batteries. In addition, Nagakane et al. [7] reported that $LiFePO_4$ prepared via glass-ceramic processing showed better performance due to the presence of an amorphous phase than commercial $LiFePO_4$ ceramic powder. More recently, we reported the fast synthesis of $Li_3V_2(PO_4)_3$ crystals via glass-ceramics processing from $37.5Li_2O$-$25V_2O_5$-$37.5P_2O_5$ precursor glass [8]. In order to improve battery performance of $Li_3V_2(PO_4)_3$ crystals prepared by glass-ceramic processing such as high discharge capacity at high discharging rates, it would be necessary to design well coating of carbon (i.e., high electronic conductivity) on $Li_3V_2(PO_4)_3$ crystal particles and to clarify the contribution of amorphous phase (i.e., maybe high Li^+ ion conductivity) on the battery performance. In this paper, $Li_3V_2(PO_4)_3$ crystals were synthesized using a glass-ceramic processing and two different carbon coating techniques of hand mixing in a mortar and ball-milling mixing were applied. The morphology of carbon coated $Li_3V_2(PO_4)_3$ crystals and the state of amorphous phase were clarified from high resolution transmission electron microscope (HRTEM) observations and their high rate battery performance was examined.

2. Experiment

A glass with the composition of $37.5Li_2O$-$25V_2O_5$-$37.5P_2O_5$ (mol%) corresponding to the stoichiometric composition of $Li_3V_2(PO_4)_3$ crystal was prepared in air by using a conventional melt-quenching method. The detailed glass preparation process has been reported elsewhere [8], in which raw materials of simple oxide compounds of $LiPO_3$ and V_2O_5 are used. In this study, the precursor glass prepared is described as LVP323 glass. The LVP323 glass was pulverized by using a planetary ball-milling method. Glucose as a reducing agent was mixed with the glass powders by two different ways: 1) 10wt% glucose was mixed with ethanol in an agate mortar by hand, and 2) 10-20wt% glucose was mixed by using a planetary ball-milling (Fritsch premium line P-7). Mixtures were heat-treated at 700ºC for 0.5-12 h under 7%H_2/Ar atmosphere to synthesize $Li_3V_2(PO_4)_3$ crystals. The crystalline phases present in the crystallized samples were identified by X-ray diffraction (XRD; Cu Kα radiation; RIGAKU ULTIMA IV) analyses at room temperature. The surface and inner morphologies of LVP323 glass ceramics were studied by scanning electron microscopy (SEM; JIB-4500) and high resolution transmission electron microscopy (HRTEM; JEM-2100F). Electrical conductivities of carbon coated glass-ceramics with a disk shape were measured using a four-terminal method, in which silver paste was painted onto the surface of the sample as blocking electrodes. Battery performances were evaluated in testing cells. Cathode composites were prepared by mixing 80wt% glass–ceramics (for active material), 15wt% acetylene black (for electronic conductor), and 5wt% polyvinylidene difluoride (PVDF) (for binder). Mixtures were then pressed onto aluminum thin sheet, and circular disks were prepared by cutting the sheet. Stainless test cells were constructed using a lithium metal as an anode and an electrolyte of 1M $LiPF_6$ consisting of a 1:1 solution of ethylene carbonate and diethyl carbonate. The lithium ion battery performance at room temperature was evaluated from charge/discharge measurements (Hokuto denko Co., HJ-1001). The cell potential was swept in the voltage range of 3.0–4.3 V, and the charge/discharge rate was 0.01–5 C.

3. Results and Discussion

A SEM image for the precursor LVP323 glass powders is shown in Fig. 1. The agglomerated particles having the diameter of >5 μm are present. The surface of particles is rough, implying that they consist of sparsely-connected primary glass particles. Such agglomerates might be produced during the pulverizing process of plate-shaped melt-quenched glass and the following drying process. The precursor LVP323 glass powders with the morphology shown in Fig. 1 were used in the following two experiments: the precursor LVP323 glass powders were mixed with glucose (10 or 20wt%) by using a hand mixing method or a ball-milling mixing method and then mixtures were heat-treated at 700ºC for 0.5-12 h under 7%H_2/Ar atmosphere. For simplicity, the sample prepared using a hand mixing method is called as “hand mixing sample”, and the sample prepared using a ball-milling mixing method is called as “ball-milling mixing sample” in this paper.

The XRD patterns for the ball-milling mixing samples (heat-treated at 700ºC for 30 min) are shown in Fig. 2. Only $Li_3V_2(PO_4)_3$ crystals are formed in the samples, indicating that $Li_3V_2(PO_4)_3$ is successfully synthesized by the crystallization of LVP323 glass powders with glucose under 7%H_2/Ar atmosphere. In the previous paper [8], it has been reported that the vanadium ions of V^{4+} and V^{5+} in the precursor LVP glass are reduced largely to V^{3+} ions during heat treatments with glucose in N_2 or 7%H_2/Ar atmosphere. The XRD pattern for the ball-milling mixing samples was refined by using Rietveld method, and the lattice parameters for $Li_3V_2(PO_4)_3$ crystals synthesized were calculated to be *a*=1.2047 nm, *b*=0.8607 nm, *c*=0.8609 nm, and *β*=90.504º. The size of crystallites was estimated from the Lorentz parameter X which relates to the full width of half maximum (FWHM) of XRD peaks. The Scherrer's equation is expressed as $p = K\lambda/\pi X$, where *p*, *K* and λ are the size of crystallites (nm), Scherrer's constant (0.9), and the wavelength (0.1540562 nm) of X-ray, respectively. The sizes of $Li_3V_2(PO_4)_3$ crystallites in the hand mixing sample and in the ball-milling mixing sample with 20wt% glucose were estimated to be 122 and 72 nm. It is, therefore, concluded that the ball-milling mixing provides more fine $Li_3V_2(PO_4)_3$ crystals compared with the hand mixing in the glass-ceramic processing.

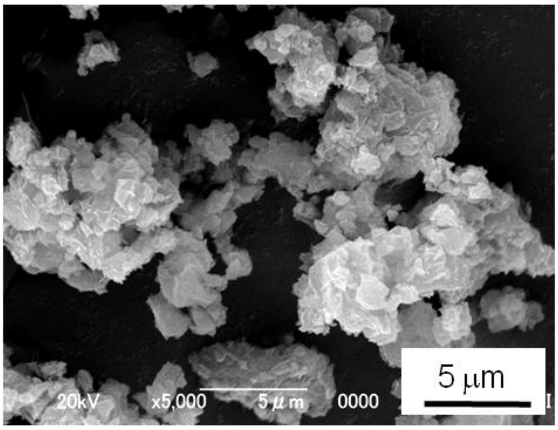

Fig. 1 SEM image for LVP323 glass powders pulverized by using a planetary ball-milling.

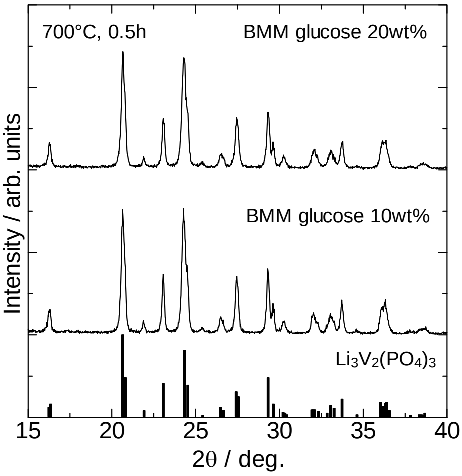

Fig. 2 XRD patterns for the ball-milling mixing (BMM) samples prepared by heat-treatments of LVP323 glass powers with glucose in 7%H_2/Ar atmosphere.

From SEM observations for the hand mixing samples (heat-treated at 700ºC for 30 min), it was found that the secondary particles having the diameter of >20 μm are present and their surface is smooth unlike the precursor glass particles with a rough surface (Fig. 1). Such a smooth surface suggests that the surfaces of the glass-ceramic particles are covered with the carbon formed by a pyrolysis of glucose. It should be pointed out that the glucose added transforms into liquid phase (melting temperature is ~146ºC) on the heating (up to 700°C) for the crystallization of glass powders. From a SEM image for the cross-section of a glass-ceramic particle obtained by a focused ion beam (FIB) method, it was found that the agglomerated particle has many fine pores or hollows in its inside. In order to clarify the morphology of the inside of glass-ceramic particle more in detail, HRTEM observations were carried out. Many hollows having the size of several dozen nanometers are again confirmed from the high angle annular dark field (STEM-HAADF) image for the cross-section. They look like open pores. These hollows might enable liquid electrolytes to penetrate into the glass-ceramics particles. It was confirmed from energy dispersed spectrum (EDS) experiments that the composition of the cross-sectioned particle corresponds to the composition of $Li_3V_2(PO_4)_3$ and any other phases with different compositions such as metal phosphides are not detected. The bright field image and electron diffraction pattern for the inside of the glass-ceramics are shown in Fig. 3. The bright field image indicates that the carbon formed by the pyrolysis of glucose is not present in the hollows, indicating that carbon is attached only on the surface of the secondary particles. It is confirmed from the electron diffraction pattern that $Li_3V_2(PO_4)_3$ crystals are formed in the inside (the region marked with a dotted line). The results on HRTEM observations demonstrate that the glass-ceramics prepared by the hand mixing with glucose and by the heat-treatment at 700ºC for 30 min are well crystallized and consist of $Li_3V_2(PO_4)_3$.

In the SEM image for the ball-milling mixing samples (heat-treated at 700ºC for 30 min), the agglomeration of particles is observed as well as the precursor LVP323 glass powders (Fig. 1). However, it is noted that the surface of each particle is not smooth unlike the glass-ceramic powders prepared by the hand mixing method. The bright field and HRTEM images for the ball-milling mixing samples are shown in Fig. 4 (a-c). Pores or hollows are not found, which are seen in the hand mixing samples, and the structure of each particle is clear, suggesting that a sintering of the precursor LVP323 glass powders is prevented by dispersed carbons on the surface of the primary glass particles. The HRTEM images showed that some particles are not coated by carbon (Fig. 4 (b)), but some particles are coated by carbon (Fig. 4 (c)), indicating that the dispersion state of carbon, i.e., the coating state of carbon, on the surface of glass-ceramic powders is not homogeneous or insufficient.

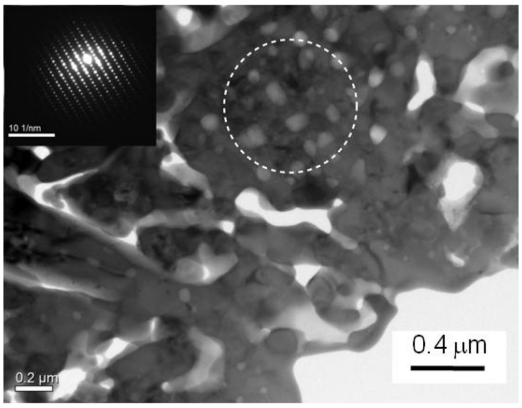

Fig. 3 Bright field image and electron diffraction pattern for the hand mixing samples prepared by a heat treatment (700^{o}C, 30 min) of LVP323 glass powers with glucose (10wt%) in 7%H_2/Ar atmosphere.

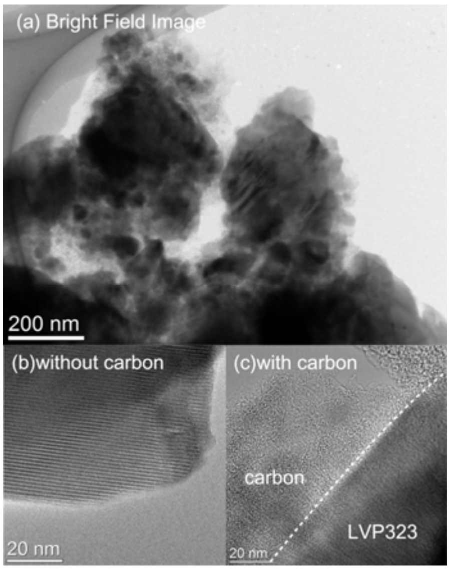

Fig. 4 Bright field image (a) and high resolution TEM images for the ball milling mixing samples prepared by a heat treatment (700^{o}C, 30 min) of LVP323 glass powers with glucose (20wt%) in 7%H_2/Ar atmosphere. (b): the surface region without the coating of glucose, (c): the surface with a carbon layer.

The electrical conductivities (σ) at room temperature for the hand mixing samples (heat-treated at 700°C for 0.5-12 h, 10wt% glucose) were measured using a direct current four-terminal method. It was found that the electrical conductivity increases with increasing heat treatment time. The glass-ceramics prepared in the heat treatments of 30 min and 12 h show the values of σ=4x10^{-3} S/cm^{-1} and σ=3x10^{-2} S/cm^{-1}, respectively. In the previous paper [8], it has been reported that the amount of carbon remained in the glass-ceramics after heat treatments decreases with increasing heat-treatment time. It is, therefore, considered that the quality of carbon coating is improved as increasing heat-treatment time. The electrochemical performance of the hand mixing samples was examined, and the discharge capacities cycled between 3.0-4.3V at the rate of 0.01-1C were obtained. At the slow rate of 0.01C, the discharged capacities are 117~126 $mAhg^{-1}$. On the other hand, the discharged capacities at the rate of 1C for the glass-ceramics obtained in the heat treatments of 0.5, 3, 6, and 12 h are 86, 89, 91, and 96 $mAhg^{-1}$, respectively. These values mean that lithium ions corresponding to the fraction of x=1.3 (for 30 min) and x=1.45 (for 12 h) in $Li_{3-x}V_2(PO_4)_3$ are inserted at the rate of 1C. It is seen that the decrease in the discharged capacity for the glass-ceramics obtained by long time heat-treatments such as 12 h is slightly smaller than that for the glass-ceramic obtained by a short time heat-treatment of 30 min. Such an improvement of the high rate discharge performance would be closely related to the coating state of carbon, i.e., the electronic conductivity of coated carbons.

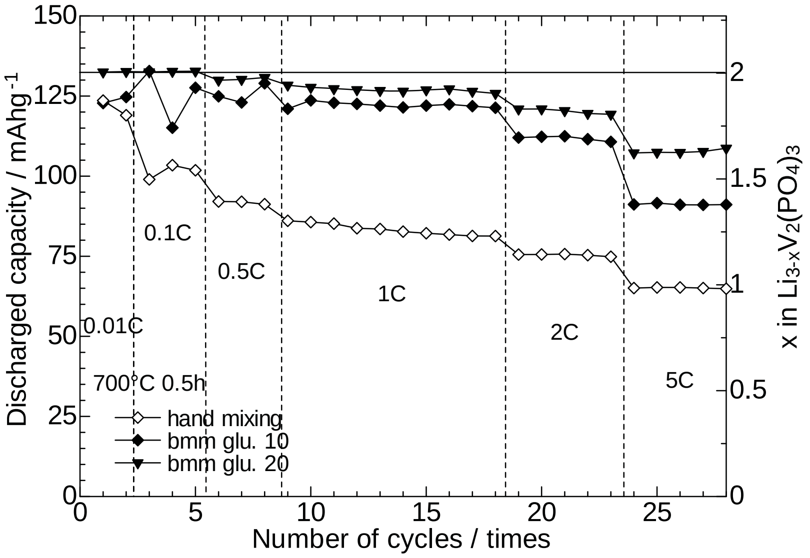

Fig. 5 Discharged capacities at the rate of 0.01-5C between 3.0-4.3 V for the ball-milling mixing (BMM) samples prepared by a heat treatment (700^{o}C, 30 min) of LVP323 glass powers with glucose 10-20 wt% in 7%H_2/Ar atmosphere.

The discharge capacities at the rate of 0.01-5C between 3.0-4.3V for the ball-milling mixing samples (heat-treated at 700ºC for 0.5 h, 10-20wt% glucose) are shown in Fig. 5. The data for the hand mixing sample (heat-treated at 700ºC for 30min, 10wt% glucose) are also shown in Fig. 5 for comparison. At the slow rate of 0.01C, the values of discharge capacities are 124-133 $mAhg^{-1}$. Especially, the discharge capacities of the glass-ceramics with 20wt% glucose at the rates of 0.01-0.5C correspond to almost 100% of the theoretical capacity of $Li_{3-x}V_2(PO_4)_3$ (x=2). At the rate of 1C, the values of discharged capacities are 124-128 $mAhg^{-1}$. In addition, even at the high rate of 5C the discharged capacities of 92 (for 10wt% glucose) and 109 (for 20wt% glucose) are obtained. As shown in Fig. 5, the battery performance of LVP323 glass-ceramics is drastically improved by applying the ball-milling mixing method. In high rate discharging process, electrical conductivity and contact between carbon and active materials are more and more important. In the ball-milling mixing method applied in this study, finer $Li_3V_2(PO_4)_3$ crystals are formed in the glass-ceramics compared with the hand mixing method. Therefore, the improvement of the battery performance shown in Fig. 5 might result from a good contact of fine $Li_3V_2(PO_4)_3$ crystals with carbon coatings. However, even in the ball-milling mixing method, still $Li_3V_2(PO_4)_3$ crystals having no carbon coatings are present as shown in HRTEM observations (Fig. 4). In this point of view, there would be a possibility to improve more the battery performance of glass-ceramics.

There have been several reports on the synthesis of $Li_3V_2(PO_4)_3$ crystals and their Li^+ ion battery performances, in which $Li_3V_2(PO_4)_3$ crystals have been fabricated using various techniques such as conventional solid state reaction, hydrothermal method, sol-gel method, carbothermal reduction method, and soft chemistry route [9-12]. In those studies [9-12], a well carbon coating and nano-scaled uniform particle size have been established, and consequently $Li_3V_2(PO_4)_3$ crystals synthesized show good Li^+ ion battery performances. The present study demonstrates that the glass-ceramic processing also provides $Li_3V_2(PO_4)_3$ crystals showing a moderate performance as cathode materials for lithium ion secondary battery. In particular, it should be emphasized that raw materials for the fabrication of $Li_3V_2(PO_4)_3$ crystals are simple oxide compounds of $LiPO_3$ and V_2O_5, suggesting that cost for their fabrication would be low.

4. Conclusion

Carbon-coated $Li_3V_2(PO_4)_3$ crystals were synthesized using glass-ceramic processing, in which the composition of the precursor glass was $37.5Li_2O$-$25V_2O_5$-$37.5P_2O_5$ (mol%) and simple oxide compounds of $LiPO_3$ and V_2O_5 were used as raw materials. Their morphology of carbon-coated $Li_3V_2(PO_4)_3$ crystals synthesized was clarified from HRTEM observations, and their high rate battery performance was examined. Two different techniques of hand mixing in a mortar and ball-milling mixing were applied. The glass-ceramics with a carbon coating (a ball-milling mixing) synthesized by a heat treatment at 700^oC for 30 min showed a discharged capacity of 109 $mAhg^{-1}$ and a good cycle performance at a high rate of 5C. The present study suggests that the glass-ceramic processing is a simple and fast method for the synthesis of $Li_3V_2(PO_4)_3$ crystals with a good lithium ion battery performance.

Acknowledgments

This work was supported by Grants-in-Aid for Scientific Research from the Ministry of Education, Science, Sports, Culture, and Technology, Japan (No. 23246114), and by Program for High Reliable Materials Design and Manufacturing in Nagaoka University of Technology. One (K. Nagamine) of the authors thanks for JSPS Research Fellowships for Young Scientists.

References

[1] A. Yamada and S.C. Chung, J. Electrochem. Soc., **148** (2001) A960.
[2] H. Huang, S.C. Yin, T. Kerr, N. Taylor, and L.F. Nazar, Adv. Mater., **14** (2002) 1525.
[3] K. Nagamine, T. Honma, and T. Komatsu, J. Am. Ceram. Soc., **91** (2008) 3920.
[4] T. Honma, K. Hirose, T. Komatsu, T. sato, and S. Marukane, J. Non-Cryst. Solids, **356** (2010) 3032.
[5] K. Nagamine, S. Reinsch, R. Mueller, T. Honma, and T. Komatsu, J. Am. Ceram. Soc., 94 (2011) 2890.
[6] T. Honma, K. Nagamine, and T. Komatsu, Ceram. Int., **36** (2010) 1137.
[7] T. Nagakane, H. Yamauchi, K. Yuki, M. Ohji, A. Sakamoto, T. Komatsu, T. Honma, M. Zou, G. Park, and T. Sakai, Solid State Ionics, **206** (2012) 78.
[8] K. Nagamine, T. Honma, and T. Komatsu, J. Power Sources, **196** (2011) 9618.
[9] Y.H. Nien, J.R. Carey, and J.S. Chen, J. Power Sources, 193 (2009) 822.
[10] L. Wang, X. Zhou, and Y, Guo, J. Power Sources, **195** (2010) 2844.
[11] Y.Q. Qiao, J.P. Tu, J.Y. Xiang, X.L. Wang, Y.J. Mai, D. Zhang, and W.L. Liu, Electrochim. Acta, 56 (2011) 4139.
[12] W. Yuan, J. Yan, Z. Tang, O. Sha, J. Wang, W. Mao, and L. Ma, J. Power Sources, 201 (2012) 301.

(Received: 17 May, 2012, Accepted: 24 May, 2012)

Transactions on GIGAKU ***1****(2012)01025/1-6*

Formation of Hierarchical Structure in Liquid Crystalline Block Copolymers

Hiroki Takeshita, Shunsuke Adachi, Shin-ichi Taniguchi, Katsuhiko Takenaka,
Masamitsu Miya, Tomoo Shiomi*
Department of Materials Science and Technology, Nagaoka University of Technology,
1603-1 Kamitomioka-cho, Nagaoka 940-2188, Japan
**E-mail: shiomi@vos.nagaokaut.ac.jp*

This paper reviews the hierarchical structure and its formation process for liquid crystalline block copolymers. Block copolymers exhibit microphase separation with various kinds of morphologies such as sphere, cylinder and lamella in the order of several ten nanometers, while the liquid crystalline polymers form mainly smectic or nematic structure with several nanometer-sizes. For the superimposed structure formed in block copolymers composed of liquid crystalline and amorphous blocks, the followings were focused on: the correlation between the microphase separation structure and liquid crystalline structure, the orientation of mesogen axis, and the process of the structure formation. Photoresponsiveness of the microphase separation structure to the liquid crystalline/isotropic transition caused by the photoisomerization of the mesogen group was also presented.

1. Introduction

Polymer molecules can contain two or more kinds of monomers, which are combined in various sequence manners. Block copolymers are composed of linear arrangement of different blocks comprising the respective constitutional monomers, like -A-A-A-A-A-A-B-B-B-B-B-B- for a block copolymer consisting of monomers A and B. When the block A is immiscible with the block B, the block A and block B segregate from each other to form so-called microphase separation (MS) structure. Various kinds of morphologies occur in the MS structure: sphere, cylinder, gyroid, lamella, *etc*., depending on the volume fraction of blocks, even in the block copolymer composed of only two blocks. The domain size of the MS structure is parallel to that of polymer molecules; usually several ten nm for polymers with common molecular weights. Such morphologies and their formation mechanism in the amorphous or molten state have been extensively investigated [1].

When one or more constitutional blocks are crystalline or liquid crystalline, the structure is formed by combination or competition between their phase transitions and microphase separation. There are various combinations among crystalline, liquid crystalline and amorphous blocks in block copolymers. For crystalline block copolymers, their phase structure and crystallization behavior have statically and dynamically studied so far [1-11].

In this paper, we will focus on liquid crystalline block copolymers containing a side-group liquid crystalline (LC) block. The liquid crystalline block copolymer has a potential to exhibit a hierarchical phase structure which consists of several ten nanometers of MS structure and a few nanometers of LC structure. Nematic (Nm) or smectic (Sm) liquid crystalline structure exists in the MS domain with various morphologies described above. In order to clarify such superimposed structure, it is required to reveal the interplay between microphase separation and liquid crystallization; the correlation between the MS structure and LC structure, the orientation of mesogenic groups to the interface of the microdomain, and in addition, the process of the structure formation on liquid crystallization from microphase-separated states.

In the liquid crystalline block copolymers, the binary combinations with amorphous [12-15,18,19], liquid crystalline [16] and crystalline [17] blocks have been investigated. In this paper, we review the hierarchical structure and its formation process for block copolymers consisting of liquid-crystalline and amorphous block chains.

2. Experimental Methods

In order to realize a well-controlled MS structure, we must use block copolymers having a narrow molecular-weight distribution. Although such block copolymers have usually been synthesized by living anionic polymerization, this polymerization method is not suitable for preparation of liquid crystalline polymers having a polar side group. Therefore, liquid crystalline block copolymers have been prepared by atomic transfer radical polymerization (ATRP) that is a kind of so-called living radical polymerizations. The liquid crystalline copolymers described here consist of a liquid crystalline block (PLC) with a cyanobiphenyl-type or azobenzene-type mesogen groups and an amorphous block of poly(*n*-butyl acrylate) (PBA) or polystyrene (PS). The chemical structure of PBA-PLC block copolymer is shown in Figure 1 as an example. The spacer length between a main chain and mesogen group was controlled by the number *x* of methylene groups.

Microphase separation structure and Sm layer can be evaluated by a small-angle X-ray scattering (SAXS) technique. Here, the scattering vector q is defined as $q=(4\pi/\lambda)\sin(\theta/2)$, where θ is the scattering angle. The time-resolved SAXS measurements using a very strong X-ray source from synchrotron radiation give a useful information on the structure formation process in the liquid crystallization. The SAXS results described here were obtained at the Photon Factory in the Institute of Materials Structure Science, High Energy Accelerator Research Organization in Tsukuba, Japan: for 1-dimensional and 2-diensional measurements at beam lines of BL-10C and BL-15A, respectively. Polarized optical microscopy (POM) and differential scanning calorimetry (DSC) are also used for observation of a texture of liquid crystals and a transition temperature, respectively.

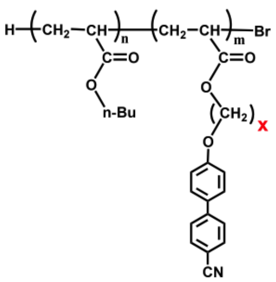

Fig. 1 An example of liquid crystalline-amorphous block copolymer.

3. Results and Discussion

(1) Liquid crystalline structure of homopolymer

The liquid crystalline/isotropic transition temperature T_{iso} increases with increasing spacer length *x* [14,15]. Also, the cyanobiphenyl-type homopolymer with a short spacer *x*=6 does not exhibit Sm structure but only Nm structure, while other ones with a longer spacer can form Sm structure [14,15].

For example, Figure 2 shows SAXS profiles for cyanobiphenyl-type PLC with *x*=11, in which two peaks can be observed below T_{iso} [12]. The ratio of these peak positions is 1:2, which means layer structure, that is, Sm structure. The layer spacing *l* is estimated from the first-order peak position around q=1.4 nm^{-1} to be about 4.5 nm. This value of the layer spacing is about twice the length of the side group with the mesogen and *trans*-zigzag conformation of $(CH_2)_{11}$, which suggests that the Sm structure is a bilayer structure consisting of two mesogenic layers

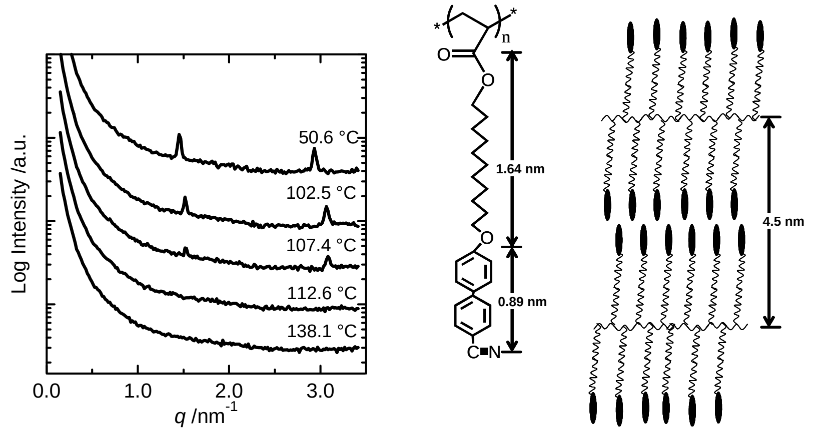

Fig. 2 SAXS profiles and liquid crystalline structure of cyanobiphenyl-type polymer with *x*=11. (Reproduced from ref. 12.)

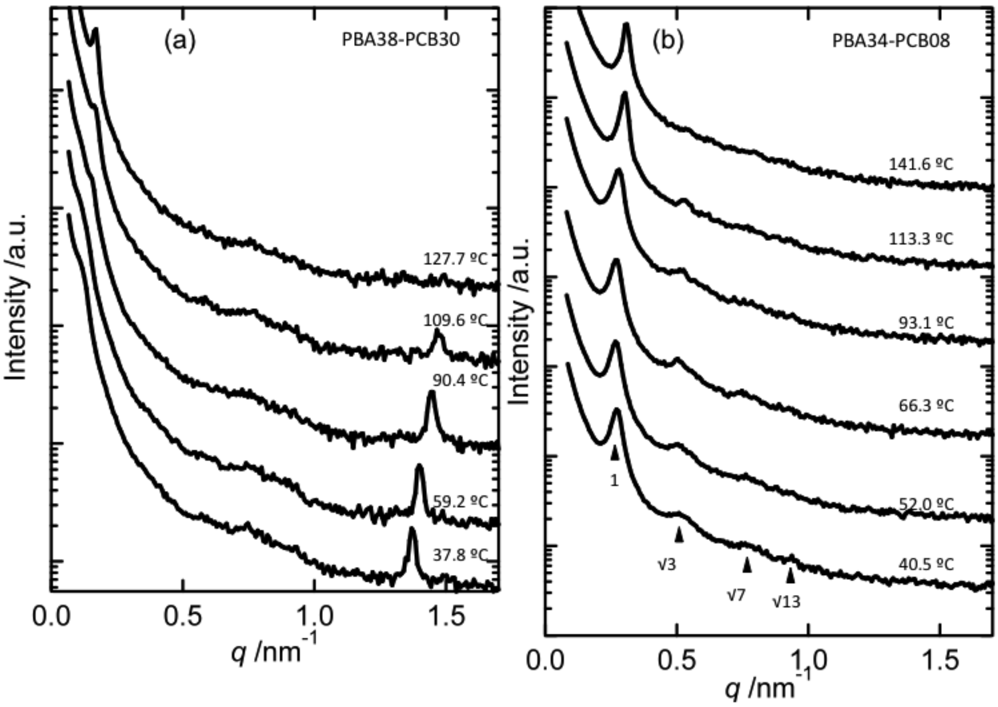

Fig. 3 SAXS profiles for PBA-PLC **(a)** with ϕ_{LC}=0.44 and **(b)** with ϕ_{LC}=0.20. (Reproduced from ref. 12)

as shown in Figure 2. A monolayer structure was also found for the azobenzene-type liquid crystalline polymers [18,19].

(2) Hierarchical structure of liquid crystalline/amorphous block copolymers

In order to elucidate the hierarchical structure, it is required to estimate the MS structure, LC structure and the orientation of the mesogen axis to the interface of the microdomain.

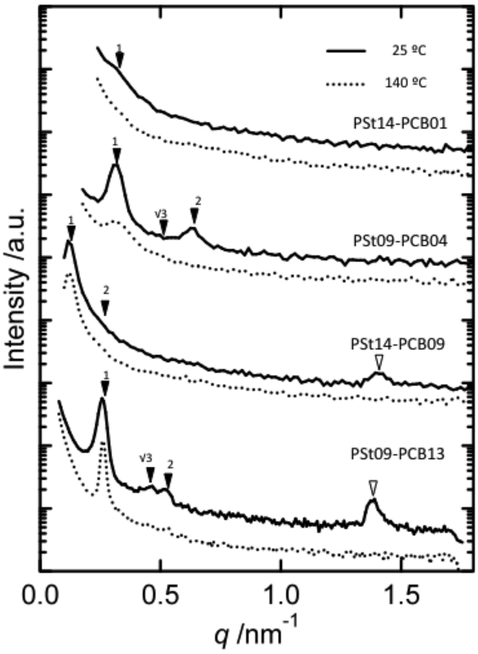

Fig. 4 SAXS profiles for PS-PLC at isotropic (140^{o}C) and liquid crystalline (25^{o}C) states. (Reproduced from ref. 13)

Figure 3a shows SAXS profiles at each temperature for PBA-PLC with ϕ_{LC}=0.44 weight fraction [12]. In both isotropic (127.7^{o}C) and liquid crystalline states, a peak due to MS structure is observed at q=0.17nm^{-1}. Although any higher-order peaks are not clearly observed, the MS structure is considered to be lamellar by taking account of the copolymer composition. A peak due to Sm layers also appears around q=1.4nm^{-1} below about 100^{o}C. This means that Sm structure is formed in the lamellar MS structure. On the other hand, as shown in Figure 3b [12], SAXS profiles for PBA-PLC with ϕ_{LC}=0.20 exhibits a hexagonal packing, that is, cylindrical MS structure, but no peak due to Sm structure is found. In this case, since the formation of liquid crystalline structure is confirmed by POM, it is concluded that the Nm structure is formed within the cylindrical MS domain.

The same result can be obtained for a series of PS-PLC block copolymers as shown in Figure 4 [13]. Sm structure is not formed in the cylindrical domain (PSt09PCB04; ϕ_2=0.22), while Sm can be formed in both lamellar and matrix domains (PSt14PCB09 with ϕ_2=0.38 and PSt09PCB13 with ϕ_2=0.59, respectively), where for PSt09PCB13, PS is located in the cylindrical domain.

The orientation of the mesogen axis can be determined using a 2-dimensional CCD X-ray detector. Figure 5 shows 2-D SAXS images for PBA-PLC (lamellar) [12] and PS-PLC (PS-cylindrical) [13] observed after applying oscillating shear flow (1 Hz). The scattering peaks from the Sm layer are located perpendicularly to those from the MS structure for both samples, which means that the Sm layer aligns perpendicularly to the microdmain interface, that is, the direction of the mesogen axis is parallel to the interface.

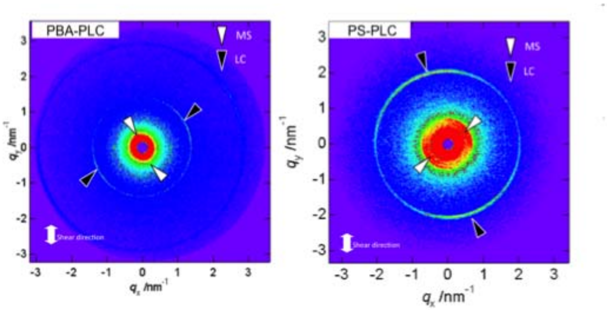

Fig. 5 2-D SAXS images for PBA-PLC (lamella) and for PS-PLC (PS, cylinder). (Reproduced from ref. 12 and ref. 13.)

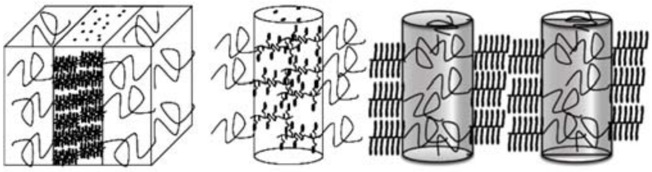

Fig. 6 Schematic pictures of superimposed structure composed of LC and MS structures. (Reproduced from ref. 12 and ref. 13.)

From the above results, we can draw schematic images of hierarchical structure as shown in Figure 6 [12,13]. Since the orientation of the Nm structure cannot be observed by the SAXS technique, it was estimated using both 2D-SAXS and POM which give orientations of the microdomain interface and of the mesogen axis, respectively [14,15].

(3) Process of MS structural change on liquid crystallization

Morphology or spacing of MS structure is expected to be changed by liquid crystallization in the same way as crystallization of crystalline block copolymers [5]. Figure 7(left) shows time development of SAXS profiles in the liquid crystallization process from the lamellar MS structure

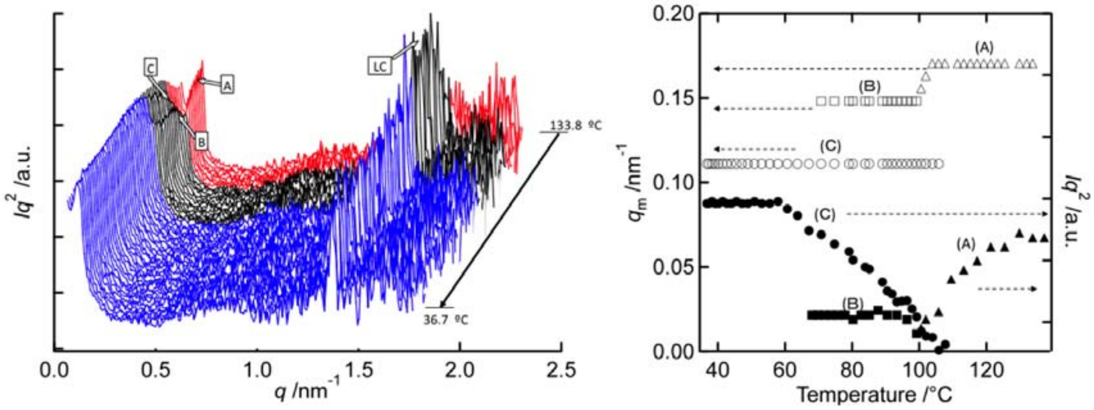

Fig. 7 The development of SAXS profiles **(left)** and the position and intensity of SAXS peak **(right)** in liquid-crystallization process from lamellar MS structure for PBA-PLC. (Reproduced from ref. 12)

for PBA-PLC [12]. The position and intensity of the peak due to the MS structure are plotted against the temperature in Figure 7(right) [12]. As a peak from the Sm layer appears at q=1.4 nm^{-1}, the intensity of a preexisting peak around q=0.17 nm^{-1} (indicated by ‘A’ in Figure 7) above T_{iso} decreases and the peak is succeeded by peak ‘B’. Furthermore, at almost the same time, a new peak (‘C’) appears at a smaller angular side and develops. The peak B disappears with developing the peak C. The peak C comes from the MS structure containing Sm LC layers, because the peak from the Sm layer exists in the whole temperature range below T_{iso}. The peak B might be assigned to the Nm structure by the POM observation.

From the above behavior of the SAXS profiles, we can conclude the structural change in the liquid crystallization process as follows: (1) the Sm layer structure is evolved through a transient Nm structure and (2) the MS structure is reorganized by the formation of the Sm structure because the peak position changes discretely. Such change of the structure is schematically shown in Figure 8(left). In the liquid crystallization from the cylindrical structure, on the other hand, the peak position changed continuously probably because of the Nm formation. In addition, (3) it should be noted that the MS peak position changes toward a low-angle side in liquid crystallization, which means that the spacing of the MS structure is larger in the liquid crystalline state as shown in Figure 8(left). This may be related to the alignment of the mesogen groups. Especially in the Sm structure, as shown in Figure 8(right), the perpendicular alignment of the Sm layer expands the main chain toward the microdomain interface, and simultaneously the main chain of the amorphous block is also expanded because the interface area per block chain must match between liquid crystalline and amorphous block chains.

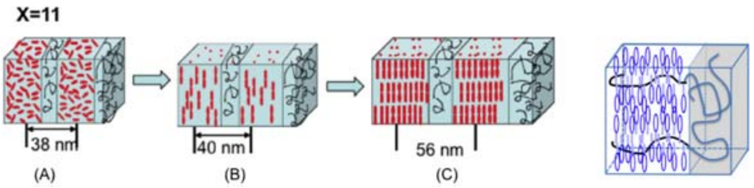

Fig. 8 **(left)** Formation of Sm structure via. Nm structure accompanied by reorganization of lamellar MS structure (A, B and C correspond to those of Fig. 7), and **(right)** the predicted main-chain conformation in Sm structure.

The morphology change such as lamellar to cylindrical has also been found for other liquid crystalline block copolymers [18,19]. This morphology change may be caused by the requirement that the entropic deficit coming from excessive expansion of the main chain should be avoided.

(4) Responsiveness of MS structure to photosensitive liquid crystalline/isotropic transition

Mesogen groups containing azobenzene derivatives exhibit a transition from liquid crystalline to isotropic state due to *trans* to *cis* photoisomerization triggered by UV irradiation. Photoresponsiveness of the MS structure has been investigated for the block copolymer consisting of PBA amorphous and azobenzene-type liquid crystalline blocks [18,19]. The spacing of the MS structure was shorter in the isotropic state caused by UV irradiation in the same way as the case in the thermal transition. The change of the spacing was reversible in the repeat of UV-On and –Off, and the responsive time was 20-30 sec. If block copolymers containing a photosensitive liquid crystalline block are employed, it is expected that the spacing or morphology of the MS structure can be changed rapidly and easily by the photoexposure, compared with the change by the thermal transition, which is a better way for practical application of the structural change.

4. Conclusion

The hierarchical structure containing liquid crystalline or crystalline phases has been explored recently for bock copolymers. Especially the formation process of the MS structure for both crystalline and liquid crystalline block copolymers was first revealed by us [5,12]. In polymeric systems, there can coexist crystalline, liquid crystalline and amorphous phases. The overall phase structure of such systems is formed by interplay between these phase transitions and phase separation, and the structure is determined dynamically as well as thermodynamically because the diffusion of polymer chains is not so fast. Therefore, in order to clarify the complicated structure systematically, the investigations on the formation process as well as the resulting structure are required.

Acknowledgments

Our works referred to in this paper were supported by the Grant-in-Aid for Scientific Research on Basic Area (B) and for Challenging Exploratory Research from Japan Society for the Promotion of Science and by the 21st Century COE Program for Scientific Research from the ministry of Education, Culture, Sports, Science and Technology. The SAXS experiments using synchrotron radiation were performed under the approval of the Photon Factory Program Advisory Committee (Proposal Nos. 2004G090, 2006G087 and 2007G090 and 2008G066).

References

[1] I.W. Hamley, The Physics of Block Copolymers. New York: Oxford; 1998.
[2] A.J. Müller, V. Balsamo, and M.L. Arnal, Advances in Polymer Science, Volume 190, 1-63; 2005.
[3] S. Nojima, K. Kato, S. Yamamoto, and T. Ashida, *Macromolecules*, **25** (1992) 2237.
[4] T. Shiomi, H. Tsukada, K. Takeshita, K. Takenaka, and Y. Tezuka, *Polymer*, **42** (2001) 4997.
[5] T. Shiomi, H. Takeshita, H. Kawaguchi, M. Nagai, K. Takenaka, and M. Miya, *Macromolecules*, **35** (2002) 8056.
[6] H. Takeshita, N. Ishii, C. Araki, M. Miya, K. Takenaka, and T. Shiomi, *J Polym Sci Part B Polym Phys*, **42** (2004) 4199.
[7] H. Takeshita, Y.J. Gao, T. Natsui, E. Rodriguez, M. Miya, K. Takenaka, and T. Shiomi., *Polymer*, **48** (2007) 7660.
[8] Y.J. Gao, H. Takeshita, Y. Takata, K. Takenaka, and T. Shiomi, *e-J Soft Mater*, **4** (2008) 12.
[9] H. Takeshita, Y.J. Gao, Y. Takata, K. Takenaka, T. Shiomi, and C. Wu, *Polymer*, **51** (2010) 799.
[10] F. Arai, H. Takeshita, M. Dobashi, K. Takenaka, M. Miya, and T. Shiomi, *Polymer*, **53** (2012) 851.
[11] H. Takeshita, K. Fukumoto, T. Ohnishi, T. Ohkubo, M. Miya, K. Takenaka, and T. Shiomi, *Polymer*, **47** (2006) 8210.
[12] S. Taniguchi, H. Takeshita, M. Arimoto, M. Miya, K. Takenaka, and T. Shiomi, *Polymer*, **49** (2008) 4889.
[13] H. Takeshita, S. Taniguchi, M. Arimoto, M. Miya, K. Takenaka, and T. Shiomi, *Polymer*, **50** (2009) 271.
[14] H. Takeshita, S. Adachi, H. Taniguchi, M. Miya, K. Takenaka, and T. Shiomi, *Polymer Prepr, Jpn*, **58** (2009) 3543.
[15] T. Shiomi, H. Takeshita, S. Adachi, H. Taniguchi, and K. Takenaka, *European Polymer Congress, Book of Abst*, **8** (2011) 1233.
[16] T. Shiomi, H. Takeshita, H. Taniguchi, S. Adachi, M. Miya, and K. Takenaka, *Polymer Prepr, Jpn*, 58 (2009) 3541.
[17] H. Takeshita, Y. Sakima, M. Miya, K. Takenaka, and T. Shiomi, *Polymer Prepr*, *Jpn*, 59 (2010) 3397.
[18] H. Takeshita, T. Fjise, K. Haginoya, M. Miya, K. Takenaka, and T. Shiomi, *Polymer Prepr, Jpn*, **60** (2011) 4489.
[19] K. Haginoya, R. Kudo, T. Fujise, H. Takeshita, M. Miya, K. Takenaka, and T. Shiomi, *Polymer Prepr, Jpn*, **61** (2012) 739.

(Received: 18 May, 2012, Accepted: 30 June, 2012)

Transactions on GIGAKU **1**(2012)01026/1-5

Alloying Effects in the Nickel-Cobalt System on Electrochemical and Adsorptive Properties of an SOFC Anode Cermet for the Direct Oxidation of Methane

Kazunori Sato*, Teoh WahTzu, Hiroshi Nishiyama[a)], Tatsuya Sawahata, Hirotaka Takayanagi
Department of Environmental Engineering, Nagaoka University of Technology
a) *Department of Materials Science and Technology, Nagaoka University of Technology*
Nagaoka, Niigata 940-2188, Japan
**E-mail: sato@analysis.nagaokaut.ac.jp*

Substitution of Co atoms for Ni atoms in the Ni-based cermet anode enhanced the electrochemical performance of a solid oxide fuel cell (SOFC) for the direct oxidation of methane. This effect was confirmed for the cells using an yttria-stabilized zirconia (YSZ) electrolyte. The result of electrochemical measurements has revealed that the enhancement of the direct oxidation of methane and hydrogen is caused by an improvement of adsorptive properties for the reactants and products due to the solid-solutioning effect in the Ni-Co binary alloy system. We found that adsorptive abilities of $Ni_{0.5}Co_{0.5}$-YSZ and $Ni_{0.5}Co_{0.5}$-CeO_2 cermet particles for CH_4 and CO are affected by the Co atoms substituted for the Ni atoms.

1. Introduction

The development of proper metal catalysts combined with a high oxide-ion conductor is required for the electrochemical oxidation of hydrocarbon fuels [1-6]. We have investigated the performance of an anode, which consists of Ni-Co solid-solution alloy particles dispersed on the zirconia-based electrolytes or ceria-based electrolytes [7,8]. However, the effect of the $Ni_{1-x}Co_x$ composition on the methane (CH_4) adsorption has not been investigated so far, and the reaction mechanism remained uncertain. The electrochemical reaction occurring at the electrode-electrolyte interface is important to improve the power generation performance of SOFCs. Both CO and graphite produced at the anode can degrade the cell performance. The strong adsorption of CO on the electrode surface results in a carbon deposition and poisoning as well as the thermal decomposition of CH_4 into graphite. To understand the reaction mechanism the adsorptive ability of cermet materials must be characterized. The objective of this research is to characterize the adsorptive properties of $Ni_{1-x}Co_x$-YSZ and $Ni_{1-x}Co_x$-CeO_2 cermet particles by Temperature-Programmed Desorption (TPD) analysis. The results were discussed in terms of the metal-support interaction for the direct oxidation of CH_4.

2. Experimental

The $Ni_{1-X}Co_XO$ solid solution was prepared by heating a mixture of reagent-grade NiO and Co_3O_4 powders at 1273 K for 10 h in air. Phase identification of the prepared powders was made by X-ray diffraction (XRD). Pulverized $Ni_{1-X}Co_XO$ powders were mixed with 8 mol%Y_2O_3-ZrO_2 (YSZ) powder or 10 mol%Sc_2O_3-1 mol%CeO_2-ZrO_2 (ScSZ) powder in a mass ratio of 30% to form a slurry using glycerol. The slurry was painted as the anode on one face of the electrolyte disk (Shinko-Denki). The disk was 15 mm in diameter and 0.3 mm thick. The painted disk was heated at 1373 K for 10 h. $(La_{0.85}Sr_{0.15})_{0.9}Mn_{0.1}O_3$ (LSM) was used as the cathode. LSM powders were mixed with glycerol to form slurry. This slurry was painted on the other face of the electrolyte disk, and the disk was heated at 1523 K for 1 h. The thickness of the anode and cathode was approximately 50 μm. Two 0.3 mm diameter platinum lead wires were attached to each electrode with a platinum mesh (#100 mesh) 3 mm x 3 mm in size. Following this fabrication procedure, the cell was fired at 1323 K for 1 h. The anode was reduced in a H_2 atmosphere at 1073 K to obtain a $Ni_{1-X}Co_X$-YSZ (or ScSZ) cermet before the cell measurement. The fuel cell test assembly with the two-electrode configuration was used to evaluate the current-voltage (*I-V*) characteristics. The anodic overvoltage measurement was conducted by the current interruption method. The reference electrode was bonded as a small circle on the anode face separated by a 2-3 mm gap from the circular working electrode. Glass ring gaskets were used to fix and seal the peripheral areas of the anode and cathode faces of the cell to the ends of alumina tubes. O_2 gas was supplied to the cathode at a flow rate of 2 x 10^{-5} m^3/min. CH_4 was also used as the fuel. CH_4 diluted with He in a volume ratio of 1:9 was used as the fuel gas at a total flow rate of 2 x 10^{-5} m^3/min. *I-V* curves of the cells were measured at 973-1073 K. Reproducibility of these *I-V* curves on increasing and decreasing the temperature was confirmed for each experiment. The outlet gas from the anode was analyzed by gas chromatography. Impedance spectra were measured with an impedance analyzer (HP-4192A).

As for the TPD analysis $Ni_{1-x}Co_x$-YSZ and $Ni_{1-x}Co_x$-CeO_2 cermet samples were prepared by the conventional impregnation method. The starting materials were $Ni(NO_3)_2$ $6H_2O$ (Wako Pure Chemical), $Co(NO_3)_2$ $6H_2O$ (Nacalai Tesque) and YSZ powder (Tosoh, 8 mol%Y_2O_3-ZrO_2: TZ-8Y), and CeO_2 powder (Nacalai Tesque). The metal nitrates were mixed in an appropriate amount, and the mass ratio of the $Ni_{1-x}Co_x$ to the oxides was adjusted to be 1:5. The impregnated samples were dried at 373 K for 1 h and subsequently calcined at 773 K for 1 h in air. The calcined samples were placed in an alumina boat and reduced at 773 K for 1 h in a 20%H_2-He atmosphere. The TPD experiment was carried out with a ChemBET-3000 (YUASA-IONICS). The prepared cermet samples were placed in a quartz vessel for TPD and kept at 623 K for 1 h in a N_2 atmosphere, and subsequently reduced at 623 K for 1 h in a 5%H_2-He atmosphere before the TPD experiment. The cermet samples were exposed in an adsorbed gaseous species at room temperature. Desorption was performed by increasing the temperature from the room temperature to 973 K at different heating rates (β). Desorbed species were detected with a thermal conductivity detector (TCD).

3. Results and Discussion

Figs. 1a and 1b show the current-voltage (*I-V*) and current-power curves (*I-P*) for the cell using a Ni-YSZ cermet (cell 1) and one using a $Ni_{0.5}Co_{0.5}$-YSZ cermet (cell 2) as the anode both combined with the YSZ electrolyte. These results have revealed that the enhancement of the cell performance by substituting Co atoms for Ni atoms in the Ni-based cermet is significant for CH_4. The maximum power densities were compared among the cells, whose alloy compositions in the $Ni_{1-X}Co_X$ system were from x = 0 through x=1, as shown in Fig. 2. We confirmed that increasing amount of Co in the $Ni_{1-X}Co_X$ system results in an increase in the cell performance up to approximately 0.8. However, the

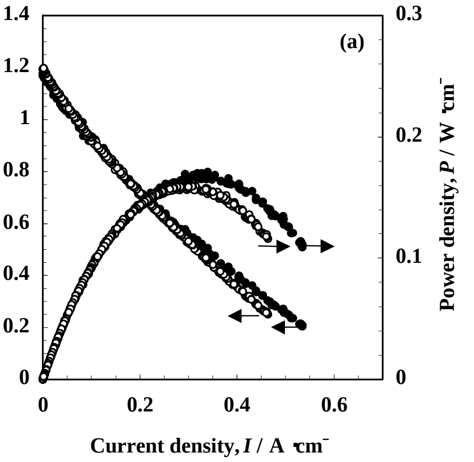

Fig. 1(a) *I-V* and *I-P* curves of cells using the Ni-YSZ (○) and $Ni_{0.5}Co_{0.5}$-YSZ (●) anodes for H_2 at 1073 K.

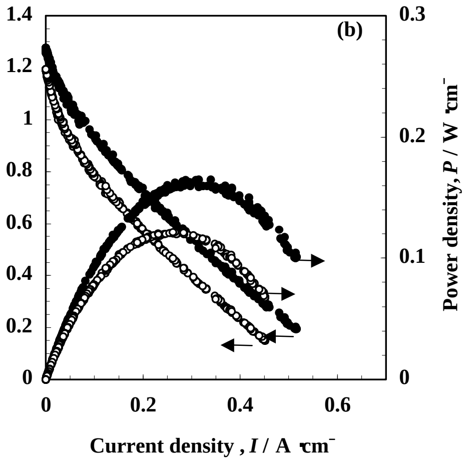

Fig. 1(b) *I-V* and *I-P* curves of cells using the Ni-YSZ (○) and $Ni_{0.5}Co_{0.5}$-YSZ (●) anodes for CH_4 at 1073 K.

Co-YSZ cermet showed the lowest cell performance both for CH_4 and H_2. This result agrees with a comparison of the anodic polarization curves at 1273 K for the M-YSZ (M = Mn, Fe, Co, Ni, Ru, Rh, Pd, Pt, and Au) cermet for H_2 [5].

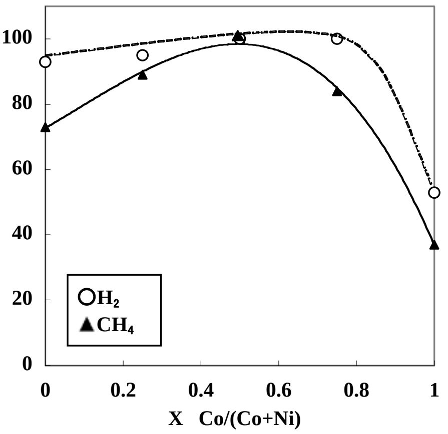

Fig. 2 Comparison of the maximum power density among the cells using $Ni_{1-X}Co_X$-YSZ cermet at 1073 K.

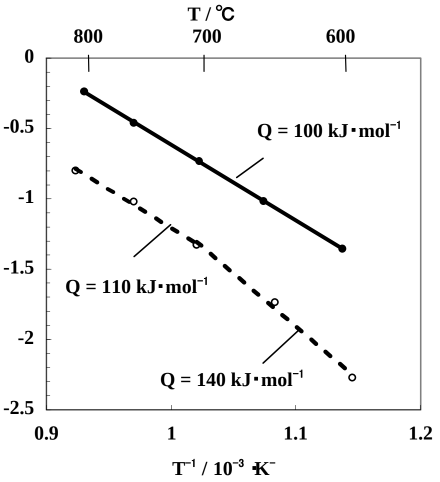

Fig. 3 Arrhenius plots of Rp^{-1} for the electrochemical oxidation of CH_4 using the Ni-YSZ (○) and $Ni_{0.5}Co_{0.5}$-YSZ (●) anodes.

Fig. 3 shows the reciprocal polarization resistance, Rp^{-1}, determined from the slope of the line showing a linear relationship between the anodic overvoltage and current density at low current densities less than approximately 50 mA/cm^2. The larger values in Rp^{-1} mean a high activity of the anode for the electrochemical oxidation of CH_4; the anodic activation overvoltage, $\eta_{act} = Rp \times I$, is caused by the charge transfer process at the interface between the anode and electrolyte. Replacement of half of the Ni atoms with Co atoms increased the activity of the anode for the electrochemical oxidation of CH_4 by about two times. However, the slope of the Arrhenius plots, shown in Fig. 3, remained almost constant above approximately 700 degrees Celsius, indicating that the solid solutioning of Co does not change the apparent activation energy for the anode reaction but increases the amount of reactants at the active sites of the anodic oxidation of CH_4. The value of Rp^{-1} for cell 1 below approximately 700 degrees Celsius showed a somewhat high value. Since in the gas phase CH_4 is thermally very stable and only begins to decompose into the elements, H_2 and C, at 785 degrees Celsius [9], the increase in Rp^{-1} for cell 1 appears to be caused by the difference in the adsorptive property for CH_4 between the Ni-YSZ and $Ni_{0.5}Co_{0.5}$-YSZ cermets. The strong adsorptive ability of Ni for CH_4 can account for this result. We have also reported an increase in the cell performance for CH_4 using the $Ni_{0.5}Co_{0.5}$-CeO_2 cermet anode combined with a samaria-doped ceria (SDC) electrolyte [7]. These results indicate that both the alloying effect in the Ni-Co system and an oxide component in the cermet affect the adsorptive property both for CH_4 and reaction products in the electrochemical oxidation of CH_4.

Figs. 4a and 4b show TPD curves of the Ni-CeO_2 and Ni-YSZ cermet samples. The TPD curve of the Ni-YSZ sample for CH_4 showed one main peak at ca. 750 K, whereas that of the Ni-CeO_2 sample exhibited two main peaks at ca. 480 K and ca. 800 K. These TPD curves of the Ni-YSZ and Ni-CeO_2 samples for CO showed almost the same peak shape. The amount of desorbed CO from the Ni-CeO_2 sample was larger than that from the Ni-YSZ sample. Quantitative TPD analysis for these samples was difficult due to the low TCD signals; however, the adsorptive property of Ni metal particles was found to be dependent on the oxide support in the cermet anode materials. Fig. 5 shows the Arrhenius plot for the prepared $Ni_{1-x}Co_x$-YSZ samples using the peak-method calculation based on the peak temperature, Tp, and the heating rate, β, during the TPD experiment. The slope of these Arrhenius plots appears to be decreased with increasing the Co content up to x = 0.5. The Polanyi-Wigner equation was used to determine the activation energy for desorption, E_d [11]. Although this equation is inapplicable to accurately describe the kinetics of thermal desorption, which is caused by the interaction between the adsorbed species and the heterogeneity of adsorption sites, the value of E_d for CH_4 apparently decreased by the partial substitution of Co atoms for Ni atoms in the fcc lattice. Since Ni atoms have a strong affinity for CH_4 and CO molecules, this causes carbon deposition and CO poisoning at SOFC operating temperatures. We have shown that the partial substitution of Co atoms for Ni atoms in the cermet anode enhances the activity for the electrochemical oxidation of CH_4, which resulted in an increase in the cell performance due to a decrease in the anodic overvoltage. This enhancement is most likely to be explained by the decrease in the activation energy for desorption as well as the increase in adsorption sites for CH_4 molecules, which results in the suppression of carbon deposition and CO poisoning. By comparison, the adsorption of H_2 molecules was not affected the composition in $Ni_{1-x}Co_x$. This adsorptive property of the $Ni_{1-x}Co_x$-YSZ sample for the TPD analysis shows an agreement with the result of the cell performance, as shown in Figs. 1a and 1b.

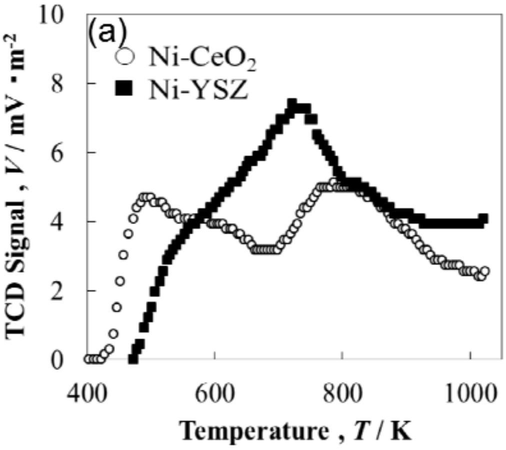

Fig. 4(a) TPD curves of the $Ni\text{-}CeO_2$ and Ni-YSZ samples for CH_4 at $\beta = 10\ K^{-1}$.

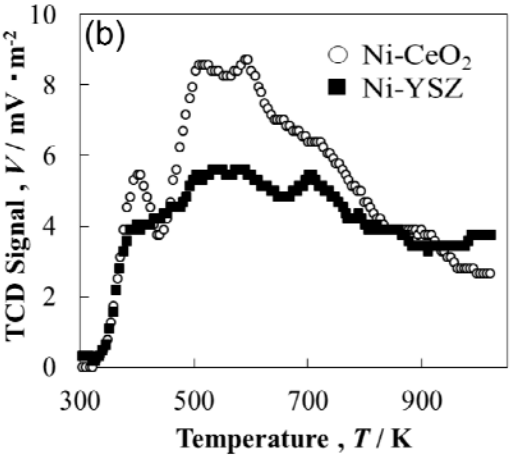

Fig. 4(b) TPD curves of the $Ni\text{-}CeO_2$ and Ni-YSZ samples for CO at $\beta = 10\ K^{-1}$.

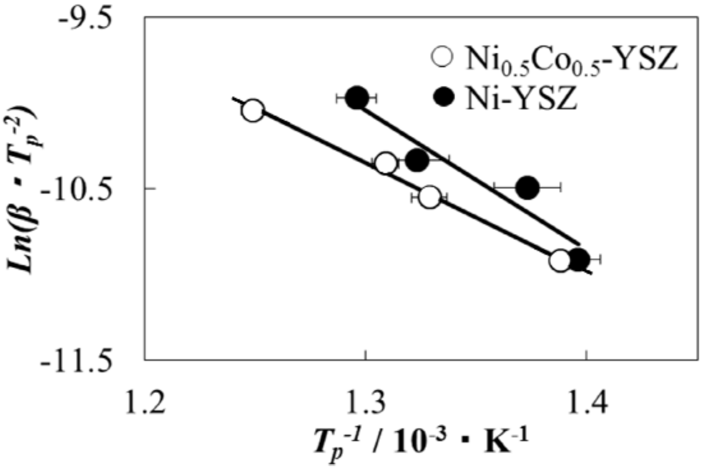

Fig. 5 Arrhenius plots for thermal desorption of the adsorbed CH_4 in the $Ni_{1-x}Co_x$-YSZ samples.

4. Conclusion

Substitution of Co atoms for Ni atoms in the Ni-based cermet anode enhanced the electrochemical oxidation of CH_4. This effect was confirmed for the cells using an YSZ electrolyte. The cell using the $Ni_{1-X}Co_X$-YSZ cermet anode showed an increase in the cell performance with increasing amount of Co content up to approximately 0.8. The decrease in the anodic overvoltage contributes to an enhancement of the cell performance. The TPD results showed that the adsorptive ability of $Ni_{1-x}Co_x$-YSZ and $Ni_{1-x}Co_x$-CeO_2 cermet particles for CH_4 and CO can well account for the cell performance of these anode materials on the direct oxidation of CH_4 by the O^{2-} ions supplied through the oxide electrolyte. The adsorptive property of $Ni_{1-x}Co_x$ particles was affected by the oxide component of the cermet materials. The partial substitution of Co for Ni in the fcc lattice increases the amount of adsorbed species, and decreases the desorption activation energy of desorption for CO and CH_4.

Acknowledgment

A part of this work was supported by a Grant-in-Aid of Scientific Research (B) (#24360304) from Japan Society for the Promotion of Science.

References

[1] A. McEvoy, “High Temperature Solid Oxide Fuel Cells”, S. C. Singhal and K. Kendall, Editors, pp.149-169, Elsevier, UK (2003).
[2] A. Hammou and J. Guindet, “The CRC Handbook of Solid State Electrochemistry”, P. J. Gellings and H. J. M. Bouwmeester, Editors, pp. 419-422, CRC Press, Boca Raton, Florida (1997).
[3] H. Uchida, T. Osuga, and M. Watanabe, J. Electrochem. Soc., **146** (1999) 1677.
[4] M. Watanabe, H. Uchida, and M. Yoshida, J. Electrochem. Soc., **144** (1997) 1739.
[5] T. Setoguchi, K. Okamoto, K. Eguchi, and H. Arai, J. Electrochem. Soc., **139** (1992) 2875.
[6] H. Yoshida and T. Inagaki, J. Alloys Compounds, **408/412** (2006) 632.
[7] H. Tsuchiya, W. Weerapakkaroon, T. Kanjanaboonmalert, T. Wahtzu, and K. Sato, ECS Trans., **25** (2009) 2169.
[8] T. Sawahata, H. Takayanagi, T. WahTzu, and K. Sato, ECS Trans., **35** (2011) 1545.
[9] W. A. Bone and H. F. Coward, J. Chem. Soc., **93** (1908) 1197.
[10] J. Zhang, H. Wang, and A.K. Dalai, Appl. Catalysis A, **339** (2008) 121.
[11] J. L. Falconer and J. A. Schwarz, Catal. Rev. Sci. Eng., **25** (1983) 141.

(Received: 21 May, 2012, Accepted: 5 June, 2012)

Transactions on GIGAKU **1***(2012)01027/1-5*

Preparation of Filter Paper Conjugated with High Mannose-Type Glycans

Kiyoshi Furukawa*, Tomomi Tadokoro, Mayumi Sato, Eriko Yamada
Department of Bioengineering, Nagaoka University of Technology,
1603-1 Kamitomioka-cho, Nagaoka 940-2188, Japan
**E-mail: furukawa@vos.nagaokaut.ac.jp*

This paper describes the method for conjugating N-glycans from animal sources to filter paper. High mannose-type glycans were released from bovine RNase B by hydrazinolysis, and then they were treated with succinic dihydrazide. Hydrazide-derivatives were incubated with filter paper which was pretreated with 100 mM sodium periodate for 60 min to generate aldehyde groups on cellulose backbones, and then they were treated with dimethylamine borane in acetate buffer (pH3.9). The resulting glycan-conjugated filter paper was incubated with peroxidase-conjugated Con A, and subjected to color development in the presence of a chromogenic substrate, showing that color intensities correlate with amounts of high mannose-type glycans conjugated to filter paper. The results from analyses of chemically modified filter paper suggest that glycan-conjugated filter paper could be useful for trapping microorganisms which express glycan-binding proteins, lectins.

1. Introduction

Many microorganisms recognize cell surface glycans as receptors for cell attachment and tissue colonization. This is because viruses, bacteria and protozoa express a large number of glycan-binding proteins so called lectins (reviewed in 1). For examples, human influenza viruses recognize the Siaα2→6Gal group by their hemagglutinins expressed on virus surfaces, and *Helicobacter pylori* binds Fucα1→2Galβ1→3(Fucα1→4)GlcNAc1β→R group (Le^b antigen) by its adhesin BabA expressed on flagella (2, 3). In fact, such glycans are expressed on cell surfaces of human respiratory tract and stomach tissues, respectively. Furthermore, *E. coli* binds high mannose-type glycans rich in intestinal mucosa and glycans with the Galα1→4Gal group in urinary tract depending on the strains, and pathogenic strains often cause enterohemorrhagy with verotoxin produced, hemolytic uremic syndrome, acute encephalopathy, pyelonephritis, cystitis and urithritis for human beings (1, 4, 5). Therefore, we are always facing the crisis of infection with pathogenic microorganisms that recognize our glycans. However, this indicates that glycans can protect us against a variety of microorganisms. Using daily necessaries and foods conjugated with glycans with respective structures, they could trap microorganisms floating in air, living in water, attached on foods and so on, and remove them resided in our air tract, and digestive and excretory organs. Since some filters and foods made from plant polysaccharides such as cellulose, mannan, and carageenan, such plant polysaccharides can be oxidized with sodium periodate to generate aldehyde groups which react quickly with hydrazide glycans, thus producing filters and foods with glycans containing respective structures. In the present paper, we report a basic method to prepare filter paper conjugated with high mannose-type glycans from animal glycoproteins.

2. Materials and Methods

Chemicals **-** Anhydrous hydrazine, dimethylamine boran, blue dextran, bovine RNase B, bovine serum albumin (fraction V), and 4-chloro-1-naphthol were purchased from Nacalai Tesque, Inc. (Kyoto) and Sigma Chemicals Co. (St. Loius, MO), respectively. Horseradish peroxidase-conjugated Con A was from Seikagaku Kogyo Co. (Tokyo). Whatman 3MM filter paper was from GE Healthcare Japan (Tokyo). Shoji paper containing 15% of a mixture of rayon, vinylon and binder was from Fujita Paper Mills Co. (Misato, Saitama), and white colored paste made of konnyaku flour was from a local food store.

Liberation of N-glycans from glycoproteins - RNase B, which has been shown to contain high mannose-type glycans (6), dried thoroughly over P_20_5 *in vacuo*, was subjected to hydrazinolysis for 10 h as described previously (7). After N-acetylation, liberated glycans were separated by paper chromatography using 1-butanol-ethanol-water (4:1:1 v/v) as a solvent for 2 days, and extracted from paper by the method described previously (8).

Conjugation of glycans with filter paper, shoji paper and konnyaku paste – Glycans were incubated with succinic dihydrazide and dimethylamine borane in a mild acidic condition to prepare hydrazide glycans. The derivatized glycans (50-100 nmoles/sample for blue dextran and 20-40 nmoles/sample for N-glycans) were then incubated for 8 hrs at 40°C with filter paper, shoji paper and konnyaku paste (surface areas of 24-40 mm^2) oxidized with sodium periodate under the conditions examined in the present study. The reaction mixture was cooled down and incubated further with dimethylamine borane in acetate buffer (pH4.0) for 36 hrs at 4°C according to the method described previously (9). A chemical reaction for conjugation of glycans to the above materials is illustrated in Fig. 1.

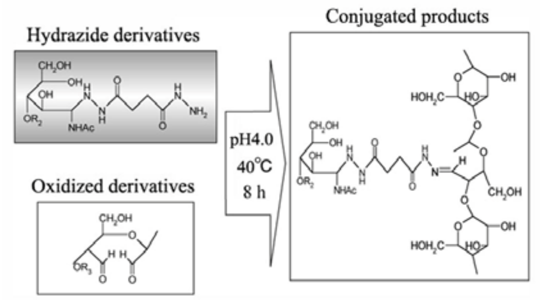

Fig. 1 A schematic illustration of the chemical reaction for conjugation.

Detection of N-glycans conjugated to filter paper, shoji paper and konnyaku paste – N-Glycan-conjugated materials were blocked with 1% bovine serum albumin in 10 mM phosphate buffered-saline (pH7.4) for 2 h, and incubated with 10 µg/ml Con A conjugated with horseradish peroxidase for 1 h at 4°C followed by 500 µg/ml of the chromogenic peroxidase-substrate, 4-chloro-1-naphthol, for 10 min according to the method described previously (10). Color intensities developed were determined by NIH image J analysis.

3. Results and Discussion

Preparation of oxidized filter paper

Optimal conditions for derivatization of N-glycans with succinic dihydrazide were established previously (9). In the present study, optimal conditions for oxidizing filter paper with sodium periodate were determined. Pieces of filter paper (40 mm^2) were treated with 10, 50 and 100 mM sodium periodate in 50 mM acetate buffer (pH 4.5) for up to 60 min at room temperature. Then, they were conjugated with hydrazide blue dextran (100 nmols/sample) and amounts of blue dextran conjugated to filter paper were determined by measuring intensities of blue color on filters by the image analysis. The results showed that not so much blue dextran is conjugated to filters treated with 10 and 50 mM sodium periodate for 60 min, but significant amounts of blue dextran is conjugated to filters treated with 100 mM sodium periodate for 60 min at room temperature (data not shown). In order to determine an optimal incubation time period of filter paper with 100 mM sodium periodate, pieces of filter paper were treated with 100 mM sodium periodate for 15, 30, 45 and 60 min, and then conjugated with hydrazide blue dextran. The results showed that more blue dextran is conjugated to filter paper treated for a longer time period with 100 mM sodium periodate (Figs. 2 and 3). However, treatment of filter paper with 100 mM sodium periodate for more than 60 min, particularly over 90 min resulted in decomposition of filter paper (unpublished data), indicating that an optimal incubation time period for oxidizing filter paper is 60 min. Hereafter, filter paper was treated with 100 mM sodium periodate for 60 min at room temperature. When pieces of filter paper (40 mm^2) treated with 100 mM sodium periodate for 60 min were incubated with different amounts of hydrazide blue dextran, 10-20 nmols of blue dextran were conjugated to the filter paper effectively (Fig. 4).

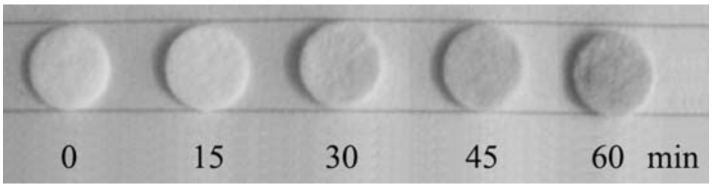

Fig. 2 Blue dextran-conjugated filters. Filters were treated with 100 mM sodium periodate for the time periods indicated, and then conjugated with blue dextran.

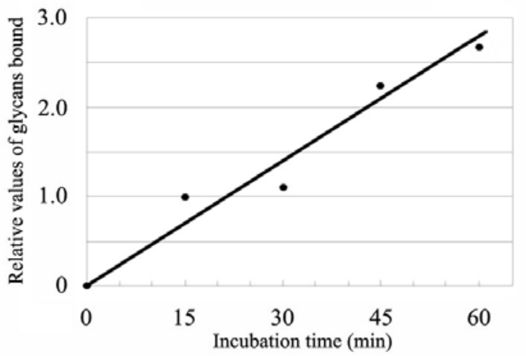

Fig. 3 Incubation time with sodium periodate-dependent conjugation of blue dextran on filters. Filters were incubated with 100 mM sodium periodate for the time periods indicated, and then conjugated with blue dextran. Blue color was monitored by the image analysis.

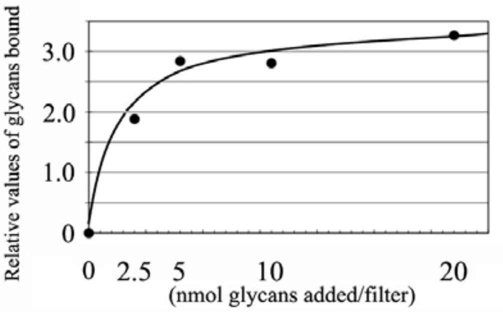

Fig. 4 Concentration-dependent conjugation of blue dextran on filters. Oxidized filters were incubated with different amounts of hydrazide blue dextran. Blue color was monitored by the image analysis.

Conjugation of hydrazide N-glycans to oxidized filter paper

Hydrazide high mannose-type glycans were prepared and conjugated to oxidized filter paper by the method described above. Conjugation of the N-glycans was monitored by binding of Con A which interacts preferentially with high mannose-type ones (11). By measuring color intensities indicating amounts of Con A which interacted with the glycans conjugated to filter paper (Fig. 5), it was shown that about 5-10 nmoles of high mannose-type glycans bind to a piece of filter paper with a surface area of 40 mm^2.

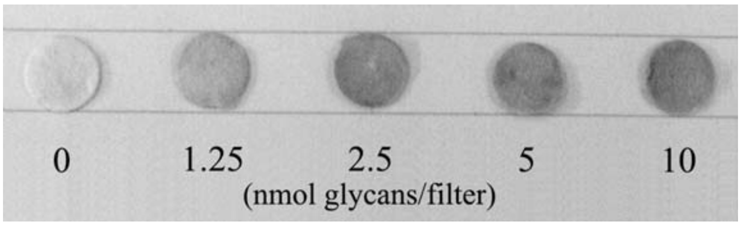

Fig. 5 High mannose-type glycan-conjugated filter paper. Oxidized filters were incubated with different amounts of hydrazide glycans, and glycans bound were detected with Con A-binding as described in the text.

Preparation of oxidized shoji paper and paste made from konnyaku flour

Since an oxidizing condition for filter paper was established, we then examined those for shoji paper and konnyaku paste. Pieces of shoji paper (36 mm^2) and of konnyaku paste (about 36 mm^2

surface area and 5 mm thickness) were similarly treated with 10, 50 and 100 mM sodium periodate for 60 min at room temperature, and oxidized materials were conjugated with hydrazide high mannose-type glycans (40 nmoles/sample) followed by visualization with peroxidase-conjugated Con A as described above. The results showed that toptimal oxidizing conditions for shoji paper and konnyaku paste are 10 mM sodium periodate for 60 min, and that other conditions bring about denature or decomposition of the materials treated (data not shown). Shoji paper and konnyaku paste oxidized with 10 mM sodium periodate for 60 min were incubated with different amounts of hydrazide high mannose-type glycans and visualized with Con A-binding as describe above (Figs. 6 and 7, respectively).

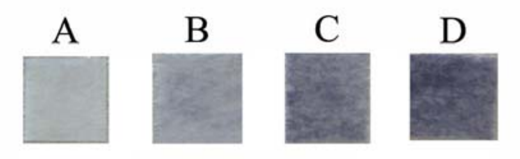

Fig. 6 Glycan concentration-dependent conjugation to shoji paper. A, B, C and D indicate 0, 2.5, 5 and 10 nmoles of glycans/ sample.

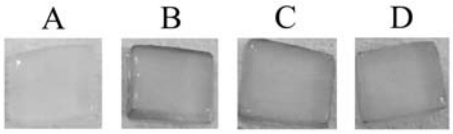

Fig. 7 Glycan concentration-dependent conjugation to konnyaku paste. A, B, C and D indicate 0, 2.5, 5 and 10 nmoles of glycans/ sample.

In the present study, blue dextran and high mannose-type glycans were used to conjugate to filter paper. However, it appeared that more blue dextran chains are conjugated to filter paper than high mannose-type glycan chains. This could be due to differences in the branching structures between them. Further examination remains to be elucidated. Since oxidized materials used in the present study were strips, glycans were conjugated on both sides of them. This indicates that even though microorganisms fail to be trapped at the front side of filter paper, they could be trapped at the backside when they pass through the filter.

Since microorganisms including pathogenic viruses and bacteria bind to glycans with respective structures expressed on cell surfaces of our organs and tissues, it is possible that glycan-conjugated daily necessaries and foods protect us against a variety of infectious microorganisms. A major strain of *E. coli* in nature contains bacterial adhesin FimH at the tip of type 1 fimbria (12), which binds to α-mannose-terminated glycans (4). Therefore, high mannose-type glycan-conjugated filter paper prepared in the present study can trap *E. coli* in nature, particularly in well water to drink and even in tap water when water supply facilities are destroyed by disasters by soaking it or filtering through it. In some underdeveloped countries, inhabitants are always scared with infection by microorganisms through drinking water. Introduction of a large scale-filtering system using glycans in waterwork of such countries will supply microorganism-free drinking water to inhabitants. In other aspects of their application, ventilating fan filters with glycans having the Siaα2→6Gal structures (2) can trap human influenza viruses floating in air under a humidified condition, and reduce absolute numbers of the viruses in living spaces, thus protecting us against infection with the viruses. Konnyaku paste, an indigestible food, with glycans having the Fucα1→2Galβ1→3(Fucα1→4)GlcNAc structure can trap *H. pylori* in stomach and take it out from us if we have been infected with the bacterium. Such ideal trapping of *H. pylori* with the glycan-conjugated foods will reduce the possibility of development and progression of stomach ulcer and eventually of stomach cancer caused by *H. pylori* (13).

The present method can extend to any types of glycans to be conjugated with polysaccharide-based materials depending on which microorganism(s) to be removed from our living spaces and from our bodies. In Japan, we have least chance to appreciate blessing of drinking water since it is free and safe. However, once Japan is hit by serious natural disasters such as earthquakes and flooding, we will be immediately placed into low quality of living environments particularly by shortage of water for daily life and secondary by spreading of infectious diseases due to collapse of sanitary condition. The glycan-conjugated daily necessaries and foods might be of help for us in those circumstances, too.

4. Conclusion

The present study showed that optimal conditions for oxidizing filter paper and for shoji paper and konnyaku paste are 100 mM and 10 mM of sodium periodate for 60 min at room temperature, respectively. The oxidized materials were conjugated with hydrazide high mannose-type glycans. The glycans attached to filter paper, shoji paper and konnyaku paste were visualized by staining with Con A that binds high mannose-type glycans, and quantified by NIH image analysis. These results indicate that not only high mannose-type glycans but also complex-type and hybrid-type glycans, and disaccharides to polysaccharides could be conjugated with these materials. Since microorganisms including pathogenic viruses and bacteria bind glycans with respective structures expressed on our cells (reviewed in 1), it is possible to protect us against infection with such pathogenic microorganisms and/or to elimination of such pathogenic microorganisms already infected us by dairy necessaries and foods conjugated with glycans having structures specific to individual microorganisms as discussed above. The method presented here was first developed in Nagaoka University of Technology, and from the point of view of “GIGAKU” (the policy and target in Nagaoka), further studies and applications of this method are strongly required for the progress in biological science and glycotechnology.

Acknowledgments

This work was supported by the Grant-in-Aid for Scientific Research from the Ministry of Education, Science, Sports, Culture and Technology, Japan, by the Research Promotion Fund from the Japan Science and Technology Agency, and by Program for the Pacific Rim Green Innovation Hub Project in Nagaoka University of Technology.

References

[1] A. Varki, R. D. Cummings, J. D. Esko, H. H. Freeze, P. Stanley, C. R. Bertozzi, G. W. Hart, and M. E. Etzler, In “Essentials of Glycobiology” (2nd ed.), Cold Spring Harbor Lab. Press, New York, 2008.
[2] J. N. Couceiro, J. C. Paulson, and L. G. Baum, Virus Res., **29** (1993) 155-165.
[3] D. Ilver, A. Amrnqvist, J. Ogren, I. M. Frick, D. Kersulyte, E. T. Incecik, D. E. Berg, A. Covacci, L. Engstrand, and T. Boren, Science, **279** (1998) 373-377.
[4] I. Ofek, and E. H. Beachey, Infect. Immun., **22** (1978) 247-254.
[5] K. Bock, M. E. Breimer, A. Bringnole, G. C. Hansson, K.-A. Karlsson, G. Larson, H. Leffler, B. E. Samuelsson, N. Stromberg, and C. S. Eden, J. Biol. Chem., **260** (1985) 8545-8551.
[6] C.-J. Liang, K. Yamashita, and A. Kobata, J. Biochem., **88** (1980) 51-58.
[7] S. Takasaki, T. Mizuochi, and A. Kobata, Methods Enzymol., **83** (1982) 263-268.
[8] T. Hironaka, K. Furukawa, P. C. Esmon, M. A. Fournel, S. Sawada, M. Kato, T. Minaga, and A. Kobata., J. Biol. Chem., **267** (1992) 8012-8020.
[9] N. Yoshitani, and S. Takasaki, Anal. Biochem., **277** (2000) 127-134.
[10] T. Sato, K. Furukawa, D. E. Greenwalt, and A. Kobata, J. Biochem. **114** (1993) 890-900.
[11] S. Ogata, T. Muramatsu, and A. Kobata, J. Biochem., **78** (1975) 687-696.
[12] E. Hahn, P. Wild, U. Hermanne, P. Sebbel, R. Glockshuber, M. Haner, N. Taschner, P. Burkhard, U. Aebi, and S. A. Muller, J. Mol. Biol., **323** (2002) 845-857.
[13] F. J. Hardin, and R. A. Wright, Hospital Physician, **May** (2002) 23-31.

(Received: 17 May, 2012, Accepted: 31 May, 2012)

Transactions on GIGAKU **1**(2012)01028/1-6

Development of *Trichoderma reesei* Strain Specialized for Cello-oligosaccharides Production from Cellulose

Yosuke Shida[1]*, Rina Yoshida[1], Tatsuki Wakayama[2], Yoshiro Konda[2], Takashi Yamaguchi[1], and Wataru Ogasawara[1]
[1]Department of Bioengineering, Nagaoka University of Technology
1603-1 Kamitomioka, Nagaoka, Niigata, 940-2188,
[2] INPEX Corporation
Akasaka Biz Tower, 5-3-1 Akasaka, Minato-ku, Tokyo 107-6332, Japan
**E-mail: yshida@vos.nagaokaut.ac.jp*

The filamentous fungus *Trichoderma reesei* is a well-known cellulolytic organism that has been widely used in industrial applications such as saccharification of cellulosic biomass. *T. reesei* produces a complete set of cellulases to degrade cellulose to glucose. However, it is difficult to control the enzyme reaction to obtain cello-oligosaccharides, which are the intermediates of cellulose degradation. In this study, we created a *T. reesei* strain in which the gene encoding ß-glucosidase I of cellulases was disrupted. The resultant *bgl1* disruptant exhibited higher accumulation of cellobiose compared to the parent PC-3-7 strain in cellulose hydrolysis experiments.

1. Introduction

Cellulose is the most abundant biomass on the earth as the major component of plant cell wall. It is a linear polymer composed of ß-D-glucose units, linked by ß-1,4-glycosidic bonds. Glucose derived from cellulosic biomass can serve not only as food, but also as raw material for chemicals and fuels [1]. In addition to monosaccharides, cello-oligosaccharides (COSs), which are intermediates of cellulose degradation, have the potential to be converted into functional foods or other raw materials [2, 3]. However, a major impediment to this process is the high refractory nature of cellulose to hydrolysis, which is due to its crystalline structure. In nature, cellulose is degraded by a variety of cellulolytic microorganisms.

The filamentous fungus *Trichoderma reesei* is a potent producer of cellulase and produces three types of cellulases, which synergistically degrade cellulose to glucose [4]. The cellobiohydrolase (CBH, EC 3.2.1.91) releases cellobiose from the end of the cellulose chain. The endoglucanase (EG, EC 3.2.1.4) is an end-acting enzyme that randomly cleaves the cellulose chain in an amorphous region. Finally, the ß-glucosidase (BGL, EC 3.2.1.21) hydrolyzes cellobiose to glucose. The weakest link of *T. reesei* cellulase preparation is the comparatively low activity of BGL, which results in the inhibition of cellobiohydrolase by accumulated cellobiose. Attempts have been made to construct genetically modified derivative of *T. reesei* to enhance ß-glucosidase activity for effective saccharification of cellulosic biomass [5]. On the other hand, production of cellobiose can be achieved by disrupting the gene encoding ß-glucosidase, and production of longer COSs can be achieved by disruption of cellobiohydrolases and ß-glucosidase genes. COSs derived from cellulosic biomass are estimated to be the most widely available nondigestible oligosacchalides, which are resistant to digestion by human gastric and pancreatic enzymes. Hence, COSs can be the potential sources for prebiotic functional foods by stimulating bacteria in the colon [6]. A low-cost efficient production system of COSs from cellulosic biomass and a subsequent separation system of specific COS are expected to interpret the physiological functions of COSs and to establish wide industrial use of COSs. In this study, we present the effect of BGL deletion in *T. reesei* on the production of COSs from cellulosic biomass.

2. Experiments

(1) Fungal strains and culture conditions

T. reesei strain PC-3-7 is a cellulase-hyperproducing mutant with enhanced ability in cellulase induction by L-sorbose [7] and was obtained from Kyowa Hakko, Japan. Strains were maintained on potato dextrose agar (PDA; Difco) slants.

For production of cellulase enzymes, conidia obtained from *T. reesei* strains grown on PDA plates were inoculated in a medium composed of 50 mM Na-tartrate buffer (pH4.0) containing 0.14% $(NH_4)_2SO_4$, 0.2% KH_2PO_4, 0.03% $CaCl_2 \cdot H_2O$, 0.03% $MgSO_4 \cdot 7H_2O$, 0.05% yeast extract, 0.1% Polypeptone, 0.1% Tween 80, 0.1% trace element solution (0.005 mg/L $FeSO_4$, 0.002 mg/L $MnSO4H_2O$, 0.001 mg/L $CuSO_45H_2O$, 0.002 mg/L $ZnSO_4 \cdot 7H2O$, 0.001 mg/L $(NH_4)_6Mo_7O_{24} \cdot 4H_2O$, 0.002 mg/L $CoCl_2 \cdot 6H_2O$ and 0.001 mg/L $NiCl_2 \cdot 6H_2O$), which was supplemented with 1% Avicel or cellobiose as a carbon source. The cultures were then incubated at 28°C on rotary shaker at 220 rpm for 5 days.

(2) Construction of bgl1 disruption cassette

The chromosomal DNA of *T. reesei* PC-3-7 was prepared as described previously [8]. DNA fragment of *bgl1* upstream region and downstream region were amplified by polymerase chain reaction (PCR). The *amdS* gene from *Aspergillus nidulans* encoding acetamidase was used as a selection marker of *T. reesei* transformant was prepared from the plasmid p3SR2. Three DNA fragments were connected in the order of *bgl1* upstream region first, followed by *amdS* and then *bgl1* downstream region. The resultant *bgl1* disruption cassette was used for transformation of *T. reesei* strains.

(3) Transformation of T. reesei

T. reesei strain PC-3–7 was transformed using a protoplast-polyethylene-glycol procedure [9]. Prior to transformation, the *bgl1* disruption cassette was subjected to restriction enzyme digestion to remove the vector backbone. Candidate transformants were streaked twice on selective plates containing acetamide as the sole nitrogen source, and were transferred to PDA plates to form conidia.

(4) Enzyme assays and protein analysis

Carboxymethyl–cellulase (CMCase) activity was determined by measuring reducing sugar using Somogyi-Nelson method [10]. CMCase activity was determined with a final concentration of 1.0% carboxymethylcellulose (low viscosity, 50-200 cps, Sigma Chemical) in 50 mM sodium acetate buffer (pH 5.0) at 50˚C for 15 min. One unit of activity was defined as the amount of enzyme that produced 1 μmol of reducing sugar per minute in glucose equivalents. BGL activity was determined by measuring the amount of pNP-ß-D-glucopyranoside (pNP-G, Sigma Chemical) released in 50 mM sodium acetate buffer (pH 5.0) at 50˚C. One unit of activity was defined as the amount of enzyme that produced 1 μmol of pNP per minute. Protein concentration was determined using the Bradford protein assay [11] (Bradford, 1976) with bovine gamma globulin as a standard. Sodium dodecyl sulfate-polyacrylamide gel electrophoresis (SDS-PAGE) was carried out in 12.5% polyacrylamide gel slabs as described [12]. Proteins were stained with Coomassie brilliant blue R-250. The molecular-mass markers used were the Precision Plus Dual Standard Marker kit for SDS-PAGE (Bio-Rad).

(5) Cellobiose production

The substrates used for cellobiose production were Avicel™, microcrystalline cellulose and phosphoric-acid swollen cellulose, which was prepared as described by Walseth [13]. The reaction was performed in an 1.5-mL microtube containing 5% (w/w) dry substrate in 100 mM sodium acetate buffer, pH 5.0 with an enzyme at a loading of 5 mg protein/g of dry weight substrate. The reaction was performed at 50˚C with vigorous shaking for the period of 6, 12, or 24 h. Samples were boiled for 5 min to inactivate enzymes, and products were measured using high performance liquid chromatography (HPLC) equipped with Prominence reducing sugar analysis system (Simadzu).

3. Results and Discussion

(1) Construction of bgl1 disruptant of T. reesei PC-3-7

Among the five genes in *T. reesei* encoding extracellular BGL, the *bgl1* product is mainly responsible for BGL activity. Therefore, disruption of the *bgl1* gene was performed. We constructed the *bgl1* disrupting cassette, in which *bgl1* was replaced by *amdS* as a selectable marker (Fig. 1A). After transformation of *T. reesei*, we successfully obtained two candidates that utilize acetamide as a sole nitrogen source. They were grown on Avicel to produce cellulase enzymes and then the culture filtrates were assayed for pNPase activity. The pNPase activities of candidates were significantly lower than that of the parental strain, PC-3-7 (Fig. 1B). In addition, the 82-kD protein band corresponding to BGL1 was not detected in the culture filtrates in SDS-PAGE analysis (Fig 1C). Thus, we concluded that *bgl1* disruptants were successfully constructed. Out of the *bgl1* disruptants obtained, Δ*bgl1*-2 was used as the representative Δ*bgl1* for subsequent experiments.

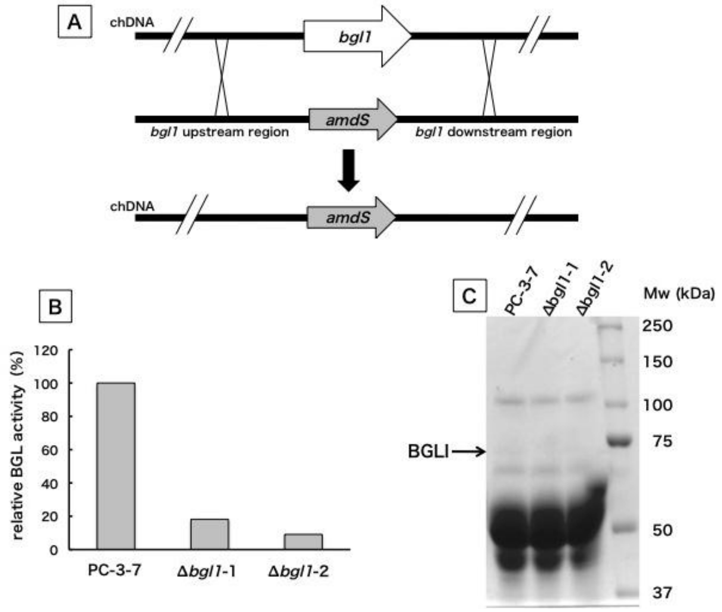

Fig. 1 Construction of *bgl1* disruption mutant by gene targeting technique. A: Schematic representation of gene replacement of *bgl1*. B: Comparison of BGL activity of parental strain PC-3-7 and two *bgl1* disruptants, Δ*bgl1*-1 and Δ*bgl1*-2. C: SDS-PAGE analysis of enzyme preparations from *bgl1* disruptants. Samples subjected to electrophoresis were prepared from culture filtrates grown on Avicel for 6 days.

(2) Cellulase production by T. reesei Δ*bgl1 strain*

When *T. reesei* was grown on cellulose as a sole carbon source, it produces a set of cellulases [14]. Although its direct assimilation of cellulose is hard to grasp due to the highly crystalline and insoluble nature of cellulose, it is generally believed that soluble cello-oligosaccharides released by the action of constitutively expressed cellulases served as inducers of inducible cellulase production [15-18]. As the major soluble product from cellulose cellobiose can be the natural inducer of cellulase. However, growth on cellobiose inhibited cellulase induction in *T. reesei* QM9414 [19] due to its rapid hydrolysis to glucose, which suppressed cellulase formation by carbon catabolite repression controlled by a transcription regulator, Cre1 [20]. Among inducers reported so far sophorose exerted the strongest cellulase induction, and sophorose has been considered as the natural inducer of cellulases and was estimated to be formed by transglycosylation by ß-glucosidase. Therefore, it has been assumed that BGL is the key enzyme for cellulase induction in *T. reesei*. Although the *bgl1* gene disruption causing reduction of cellulase formation has been reported in *T. reesei* QM9414 [21], the effect of *bgl1* disruption has not been examined in PC-3-7, a mutant strain obtained after six generations from QM9414 by UV irradiation and chemical mutagenesis that produces large amount of cellulose. The time course measurement of CMCase activity was performed during the growth on Avicel and cellobiose and the results were compared between PC-3-7 and Δ*bgl1*. When PC-3-7 and Δ*bgl1* were grown on Avicel, CMCase activity of Δ*bgl1* was slightly higher than that of PC-3-7 (Fig. 2A). However, when they were grown on cellobiose, significantly higher CMCase activity was observed in Δ*bgl1* compared to PC-3-7 strain (Fig. 2B). These results are dramatically opposite to those previously reported for QM9414. Recently, it was reported that cellulase production of PC-3-7 was highly responsive to cellobiose in the liquid medium and that a mutation of the gene encoding a transcription regulator in PC-3-7 altered both cellobiose utilization and cellulase production [22]. These phenotypes were due to some mutation in the PC-3-7 genome, which has been demonstrated previously [22]. The results obtained in this study suggest that the accumulation of cellobiose during the growth period caused higher cellulase induction in Δ*bgl1* strain, and the mutation in PC-3-7 is also involved in the phenotypes observe.

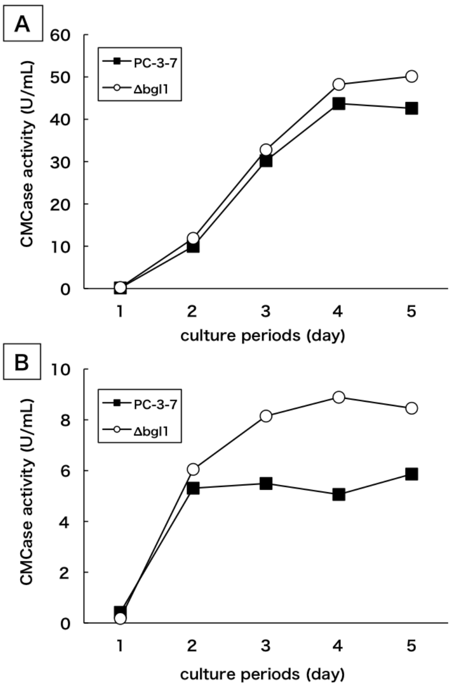

Fig. 2. Time course of CMCase activity produced by PC-3-7 and Δ*bgl1*. These strain**s** were grown on Avicel **(A)** and cellobiose **(B)** as a sole carbon source. The CMCase activity in the culture supernatant was assayed. Open circle**s** and filled square**s** represent Δ*bgl1* and PC-3-7, respectively.

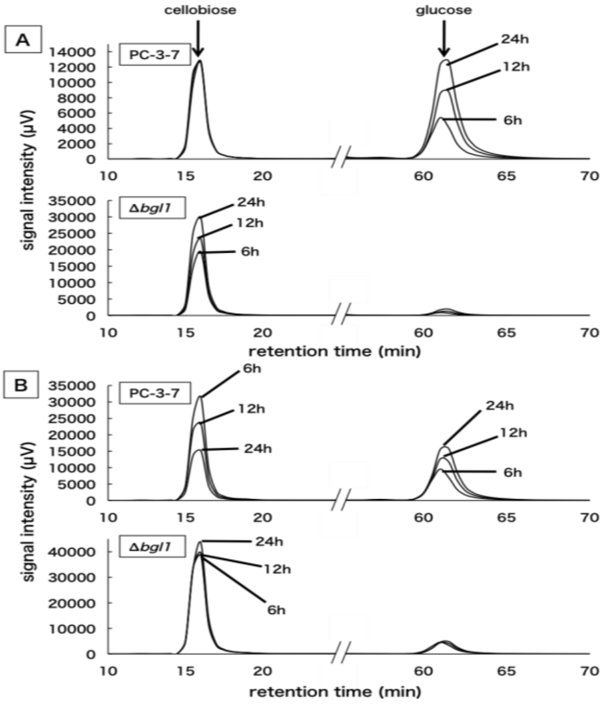

Fig. 3. HPLC analysis of hydrolytic products of cellulosic material by cellulase preparation. Avicel, micro crystalline cellulose (A) and PSC, phosphoric-acid swollen cellulose (B) were used as substrates.

(3) Cellobiose production from cellulosic material

To assess cellobiose accumulation by enzyme preparations, two kinds of celluloses, Avicel and PSC, were used as substrates, and cellobiose and glucose accumulation were compared between Δ*bgl1* and PC-3-7 strains. When Avicel was added to the enzyme preparation of Δ*bgl1*, the amount of cellobiose increased and glucose remained at a significantly lower level over the course of the reaction time. In contrast, cellobiose level stayed constant and glucose increased during the reaction period in the PC-3-7 enzyme preparation (Fig. 3A). Similar results were obtained when PSC was used as a substrate. The enzyme preparation of Δ*bgl1* exhibited higher cellobiose accumulation and reduced glucose accumulation compared to the PC-3-7 enzyme preparation (Fig. 3B). Because PSC is susceptible to degradation by endoglucanases owing to the swollen nature of its cellulose, we expected to observe longer cello-oligosaccharides from PSC, but no other COSs than cellobiose was detected.

4. Conclusions

A novel mutant strain of *T. reesei* PC-3-7 with the disruption of *bgl1* gene was constructed using gene replacement technique. The resulting mutant showed significant reduction of ß-glucosidase activity. In addition, *bgl1* disruption brought increased production of cellulase compared to the parent PC-3-7 strain. When Avicel and PSC were treated with the enzyme preparation of Δ*bgl1*, accumulation of cellobiose was observed. Mass production of cellobiose from cellulosic materials is expected using this Δ*bgl1* strain and development of a strain with the cellobiohydrolase gene disruption on the background of Δ*bgl1* is also expected to produce longer cello-oligosaccharides. Exploitation of a more practical purification method of COSs from the reaction mixture is required to achieve mass production of these intermediary products of cellulose degradation.

Acknowledgement

This work was mainly supported by INPEX Corporation. This work was partially supported by Establishment of Carbon-Cycle-System with Natural Rubber program of Science and Technology Research Partnership for Sustainable Development in Japan science and technology agency (JST) and Japan International Cooperation Agency (JICA).

References

[1] B. Kamm, and M. Kamm, Adv. Biochem. Eng. Biotechnol., 105 (2007) 175–204

[2] M. Satouchi, T. Watanabe, S. Wakabayashi, T. Ohokuma, T. Koshijima, and M. Kuwahara, J Jpn soc nutr food sci 49 (1996) 143– 148. (in Japanese).

[3] S. R. Hall, S. C. Wimbush, Y. Shida, and W. Ogasawara, *Chem. phys. lett.*, **507** (2011) 144-150 (2011)

[4] A. Schuster, and M. Schmoll, Appl. Microbiol. Biotechnol 87(2010) 787–79

[5] H. Nakazawa, T. Kawai, N. Ida, Y. Shida, Y. Kobayashi, H. Okada, S. Tani, J. Sumitani, T. Kawaguchi, Y. Morikawa, and W. Ogasawara, Biotechnol. Bioeng. 109 (2012) 92-99

[6] G.R. Gibson, and M. B. Roberfroid, *J. Nutr.* 125 (**1995**) 1401-1412.

[7] M. Kawamori, Y. Morikawa, and S. Takasawa, Appl. Microbiol. Biotechnol. 24(2986) 449–453.

[8] B. Seiboth, L. Hartl, M. Pail, E. Fekete, L. Karaffa, and C.P. Kubicek, Mol. Microbiol. 51(2004) 1015–1025

[9] M. Penttilä, H. Nevalainen, M. Rättö, E. Salminen, and J.K.C. Knowels, Gene 61(1987) 155–164

[10] M. Somogyi, J Biol Chem 195(1952) 19-23

[11] M. M. Bradford, Anal Biochem 72(1976) 248–254

[12] U. K. Laemmli, Nature 227 (1970) 680–685

[13] C. S. Walseth, Am Tech Assoc Pulp Paper Ind 35(1952) 228-233

[14] Nogawa M, Goto M, Okada H, Morikawa Y (2001) L-Sorbose induces cellulase gene transcription in the cellulolytic fungus Trichoderma reesei. Curr Genet 38:329–334

[15] M. Gritzali, and R. D. Brown, Adv. Chem. Ser. 181(1960) 816-826

[16] M. Mandels, F. W. Parrish, and E. T. Reese, J. Bacteriol 83(1962) 400-408

[17] S. El-Gogary, A. Leite, O. Crivellaro, D. E. Eveleigh, and H. El-Dorry, Proc. Natl. Acad. Sci. USA 86(1989) 6138-6141

[18] J. C. Carle-Urioste, J. Escobar-Vera, S. El-Gogary, F. Henrique-Silva, E. Torigoi, O. Crivellaro, A. Herrera-Estrella, and H. El-Dorry, J. Biol. Chem. 272(1989) 10169-10174
[19] C. Fritscher, R. Messner, and C. P. Kubicek, Exp. Mycol. 14(1990) 451-461
[20] J. Strauss, R. L. Mach, S. Zeilinger, G. Hartler, G. Stöffler, M. Wolschek, and C. P. Kubicek, FEBS Lett. 376(1995) 103-107
[21] R. L. Mach, B. Seiboth, A. Myasnikov, R. Gonzalez, J. Strauss, A. M. Harkki, and C. P. Kubicek, Mol Microbiol 16(1995) 687-697
[22] M. Nitta, T. Furukawa, Y. Shida, K. Mori, S. Kuhara, Y. Morikawa, and W. Ogasawara, Fungal Genet Biol 49(2012) 388-397

(Received: 30 May, 2012, Accepted: 18 June, 2012)

Transactions on GIGAKU ***1****(2012)01029/1-6*

Identification of Amino Acid Residues Essential for the Activity of 3-*O*-Methylgallate 3,4-Dioxygenase from *Sphingobium* sp. Strain SYK-6

Daisuke Kasai* and Eiji Masai

Department of Bioengineering, Nagaoka University of Technology,
Nagaoka, Niigata 940-2188, Japan
**E-mail: dkasai1@vos.nagaokaut.ac.jp*

The 3-*O*-methylgallate 3,4-dioxygenase gene, *desZ*, is involved in the syringate catabolism of the lignin-derived aromatic degrader *Sphingobium* sp. strain SYK-6. Its product, DesZ is classified as a type II extradiol dioxygenase, which usually contains two histidines and one glutamate to coordinate active site non-heme Fe(II) and another histidine to deprotonate the hydroxyl group of a substrate. Based on the amino acid sequence alignment of DesZ with the related type II extradiol dioxygenases His250 is predicted to be involved in deprotonation of the substrate hydroxyl group. His12 and Glu287 are estimated to coordinate Fe(II) and the other histidine is deduced to be replaced by Glu100 in DesZ. Each of DesZ mutants with His12Ala, Glu100Ala, His250Ala, or Glu287Ala replacements lost its catalytic activity completely. These results indicate that these four amino acid residues are essential for the DesZ activity and sauggest that His12, Glu100, and Glu242 coordinate Fe(II) in DesZ.

1. Introduction

Extradiol dioxygenases play a critical role in the aerobic bacterial degradation of aromatic compounds. These enzymes catalyze the cleavage of the aromatic ring of catechol derivatives, such as catechol, protocatechuate (PCA), and homoprotocatechuate (HPCA), through the incorporation of two oxygen atoms at a position adjacent to the hydroxyl groups. It has been reported that a large number of extradiol dioxygenases contain Fe(II) at the active site. According to the similarity of their amino acid sequences, the extradiol dioxygenases have been classified into three different evolutionarily independent families. Type I extradiol dioxygenases belong to the vicinal oxygen chelate superfamily, including 2,3-dihydroxybiphenyl 1,2-dioxygenase of *Burkholderia xenovorans* LB400 and *Acidovorax* sp. strain KKS102 and catechol 2,3-dioxygenase of *Pseudomonas putida* mt-2. Type II extradiol dioxygenases comprise enzymes consisting of one or two different subunits. For example, 2,3-dihydroxyphenylpropionate 1,2-dioxygenase from *Escherichia coli* K-12 and HPCA 2,3-dioxygenase of *E. coli* W are homooligomers of a single subunit, whereas PCA 4,5-dioxygenase (4,5-PCD) of *Sphingobium*, *Pseudomonas*, and *Comamonas* strains and 2-aminophenol 1,6-dioxygenase of *Pseudomonas* and *Comamonas* strains have α and β subunits. Type III dioxygenases belong to the cupin superfamily, which includes such enzymes as gentisate dioxygenase, homogentisate dioxygenase, and 1-hydroxy-2-naphthoate dioxygenase. Despite their different primary structures, these three types of enzymes have similar active sites and usually possess the same iron ligands, two histidines and one glutamate called 2-His-1-carboxylate structural motif. In addition to these residues, another histidine in the active site, which is involved in the deprotonation of the hydroxyl group of the substrate, is conserved among the extradiol dioxygenases.

Sphingobium sp. strain SYK-6 is able to grow on a wide variety of lignin-derived aromatic compounds, including 5,5'-dehydrodivanillate, vanillate, and syringate, as the sole source of carbon and energy [2, 3]. The catabolic pathway for syringate has been characterized and is shown in Fig. 1. 3-*O*-Methylgallate (3MGA), a metabolite of syringate via the reaction catalyzed by syringate *O*-demethylase (DesA), is degraded through three different pathways in which LigAB, 3MGA 3,4-dioxygenase (DesZ), and 3MGA *O*-demethylase (LigM) and gallate dioxygenase (DesB) participate [4-7]. DesZ catalyzes the ring cleavage between C3 and C4 of 3MGA to generate

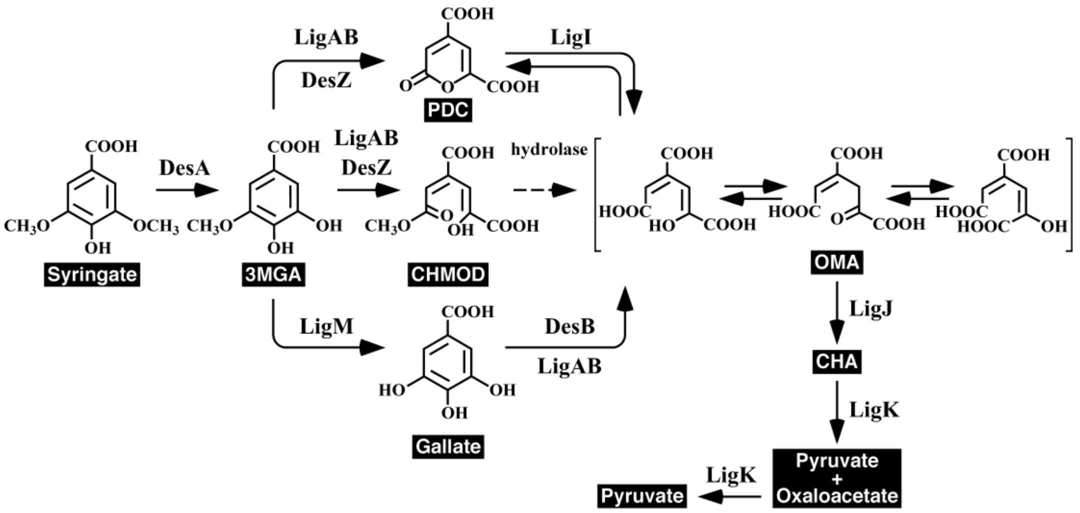

Fig. 1. Catabolic pathways of syringate by *Sphingobium* sp. strain SYK-6. Enzymes: DesA, syringate *O*-demethylase; DesZ, 3MGA 3,4-dioxygenase; LigA and -B, small and large subunits, respectively, of 4,5-PCD; LigM, vanillate/3MGA *O*-demethylase; DesB, gallate dioxygenase; LigI, PDC hydrolase; LigJ, OMA hydratase; LigK, CHA aldolase/oxaloacetate decarboxylase. Compounds: 3MGA, 3-*O*-methylgallate; PDC, 2-pyrone-4,6-dicarboxylate; CHMOD, 4-carboxy-2-hydroxy-6-methoxy-6-oxohexa-2,4-dienoate; OMA, 4-oxalomesaconate; CHA, 4-carboxy-4-hydroxy-2-oxoadipate.

4-carboxy-2-hydroxy-6-methoxy-6-oxohexa-2,4-dienoate and 2-pyrone-4,6-dicarboxylate [4]. According to the amino acid sequence similarity, DesZ appeared to belong to the type II extradiol dioxygenase family. However, the second histidine, which is the constituents of the 2-His-1-carboxylate structural motif, is not found in DesZ. In the present study, we investigated the amino acid residues involved in the activity of DesZ using site-directed mutagenesis.

2. Experiment

Strains and plasmids

The *Escherichia coli* strains were grown in Luria-Bertani (LB) medium at 37°C or 30°C. For culturing the cells carrying an antibiotic resistance marker, the media for the *E. coli* transformants were supplemented with 100 mg of ampicillin (Ap) per liter.

DNA manipulations, site-directed mutagenesis, and nucleotide sequencing

The DNA manipulations were performed essentially as previously described [8, 9]. The site-directed mutagenesis was performed using a QuikChange site-directed mutagenesis kit (Stratagene, San Diego, CA) following the manufacturer's instructions. The pTZNE6 and pTZEN3 recombinant plasmids carrying the 0.7-kb NdeI-EcoRI fragment and 0.3-kb EcoRI-NdeI fragment, respectively, were used as the templates for the amino acid changes H12A, E100A, H250A, and E287A in DesZ, together with the appropriate primers (Primer sequences are available upon request), to obtain pT6, pT8, pT11, and pT12. The mutated *desZ* genes were constructed by inserting the 0.3-kb EcoRI fragment from pBH700 into pT6 and pT8 and by inserting the 0.7-kb EcoRI fragment from pBE660 into pT11 and pT12. The 1.0-kb NdeI fragments from the resulting plasmids, pSD6, pSD8, pSD11, and pSD12, were cloned into pET21a(+) to obtain pETZM6 (H12A), pETZM8 (E100A), pETZM11 (H250A), and pETZM12 (E287A), respectively. Mutagenesis of each nucleotide base was verified by sequencing both strands of the cloned insert using the dideoxy termination method [10] with a CEQ 2000XL genetic analysis system (Beckman Coulter, Inc., Fullerton, CA). A Sanger reaction was performed using a CEQ Dye terminator cycle sequencing-quick start kit (Beckman Coulter, Inc.). The analysis of the nucleotide sequence was performed as described in a previous study [6]. The multiple sequence alignment was produced using the Clustal W program, and the phylogenetic tree was inferred from the alignments using the neighbor-joining method [11]. The graphics for the phylogenetic trees were produced using the TreeView program [12]. The DDBJ, EMBL, and GenBank databases were used for searching for homologous proteins.

Expression of desZ *and its mutants in* E. coli *and preparation of crude enzymes*

E. coli BL21(DE3) cells carrying either the wild-type or mutant *desZ* gene were grown in 100 ml of LB medium containing Ap at 30°C. The expression of the genes was induced for 4 h by adding 1 mM isopropyl-β-D-thiogalactopyranoside when the absorbance of the culture at 600 nm reached 0.5. The cells were harvested and resuspended in FE2 buffer consisting of 50 mM Tris-HCl buffer (pH 7.0), 10% glycerol, 0.1 mM ferrous ammonium sulfate, and 2 mM L-cysteine hydrochloride. The suspended cells were sonicated, and the cell lysate was centrifuged at 15,000 × *g* for 15 min. The resulting supernatant was then used as the crude enzyme fraction. The protein concentration was determined by the method of Bradford [13]. The expression of the gene was confirmed by sodium dodecyl sulfate-12% polyacrylamide gel electrophoresis (SDS-PAGE).

Enzyme assays

The dioxygenase activities of DesZ and its mutants were assayed by measuring the substrate-dependent oxygen consumption rate. The 2-ml assay mixture contained 50 mM GTA buffer (pH 7.0) consisting of 50 mM 3,3-dimethylglutarate, 50 mM Tris, 50 mM 2-amino-2-methyl-1,3-propanediol, the crude enzyme (500 μg of protein), and 1 mM of 3MGA. The reaction was performed at 30°C, and the oxygen consumption rate was measured using an oxygen electrode (B-505; Iijima Electronics Manufacturing Co., Ltd.). The enzyme activity (one unit) was defined as the amount that consumed 1 μmol of O_2 per min at 30°C. The specific activity was expressed as units per milligram of protein.

3. Results

Amino acid sequence alignment of DesZ with type II extradiol dioxygenases

Based on the three dimensional structure of LigB, His12, His61, and Glu242 in LigB are estimated to coordinate non-heme iron and constitute an active center and His195 is predicted to act as the catalytic base [14]. Alignment of the deduced amino acid sequence of the *desZ* gene with that of LigB indicated that DesZ conserved residues His12, His250, and Glu287, which correspond to His12, His195, and Glu242 of LigB, respectively (Fig. 2). The alignment also revealed that the

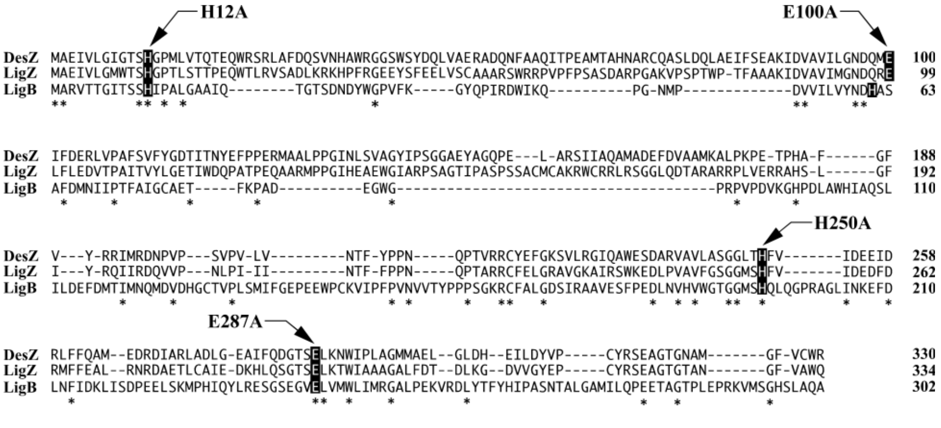

Fig. 2. Alignment of the deduced amino acid sequences of *desZ, ligZ*, and *ligB*. Identical amino acids are indicated with asterisks. The conserved residues among the type II extradiol dioxygenases that are thought to be active site residues in LigAB are shaded in black. The arrows show the positions subjected to mutagenesis.

residue corresponding to His61 of LigB was not conserved in DesZ and 2,2′,3-trihydroxy-3′-methoxy-5,5′-dicarboxybiphenyl dioxygenase (LigZ) of SYK-6 [4, 15]. Because Glu242 coordinates non-heme iron along with His12 and His61 in LigB, Glu100 of DesZ appeared to coordinate non-heme iron along with His12 and Glu287. In LigZ Glu99 is conserved at the corresponding position of Glu100 in DesZ.

Site-directed mutagenesis of the putative active site residues of DesZ

To investigate whether His12, His250, Glu287, and Glu100 are involved in the activity of DesZ, each of the residues was replaced with an Ala residue as indicated in Fig. 2 using site-directed mutagenesis. Each *desZ* mutant gene was inserted in pET21a(+) and expressed in *E. coli* BL21(DE3) under the control of the T7 promoter. The SDS-PAGE analysis revealed that there was no difference in the production of DesZ protein between the wild-type *desZ* (*E. coli* harboring pEDZA) and the mutant *desZ* genes (Fig. 3), suggesting that the sequence alterations in mutant DesZ genes did not affect the expression of mutant genes in *E. coli*.

3MGA 3,4-dioxygenase activities of DesZ and its mutants

The crude extracts of *E. coli* carrying the *desZ* gene or its mutants (250 μg of protein/ml) were incubated with 1 mM 3MGA at 30°C to determine the dioxygenase activity on 3MGA. No dioxygenase activities were detected with any of the four mutants, whereas wild-type DesZ exhibited a specific activity of 1.87 ± 0.15 U/mg. These results suggest that His12, Glu100, His250, and Glu287 were essential for the 3MGA 3,4-dioxygenase activity of DesZ.

4. Discussion

The substitutions of His12, Glu100, His250, and Glu287 in DesZ with an Ala residue resulted in the complete loss of the dioxygenase activity on 3MGA. These results indicate that all these residues are essential for the dioxygenase activity, and suggest that Glu100 as well as His12 and Glu287 are involved in the coordination of non-heme iron, Fe(II) and His250 acts as the catalytic base.

A sequence database search revealed that the amino-acid sequences of DesZ and LigZ are closely related to those of the putative extradiol dioxygenase genes of *Ralstonia eutropha* JMP134, *Mycobacterium* sp. strains KMS and JLS as illustrated in the phylogenetic tree of the type II extradiol dioxygenases in Fig. 4. The deduced amino acid sequences of putative dioxygenase genes YP_299962 and YP_298976 of JMP134, ZP_01286210 of KMS, and ZP_01280861 of JLS showed 57%, 37%, 23%, and 23% identities with that of *desZ* and 38%, 33%, 26%, and 24% identities with that of *ligZ*, respectively. These enzymes constitute a kind of subfamily in the phylogenetic tree of the type II extradiol dioxygenases (Fig. 4). Interestingly, the Glu residues corresponding to Glu100 of DesZ are completely conserved among these enzymes as presented in Fig. 5, suggesting that Glu residue of these enzymes are involved in the coordination of non-heme iron. Employment of one His and two Glu for Fe(II) ligands instead of two His and one Glu appears to common feature of this subfamily and may be extended to other enzymes surrounding this subfamily.

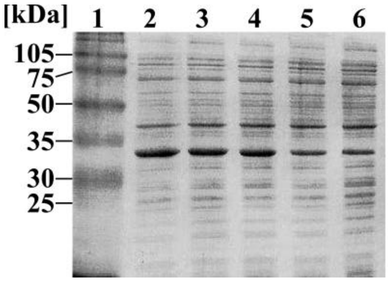

Fig. 3. SDS-PAGE analysis of extracts of the *E. coli* cell expressing mutant DesZ enzymes. Proteins (10 μg) were separated on a 12% SDS-PAGE and stained with Coomassie brilliant blue. Lanes: 1, molecular weight markers; 2 to 6, cell extracts of *E. coli* BL21(DE3) harboring pEDZA (DesZ), pETZM6 (H12A), pETZM8 (E100A), pETZM11 (H250A), and pETZM12 (E287A), respectively. The molecular masses are given on the left.

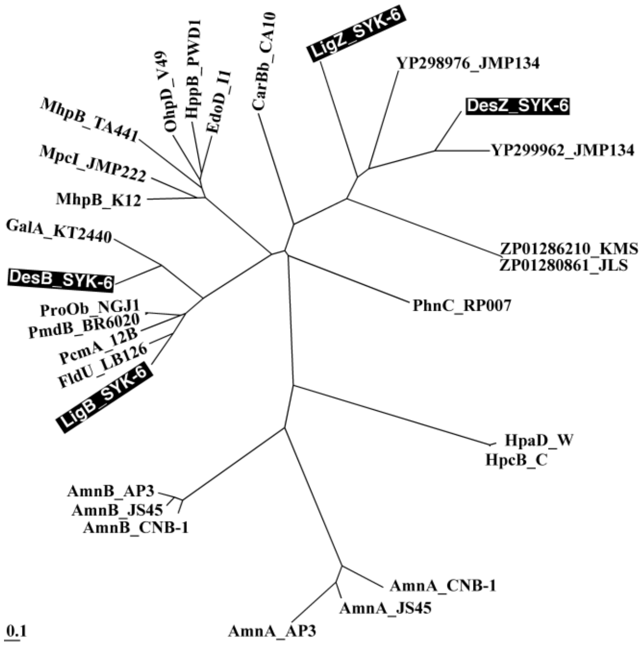

Fig. 4. Phylogenetic tree of type II extradiol dioxygenases. The scale corresponds to a genetic distance of 0.1 substitution per position (10% difference). Enzymes: LigB_SYK-6, β subunit of 4,5-PCD of SYK-6 (BAA97118); FldU_LB126, β subunit of putative 4,5-PCD of *Sphingomonas* sp. LB126 (CAB87561); PcmA_12B, 4,5-PCD of *Arthrobacter keyseri* 12B (AAK16524); PmdB_BR6020, β subunit of 4,5-PCD of *Comamonas testosteroni* BR6020 (AAM09637); ProOb_NGJ1, β subunit of 4,5-PCD of *Pseudomonas ochraceae* NGJ1; DesB_SYK-6, gallate dioxygenase of SYK-6 (BAD80871); GalA_KT2440, gallate dioxygenase of *P. putida* KT2440 (AE016783); MhpB_K12, 2,3-dihydroxyphenylpropionate 1,2-dioxygenase of *E. coli* K-12 (CAA70748); MpcI_JMP222, catechol 2,3-dioxygenase I of *Cupriavidus necator* JMP222 (CAA36665); MhpB_TA441, 3-(2,3-dihydroxyphenyl)propionate 1,2-dioxygenase of *C. testosteroni* TA441 (BAA82879); OhpD_V49, 2,3-dihydroxyphenylpropionate 1,2-dioxygenase of *Rhodococcus* sp. V49 (AAF81826); HppB_PWD1, 2,3-dihydroxyphenylpropionate 1,2-dioxygenase of *R. globerulus* PWD1 (AAB81314); EdoD_I1, extradiol dioxygenase of *Rhodococcus* sp. I1 (CAA06875); CarBb_CA10, catalytic subunit of 2'-aminobiphenyl-2,3-diol 1,2-dioxygenase of *P. resinovorans* CA10 (BAA21731); LigZ_SYK-6, 2,3,2'-trihydroxy-3'-methoxy-5,5'-dicarboxybiphenyl dioxygenase of SYK-6 (BAA75884); YP298976_JMP134, extradiol dioxygenase of *Ralstonia eutropha* JMP134 (YP_298976); DesZ_SYK-6, 3MGA 3,4-dioxygenase of SYK-6 (BAC79261); YP299962_JMP134, extradiol dioxygenase of *R. eutropha* JMP134 (YP_299962); ZP01286210_KMS, extradiol dioxygenase of *Mycobacterium* sp. KMS (ZP_01286210); ZP01280861_JLS, extradiol dioxygenase of *Mycobacterium* sp. JLS (ZP_01280861); PhnC_RP007, extradiol dioxygenase of *Burkholderia* sp. RP007 (AAD09870); HpaD_W, HPCA 2,3-dioxygenase of *E. coli* W (CAA86042); HpcB_C, HPCA 2,3-dioxygenase of *E. coli* C (CAA38985); AmnA_CNB-1 and AmnB_CNB-1, α and β subunits of 2-aminophenol 1,6-dioxygenase of *Comamonas* sp. CNB-1 (AAT35227 and AAT35226); AmnA_JS45 and AmnB_JS45, α and β subunits of 2-aminophenol 1,6-dioxygenase of *P. pseudoalcaligenes* JS45 (AAB71525 and AAB71524); and AmnA_AP3 and AmnB_AP3, α and β subunits of 2-aminophenol 1,6-dioxygenase of *Pseudomonas* sp. AP-3 (BAB03532 and

Acknowledgments

This work was supported in part by research fellowship 5468 from the Japan Society for the Promotion of Science for Young Scientists.

References

[1] C. C. Tseng, F. H. Vaillancourt, S. D. Bruner, C. T. Walsh, Chem. Biol., **11** (2004) 1195.

[2] Y. Katayama, S. Nishikawa, M. Nakamura, K. Yano, M. Yamasaki, N. Morohoshi, T. Haraguchi, Mokuzai Gakkaishi, **33** (1987) 77.

[3] Y. Katayama, S. Nishikawa, A. Murayama, M. Yamasaki, N. Morohoshi, T. Haraguchi, FEBS Lett., **233** (1988) 129.

[4] D. Kasai, E. Masai, K. Miyauchi, Y. Katayama, M. Fukuda, J. Bacteriol., **186** (2004) 4951.

[5] E. Masai, M. Sasaki, Y. Minakawa, T. Abe, T. Sonoki, K. Miyauchi, Y. Katayama, M. Fukuda, J. Bacteriol., **186** (2004) 2757.

[6] T. Abe, E. Masai, K. Miyauchi, Y. Katayama, M. Fukuda, J. Bacteriol., **187** (2005) 2030.

[7] D. Kasai, E. Masai, K. Miyauchi, Y. Katayama, M. Fukuda, J. Bacteriol., **187** (2005) 5067.

[8] F. M. Ausubel, R. Brent, R. E. Kingston, D. D. Moore, J. G. Seidman, J. A. Smith, K. Struhl, John Wiley & Sons, Inc., New York, N.Y. (1990).

[9] J. Sambrook, E. F. Fritsch, T. Maniatis, Cold Spring Harbor Laboratory Press, Cold Spring Harbor, N.Y. (1989).

[10] F. Sanger, S. Nicklen, C. A. R., Proc. Natl. Acad. Sci. USA, **74** (1977) 5463.

[11] N. Saitou, M. Nei, Mol. Biol. Evol., **4** (1987) 406.

[12] R. D. M. Page, Appl. Biosci., **12** (1996) 357.

[13] M. M. Bradford, Anal. Biochem., **72** (1976) 248.

[14] K. Sugimoto, T. Senda, H. Aoshima, E. Masai, M. Fukuda, Y. Mitsui, Structure, **7** (1999) 953.

[15] X. Peng, T. Egashira, K. Hanashiro, E. Masai, S. Nishikawa, Y. Katayama, K. Kimbara, M. Fukuda, Appl. Environ. Microbiol., **64** (1998) 2520.

(Received: 19 May, 2012, Accepted: 22 June, 2012)

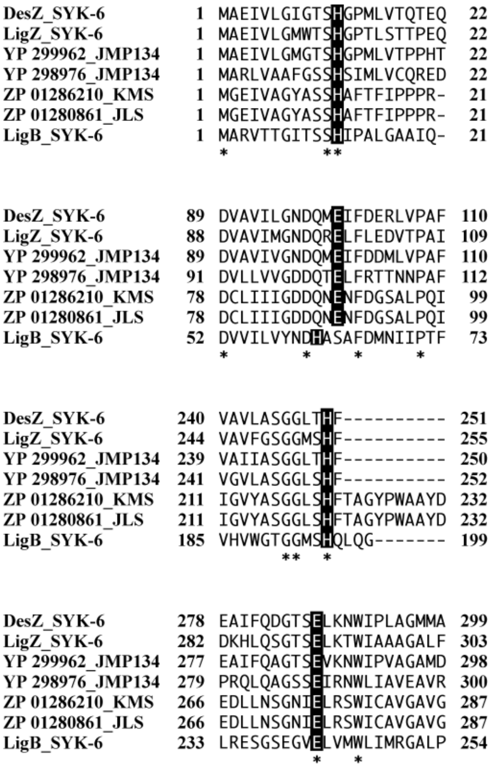

```
DesZ_SYK-6            1  MAEIVLGIGTSHGPMLVTQTEQ   22
LigZ_SYK-6            1  MAEIVLGMWTSHGPTLSTTPEQ   22
YP 299962_JMP134      1  MAEIVLGMGTSHGPMLVTPPHT   22
YP 298976_JMP134      1  MARLVAAFGSSHSIMLVCQRED   22
ZP 01286210_KMS       1  MGEIVAGYASSHAFTFIPPPR-   21
ZP 01280861_JLS       1  MGEIVAGYASSHAFTFIPPPR-   21
LigB_SYK-6            1  MARVTTGITSSHIPALGAAIQ-   21
                         *         **

DesZ_SYK-6           89  DVAVILGNDQMEIFDERLVPAF  110
LigZ_SYK-6           88  DVAVIMGNDQRELFLEDVTPAI  109
YP 299962_JMP134     89  DVAVIVGNDQMEIFDDMLVPAF  110
YP 298976_JMP134     91  DVLLVVGDDQTELFRTTNNPAF  112
ZP 01286210_KMS      78  DCLIIIGDDQNENFDGSALPQI   99
ZP 01280861_JLS      78  DCLIIIGDDQNENFDGSALPQI   99
LigB_SYK-6           52  DVVILVYNDHASAFDMNIIPTF   73
                         *       *    *     *

DesZ_SYK-6          240  VAVLASGGLTHF----------  251
LigZ_SYK-6          244  VAVFGSGGMSHF----------  255
YP 299962_JMP134    239  VAIIASGGLTHF----------  250
YP 298976_JMP134    241  VGVLASGGLSHF----------  252
ZP 01286210_KMS     211  IGVYASGGLSHFTAGYPWAAYD  232
ZP 01280861_JLS     211  IGVYASGGLSHFTAGYPWAAYD  232
LigB_SYK-6          185  VHVWGTGGMSHQLQG-------  199
                               **  *

DesZ_SYK-6          278  EAIFQDGTSELKNWIPLAGMMA  299
LigZ_SYK-6          282  DKHLQSGTSELKTWIAAAGALF  303
YP 299962_JMP134    277  EAIFQAGTSEVKNWIPVAGAMD  298
YP 298976_JMP134    279  PRQLQAGSSEIRNWLIAVEAVR  300
ZP 01286210_KMS     266  EDLLNSGNIELRSWICAVGAVG  287
ZP 01280861_JLS     266  EDLLNSGNIELRSWICAVGAVG  287
LigB_SYK-6          233  LRESGSEGVELVMWLIMRGALP  254
                                  *   *
```

Fig. 5. Alignment of the deduced amino acid sequences of the DesZ-LigZ subfamily of enzymes and LigB. Identical amino acids are indicated with asterisks. The conserved active site residues are shaded in black.

Transactions on GIGAKU **1**(2012)01030/1-6

In vitro study of BphT1 two-component response regulator protein of *Rhodococcus jostii* RHA1

Jun Shimodaira*,[1] Yuta Miyazawa,[1] Daisuke Kasai,[1] Keisuke Miyauchi,[2] Masao Fukuda[1]
[1]Department of Bioengineering, Nagaoka University of Technology, 1603-1 Kamitomioka-cho, Nagaoka 940-2188, Japan; and [2]Department of Civil and Environmental Engineering, Tohoku Gakuin University, 1-13-1 Chuo, Tagajo, Miyagi 985-8537
**E-mail: jshimo@stn.nagaokaut.ac.jp*

BphT1 is a response regulator (RR) protein of the BphS1-BphT1 two-component system regulating the transcription of gene clusters for degradation of biphenyl/polychlorinated biphenyls (PCBs) in *Rhodococcus jostii* RHA1. BphT1 is estimated to bind to the degradation-gene promoters including the *bphAa* promoter (*bphAap*) to activate their transcription because its C-terminal domain contains a helix-turn-helix DNA binding motif. In this study, BphT1 was overexpressed in *E. coli* and purified as N-terminal histidine-tagged protein (ht-BphT1). Purified ht-BphT1 did not bind to the *bphAap* DNA fragment in the gel shift assays. The *ht-bphT1* gene complemented transcriptional activation activity of the original *bphT1* gene in *bphT1/T2* double disruption mutant, TDR12, and restored the growth on biphenyl. Because DNA-binding activity of RR usually depends on its phosphorylation status, *in vitro* phosphorylation of ht-BphT1 by low-molecular-weight phosphate donors, carbamoyl phosphate and acetyl phosphate was examined using phos-tag acrylamide SDS-PAGE. However, phosphorylation of ht-BphT1 was not detected. These results suggested that ht-BphT1 purified from *E. coli* is dephosphorylated and hard to be phosphorylated *in vitro*. ht-BphT1 appears to require phosphorylation to exhibit its binding activity to the target promoter sequence.

1. Introduction

Polychlorinated biphenyls (PCBs) had been widely used for industrial purposes because of their excellent stability, insulation properties, and resistance to combustion. The production and use of PCBs have been banned because of their toxicity and their contamination and persistence in the environment. However, PCBs still remain widely in the environmental and cause environmental problems. Microbial degradation of PCBs has been regarded as a promising procedure for their removal from the environment. A variety of bacteria, which aerobically degrade PCBs, have been isolated, and their degradation enzymes and genes have been characterized [1, 6, 14, 20]. Most of these bacteria cometabolize PCBs through the metabolic pathway of biphenyl. A PCB degrader, *Rhodococcus jostii* RHA1, was isolated from the γ-hexachlorocyclohexane-contaminated upland soil and has a great capacity to degrade mono- to octa-chlorobiphenyls by cometabolism with biphenyl [23, 24].

The biphenyl/PCB degradation enzyme genes of the upper biphenyl degradation pathway of RHA1 are distributed among the gene clusters including *bphAaAbAcAdC1B1*, *etbD1*, *etbAa1Ab1CbphD1*, *etbAa2Ab2AcD2*, and *etbAdbphB2*. The transcription of these gene clusters from the promoters of *bphAa*, *etbAa1*, *etbAa2*, *etbAd*, and *etbD1* (*bphAap*, *etbAa1p*, *etbAa2p*, *etbAdp*, and *etbD1p*, respectively) are simultaneously induced in the presence of aromatic compounds such as biphenyl and ethylbenzene [27]. These five promoters are under the control of dual two-component systems coded by *bphS1T1* and *bphS2T2* [28, 29]. Two-component systems are employed by a number of bacteria and certain higher organisms [26]. The typical two-component system consists of a sensor protein-histidine kinase (HK) and a cognate response regulator (RR) [16, 18]. HK perceives an environmental stimulus via its N-terminal input domain and autophosphorylates the conserved histidine residue in its C-terminal transmitter domain. This phosphoryl group is subsequently transferred to the conserved aspartic acid residue in the receiver domain of RR. This phosphorylation causes a conformational change of RR and activation of its output domain which usually retains DNA-binding property [16]. The receiver and output domains usually occupy N- and C-termini of RR.

The bphS1 and bphS2 products, BphS1 and BphS2, and the bphT1 and bphT2 products, BphT1 and BphT2, are estimated to be the HK and RR of a two component system, respectively. BphS1 and BphS2 are 92% identical between their amino acid sequences. BphT1 and BphT2 are 97% identical. The BphS1T1 and BphS2T2 (BphSTs) systems share the same broad inducing substrate spectrum containing benzene, toluene, ethylbenzene, xylenes, isopropylbenzene, and chlorinated benzenes [28, 29]. The exception is biphenyl, which is an inducing substrate only for the BphS1T1 system. The C-terminal domains of the BphT1 and BphT2 (BphTs) contain a helix-turn-helix (HTH) DNA-binding motif. Thus, BphTs are deduced to bind directly to some sequence in the promoter to induce the transcription. In the previous study, the 24-bp consensus sequence conserved among five BphSTs-dependent promoters was identified and the significance of the 24-bp consensus sequence in transcriptional regulation by BphS1T1 was demonstrated by the hybrid promoter analysis [25]. This 24-bp consensus sequence appears to be the BphTs binding sequence.

In this study, BphT1 was overexpressed in *E. coli*, purified, and subjected to the *in vitro* phosphorylation to examine its binding to the 24-bp consensus sequence.

2. Experiment

Bacterial strains, plasmids, and culture conditions.

The strains and plasmids used in this study are listed in Table 1. *Rhodococcus jostii* TDR12 was grown at 30°C in 1/5 LB (2 g/l Bacto-tryptone, 1 g/l yeast extract, and 5 g/l NaCl) and on a W minimal salt medium plate [2]. A host strain, *Escherichia coli* JM109 was grown at 37°C in LB (10 g/l Bacto-tryptone, 5 g/l yeast extract, and 5 g/l NaCl). If necessary, antibiotics were used at the following concentrations: ampicillin, 100 μg/ml and kanamycin, 50 μg/ml.

DNA manipulations and analysis.

DNA manipulations, including electrotransformation (electroporation), were performed as previously described [17]. Nucleotide sequences were determined by the dideoxy termination method using a CEQ 8000 genetic analysis system (Beckman Coulter, Inc., Fullerton, CA). A Sanger reaction [22] was performed using the CEQ Dye Terminator Cycle Sequencing Quick Start kit (Beckman Coulter, Inc.). Sequence analysis was performed using BioEdit [7] and in silico MolecularCloning (in silico biology, Inc., Yokohama, Japan).

Construction of overexpression and complementation plasmids.

The *bphT1* gene was amplified by PCR using pG1013F as a template and the primers, BglII-T1F and Pst-EcoRI-T1R, which had the BglII and PstI sites at their 5’ termini, respectively. The PCR product was subcloned into pT7Blue T-Vector to verify its nucleotide sequence. The 0.6-kb BglII-PstI fragment containing *bphT1* of the resulting plasmid, pT7T1BEP was cloned into BamHI-PstI site of an expression vector, pColdI to obtain pColdIT1. The *ompR* gene was amplified from the total DNA of *E. coli* JM109 using the primers, ompR-F and ompR-R, which had the BamHI and NdeI sites at their 5’ termini, respectively. The PCR product was subcloned into a pT7Blue T-Vector to verify its nucleotide sequence. The resulting plasmid was named pT7ompR. The 0.8-kb BamHI-SalI fragment of pT7ompR containing the *ompR* gene was cloned into the BamHI-SalI site of the pColdI to obtain pColdIompRF. The histidine-tagged *bphT1* (*ht-bphT1*) gene fragment was amplified by PCR using pColdIT1 as a template and the primers, EcoRI-SDpColdIF and EcoRI-T1AR. These primers had EcoRI sites at their 5’ termini. The PCR product was subcloned into pT7Blue T-Vector to verify its nucleotide sequence. The 0.8-kb EcoRI fragment containing *ht-bphT1* of the resulting plasmid, pT7SDColdIT1 was cloned into the EcoRI site of a vector, pKPA1 to obtain pKPA1SDColdIT1. The nucleotide sequences of primers used are listed in Table 1.

Table 1. Strains plasmids, and primers used in this study

Strain, plasmid, or primers	**Relevant characteristic(s)**^{a}	**Source or reference**
Strains		
R. jostii		
RHA1	PCB degrader, BPH$^+$, ETB$^+$, Nal^r	[23]
TDR12	RHA1 derivative, BPH$^-$, ETB$^-$, Nal^r; Δ*bphT1*, Δ*bphT2*	This study
Escherichia coli JM109	*endA1 glnV44 thi-1 relA1 gyrA96 recA1 mcrB*$^+$ Δ(*lac-proAB*) *e14- hsdR17*(r_K^- m_K^+) [F' *traD36 proAB*$^+$ *lacI*^{q}*ZΔM15*]	[32]
Plasmids		
pBluescript II KS(+)	Cloning vector, Ap^r	Stratagene
pColdI	Cold shock-based expression vector, Ap^r	Takara
pColdIT1	pColdI with 0.6-kb BglII-PstI *bphT1* fragment, Ap^r	This study
pColdIompR	pColdI with 0.8-kb BamHI-SalI *ompR* fragment, Ap^r	This study
pG1013F	pBluescript II KS(+) with an 8.8-kb HindIII fragment containing *bphS1T1* in the forward orientation to *lacZ* gene, Ap^r	[29]
pK4	*Rhodococcus-E. coli* shuttle vector, Km^r	[8]
pKPA1	pK4 with a insertion of *bphAap* in the reverse orientation to kanamycin resistance gene, Km^r	[10]
pKPA1SDColdIT1	pKPA1 with 0.8-kb EcoRI *ht-bphT1* fragment, Km^r	This study
pT7Blue T-vector	TA Cloning vector	Novagene
pT7BEP	pT7Blue T-vector with 0.6-kb BglII-PstI *bphT1* fragment, Ap^r	This study
pT7ompR	pT7Blue T-vector with 0.8-kb BamHI-NdeI *ompR* fragment, Ap^r	This study
pT7SDColdIT1	pT7Blue T-vector with 0.8-kb EcoRI *ht-bphT1* fragment, Ap^r	This study
Primers		
BglII-T1F	5'-AGATCTATCAGCGTTGTGGTGTGTGACG-3'	This study
Pst-EcoRI-T1R	5'-CTGCAGGAATTCCTAGTCCAAAAGACCTGCG-3'	This study
ompRF	5'-GGATCCATGCAAGAGAACTACAAGATTC-3'	This study
ompRR	5'-CATATGTCATGCTTTAGAGCCGTC-3'	This study
EcoRI-SDpColdIF	5'-GAATTCTTAAGAGGTAATACACC-3'	This study
EcoRI-T1AR	5'-GAATTCCCTAGTCCAAAAGACC-3'	This study

[a] BPH$^+$, growth on biphenyl; BPH$^-$, no growth on biphenyl; ETB$^+$, growth on ethylbenzene; ETB$^-$, no growth on ethylbenzene; Ap^r, ampicillin resistance; Km^r, kanamycin resistance, Nal^r, nalidixic acid resistance.

Purification of the histidine-tagged recombinant proteins.

For the overexpression of histidine-tagged BphT1 (ht-BphT1) and OmpR (ht-OmpR), *E. coli* JM109 harboring each expression plasmid was grown at 37°C in LB medium containing ampicillin. When the optical density at 600 nm reached 0.6, cells were kept at 15°C for 30 min and incubated at 15°C for a further 24 h after adding 0.5 mM isopropyl-β-D-thiogalactopyranoside. Cells were harvested by centrifugation, resuspended in the elution buffer [50 mM Tris-HCl, 500 mM NaCl; pH7.4] containing 100 mM imidazole, and disrupted by sonication. A crude cell lysate was prepared by the removal of cell debris by centrifugation at 18,800 × g for 20 min at 4°C. Proteins were purified by using a Ni Sepharose Fast Flow column (GE Healthcare UK Ltd., Buckinghamshire, England). ht-BphT1 and ht-OmpR were eluted with the elution buffer containing 500 mM and 300 mM imidazole, respectively. The purified proteins were desalted and concentrated with the elution buffer or phosphorylation buffer [50 mM Tris-HCl, 50 mM KCl, pH 7.4] using an Amicon Ultra-15 Ultracel-10 k (Millipore Corporation, Billerica, MA,).

In vitro ***phosphorylation of ht-BphT1.***

Treatment of purified ht-BphT1 (12.9 μM) with 50 mM carbamoyl phosphate was carried out for 120 min at 30°C or 37°C in the phosphorylation buffer containing either 10 mM or 20 mM $MgCl_2$. The resultant solution was mixed with 2 × SDS-PAGE loading buffer [220 mM Tris-HCl, 8.9% sodium dodecyl sulfate (SDS), 10% glycerol, 100 mM dithiothreitol, 0.1% bromophenol blue, pH 6.8], incubated at room temperature for 2 min, and applied onto a 10% polyacrylamide gel containing 75 μM Phos-tag acrylamide (NARD Institute Ltd., Amagasaki, Japan) and 150 μM $MnCl_2$. After electrophoresis, the gel was stained with Coomassie brilliant blue.

3. Results and Discussion

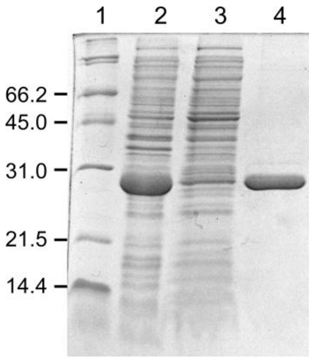

Fig. 1. SDS-PAGE analysis of purified ht-BphT1. Proteins were separated on an SDS-15% polyacrylamide gel and stained with Coomassie brilliant blue. Lanes: 1, molecular weight markers; 2 and 3, insoluble and soluble fractions of *E. coli* JM109 harboring pColdIT1, respectively; 4, elute from Ni sepharose column chromatography. The molecular weights (kDa) of the marker proteins are indicated on the left.

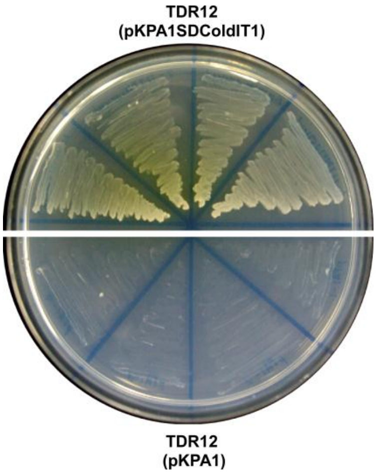

Fig. 2. Complementation of the *bphT1T2* double disruption mutant, TDR12 by *ht-bphT1* gene. Four transformants of pKPA1SDColdIT1 containing *ht-bphT1* (upper half) and those with a vector pKPA1 (lower half) were streaked and grown on biphenyl on a W minimal medium plate.

Overexpression and purification of ht-BphT1

The BphT1 protein was overexpressed as an N-terminally histidine-tagged protein (ht-BphT1) in *E. coli* JM109 harboring pColdIT1. ht-BphT1 was purified to near homogeneity by Ni^{2+}- nitrilotriacetic acid (Ni^{2+}-NTA) affinity chromatography and subjected to SDS-PAGE analysis (Fig. 1). ht-BphT1 migrated with apparent molecular mass of approximately 28 kDa, which is close to the calculated molecular mass of ht-BphT1 (25,734 Da).

Binding of the ht-BphT1 to **bphAap**

To investigate the ability of BphT1 to bind to *bphAap*, the gel shift assays using ht-BphT1 and the *bphAap* fragment containing the 24-bp consensus sequence was performed. No shifted band was observed at any tested concentration (data not shown). It was reported that the histidine-tag sometimes affected the activity of recombinant protein [9, 12, 21]. To confirm whether ht-BphT1 maintain its activity *in vivo*, pPA1SDColdIT1 containing the *ht-bphT1 gene* was constructed and introduced into the mutant strain TDR12 with double disruption of *bphT1* and *bphT2*, which could not grow on biphenyl as a sole souse of carbon. The resulting transformant grew well on biphenyl (Fig. 2). These results indicate that ht-BphT1 maintain its *in-vivo* activity in transcriptional regulation.

Phosphorylation of the ht-BphT1 **in vitro**

The DNA-binding activity of RR usually depends on its phosphorylation status. *In vitro* phosphorylation of RR proteins have been performed using low-molecular-weight phosphate donors, such as acetyl phosphate and carbamoyl phosphate [4, 31]. To examine *in vitro* phosphorylation of ht-BphT1, ht-BphT1 was incubated with carbamoyl phosphate, and was subjected to phos-tag acrylamide SDS-PAGE, which specifically retards the migration of phosphoproteins [3, 15]. histidine-tagged OmpR (ht-OmpR) protein of *E. coli* was used as a positive control. OmpR has been shown to be efficiently phosphorylated by carbamoyl phosphate *in vitro* [13]. ht-OmpR was overexpressed in *E. coli* JM109 harboring pColdIompR and purified to near homogeneity by Ni^{2+}-NTA affinity chromatography. As shown in Fig. 3, the retarded band of phosphorylated ht-OmpR was detected after incubation with carbamoyl phosphate in the presence of Mg^{2+}, which is required for phosphorylation [13, 19]. The retarded band was not observed after incubation with carbamoyl phosphate in the absence of Mg^{2+}. No retarded band of phosphorylated ht-BphT1 was detected regardless of the concentrations of Mg^{2+} and the incubation temperatures. We also incubated ht-BphT1 with acetyl phosphate, but phosphorylated ht-BphT1 was not detected (data not shown). These results suggest that carbamoyl phosphate and acetyl phosphate are not suitable for *in vitro* phosphorylation of ht-BphT1.

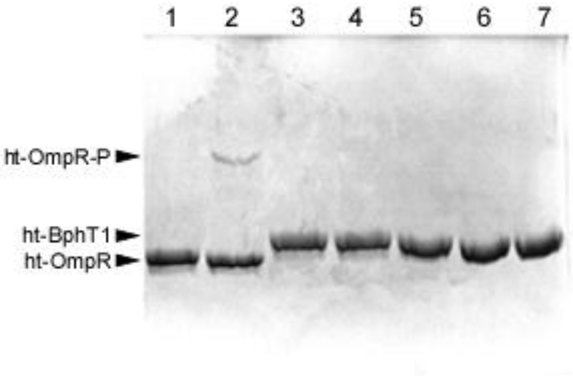

Fig. 3. *In vitro* phosphorylation of ht-BphT1 with carbamoyl phosphate. ht-OmpR (Lanes 1 and 2) and ht-BphT1 (Lanes 3-7) were incubated with carbamoyl phosphate for 120 min at 30°C (Lanes 4 and 6) or 37°C (Lanes 1, 2, 3, 5, and 7), and analyzed by phos-tag acrylamid gel SDS-PAGE. The reaction solutions contained 10 mM (Lanes 2, 4, and 5) or 20 mM (Lanes 6 and 7) $MgCl_2$. In lanes 1 and 3, $MgCl_2$ was omitted from the reaction solutions to prevent phosphorylation. The expected positions of ht-OmpR and ht-BphT1 and phosphorylated ht-OmpR (ht-OmpR-P) are indicated on the left.

Dephosphorylation of RRs was reported to eliminate their binding activities completely [5, 11, 30]. These reports imply that phosphorylation is required for binding of RR to the target DNA. The results of this study suggest that ht-BphT1 purified from E. coli is not phosphorylated and that ht-BphT1 in the mutant strain TDR12, which exhibited complete activity in transcriptional regulation, is phosphorylated in vivo. Because the low-molecular-weight phosphate donors examined in this study did not work in phosphorylation of ht-BphT1, *in vivo* phosphorylation in the original *Rhodococcus* strain, RHA1 is expected to be useful for phosphorylation of ht-BphT1. Because BphT2, which is mostly identical to BphT1, governs transcription of the same five promoters as BphT1 and cross-communicate with BphS1 [28], the results obtained in this study appear to be extended to BphT2.

References

[1] D. Ahmad, R. Massé, M. Sylvestre, Gene, **86** (1990) 53.

[2] N. Araki, T. Suzuki, K. Miyauchi, D. Kasai, E. Masai, M. Fukuda, J. Mol. Microbiol. Biotechnol., **20** (2011) 125.

[3] C. M. Barbieri, A. M. Stock, Anal. Biochem., **376** (2008) 73.

[4] R. B. Bourret, Curr. Opin. Microbiol., **13** (2010) 142.

[5] L. E. Cybulski, G. del Solar, P. O. Craig, M. Espinosa, D. de Mendoza, J. Biol. Chem., **279** (2004) 39340.

[6] K. Furukawa, A. M. Chakrabarty, Appl. Environ. Microbiol., **44** (1982) 619.

[7] T. A. Hall, Nucleic Acids Symp. Ser., **41** (1999) 95.

[8] Y. Hashimoto, M. Nishiyama, F. Yu, I. Watanabe, S. Horinouchi, T. Beppu, J. Gen. Microbiol., **138** (1992) 1003.

[9] H. Horchani, S. Ouertani, Y. Gargouri, A. Sayari, Journal of Molecular Catalysis B: Enzymatic, **61** (2009) 194.

[10] T. Iwasaki, H. Takeda, K. Miyauchi, T. Yamada, E. Masai, M. Fukuda, Biosci. Biotechnol.

Biochem., **71** (2007) 993.
[11] Y. Jeon, Y. S. Lee, J. S. Han, J. B. Kim, D. S. Hwang, J. Biol. Chem., **276** (2001) 40873.
[12] L. Jessop, T. Bankhead, D. Wong, A. M. Segall, J.. Bacteriol., **182** (2000) 1024.
[13] L. J. Kenney, M. D. Bauer, T. J. Silhavy, Proc. Natl. Acad. Sci. USA, **92** (1995) 8866.
[14] K. Kimbara, T. Hashimoto, M. Fukuda, T. Koana, M. Takagi, M. Oishi, K. Yano, J. Bacteriol., **171** (1989) 2740.
[15] E. Kinoshita, E. Kinoshita-Kikuta, M. Matsubara, S. Yamada, H. Nakamura, Y. Shiro, Y. Aoki, K. Okita, T. Koike, Proteomics, **8** (2008) 2994.
[16] M. T. Laub, M. Goulian, Annu Rev Genet, **41** (2007) 121.
[17] E. Masai, A. Yamada, J. M. Healy, T. Hatta, K. Kimbara, M. Fukuda, K. Yano, Appl. Environ. Microbiol., **61** (1995) 2079.
[18] T. Mascher, J. D. Helmann, G. Unden, Microbiol. Mol. Biol. Rev., **70** (2006) 910-38.
[19] W. R. McCleary, J. B. Stock, J. Biol. Chem., **269** (1994) 31567.
[20] F. J. Mondello, J. Bacteriol., **171** (1989) 1725.
[21] C. L. Richard-Fogal, E. R. Frawley, R. G. Kranz, J. Bacteriol., **190** (2008) 3489.
[22] F. Sanger, S. Nicklen, A. R. Coulson, Proc. Natl. Acad. Sci. U. S. A., **74** (1977) 5463.
[23] M. Seto, K. Kimbara, M. Shimura, T. Hatta, M. Fukuda, K. Yano, Appl. Environ. Microbiol., **61** (1995) 3353.
[24] M. Seto, E. Masai, M. Ida, T. Hatta, K. Kimbara, M. Fukuda, K. Yano, Appl. Environ. Microbiol., **61** (1995) 4510.
[25] J. Shimodaira, Y. Furusawa, Y. Miyazawa, D. Kasai, K. Miyauchi, E. Masai, M. Fukuda, J. Biosci. Bioeng., **113** (2012) 279.
[26] A. M. Stock, V. L. Robinson, P. N. Goudreau, Annu. Rev. Biochem., **69** (2000) 183.
[27] H. Takeda, N. Hara, M. Sakai, A. Yamada, K. Miyauchi, E. Masai, M. Fukuda, Biosci. Biotechnol. Biochem., **68** (2004) 1249.
[28] H. Takeda, J. Shimodaira, K. Yukawa, N. Hara, D. Kasai, K. Miyauchi, E. Masai, M. Fukuda, J. Bacteriol., **192** (2010) 4741.
[29] H. Takeda, A. Yamada, K. Miyauchi, E. Masai, M. Fukuda, J. Bacteriol., **186** (2004) 2134.
[30] J. R. Wei, Y. H. Tsai, P. C. Soo, Y. T. Horng, S. C. Hsieh, S. W. Ho, H. C. Lai, J. Bacteriol., **187** (2005) 5683.
[31] A. J. Wolfe, Microbiol. Mol. Biol. Rev., **69** (2005) 12.
[32] C. Yanisch-Perron, J. Vieira, J. Messing, Gene, 33 (1985) 103.

(Received: 18 May, 2012, Accepted: 18 June, 2012)

Transactions on GIGAKU ***1****(2012)01031/1-6*

Overexpression of ACEII, and transcriptional analysis of cellulase genes in *Trichoderma reesei* PC-3-7

Takanori Furukawa, Naoki Kitagami, Yosuke shida, Yasushi Morikawa, Wataru Ogasawara*
Department of Bioengineering, Nagaoka University of Technology,
1603-1 Kamitomioka-cho, Nagaoka 940-2188, Japan
**E-mail: owataru@vos.nagaokaut.ac.jp*

The transcription factor ACEII (Activator of cellulase 2) of *Trichoderma reesei* is the first identified transactivator for cellulase and xylanase genes. However, relatively little information is available about the regulatory function of ACEII. In this study, strains expressing tagged-ACEII under the control of the *cbh1* and the *xyn3* promoters were developed to investigate the effect of overexpression of ACEII. The resultant strains expressed markedly higher amount of *ace2* transcript in the cellulase-inducing conditions, and the maximum level of the transcript induction was estimated to be 570-fold for the *cbh1* construct and 20-fold for the *xyn3* construct. Analysis of production and expression profiles of cellulase revealed the possible involvement of ACEII in the regulation of cellulase and xylanase gene expressions in *T. reesei*. Our study provides insights into the effect of overexpresion of ACEII in *T. reesei*.

1. Introduction

Plant biomass, which primarily consists of lignocellulosic material, is the most abundant renewable resource in nature. The major components of lignocellulose are polysaccharides, such as cellulose and hemicellulose, which can potentially be converted into biofuels by hydrolysis into fermentable sugars followed by downstream fermentation. Many microorganisms secrete a wide variety of hydrolases that can degrade plant polysaccharides, and their potential application in the biorefinery area has received considerable attention in the last decades.

The filamentous fungus *Trichoderma reesei* is one of the most efficient producers of cellulolytic and xylanolytic enzymes, and its hydrolytic enzyme system has been subjected to extensive biochemical and genetic analyses. *T. reesei* produces at least two cellobiohydrolases (CBHI and CBHII), eight endoglucanases (EGLI to EGLVIII), and two ß-glucosidases (BGLI and BGLII) that act synergistically to degrade crystalline cellulose to glucose. The xylanolytic enzymes produced by *T. reesei* include at least four endoxylanases (XYNI to XYNIII), and one ß-xylosidase (BXL1) [1].

In *T. reesei*, the production of cellulolytic and xylanolytic enzymes is regulated at the transcriptional level depending on the carbon source available. Transcription of cellulase genes is induced by cellulose, its derivatives, lactose, and a monosaccharide L-sorbose, and is subject to carbon catabolite repression [2]. It has been reported that major cellulase genes are co-ordinately expressed under various inducing conditions, suggesting the presence of common regulatory mechanisms. However, the independent gene exprepression of xylanases from cellulases suggest that expression of cellulase and xylanase genes is modulated by a complex regulatory network [3].

Even though significant progress has been made in the molecular biology of the cellulase and xylanase system of *T. reesei*, our knowledge about the regulatory mechanisms of production of these enzymes is rather fragmentary. So far, four transcriptional activators, Xyr1, ACEII, BglR, and the HAP 2/3/5 complex, as well as two repressors including ACEI and the carbon catabolite repressor CREI were identified [14-17]. Xyr1 is the main activator of the cellulolytic and xylolytic genes, controlling the enzyme production regardless of the inducer and the mode of expression. Deletion of *xyr1* is reported to eliminate the induction of the hydrolase and hemicellulase genes involved in arabinan degradation [4]. The Xyr1-binding consensus, 5’-GGC(A/T)$_4$-3’ have been identified [5].

ACEII belongs to the zinc binuclear cluster protein family. The *ace2* gene was originally isolated from *T. reesei* by applying a yeast expression screening system using *T. reesei cbh1* promoter [6]. ACEII has been shown to bind to a 5’-GGCTAATAA-3’ motif in the *cbh1* promoter and 5’-GGGTAA-3’ sequences in the *cbh2* and *xyn2* promoters [2]. Deletion of *ace2* is reported to reduce the expression of the major cellulase genes particularly at the early stage of induction by cellulose but not by sophorose [6]. Hence ACEII appears to play a role in the regulation of the hydrolase genes as a narrow domain activator by modulating Xyr1 activation. However, relatively little information is available about the transcriptional targets and true function of ACEII.

In this study, we investigated the effect of overexpression and deletion of *ace2* on transcriptional regulation of the major cellulase and xylanase genes under different inducing conditions.

2. Experiments

Microbial strains and culture conditions *Trichoderma reesei* PC-3-7, which is a hypercellulolytic mutant with enhanced cellulase and xylanase inducibility by L-sorbose [7], was used throughout this study. For induction experiments, PC-3-7 and its transformants were grown for 48 h at 28°C on a rotary shaker (220 rpm) in a glucose medium as described [7]. Mycelia collected by filtration were washed twice with saline, and transferred to a basal medium [7] containing 0.5 mg/mL L-sorbose as an inducer. As a control of inducer glucose was added at 1.0 mg/mL. Induction was performed for 6 h at 28°C on a rotary shaker (220 rpm). After induction, mycelia harvested by filtration and washed twice with saline were used for RNA extraction.

Construction of an *ace2*-knockout strain of *T. reesei* To construct the *ace2*-disruption cassette, a 4.2-kbp fragment containing the *ace2* structural gene with 1.6-kbp of 5’- and 3’-flanking regions was amplified from the PC-3-7 genomic DNA by PCR using the primers, ace2-5’Fw and ace2-3’Rv (Table 1). The PCR product was cloned into the HincII site of pUC118 to yield pUace2FFL. A 3.1-kbp fragment containing the selective marker, *A. nidulans amdS* was excised from p3SR2 [8] by SpeI and XbaI digestion and blunted using a blunting kit (TaKaRa Bio). The blunted fragment was inserted into the blunted-BspEI site located in the *ace2* coding region of pUace2FFL to obtain pΔace2-amdS. The disruption cassette released from pΔace2-amdS by KpnI digestion was used for transformation.

Table 1. Primers used in this study

Primer	Sequence
ace2-5’Fw	5’-CGCTCCTTGAGCTCTTCCTTGGTACCTTCCTTTGG-3’
ace2-3’Rv	5’-GGGAGGTACCTGCGTCTGCCAAAGAGGGGT-3’
ace2-MatFragFw	5’-CCCTTCTCTGAAAGCTTATGGACCTCCGGC-3’
ace2-MatFragRv	5’-CCATATGGGTACCTCACTTCAGCAGTCTGGC-3’
ace2N-tagFw	5’-ATGGCTCACAACCACCGTCACAAACACG-3’
ace2pPICZCFw	5’-CCCTTCGAATTCAAAATGGACCTCCGGC-3’
ace2pPICZCRv	5’-CCATATGAGATACGTACTTCAGCAGTCTGGC-3’
ace2CterFw	5’-ATGGACCTCCGGCAAGCATGTG-3’
ace2CterRv	5’-CATTGAGTTTGTAGCCTTAGGTACCACTGTTCC-3’

Construction of an *ace2* over-expressing strains of *T. reesei* To construct the N-terminal tagged *ace2* over-expression cassette, the *ace2* coding region was amplified from the PC-3-7 genomic DNA by PCR using the primers, ace2-MatFragFw and ace2-MatFragRv (Table 1). The amplified fragment was digested with HindIII and KpnI and cloned into the HindIII/KpnI site of pT7-MAT-FLAG1 to yield pT7MFace2. N-terminal tagged *ace2* was amplified from pT7MFace2 by PCR using the primers, ace2N-tagFw and ace2-MatFragRv (Table 1). The resultant fragment was cloned in-frame into an inverse PCR product of pcbh1-gus [9] harboring *cbh1* expression signals and the *amdS* to yield pcbh1-N-tagace2, and inserted into an inverse PCR product of pBxyn3D0-ag [10], containing *xyn3* expression signals and the *amdS* to yield pBD0N-tagace2. The *ace2* overexpression cassettes were excised from pcbh1-N-tagace2 and pBD0N-tagace2 with KpnI, and used for transformation.

To construct the C-terminal tagged *ace2* over-expression cassette, the coding region of *ace2* was amplified from the PC-3-7 genomic DNA by PCR using the primers, ace2pPICZCFw and ace2pPICZCRv (Table 1). The PCR product was digested with EcoRI and SnaBI and cloned into the EcoRI/SnaBI site of pPICZC to yield pPICace2. C-terminal tagged *ace2* gene was amplified from pPICace2 by PCR using the primers ace2CterFw and ace2CterRv (Table 1). The amplified fragment was cloned in-frame into the inverse PCR product of pcbh1-gus and pBxyn3D0-ag to yield pcbh1-C-tagace2 and pBD0C-tagace2, respectively. The C-terminal tagged *ace2* expression cassettes were excised with KpnI and used for transformation.

Determination of gene copy number and integration locous in the genome of the transformants Chromosomal DNA of transformant was extracted as described previously [10]. Southern hybridization was done using an AlkPhos Direct kit (GE Healthcare Bio Science). Standard methods were used for electrophoresis, blotting, and hybridization. Chromosomal DNA of the *ace2*-disrupted mutant was digested by XhoI and hybridized with an alkaline-phosphatase-labeled *ace2* gene probe. Integration of the *ace2* overexpression cassette was verified by hybridization with the *ace2* probe.

Enzyme assay Cellulase activity was determined at 50°C for 15 min in 50 mM sodium acetate buffer (pH 5.0) using 1% carboxy methyl cellulose (CMC) as a substrate. Released reducing sugar was measured by the Somogyi-Nelson method. One unit of activity (U) was defined as the amount of enzyme that released 1 μmol of glucose-equivalent reducing sugar per minute. Protein concentration was determined by the Lowry method using bovine serum albumin as standard.

RNA extraction, cDNA synthesis and qRT-PCR Total RNA was extracted from frozen mycelia by a modified hot-phenol method using TRIZOL LS reagent, and purified with an RNAspin Mini RNA isolation kit (GE Healthcare Bio Science). Synthesis of cDNA from total RNA was carried out using a Transcriptor First-Strand cDNA Synthesis kit (Roche Diagnostics) with an Anchored-oligo $(dT)_{18}$ and random hexamer primers.

qRT-PCR was performed in a final volume of 20 μL containing 0.5 μM each of forward and reverse primers and 2 μL of 100-fold diluted cDNA using a LightCycler 480 System and LightCycler 480 SYBR Green I Master kit (Roche Diagnostics). Primers used in real-time PCR were described previously [5]. Conditions for thermal cycling are as follows: 5 min at 95°C followed by 45 cycles of 10 s at 95°C, 10 s at 60°C and 10 s at 72°C. All assays were performed in triplicate with a no-amplification control. The specificity of amplification was documented by melting curve analysis. The actin gene (*act1*) was used as a reference for quantification.

3. Results and Discussion

(1) Deletion and overexpression of the ace2 gene in T. reesei PC-3-7.

To investigate the roles of ACEII in the transcriptional regulation of cellulase and xylanase genes, an *ace2*-knockout mutant was constructed by inserting the *A. midulans amdS* into the coding region of *ace2* in PC-3-7 background. We also developed strains expressing N-terminal or C-terminal tagged ACEII under the control of either the *cbh1* promoter or the *xyn3* promoter. The *cbh1* promoter is the strongest inducible promoter in *T. reesei*. Expression level of *xyn3* was estimated to be about 6–9% of that of *cbh1*[9], which is still high and 100-fold stronger than that of the phosphoglycerate kinase 1 gene (*pgk1*). The transformation cassettes were introduced into chromosomal DNA of PC-3-7 and the resulting transformants were screened by Southern blot analysis (data not shown). Both the homologously and heterologously integrated transformants were selected for the tagged-ACEII expressing strains.

(2) Screening of ace2 overexpessing strains.

After pre-cultivation, the tagged-ACEII expressing strains and the wild-type (WT) were transferred into basal media containing L-sorbose as an inducer and were incubated for 6 h. The levels of the *ace2* transcripts were analyzed by quantitative real-time PCR (qRT-PCR). As shown in Table 1, *ace2* expression levels in the transformants of the *cbh1* construct were markedly higher than those in the WT, and the maximum elevation of the expression from the WT was estimated to be 570-fold in the transformant CN6. The maximum elevation of the *ace2* expression in the transformants of the *xyn3* consyruct was as low as 20-fold (data not shown). This is in good agreement with the previous results on the relative strength of these promoters, which was obtained using a heterologous *Escherichia coli* ß-glucuronidase gene, *gus* as a reporter [9]. It was reported earlier that calf chymosin, when expressed heterologously using the *T. reesei cbh1* promoter, showed reduced levels of expressed mRNA (only 1-5% compared to the native *cbh1* mRNA) [9]. This difference could be attributed to the origin of the gene, because our previous study also suggested that expression of the heterologous gene in *T. reesei* is limited at the level of tranasctiption [9]. The results of the qRT-PCR analysis indicate that the transformants could successfully overexpress the tagged-ACEII gene constructs in the cellulase-inducing condition. Disruption of *cbh1* has been reported to decrease total cellulase activity that could affect cellulase production profiles of the transformants [9]. Thus, the CC2 stain harboring the Pcbh1: C-terminal tagged-ACEII construct at an ectopic locus (which shows about 460-fold overexpression), was chosen to perform further analysis.

Table 2. Relative expression levels of *ace2* in the *cbh1* construct transformants.

Transformant	Relative expression (×*act1*)	
	ace2	*cbh1*
WT	0.1	54
Homologous strains		
CN5	47	0.0
CN6	57	0.0
CC5	29	0.0
Heterologous strain		
CC2	46	120

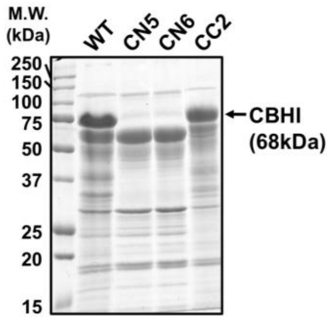

Fig. 1. SDS-PAGE analysis of the enzymes secreted by the transformants.

(3) Effect of overexpression of ace2 on cellulase production.

To determine whether increased levels of *ace2* transcripts affect cellulase formation of the transformant, we evaluated production levels of the enzyme in WT, CC2, and Δ*ace2* in Avicel culture over a period of 6 days. As shown in Fig. 2, no significant differences were observed in the production profiles of CMCase between WT and Δ*ace2* in the time-course experiment. In contrast, CC2 strain produced significantly lower levels of CMCase after 3 days of cultivation, and it reached only 25% of WT after 6 days. At the earliest time point (day 2), CC2 produced almost the same levels of CMCase as WT, but it only slightly increased by day 6. Because we used the *cbh1* promoter for expression of *ace2*, overproduction of ACEII was expected to start after 2 days of cultivation. It was previously reported that disruption of *ace2* in a hyper-celluolytic mutant *T. reesei* ALKO2221 led to 70% and 40% reduction of CMCase production after 3 days and 6 days of cultivation on Avicel, respectively [6]. However, the Δ*ace2* mutation in PC3-7 background did not result in apparent reduction of the production of CMCase. Enhancement of the xylanolytic and cellulolytic enzyme production by the overexpression of the trasncavtivator XlnR was reported in *Aspergillus niger* and *A. oryzae* [11,12], but that by the ACEII overexpression was not detected in the enzyme assay and SDS-PAGE analysis of the Δ*ace2* strain.

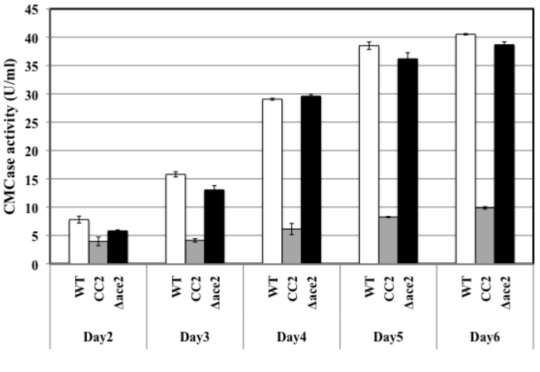

Fig. 2 Cellulase production profiles of the *ace2* overexpressing and deletion strain.

(4) Effect of overexpression of ace2 on cellulase and xylanase gene transcription.

To investigate the effect of *ace2* overexpression and deletion at the transcriptional level, the expression profiles of the major cellulases (*cbh1*, *cbh2*, *egl1 to egl3*, *and bgl1 to bgl2*) were analyzed by qRT-PCR every 24 hours for up to 120 hours (Figures 3 and 4). Consistent with the CMCase production profiles, WT expressed cellulase and xylanase genes in a coordinate manner from 24 h, and the maximum expression was attained at 72 h of cultivation. In contrast, the gene expression in the CC2 strain reached the maximum at 24 h, decreased to approximately 50% of the maximum after 48 h, and was maintained at the same level for the rest of the experiment. Cellulase expression in the Δ*ace2* strain followed the similar patter as that of WT except for a precipitous drop in the gene expression at 96 h. In ALKO2221 strain a substantial reduction in transcript levels (from 30 to 70%) has been reported at the early stages of inductionn, as a result of disruption of *ace2* [6]. This may be due to differences in the genetic backgrounds of the isogenic mutans PC3-7 and ALKO2221.

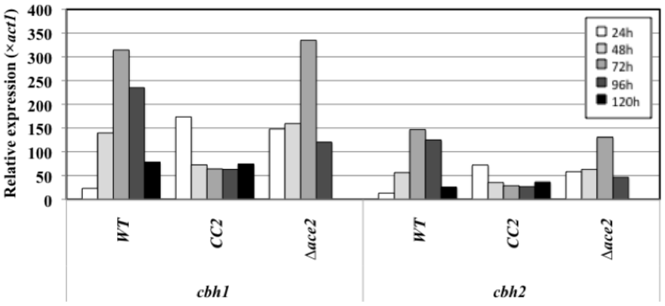

Fig. 3. qRT-PCR expression analysis of the major cellulase genes in the *ace2* overexpressing and deletion strain

Bearing in mind the proposed activating function of ACEII [6, 13], it can be assumed that high-levels of cellulase gene expression observed at 24 h in the CC2 strain results from the overexpression of ACEII. There are quite a few studies that described the binding properties of these transcription factors. The heterologously expressed DNA-binding domain of ACEII has been shown to bind *in vitro* to the 5’-GGCTAATAA-3’ and 5’-GGGTAA-3’ sequences [6]. A similar consensus binding sequence, 5’-GGC(A/T)$_4$-3’[5], has also been determined for the other main transcriptional activator, Xyr1. It was recently reported that not only the *in vitro* translation product of full-length ACEII but also Xyr1 bound to an inverted repeat consisting of a 5’-GGCTAA-3’ and a 5’-GGCTGG-3’ motifs within the *xyn2* promoter region [13]. It was proposed that there may be a regulatory interplay between Xyr1 and ACEII on the promoter region. Hence the results obtained in this study suggest that ACEII can act as an antagonist of Xyr1 at the early stage of induction.

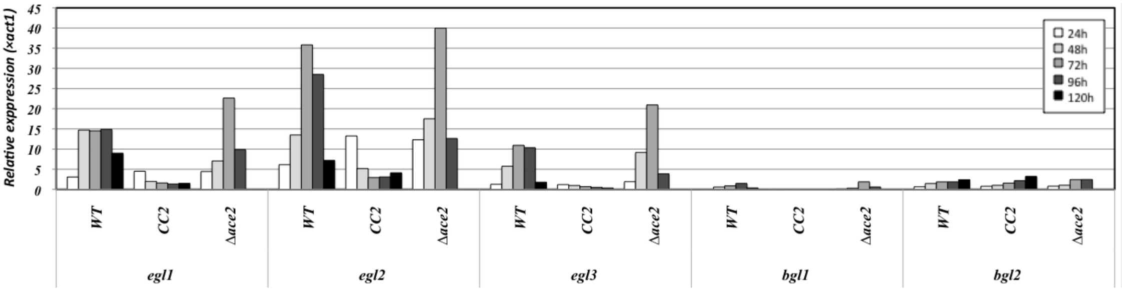

Fig. 4. qRT-PCR analysis of the *egl* and *bgl* genes in the *ace2* overexpressing and deletion strains.

Since the CC2 strain expressed about 470-fold *ace2* transcripts, the reduced gene expression detected in the later stage of induction (48 to 96h) is deduced to be a result of competition for the *cis*-acting elements between Xyr1 and ACEII. Overexpressed ACEII might occupy many of the binding sites for Xyr1, causing transcriptional downregulation of the Xyr1-target genes. On the other hand we observed that overexpression of ACEII did not evoke any enhancement of the transcript formation. This suggests that the transcriptional activation by ACEII needs co-activating protein(s) for its overall function. Taken together, our results suggest a possible involvement of ACEII in the regulation of cellulase and xylanase gene expression in *T. reesei*.

Further experiments are needed to clarify the role of ACEII and its target genes. We are currently analyzing the target genes of ACEII using microarray analysis to reveal genome-wide responses to overexpression of ACEII. The ACEII overexpressing strains constructed in this study would be good candidates to dissect the true function of ACEII.

4. Conclusion

We have successfully developed novel *T. reesei* strains expressing tagged-ACEII under the control of the *cbh1* and the *xyn3* promoters. The strains expressed markedly higher amounts of *ace2* transcripts in cellulase-inducing conditions, and the maximum level of the expression was estimated as 570-fold higher for the *cbh1* construct and as 20-fold higher for the *xyn3* construct. Analysis of cellulase production profiles and the gene expression profiles revealed the possible involvement of ACEII in the regulation of cellulase and xylanase gene expression in *T. reesei*. Our study provides the first insights into ACEII overexpresion in *T. reesei*.

Acknowledgments

This work was supported in part by a grant to W. Ogasawara from the NEDO (The New Energy and Industrial Technology Development Organization) project of the Ministry of Industrial and Technology of Japan, and JST-JICA.

References

[1] Martinez, D., Berka, R.M., Henrissat, B., Saloheimo, M., Arvas, M., Baker, S.E., Chapman, J., Chertkov, O., Coutinho, P.M., Cullen, D., Danchin, E.G., Grigoriev, I.V., Harris, P., Jackson, M., Kubicek, C.P., Han, C.S., Ho, I., Larrondo, L.F., de Leon, A.L., Magnuson, J.K., Merino, S., Misra, M., Nelson, B., Putnam, N., Robbertse, B., Salamov, A.A., Schmoll, M., Terry, A., Thayer, N., Westerholm-Parvinen, A., Schoch, C.L., Yao, J., Barbote, R., Nelson, M.A., Detter, C., Bruce, D., Kuske, C.R., Xie, G., Richardson, P., Rokhsar, D.S., Lucas, S.M., Rubin, E.M., Dunn-Coleman, N., Ward, M., Brettin, T.S., Nat. Biotechnol. **26** (2008) 553-560.

[2] Schmoll, M., Kubicek, C.P., Acta. Microbiol. Immunol. Hung. **50** (2003) 125-145.

[3] Xu, J., Nogawa, M., Okada, H., Morikawa, Y., Appl. Microbiol. Biotechnol. **54** (2000) 370-375.

[4] Stricker, A.R., Mach, R.L., de Graaff, L.H. Appl. Microbiol. Biotechnol. **78** (2008) 211-220.

[5] Furukawa, T., Shida, Y., Kitagami, N., Ota, Y., Adachi, M., Nakagawa, S., Shimada, R., Kato, M., Kobayashi, T., Okada, H., Ogasawara, W., Morikawa, Y., 2008. Identification of the *cis*-acting elements involved in regulation of xylanase III gene expression in *Trichoderma reesei* PC-3-7. Fungal Genet. Biol. 45, 1094-1102.

[6] Aro, N., Salheimo, A., Ilmen, M., Penttilä, M., J. Biol. Chem. **276** (2001) 24309-24314.

[7] Kawamori, M., Morikawa, Y., Takasawa, S., Appl. Microbiol. Biotechnol. **24** (1986) 449-453.

[8] Hynes, M.J., Corrick, C.M., King, J.A., Mol. Cell. Biol. **3** (1983) 1430-1439.

[9] Rahman, Z., Shida, Y., Furukawa, T., Suzuki, Y., Okada, H., Ogasawara, W., Morikawa, Y., Appl. Microbiol. Biotechnol. **82** (2008) 899-908.

[10] Furukawa, T., Shida, Y., Kitagami, N., Ota, Y., Adachi, M., Nakagawa, S., Shimada, R., Kato, M., Kobayashi, T., Okada, H., Ogasawara, W., Morikawa, Y., Fungal Genet. Biol. **45** (2008) 1094-1102.

[11] de Vries, R.P., van de Vondervoort, P.J.I., Hendriks, L., van de Belt, M., Visser, J., Mol. Genet. Genomics **268**, (2002) 96-102.

[12] Marui, J., Kitamoti, N., Kato, M., Kobayashi, T., Tsukagoshi, N., FEBS Letters **528** (2002) 279-282.

[13] Stricker, A.R., Trefflinger, P., Aro, N., Penttilä, M., Mach, R.L., Fungal Genet. Biol. **45** (2008), 436-445

[14] Rauscher, R., Würleitner, E., Wacenovsky, C., Aro, N., Stricker, A.R., Zeilinger, S., Kubicek, C.P., Penttilä, M., Mach, R.L., Eukaryot. Cell **5** (2006), 447-456.

[15] Strauss, J., Mach, R.L., Zeilinger, S., Hartler, G., Stöffler, G., Wolschek, M., Kubicek, C.P., FEBS Lett. **376** (1995), 103-107.

[16] Zeilinger, S., Ebner, A., Marosits, T., Mach, R., Kubicek, C.P., Mol. Genet. Genomics. **266** (2001), 56-63.

[17] Saloheimo, A., Aro, N., Ilmen, M., Penttilä, M., J. Biol. Chem. **275** (2001), 5817-5825.

[18] Nitta, M., Furukawa, T., Shida, Y., Mori, K., Kuhara, S., Morikawa, Y., Ogasawara, Y., Fungal Genet. Biol. **49** (2012), 388-397.

(Received: 30 May, 2012, Accepted: 18 June, 2012)

Transactions on GIGAKU ***1****(2012)01032/1-6*

Thermal Gradient Creep of Ni-based Superalloy Coatings

Subramanian Rajiv Gandhi, Ryohei Nomura, Masakazu Okazaki*,
Satoshi Yamagishi
Department of Mechanical Engineering, Nagaoka University of Technology,
1603-1 Kamitomioka-machi, Nagaoka 940-2188, Japan
**E-mail: okazaki@mech.nagaokaut.ac.jp*

Thermo-mechanical fatigue tests were carried out for thermal barrier coatings on three different substrate materials SUS316 stainless steel alloy, Mar-M247 and Inconel 738 Ni-based alloys, under a combined condition where the external load was superimposed on thermal cycling in a controlled manner. Special attention was paid to specific failure modes under this kind of complicated TMF loadings. Finally, the failure mechanism and crack density were investigated for all these materials.

1. Introduction

Gas turbines are extensively used for aircraft propulsion and in power generation. The most severely loaded parts in a turbine are the rotor blades, which are made up of nickel-based superalloys [1]. These alloys are being used extensively because of their excellent creep rupture strength, rupture ductility, and thermal fatigue [2]. However, when these alloys are exposed to elevated temperatures, their oxidation resistance becomes a more pivotal factor to dominate turbine blade longevity. Thermal barrier coatings are more essential to increase the lifetime and efficiency of highly loaded turbine blades and vanes at elevated temperature by reducing the average metal temperature and mitigating the detrimental effects of hot spots. They are regarded as one of the most successful innovations and applications of coatings in aircraft industry. Thermal barrier coatings (TBCs) consist of three layers; the prevalent outer layer is yttria-stabilized zirconia (YSZ), acting as the thermal barrier coating, an oxidation resistant bond coat, consisting of a metallic alloy like MCrAlY and a nickel-based superalloy substrate [3-4]. When superalloys along with thermal barrier coatings are exposed to high temperature, the turbine blade system is subjected to high thermo-mechanical fatigue (TMF) loading. Understanding of resistance to this kind of damage has gained more importance in recent years. The basic principles of failure seem to be understood under idealized laboratory conditions, however, a detailed analysis of the mechanisms and the possibilities of avoiding damages are still lacking. Especially, under a significant thermal gradient condition in actual combustion gas environment, unexpected modes of failures may be experienced. There is such an aspect that few adequate test beds impede us to get these understandings.

In this study, a novel test system has been originally developed which enables us to apply the complicated TMF loadings to superalloy–TBC specimen under a significant thermal gradient in an actual combustion gas environment. By employing this system, failure mechanism was investigated for TBCs on three different substrate materials Mar-M247 and Inconel 738 Ni-based alloys, SUS316 stainless steel alloy. The TBC had nominally the same composition for all those substrate materials. Finally, failure mechanism and crack density were investigated for all these materials.

2. Experiment

Test System

A new test facility illustrated in Fig. 1 has been developed, where the system consists of a combustion part and a test section. In the former part, a simulated combustion atmosphere is produced employing a type of combustor, so that the test section inlet temperature (TSIT) reaches up to 1500°C maximum. Associating this with a servo-electro hydraulic testing machine, the static or cyclic mechanical loading is superimposed in a synchronized manner to the thermal cycling. The system temperature is controlled by TSIT; the temperatures at some representative positions in the specimen, e.g., upstream and downstream gas temperatures just above the specimen surface (as well as the inside temperatures in some cases), are continuously monitored. The temperatures measured for the present TBC specimen are summarized in Table 1 where the TSIT was cyclically changed between 1100/750°C with a frequency of 300/300 s in heating/cooling duration time, respectively. Thus, the new test system successfully gives external load associated with a significant thermal gradient inside the specimen.

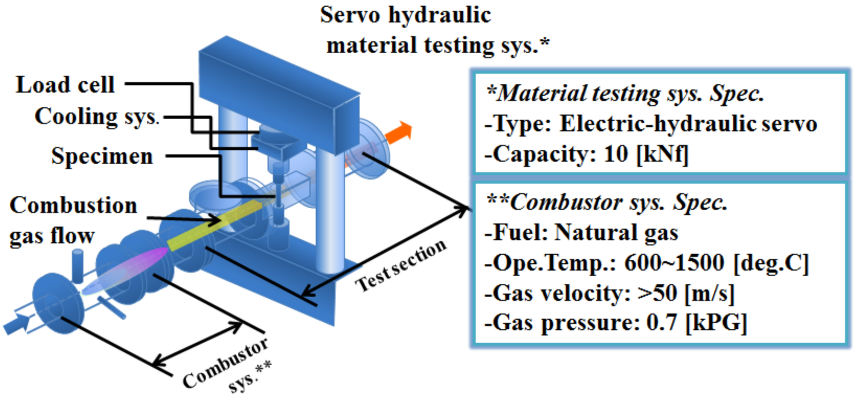

**Material testing sys. Spec.*
-Type: Electric-hydraulic servo
-Capacity: 10 [kNf]

***Combustor sys. Spec.*
-Fuel: Natural gas
-Ope.Temp.: 600~1500 [deg.C]
-Gas velocity: >50 [m/s]
-Gas pressure: 0.7 [kPG]

Fig. 1 Illustration of newly developed test system

Table 1 Summary of thermal gradient at the representative parts inside the TBC specimen when thermal cycle was applied between 1100/750°C (in TSIT) by means of a new test facility developed

	Up stream		**Side stream**		**Down stream**	
Test section inlet gas temperature* (°C)	Gas temp. above TBC specimen surface (°C)	Interface** temp. in TBC specimen (°C)	Gas temp. above TBC specimen surface (°C)	Interface** temp. in TBC specimen (°C)	Gas temp. above TBC specimen surface (°C)	Interface** temp. in TBC specimen (°C)
1100	990	950	960	930	900	880
750	675	650	665	640	630	620

* Changed cyclically with a frequency of 300/300 s in heating/ cooling, respectively.

** Bond coat/ substrate interface (mounted R type thermocouples)

Outline of Test

Solid cylindrical substrate specimens were prepared from Mar-M247 polycrystalline and Inconel 738 Ni-based alloys, SUS316 stainless steel alloy. The TBC specimens used, whose gauge section dimension is explained in Fig. 2. The TBC specimen consists of three layers; a Ni-base superalloy, bond coat (of CoNiCrAlY alloy, or AMDRY9951, 100 μm thick produced by low pressure plasma spraying), and a top coat (made with 8 wt% YSZ, or METCO 204NS, 500 μm in thickness by atmospheric plasma spraying). Employing the above new testing system, the TMF tests were carried out, where a static, or constant axial stress was superimposed on the thermal cycling, which is summarized in Table 2, between 1280 and 700°C in TSITs with a frequency of 1/360 s.

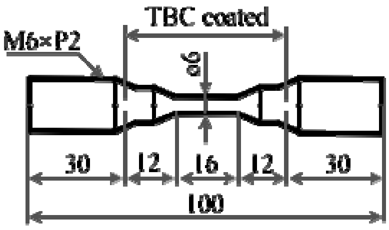

Fig. 2 TBC specimen

Table 2 Summary of thermal cycles and mechanical load

Substrate	**MarM 247**	**Inconel 738**		**SUS316**	
Thermal cycling	700–1280°C	700–1280°C	700–1280°C	750–1113°C	750–1113°C
Mechanical loading	170 MPa	170 MPa	100 MPa	60 MPa	0 MPa

3. Results and Discussion

3.1. Thermal Cycles with Mechanical Load

The crack initiation and growth of TBC coating were observed after a significant number of thermal cycles.The average number of thermal cycles to failure for TBCs on Mar-M247, Inconel 738, and SUS316 substrates was 99 cycles, 50 cycles at 170 MPa, and 130 cycles at 60 MPa, respectively, as illustrated in Figs. 3, 4, and 5. TBCs on Mar-M247 substrates averaged about twice the thermal cycle life as those on Inconel 738 substrates. The micrograph observations clearly illustrate that crack growth occurred perpendicular to the external load direction (Fig. 6). In addition, notable changes in shape of the test piece were observed. The length of the specimen during the test is extended with the number of cycles. At the end of 130 cycles, a permanent strain of 1.4% was measured in SUS316, 0.35% strain in Mar-M247 at 99 cycles, and 0.82% strain in Inconel 738 at 50 cycles as illustrated in Fig. 7. The phenomenon of the TBC failures is deeply related with deformation of the substrate. When the coating material is subjected to external load at elevated temperature, both coating and substrate start to deform. Due to variation in the thermal expansion coefficient between the substrate and the TBC, the thermal stresses increase at the interface. Finally, crack initiate in the coating and growth occurs uniformly throughout the specimen. Hence, deformation of the substrate is also one of the main factors for the failure of TBC coatings.

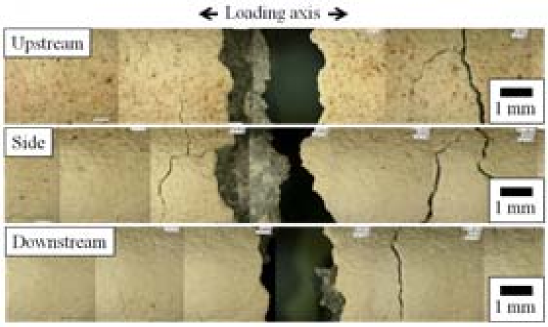

Fig. 3 Micrographs of the TBC surface after 99 thermal cycles with 170 MPa tensile loading at 700/1280°C (Mar-M247-1 TBC specimen)

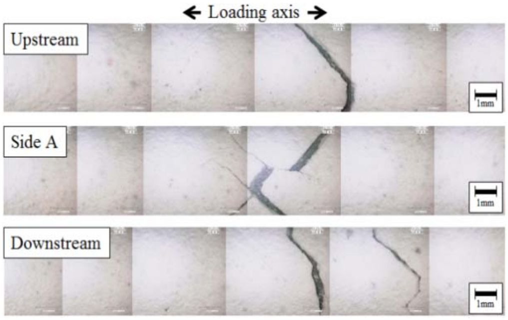

Fig. 4 Micrographs of the TBC surface after 50 thermal cycles with 170 MPa tensile loading at 700/1280°C (Inconel 738 TBC specimen)

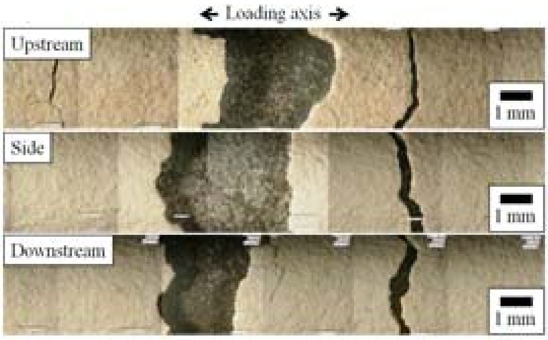

Fig. 5 Micrographs of the TBC surface after 130 thermal cycles with 60 MPa tensile loading at 700/1280°C (SUS316 TBC specimen)

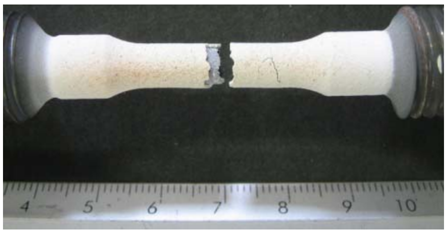

Fig. 6 Micrographs of the TBC surface after 130 thermal cycles with 60 MPa tensile loading at 700/1280°C (SUS316 TBC specimen)

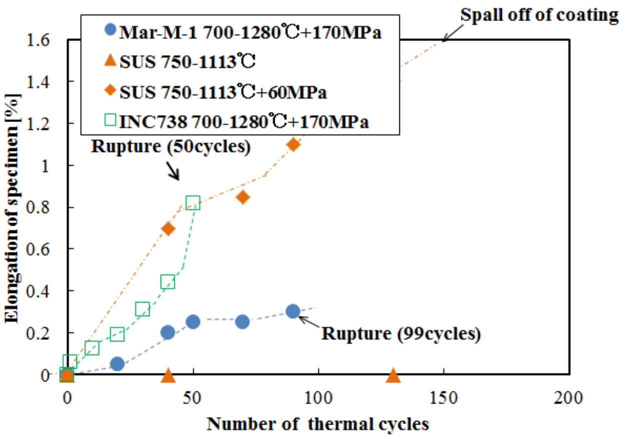

Fig. 7 Schematic illustrations on damage evolution in the respective TBC specimens

3.2. Microstructural Analysis

Microstructural features of TBC specimens were examined before the thermal cycle (Fig. 8) and after failure. Evolution of the TBC microstructure during the thermal cycle for TBCs on SUS316 substrates is shown in Fig. 9 after 130 thermal cycles. Three notable changes occurred at the TBC–substrate interface during thermal exposure [5]. First, there was a continuous increase in the thickness of the TGO layer between the bond coat and the YSZ top coat. Second, the interface roughness progressively increased. Third, interface delamination defects formed between the TGO and the top coat [6-8].

TBCs on inconel 738 and Mar-M247 substrates exhibited similar to those observed in Fig. 9 for TBCs on SUS316 substrates. The interface at which spalling occurred during the thermal cycle is shown in Figs. 9, 10, and 11. And, also shows regions from which the TBC spalled from the bond coat and regions where the TBC remained intact. There was evidence that the interface crack originated at the YSZ–TGO interface (above the alumina) and, only during the course of the catastrophic crack propagation that led to spallation for the SUS316, Inconel 738, and Mar-M247 substrates occasionally ran below the alumina at the TGO–bond coat interface. The delamination defects tended to become deeper and longer with increased number of cycles.

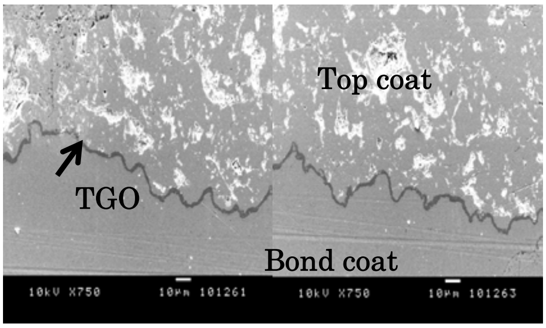

Fig. 8 Micrographs of SUS316 TBC specimen before thermal cycle

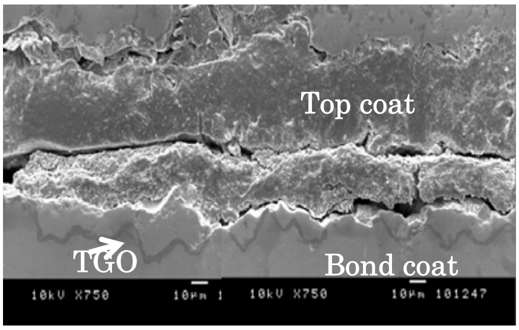

Fig. 9 TBC surface after 130 thermal cycled with 60 Mpa tensile loading at 700/1280°C (SUS316)

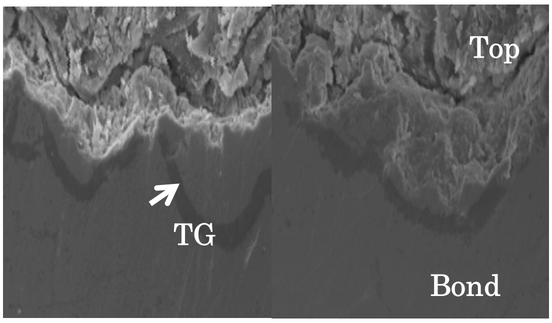

Fig. 10 Micrographs of the TBC surface after 50 thermal cycles with 170 MPa tensile loading at 700/1280°C (Inconel 738 TBC specimen)

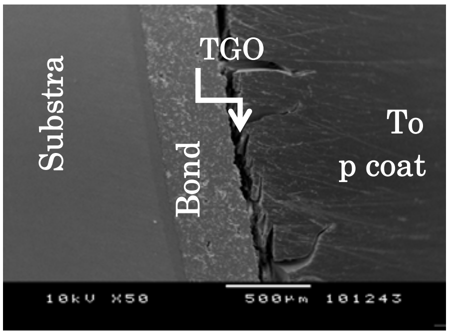

Fig. 11 Micrographs of the TBC surface after 99 thermal cycles with 170 MPa tensile loading at 700/1280°C (Mar-M247 specimen)

3.3. Crack Density Measurement

Two types of cracks were observed within the coating after the thermal cycles, vertical oriented (parallel to the load axis) and horizontally oriented (perpendicular to the load axis). These cracks were found to occur specially at the interface between TGO and top coat [9], [10]. Horizontally oriented cracks density is greater than vertical oriented cracks. Figure 12 shows very strong channel cracking in the coating. Normally, this kind of cracking occurs perpendicular to the loading direction. The crack density was very large about 0.81 at downstream side rather than upstream side about 0.50 (Figs. 12 and 13). This difference is may be due to the large compressive stress on the downstream side when there is some thermal gradient. However, this phenomenon is not understood completely. The horizontally oriented crack density measured by the following equation.

$$Z\ \text{crack density} = \frac{\text{No. of cracks in the } Z \text{ direction } (n)}{\text{Gage length (mm)}}$$

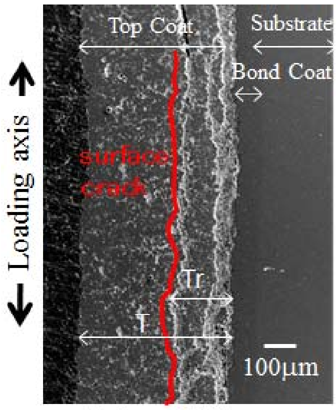

Ex.Inconel738-Upstream
(TMF, 1280/700℃, 170MPa)

Fig. 12 Micrograph of horizontal cracks at upstream side

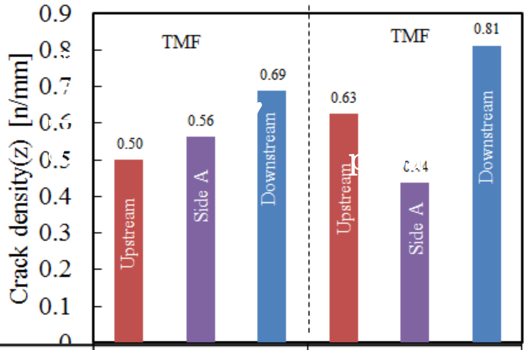

Temperature	700/1280 [deg.C]	700/1280 [deg.C]
Mechanical stress	170 [MPa]	100 [MPa]
Inelastic strain	2.4[%]	1.9 [%]

Fig. 13 Crack density measurement with thermal gradient at 1280/700°C

4. Conclusion

A new test system has been originally developed that enables us to apply the complicated TMF loadings to superalloy and TBC specimen under a significant thermal gradient in an actual combustion gas environment. By employing this system, the following results have been found. The failure mechanism was investigated for TBCs on three different substrate materials Mar-M247 and Inconel 738 Ni-based alloys, SUS316 stainless steel alloy. From these results, it was clearly observed that Mar-M247 can withstand more thermal cycles and stresses than other materials tested. The phenomenon of the TBC failures was deeply related with deformation of the substrate, which was due to variation in temperature between upstream and downstream. From the SEM observation, three notable changes occurred at the TBC–substrate interface during thermal exposure. First, there was a continuous increase in the thickness of the TGO layer between the bond coat and the YSZ top coat. Second, the interface roughness progressively increased. Third, interface delamination defects were formed between the TGO and the top coat. Two types of cracks were observed within the coating after the TMF and creep test, those were vertical oriented and horizontally oriented. From that result, the crack density was higher under the tests with thermal gradient than those without thermal gradient.

References

[1] N.P. Padture, M. Gell, and E.H. Jordan, Science, **296** (2002) 280.
[2] B. Sarhan and M. Bartsch, Key Eng. Mater., **333** (2007)137.
[3] G.W. Goward, Surf. Coat. Technol., **108–109** (1998) 73.
[4] Y.H. Sohn, J. Am. Ceram. Soc., **85** [8] (2002) 2065.
[5] A.A. Ruud, J. Am. Ceram. Soc., **84(**7) (2001)1545.
[6] J.P. Singh, J. Am. Ceram. Soc., **84** [10] (2001) 2385.
[7] C.G. Levi, E. Sommer, and S.G. Terry, J. Am. Ceram. Soc., **86** [4] (2003) 676.
[8] P. Ke, Q. Wang, W. Hua, and J. Gong, J. Am. Ceram. Soc., **90** [3] (2007) 936.
[9] H. Chen, Y. Liu, and Y. Gao, J. Am. Ceram. Soc., **93** [6] (2010) 1732.
[10] A.G.Evans and J.W.Hutchinson, Surf. Coat. Technol., **201** (2007) 7905.

(Received: 23 March, 2012, Accepted: 27 April, 2012)

Transactions on GIGAKU ***1****(2012)01033/1-6*

Characteristics and Directed Evolution of *Trichoderma reesei* Endoglucanase III (Cel12A) – A Review

Hirofumi Okada*, Hikaru Nakazawa, Wataru Ogasawara, Yasushi Morikawa
Department of Bioengineering, Nagaoka University of Technology,
1603-1 Kamitomioka-cho, Nagaoka 940-2188, Japan
**E-mail: hirofumi@vos.nagaokaut.ac.jp*

This paper reviews shortly characteristics of the *Trichoderma reesei* endoglucanase III (Cel12A) and improvement of the enzymatic properties by directed evolution. EG III gene contains a 702-bp open reading frame that encodes a 234-amino-acid peptide with the 16-amino-acid signal sequence. The deduced protein sequence has significant homologies with glycoside hydrolase family 12. The protein has been expressed as a mature form in *Escherichia coli* strains JM109 or Rosetta-gami B (DE3) pLacI. The site-directed mutagenesis experiment of the enzyme demonstrated that Glu116 and Glu200 are important for catalytic function as the mucleophilic and acid-base residues, respectively. It is also described that directed evolution allowed Cel12A to enhance the stability and specific activity.

1. Introduction

Cellulose, which is a major constituent of plant cell walls, is the most abundant form of biomass on earth and can be converted into bioethanol and other chemical products via fermentation following hydrolysis to fermentable sugars. Cellulose is composed of linear homopolymers of D-glucose linked by β-1,4 bonds and includes crystalline structures stabilized by intermolecular and intramolecular hydrogen bonds.

Glycoside hydrolases, including plant cell-wall hydrolases, such as cellulases and hemicellulases, are conveniently classified into a number of families based on their amino-acid sequence similarities [1]. With the accumulation of three-dimensional structural data, the related families have been grouped into clans, since their members share a common fold and the position of their catalytic residues is conserved despite the dissimilarities of their sequences. In addition, it has been found that most glycoside hydrolases are modular enzymes consisting of a discrete catalytic domain and a carbohydrate binding module such as a cellulose binding domain [1]. Glycoside hydrolases cleave their target substrates by either a single or double displacement mechanism, resulting in the inversion of the product, respectively [2].

Cellulase, including cellobiohydrolase (CBH), endoglucanase (EG), and β-glucosidase, hydrolyzes the β-1,4-D-glycoside bonds of cellulose. CBH releases cellobiose from either the reducing or non-reducing ends of the cellulose chain, whereas EG randomly degrades the internal bonds of the amorphous region of cellulose. Cellulolytic enzymes are widely distributed among plants, animals, bacteria, and fungi. The filamentous fungus *Trichoderma reesei* is known as a potent cellulase producer because of its remarkable ability to secrete cellulolytic enzymes. It has been reported that this fungus possesses two CBH genes, *cbh1* and *cbh2*, and eight EG genes, *egl1* to *egl8* [3], and that its CBH I and II and EG I to VII are secreted proteins. In this review, we report mainly the enzymatic characteristics and the improvement of EG III (Cel12A).

2. Molecular Characterization of EG III

EG III purified from the culture of *T. reesei* PC-3-7 has a molecular mass of 25 kDa and a specific activity of 11.2 U/mg for carboxy methyl cellulose (CMC) as a substrate and a slight activity toward Avicel [4]. The enzyme is inactive toward xylan, *p*-nitrophenyl β-D-glucopyranoside (PNPG), and chitosan. Analysis of hydrolysis products of cellooligosaccharide, phosphoric acid-swollen cellulose (PASC) and Avicel revealed that EG III finally gave a small amount of glucose, cellobiose and cellotriose. Cellotriose could not be completely hydrolyzed after prolonged incubation with the enzyme. EG III exhibited synergism with CBH I in degradation of Avicel.

EG III gene contains a 702-bp open reading frame that encodes a 234-amino-acid peptide as shown in Fig. 1 [5]. The mature protein presumably starts at amino acid 17, glutamine, which seemed to be pyroglutamylated [4]. The N-terminal 16-amino-acid peptide of the immature protein showed the typical structure of a signal peptide that contains the region with a high hydrophobic index following a positively charged amino acid. The 234 amino acid protein deduced from the nucleotide sequence has a molecular mass of 25,158 Da for the unprocessed form, and if the initial 16 amino acids are excluded, the calculated molecular mass of the mature protein is 23,480 Da, which is in good agreement with the biochemical data. When the EG III sequence was compared with those available from the databases, FI-CMCase from *Aspergillus aculeatus*, CMCase-I from *A. kawachii*, and CelS from *Erwinia cartovora* subsp. cartovola showed 56, 47, and 26 % homology with EG III at the amino acid level, respectively (Fig. 1). These are all EGs which belong to glycoside hydrolase (GH) family 12. GH12 family is further classified into four subgroups; archaea, bacteria, fungal EG, and fungal xyloglucanase subgroups (Fig.2). EG III is categorized as fungal EG subgroup.

```
EG III       1 M--------K-FLQVL--PAL---IPA-ALAQT-SC--DQWATFTGNGYTVSNNLWGASA 42
F1-CMCase    1 M--------K-AFHLL--AALA--GAA-VAQQAQLC--DQYATYTGGVYTINNNLWGKDA 44
CMCase-I     1 M--------K-LSMTL--SLFA--ATA-MG-QT-MC--SQYDSASSPPYSVNQNLWGEYQ 42
CelS         1 MQTVNTQPHRIFRVLLPAVFSSLLLSSLTVSAASSSNDADKLYFGNNKYYLFNNVWGKDE 60
consensus      M              L                                Y    N WG

EG III      43 GSGFGCVTAVSLSG-GASWHADWQWSGGQNNVKSYQN--S-QIAIP---QK--RTVNSIS 93
F1-CMCase   45 GSGSQCTTVNSASSAGTSWSTKWNWSGGENSVKSYAN--S-GLTF----NK--KLVSQIS 95
CMCase-I    43 GTGSQCVYVDKLSSSGASWHTKWTWSGGEGTVKSYSN--S-GLTF----DK--KLVSDVS 93
CelS        61 IKGWQ-QTIFYNSPISMGW--NWHWPSSTHSVKAYPSLVSGWHWTAGYTENSGLPIQLSS 117
consensus        G         S     W   W W      VK Y    S                   S

                                                       *
EG III      94 SMPTTASWSYSGSNIRA-NVAYDL-FTAANPNHVTYSGDYELMIWLGKYGDIGPIGSSQG 151
F1-CMCase   96 QIPTTARWSYDNTGIRA-DVAYDL-FTAADINHVTWSGDYELMIWLARYGGVQPIGSQIA 153
CMCase-I    94 SIPTSVTWSQDDTNVQA-DVSYDL-FTAANADHATSSGDYELMIWLARYGSVQPIGKQIA 151
CelS       118 NKSITSNVTYSIKATGTYNAAYDIWFHTTDKANWDSSPTDELMIWLND-TNAGPAGDYIE 176
consensus                           YD  F          S   ELMIWL       P G

EG III     152 TVNVGGQSWTLYYG----YNGAMQ-VYSFVAQTNTTNYSGDVKNFFNYLRDNKGYNAAGQ 206
F1-CMCase  154 TATVDGQTWELWYG---AN-GS-QKTYSFVAPTPITSFQGDVNDFFKYLTQNHGFPASSQ 208
CMCase-I   152 TATVGGKSWEVWYG-TSTQAGAEQKTYSFVAGSPINSWSGDIKDFFNYLTQNQGFPASSQ 210
CelS       177 TVFLGDSSWNVFKGWINADNGGGWNVFSFVHTSGTNSASLNIRHFTDYLVQTKQWMSDEK 236
consensus      T       W    G      G      SFV              F  YL

                        *
EG III     207 YVLSYQFGTEPFT-GSGTLNVASWTASIN                                234
F1-CMCase  209 YLITLQFGTEPFTGGPATLSVSNWSASVQ                                237
CMCase-I   211 HLITLQCGTEPFTGGPATFTVDNWTASVN                                239
CelS       237 YISSVEFGTEIF-GGDGQIDITEWRVDVK                                264
consensus             GTE F  G        W
```

Fig. 1 Alignment of the EG III sequence with those of GH12 EGs.
Asterisks represents the conserved Glu residues among family-12 cellulases

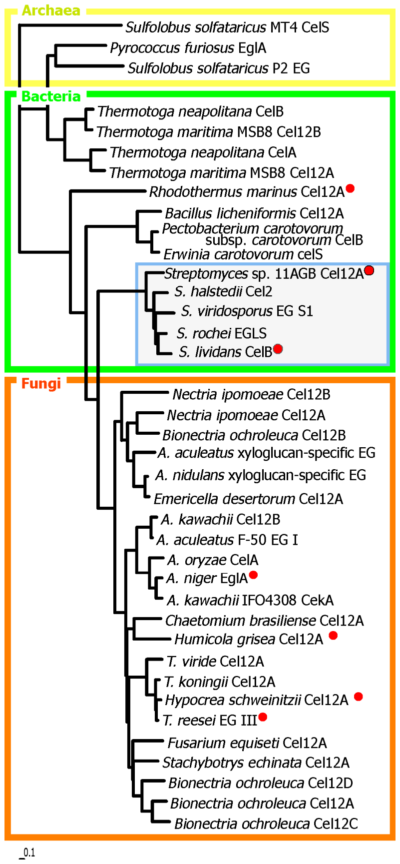

Fig. 2 Pylogenetic tree of GH12 enzymes.

3. Identification of catalytic residues in EG III

To identify the catalytic residues in EG III, the mature part of *egl3* cDNA was expressed in *E. coli* JM109 using the *tac* promoter. The *E. coli* transformant produced EG III protein largely as insoluble inclusion bodies in the cytoplasm of the cells. The insoluble fraction was solubilized with urea and EG III was purified by cation chromatography to electrophoretic homogeneity. The purified enzyme was immunologically and enzymologically identical to EG III purified from *T. reesei* (Table 1)[6].

Table 1 Properties of the EG IIIs from *T. reesei* and *E. coli*

	T. reesei	*E. coli*
Molecular mass (kDa)	25	25
Specific activity (U/mg)	12.7	13.1
Optimum pH	5.5	5.5
Optimum temperature (ºC)	55	55
pH stability	5.0-5.5	5.0-5.5
Temperature stability	up to 45ºC	up to 45ºC

Two glutamic acid residues, Glu-116 and Glu-200 of *T. reesei* EG III are conserved among family-12 cellulases (Fig. 1) and presumed to act as the nucleophile and the acid/base in the double displacement mechanism. To confirm this, Glu-116 and Glu-200 were separately replaced with Asp or Gln by site-directed mutagenesis. A double mutant, E116D:E200D, having two aspartates at these putative catalytic residues was also prepared. All the mutants were expressed in *E. coli* as inclusion bodies, which were solubilized and purified according to the same procedure as that for the wild-type (wt) EG III. Based on the results of SDS-PAGE analysis, the mutant enzymes were obtained with similar yields to that of the wt enzyme, and the molecular mass of each mutant was estimated to be the same as that of the wt EG III (data not shown). Comparison of CD spectra of the mutants with that of the wt enzyme in the far-UV regions did not reveal any significant difference, indicating that the mutations did not affect the fold of the enzyme (data not shown).

Specific activity and kinetic parameters, K_m and k_{cat}, of the wt EG III and the mutants were determined using CMC as a substrate (Table 2). The specific activities of the Asp mutants, E116D and E200D, were 1.7% and 0.4% of that of the wt EG III, respectively, while the double mutant E116D:E200D displayed little activity. The k_{cat} values of the mutant enzymes E116D and E200D were 50- and 200-fold lower than that of the wt enzyme, respectively, which corresponded to the decreases in specific activity. On the other hand, both of the Gln mutants, E116Q and E200Q, had little activity, namely 0.01-0.02% of that of the wt enzyme, strongly suggesting that these glutamic acids play an important role in the catalysis of hydrolysis The K_m value of the E116D mutant (4.2 g/L) was twofold higher than that of the wt EG III (2.0 g/L), while that of the E200D mutant (0.5 g/L) was reduced to one fourth of that of the wt EG III. Furthermore, the catalytic efficiency (k_{cat}/K_m) of the mutant enzyme E116D was more than two orders of magnitude lower than that of the wt enzyme. Reduction of catalytic efficiency was less pronounced when E200 was replaced by D. The results observed in other double-replacement-mechanism glycosidases [7] indicate that the acid/base residues usually less contribute to catalysis than the nucleophile residues. From these findings, it is plausible that Glu-116 and Glu-200 act as the nucleophile and the general acid/base, respectively, in the catalysis of hydrolysis.

Table 2 Specific activities and kinetic parameters of wild-type and mutant enzymes with CMC as a substrate

Enzyme	Specific activity		K_m (g/L)	k_{cat} (s^{-1})	k_{cat}/K_m (L/g・s)
	(U/mg)	(%)			
Wild type	13.1	(100)	2.00	5.50	2.8
E116D	0.214	(1.7)	4.17	0.106	0.025
E200D	0.0483	(0.40)	0.500	0.0265	0.053
E116:E200D	1.82×10-3	（0.015）	−	−	−
E116Q	1.61×10-3	（0.013）	−	−	−
E200Q	2.39×10-3	（0.019）	−	−	−

4. Directed evolution of EG III

Recently, improvement of individual cellulase enzymes has been attempted by protein engineering (rational protein engineering or directed evolution) in order to enhance cellulose degradation ability in *T. reesei* [8, 9]. It is difficult to obtain the desired enzyme by rational protein engineering because enzyme structure-function relationships are poorly understood. Directed evolution following random mutagenesis, which is not dependent on an understanding of structure-function relationships appears to be a better approach. The use of *E. coli* as a host for directed evolution of cellulase has obvious advantages. *E. coli* is amenable to molecular genetic analysis, grows rapidly, and is transformed at high frequency. EG III was slightly expressed as an active enzyme in the soluble fraction in *E. coli* JM109, but most of the recombinant protein was found in an inclusion body as described in section 3 [6]. Improvement of *E. coli* expression system to increase expression of EG III as an active form was performed with the pET expression vector system [10]. The *egl3* gene was subcloned from the *E. coli* expression vector into pET22b. Rosetta-gami B (DE3) pLacI exhibited the highest amount of CMCase activity among eight *E. coli* strains. The optimal temperature for maximal productivity of EG III was 37ºC (0.76 U/ml broth). Furthermore, in order to increase yields of functional EG III from *E. coli*, a simple purification method was developed. The method was based on the differential precipitation of *E. coli* proteins at pH4.0 that does not precipitate functional EG III. Thus, recombinant EG III from *E. coli* was easily separated from native *E. coli* proteins and inactive form EG III, yielding single band in SDS-PAGE. Enzymatic characteristics of the purified recombinant enzyme were the same as those of the native and renatured recombinant enzymes in Table 1. Employment of Rosetta-gami B (DE3) pLacI as a recombinant host and differential precipitation at acidic pH greatly facilitate development of improved EG III, through high-throughput screening of candidate enzymes obtained by directed evolution without refolding an inclusion body.

To improve the specific activity of EG III, directed evolution in *E. coli* was performed using error-prone PCR and activity screening in *E. coli* RosettaBlue (DE3) pLacI. This *E. coli* strain was a very suitable host for directed evolution because a very low basal activity of wild-type EG III was desirable for the identification of the mutant enzymes with enhanced enzymatic activity by high-throughput screening on plates. The clone harboring the highest stability and the highest specific activity produced the mutant enzyme, 2R4 with multiple mutations, G41E, T110P, K173M, Y195F, P201S, and N218I, which was selected via the second-round mutagenesis after the optimal first-round mutagenesis and screening. It produced 130-fold higher amount of the 2R4 enzyme than the transformant producing the wild-type EG III [11]. 2R4 showed broad pH stability ranging from pH4.4 to pH8.8 and complete thermotolerance at 55ºC for 30 min compared with those of the wild-type EG III with pH stability ranging from pH4.4 to pH5.2 and absolute thermosensitivity at 55ºC for 30 min. k_{cat} of 2R4 against carboxymethyl-cellulose was about 1.4-fold higher than that of the wild type, though the K_m was twice of that of the wild type (Table 3).

Table 3 Kinetic parameters of 2R4 mutant

Enzyme	Specific activity (U/mg)	k_{cat} (min^{-1})	K_m (g/L)	k_{cat}/K_m (L/g・min)
Wild type	22	630±10	1.5±0.2	440±50
2R4	26	860±30	3.0±0.4	290±20

Enzyme stabilization extends the duration of enzyme activity and the range of the reaction temperature, which is important for industrial application of enzymes, for example, laundry detergents, biomass saccharification, or the stonewashing of denim.

Acknowledgments

This work was supported by the Grant-in-Aid for Scientific Research from the Ministry of Education, Science, Sports, Culture and Technology, Japan, and by the grant from the Research Institute of Innovative Technology for the Earth (RITE) project.

References

[1] B. Henrissat, G. J. Davies, Plant Physiol. **124** (2000) 1515.
[2] C. S. Rye, S. G. Withers, Curr. Op. Chem. Biol. **4** (2000) 573.
[3] P. K. Foreman, D. Brown, L. Dankmeyer, R. Dean, S. Diener, N. S. DunnColeman, F. Goedegebuur, T. D. Houfek, G. J. England, A. S. Kelly, H. J. Meerman, T. Mitchell, C. Mitchinson, H. A. Olivares, P. J. M. Teunissen, J. Yao, M. Ward, J. Biol. Chem. **278** (2003) 31988.
[4] Y. Morikawa, A. Takahashi, K. Yano, M. Yamasaki, H. Okada, Genetics, Biochemistry and Ecology of Lignocellulose Degradation (eds. K. Shimada et al.) UNI Publishers, (1994) pp 458.
[5] H. Okada, K. Tada, T. Sekiya, K. Yokoyama, A. Takahashi, H. Tohda, H. Kumagai, Y. Morikawa, Appl. Environ. Microbiol. **64** (1998) 555.
[6] H. Okada, K. Mori, K. Tada, M. Nogawa, Y. Morikawa, J. Mol. Cat. B: Enzymatic **10** (2000) 249.
[7] S. L. Lawson, W. W. Wakarchuk, S. G. Withers, Biochemistry **36** (1997) 2257.
[8] A. G. Day (Genencor International IU) Patent (2003) 2,004,016,760.
[9] S. Teter, J. Cherry, Ward, C., A. Jones, P. Harris, J. Yi (Novozymes Biotech. IU) Patent (2004) 20050048619.

[10] H. Nakazawa, K. Okada, R. Kobayashi, T. Kubota, T. Onodera, N. Ochiai, N. Omata, W. Ogasawara, H. Okada, Y. Morikawa, Appl. Microbiol. Biotechnol. **81** (2008) 681.

[11] H. Nakazawa, K. Okada, T. Onodera, W. Ogasawara, H. Okada, Y. Morikawa, Appl. Microbiol. Biotechnol. **83** (2009) 649..

[12] T. Honma and T. Komatsu, Opt. Express **18** (2010) 8019.

[13] F. Suzuki, T. Honma, and T. Komatsu, Mater. Chem. Phys., **125** (2011) 377.

[14] F. Suzuki, K. Ogawa, T. Honma, and T. Komatsu, J. Solid State Chem., **185** (2011) 130.

[15] H. Tanaka, T. Honma, Y. Benino, T. Fujiwara, and T. Komatsu, J. Phys. Chem. Solids, **64** (2003) 1179.

[16] T. Honma, Y. Benino, T. Fujiwara, R. Sato, and T. Komatsu, J. Phys. Chem. Solids, **65** (2004) 1705.

Transactions on GIGAKU ***1****(2012)01034/1-6*

Electrostatic Layer-by-Layer Polymer Membranes for Heavy Metal Ion Desalination

Wei Min Zhou, Huitan Fu, Motohiro Tagaya, Takaomi Kobayashi *
Department of Materials Science and Technology, Nagaoka University of Technology,
1603-1 Kamitomioka-cho, Nagaoka 940-2188, Japan
**E-mail: takaomi@nagaokaut.ac.jp*

In the present review, we introduced the electrostatic self-assembly (ESA) modified membrances by forming ionic alternate layers of cetyl trimethyl ammonium chloride (CTAC) and poly(acrylic acid) (PAA) onto charged copolyacrylonitrile membranes. Along with surface characterization of the ESA multilayer, the desalination properties of the membranes with ESA multilayer were evaluated by investigating the metalion removal capability. Based on the experiment results, positively charged membrane terminated with CTAC on the ESA layer showed considerable high rejection for Fe^{3+}. Alternately deposited cationic chitosan microspheres showed effective ESA layer of PAA onto the desalination by charged polyacrylonitrile (PAN) membrane. It was confirmed that the alternative multilayer of chitosan micro sphere and PAA deposited on the base membrane surface presented removal capability of Cu^{2+}. Especially, membranes with chitosan microspheres / PAA ESA layers on the surface showed relatively higher adsorption capability as compared with membranes with chitosan / PAA ESA layers.

1. Introduction

It has been known that layer-by-layer (LbL) self-assembly is a spontaneous and reversible organization process of interacting organic and polymeric components by their aggregation into ordered structures on substrate. This technique has been widely applied for the fabrication of multilayer films of organic and polymeric compounds, organic-inorganic hybrid structures, larger objects such as latex particles, and even purely inorganic thin films. By combining various functional materials for the formation of self-assembly multilayer, the LbL technique has led to a wide range of novel materials for various applications [1,2]. It is noticed that the LbL fabrication is usually guided by a driving force of hydrophobic interaction [3], hydrogen-bond [4], covalent bonding [5], and electrostatic interaction [6] between assembled compounds. Among those driving forces, electrostatic interaction between oppositely charged molecules becomes a very fascinating and attractive approach because of its simplicity and efficiency. The technique of alternate layer-by-layer assembly of cationic and anionic polyelectrolytes, generally referred to electrostatic self-assembly (ESA) in 1991 [7]. They took advantage of the charge-charge interaction between oppositely charged layers to create electrolytes multilayer. The polyelectrolyte conformation and layer interpenetration were due to an idealization of the surface charge reversal with each adsorption step which was based on the electrostatically driven multilayer build-up depicted [8,9]. Because the substrate surface contained negatively or positively charged due to the alternate deposition of polycation or polyanion on the transmission of charged particles like ions through self-assembly polyelectrolyte multilayer membrane might be affected by the charged surface. Selectively ion transport behavior through ESA composite multilayer films was studied by Take [8] and Schelenoff [9]. The results suggested that highly specific ion separation was achieved and was affected by the charge and size of ion that pass through the composite multilayer. These researches made the polyelectrolytes multilayers interesting for the application of water desalination like heavy metal ion removal.

In this review, we introduce the ESA modified membranes by forming electrostatic alternate layers of cetyl trimethyl ammonium chloride (CTAC) and poly(acrylic acid) (PAA) onto charged copolyacrylonitrile membranes (Fig. 1). Along with surface characterization of the ESA multilayer, infrared analysis was carried out. Finally, we evaluated the adsorptive properties of ESA multilayer for Fe^{3+} and Fe^{2+} and ESA membranes with chitosan microspheres / PAA for removing of Cu^{2+}.

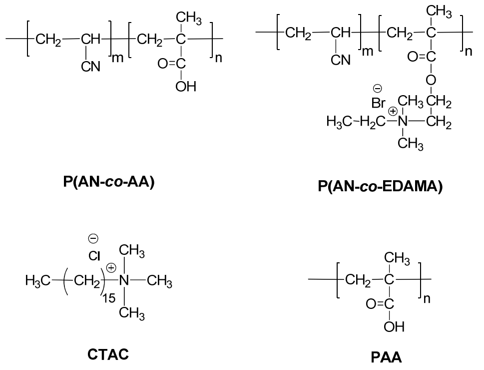

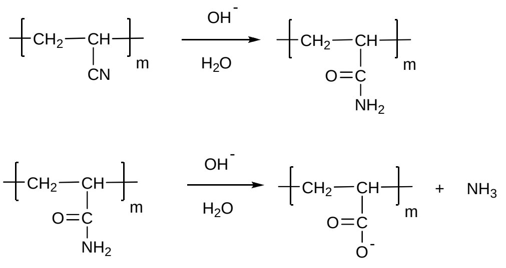

Fig. 1 Preparation procedure of ESA multi-layer on polymer membrane having negative charge.

Fig. 2 Chemical reaction of PAN treated by alkali solution.

2. Preparation of multilayer composite surfaces prepared by ESA technique and desalination behaviour

As presented in Fig. 3, quaternized *N*,*N*-dimethylethyl ammonium bromide (EDAMA) was polymerized with AN for preparation of cationic base membrane. AA and the quaternized EDAMA were used for their functional groups in order to provide charged sites for polyacrylonitrile base membranes. Also, poly(acrylonitrile-*co*-acrylic acid) [P(AN-*co*-AA)] membrane was used as a negatively charged base, while poly(acrylonitrile-*co*-N,N-dimethyethyl ammonium bromide P(AN-*co*-EDAMA) was used as a positively charged substrate [10,11]. Their base membranes of P(AN-*co*-AA) and P(AN-*co*-EDAMA) were prepared by phase-inversion of their respective dimethyl sulfoxide solutions in water [12]. The base membranes of P(AN-*co*-AA) or P(AN-*co*-EDAMA) were orderly dipped in positive CTAC and negative PAA aqueous solutions. After each deposition step, the resulting membranes were rinsed thoroughly with water. Such deposition process was repeated to obtain desired number of self-assembled layers.

As presented in Fig. 3, the base membrane surface was modified alternately by layer-by-layer formation of CTAC and PAA via ESA treatment. In Fig. 4, the FT-IR spectrum indicated that for the positively charged substrate of P(AN-*co*-EDAMA), the ESA treatment was performed in the deposition cycle order of PAA/CTAC/PAA/CTAC. As a result of the first deposition of the PAA layer, the band strength of the carboxylic group at about 1720 cm^{-1} became stronger. This confirmed the assembly of the PAA layer onto the positively charged base membrane. However, after the deposition of CTAC layer, the carboxylic groups bound on the CTAC layer resulted that the carboxylic acid absorption peak became weaker relative to that of P(AN-*co*-EDAMA)/PAA. A similar tendency repeated itself in accordance with the self-assembly of the first cycle of PAA layer and CTAC layer.

Since the alternate ESA layers on the membrane surface contained charged groups, it was expected that the permeate behavior of metal ions through the modified membrane could be affected by the ESA layers formed on the membrane surface [13,14]. Thus, the desalination of the ESA modified membranes was evaluated by testing the permeability for metal ion solution. Fig. 5 shows rejection for metal ions of Fe^{3+} and Fe^{2+} of resultant membranes of the P(AN-*co*-AA)/CTAC/PAA system and with solid lines for Fe^{3+} and dotted lines for Fe^{2+}. It could be seen that the membrane modified with ESA layers showed considerable high rejection for metal ion of Fe^{3+} and the rejection for Fe^{3+} was higher than for Fe^{2+}. This means that Fe^{2+} has a bigger ion radius of about 0.78 nm than the 0.64 nm of Fe^{3+}. Additionally, the change tendency of the rejection curves of the two systems for both metal ions behaved oppositely to each other as revealed in Fig. 3. These indicate that P(AN-*co*-AA) base membrane having COO^- on the surface was negatively charged, while P(AN-*co*-EDAMA) base membrane having quatemary ammonium groups on the surface was positively charged. Their different charge properties of base membrane surface resulted in different cycle order of self-assembled multilayer deposited on the base membrane surface, as performed in cycle of CTAC/PAA/CTAC/PAA for the former and PAA/CTAC/PAA/CTAC for the latter. The opposite change tendency of the permeability of resultant membranes further confirmed the influence of the ESA terminal layer on its permeability.

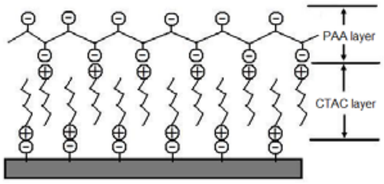

(a) P(AN-co-AA)/CTAC/PAA system

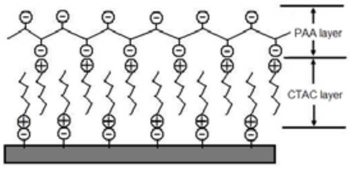

(b) P(AN-co-EDAMA)/PAA/CTAC system

Fig. 3 Illustration images of layer-by-layer assembling of CTAC and PAA on negatively charged P(AN-*co*-AA) membrane surface (a) and on positively charged P(AN-*co*-EDAMA) membrane surface (b).

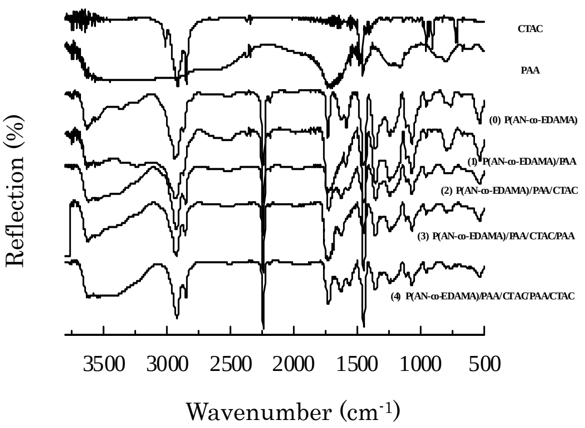

Fig. 4 FT-IR spectra of base membrane and membrane with self-assembled layers.

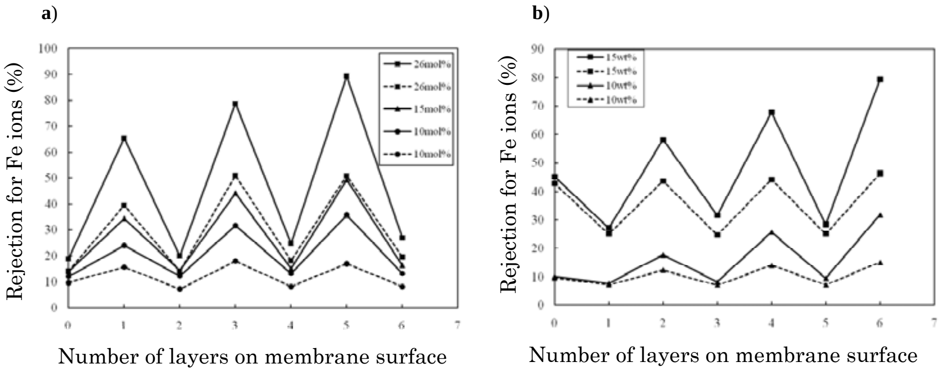

Fig. 5 a) The effect of AA fraction contained in base membrane on the rejection of Fe^{3+} (—) and Fe^{2+} (…) for P(AN-*co*-AA)/CTAC/PAA system (cast solution concentration for base membrane: 15wt%; pH of metal ions solution: 7). b) The effect of P(AN-*co*-EDAMA) base membrane on the rejection of Fe^{3+} (—) and Fe^{2+} (…) for P(AN-*co*-EDAMA)/PAA/CTAC system. (EDAMA contained in base membrane: 2 mol%; pH of metal ions solution: 7).

In different amounts of AA segments, three kinds of P(AN-*co*-AA) copolymers prepared with a AA fraction of 10 mol%, 15 mol% and 26 mol% [15], were used as base membranes for ESA treatment. Then, the surfaces were modified with ESA layers of CTAC and PAA to study the effect of AA fractions contained in the base membrane on the removal properties of modified membranes. It was found that, when the base membrane used for self-assembly treatment contained higher AA mol%, the corresponding resultant membranes showed higher removal properties for both Fe^{3+} and Fe^{2+}. This means that base membrane which contained higher AA mol% has more ionized carboxyl charged sites on the surface.

3. Self-assembly functionalized membranes with chitosan microsphere / polyacrylic acid layers.

In order to use negatively charged PAN, we converted the CN groups to negatively charged COO^- group on the PAN membrane surface, the chemical reaction (Fig. 2) was performed by using KOH solution. The FT-IR measurement was carried out to study the chemical composition of the PAN membrane surface before and after the KOH treatment. In the spectrum of the PAN membrane treated by KOH for 24 h, the characteristic absorption peak for the CN group at about 2300 cm^{-1} became weaker while the characteristic peak assigned to carboxyl group in the range from 2800 cm^{-1} to 3700 cm^{-1} appeared stronger. Especially, the band at 1700 cm^{-1} assigned to the carbonyl group from COO^- existed in the FT-IR spectrum. So, it was concluded that the PAN membrane surface was negatively charged due to the formation of carboxyl groups resulting from the KOH treatment.

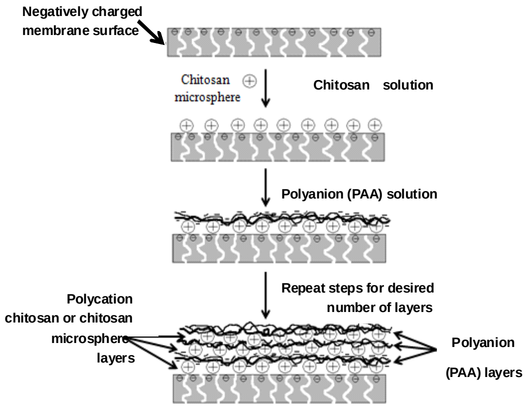

Fig. 6 Illustration images of layer-by-layer assembling of chitosan/PAA and chitosan microsphere/PAA layers onto charged base membrane.

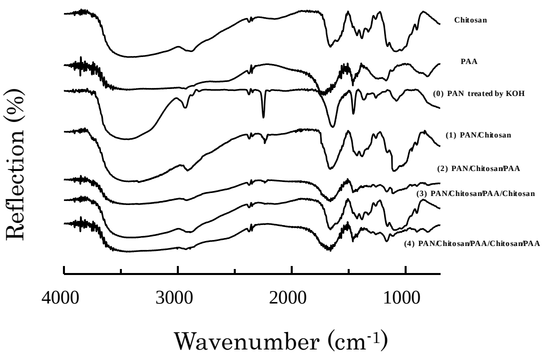

PAN/Chitosan microsphere/PAA system

Fig. 7 FT-IR spectra of membranes with self-assembled layers.

Fig. 6 shows the surface of treated PAN membrane which was negatively charged due to the KOH treatment. Then, the positively charged chitosan and negatively charged PAA were alternatively coated to form self-assembly layers onto the charged PAN membrane. Also, chitosan polycation microspheres cross-liked by sulfate groups were used instead of chitosan to form electrostatical self-assembled layers onto the negatively charged base membrane. The deposition process of the alternate formation of chitosan or chitosan microspheres and PAA layers was repeated 4 times.

The surface of membranes having alternate ESA multilayer was investigated by using reflection FT-IR spectroscopy (Fig. 7) for PAN/Chitosan/PAA system and PAN/chitosan microspheres/PAA system, respectively. It was found that the characteristic band of CN group from the charged PAN base membrane at about 2300 cm^{-1} became weaker due to the deposition of ESA layers of chitosan microgel and PAA. In addition, the characteristic band at about 1170 cm^{-1} corresponding to the primary alcoholic group of chitosan. The peak at about 1400 cm^{-1} was assigned to the stretching vibration of amide band from chitosan appeared in the spectra, especially for cycled 1 and 3, for which the surface was terminated with chitosan layer or chitosan microspheres layer. In the cases of cycle 2 and 4 for surfaces terminated with PAA layer, similar spectra with PAA were observed and it was believed to be resulted by the coverage of PAA on membrane surface. It was also noted for the PAN/Chitosan microsphers/PAA system, that the disappearance of the peak of the CN group from the charged PAN base membrane was drastic due to the coverage of the ESA layers. Surface roughness of the chitosan microspheres/PAA membranes were represented in Fig. 8. The surface roughness of -1 and 0 which referred to membranes before and after NaOH treatment, indicated that the membrane surface became rougher due to the existence of hydrophilic carboxyl groups resulting from NaOH treatment. Here, the -1 symbol means that the PAN membranes treated. It was also apparent that the surface morphology was dramatically altered by the formation of the chitosan microspheres/PAA ESA multilayer. While the corresponding surface roughness values was 8.0, 23.1, 15.0, 39.9, and 36.4 nm for the chitosan microspheres/PAA membranes with cycle layers of 0, 1, 2, 3 and 4, respectively. Therefore, the introduction of the chitosan microspheres for the ESA multilayer could be effectively for roughing the base of membrane surfaces.

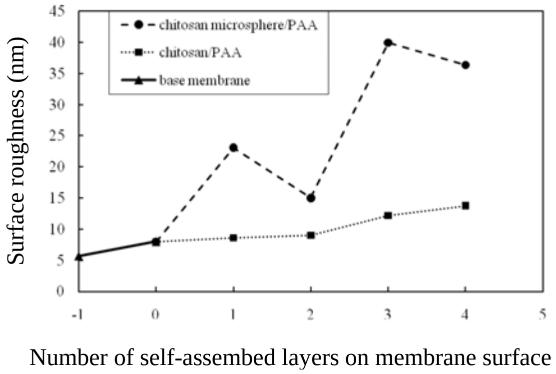

Fig. 8 Influence of numbers of self-assembled layers onto the membrane surface on the surface.

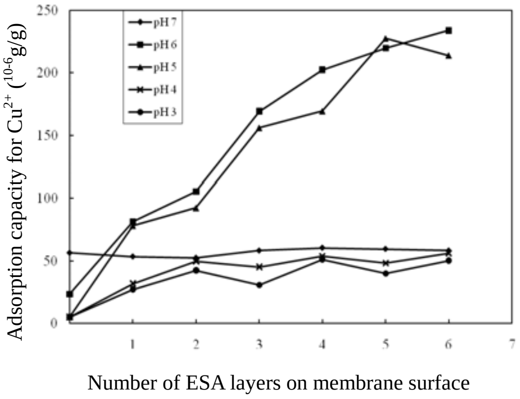

Fig. 9 Effect of the copper solution pH on the adsorption capacity of the resultant membranes of PAN/chitosan microsphere/PAA system.

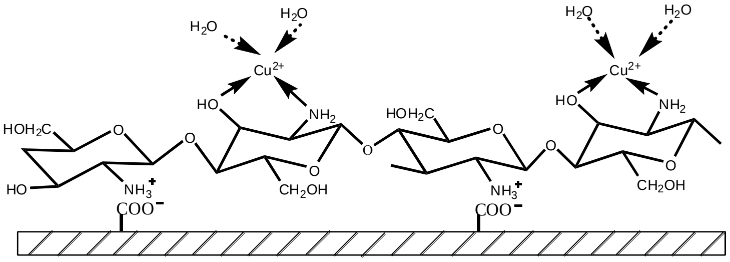

Fig. 10 Illustration images of the chelation for Cu^{2+} by the assembled chitosan on negatively charged membrane surface.

It is known that chitosan could be applied for adsorption of metal ions since the amino group is capable of binding metal ions as served as coordination sites. For example, Juang et al. [16] reported high selectivity for Cu^{2+} ion was observed by chitosan adsorbents. Chang et al. [17] found that the chitosan-modified microsphere showed the largest equilibrium adsorption capacity at pH 5.5. Therefore, in the present work, we studied the binding capability for Cu^{2+} ion of the resultant membrane at various pHs. Fig. 9 shows the effect of the pH of Cu^{2+} ion solution on the Cu^{2+} adsorption of resultant membranes with Chitosan microspheres/PAA multiple-layers. The adsorption amounts of the Cu^{2+} ion were plotted at the cycle number for the ESA multilayer formation. The odd layers were for the chitosan or chitosan microspheres layers exposed on the membrane surface outmost and evens were for PAA layers on the outmost. It is seen that when the adsorption was carried out at pH 3, the membranes terminated with PAA layers showed higher adsorption capacity rather than those with terminal chitosan or chitosan microspheres layers. But, when the pH increased, the change regulation could not be seen at pH 7 in both (a) and (b) systems. In the case of the chitosan microspheres/PAA system, the values of the adsorption capacity were significantly decreased to be in the range of about 50 ppm / g-membrane. However, at pH 5 and 6, the values of the adsorption capacity increased with increasing the cycled number of the ESA operation and then ranged in about 200-240 ppm/g-membrane. It was thought that the adsorption capacity of the resultant membrane depended on the isoelectric point of chitosan, which was at about 6.3. At below the pH, the protonation of amine groups of chitosan could occur, while at higher pH the group behaved as non-protonated group. However, the binding ability of chitosan for copper ions was mainly due to the amine groups which were served as coordination sites for the sequestration of copper ion [18]. At lower pH, most of the amine groups in the chitosan segments was protonated and not available for copper uptaking by chelation. Thus, the values of the adsorption capacity decreased with decreasing pH. However, as the protonated chitosan at low pH was able to bind anions by electrostatic attraction [19], according with Fig. 10.

4. Conclusion

In the present reviews, layer-by-layer electrostatic self-assembly technique was used for the preparation of functional polymeric membranes with metal ion removal capability. The fabrication process and properties of the resultant membranes were mentioned by using data of FT-IR spectra in detail. The negatively charged P (AN-*co*-AA) membrane and positively charged P (AN-*co*-EDAMA) were used as the substrates for the ESA treatment. The desalination behavior of the ESA multilayer modified resultant membranes was studied by evaluating the metal-ion removal properties for Fe^{3+} and Fe^{2+}. Also, membranes with chelation capability were prepared by the alternate self-assembled of chitosan layer and PAA layer on PAN membrane surface. Taking advantage of the adequate surface area and a large amount of loading sites for metal ions, chitosan microspheres were introduced to use as cationic species for complex formation with Cu^{2+} ion by the ESA multilayer. The result of adsorption experimental for Cu(II) showed that the layer-by-layer deposition of chitosan/PAA or chitosan microspheres/PAA on charged base membrane surface was functionally equipped it with chelating ability for Cu^{2+}.

Acknowledgment

We thank the supporting of Program for Project supported by forming a Hub for Human Resources Development and New Industry Creation Building a Sustainable Society Through Highly Interactive, Cooperative Educational Research with Pacific Rim Countries.

References

[1] S. Zapotoczny, M. Golonka, and M. Nowakowska, Macromol. Rapid Commun., **26** (2005) 1049.
[2] D. K. Kweon, S. B. Song, and Y. Y. Park, Biomaterials, **24** (2003)1595.
[3] E. Lojou, and P. Bianco, Langmuir. **20** (2004) 748.
[4] V. Kozlovskaya, S. Ok, S. Sousa, M. Libera, S. A. Sukhishvili, Macromolecules **36** (2003) 8590.
[5] Y. S. Kim, J. Y. Koo, and H. M. Kim, Phys. Rev. Lett., **100** (2008) 256105/1-4.
[6] S. P. Jiang, Z. Liu, and Z. Q. Tian, Adv. Mater., **18** (2006) 1068.
[7] G. Decher, Science, **277** (1997) 1232.
[8] L. Krasemann and B. Tieke, Langmuir, **16** (1999) 287.
[9] T. R. Farhat, and J. B. Schlenoff, J. Am. Chem. Soc., **125** (2003) 4627.
[10] Y. Ding, B. Bikson, and J. K. Nelson, Macromolecules, **35** (2002) 912.
[11] T. Kobayashi, H. T. Fu, Q. Cui, and H. Y. Wang, J. Appl. Polym. Sci., **110** (2008) 3234.
[12] T. Kobayashi, K. Kumagai, Y. Nosaka, H. Miyama, N. Fujii, and H. Tanzawa, J. Appl. Polym. Sci., **43** (1991)1037.
[13] M. Y. Arica, M. Yilmaz, and G. Bayramoglu, J. Appl. Polym. Sci., **103** (2007) 3084.
[14] D. X. Wang, M. Su, Z. Y. Yu, X. L. Wang, M. Ando, and T. Shintani, Desalination., **175** (2005) 219.
[15] X. L. Wang, T. Tsuru, S. Nakao, and S. Kimura, J. Membr. Sci., **135** (1997) 19.
[16] R. S. Jang, and H. J. Shao, Adsorption, **8** (2002) 71.
[17] Y. C. Chang, S. W. Chang, and D. H. Chen, Reac. Func. Polym., **66** (2006) 335.
[18] L. Dambies, C. Guimon, S. Yiacoumi, and E. Guibai. Colloids Surf. A., **77** (2000) 203.
[19] E. Guibal, Sep. Purif. Technol., **38** (2004) 43.

(Received: 23 March, 2012, Accepted: 27 April, 2012)